

**Understanding the mechanisms regulating liver fibrosis  
(including the use of imaging techniques in its study and  
diagnosis)**

**Stephen John Hill (BSc, MRes)**



Thesis submitted in fulfillment of the requirements for the degree Doctor of  
Philosophy

**Institute of Cellular Medicine**

**Faculty of Medical Sciences**

**Newcastle University**

**September 2012**

**Declaration**

I hereby declare that all the work presented in this thesis is my own unless stated otherwise within the text or acknowledged accordingly within the references. The data has not been submitted previously for any alternative degrees.

Stephen Hill

**Abstract**

Fibrosis is characterised by the excessive accumulation of extracellular matrix (ECM) proteins, resulting in a loss of tissue architecture and function. Central in liver fibrosis development is the transdifferentiation of hepatic stellate cells (HSCs) to a myofibroblast phenotype, responsible for increased deposition of ECM. Presently there are no treatments available for fibrosis. Critical to the discovery of novel anti-fibrotics is the development of a non-invasive imaging modality to accurately diagnose fibrosis severity.

The hepatic myofibroblast specific single chain antibody (scAb) C1-3 was conjugated with a fluorophore and administered to mice with liver fibrosis prior to IVIS imaging to diagnose fibrosis severity. The expression of C1-3's target antigen (synaptophysin) was confirmed by quantitative real-time PCR (qRT-PCR) and immunocytochemistry (ICC) in both quiescent and activated HSCs. The anti-inflammatory effects of PXR agonists were investigated utilising an *in vivo* model of liver fibrosis. Finally the pro-inflammatory properties of hepatic myofibroblasts were studied *in vitro* and *in vivo*.

There was a statistically significant increase in fluorescence detected *ex vivo* in fibrotic livers versus the controls. qRT-PCR confirmed that quiescent HSCs (qHSCs) and hepatic myofibroblasts express similar levels of synaptophysin. The PXR agonist PCN significantly reduced the level of liver inflammation (NF- $\kappa$ B activity) following liver injury *in vivo*, 24 hours after its administration. The data presented indicates hepatic myofibroblasts release a pro-inflammatory soluble factor and induce NF- $\kappa$ B activity when injected *in vivo*.

These findings suggest that hepatic myofibroblast number is an indicator of fibrosis severity. Hepatic myofibroblasts possess pro-inflammatory characteristics, which may contribute to fibrosis development. Finally PXR agonists exhibited anti-inflammatory properties that may be beneficial in the treatment of liver fibrosis.

## Acknowledgements

Firstly I would like to say a massive thank you to Professor Matthew Wright for his endless supply of expertise, advice and support over the last four years. I will always be grateful to him for giving me this opportunity and helping me evolve as a scientist (and possibly as a person?). It has been an absolute privilege to work under his tutelage with his inspiring words and analogies 'data cows' whether in the lab 'they love it', pub 'inappropriate drunken comment' or even on the football pitch 'come on guys'.

In addition thanks must go to the other members of Team Wright both past and present – Karen Wallace, Dave Cowie, Andy Axon, Helen Tovey, Emma Fairhall, Izzy Swidenbank, Anne Lakey, Philip Probert, Aiman Amir and Michelle Charles. I would like to thank them for their assistance throughout my studies whether it was technical or emotional. However mainly for just making work that little bit more entertaining every day, with the exception of Probert's terrible one liners.

Special acknowledgement must be given to Dr Harald Carlsen and his staff at the University of Oslo for their technical assistance in performing the IVIS work in the PXR *in vivo* study (chapter 5). Likewise I must acknowledge the contribution of Emma Fairhall and Ian Broadbent (Pfizer, Wyeth, UK) for carrying out the C1-3-750 BIACORE analysis (Figure 3.5).

As well thanks must go to the other major group in my life Team Hill, Mum, Dad, Rob, Claire, Lil Elizabeth, Jimmi and Julie for helping me. I have so much to thank my mum and dad for it is impossible to put into words, I would not be here without all their help and love over the years.

Finally I would like to thank my girlfriend Laura who has been with me every step of the way, through the good times and the not so good times with endless amounts of love and support. I know I would not have been able to complete this without her and that is why this thesis is dedicated to her.

## Table of Contents

<b>Declaration</b> .....	<b>i</b>
<b>Abstract</b> .....	<b>ii</b>
<b>Acknowledgements</b> .....	<b>iii</b>
<b>List of Figures</b> .....	<b>ix</b>
<b>List of Tables</b> .....	<b>xvii</b>
<b>List of Abbreviations</b> .....	<b>xviii</b>
<b>Chapter 1.0 - Introduction</b> .....	<b>1</b>
<b>1.1 The liver</b> .....	<b>2</b>
1.1.1 General liver anatomy and physiology .....	2
1.1.2 Functional units.....	4
1.1.3 Liver functions.....	5
1.1.4 Hepatic cell types and their specific functions.....	6
<b>1.2 Liver disease</b> .....	<b>8</b>
1.2.1 Epidemiology & background .....	8
1.2.2 Liver fibrosis pathogenesis .....	9
1.2.3 HSCs and hepatic myofibroblast.....	10
1.2.4 In vitro/ vivo models of liver fibrosis .....	12
<b>1.3 Treatments of liver disease</b> .....	<b>15</b>
1.3.1 Reducing the initial immune response/ inflammation to avoid HSC activation.....	15
1.3.2 Directly prevent HSC activation. ....	16
1.3.3 Neutralise the proliferative, fibrogenic, contractile and pro- inflammatory responses of HSCs. ....	17
1.3.4 Induction of hepatic myofibroblast apoptosis. ....	17
1.3.5 Increase MMP activity and fibrotic scar degradation.....	18
<b>1.4 Targeting hepatic myofibroblasts</b> .....	<b>18</b>
1.4.1 Synaptophysin expression in the liver and the heterogeneity of hepatic myofibroblasts .....	19
1.4.2 C1-3 a recombinant human single chain antibody fragment (scAb) and synaptophysin.....	20
<b>1.5 Diagnosis of liver fibrosis</b> .....	<b>21</b>
1.5.1 Liver biopsy.....	21
1.5.2 Serum markers .....	23
1.5.3 Non-invasive imaging modalities .....	25
<b>1.6 The pregnane X receptor (PXR)</b> .....	<b>27</b>
1.6.1 The PXR pathway .....	27
1.6.2 PXR ligands and drug-drug interactions .....	29
1.6.3 PXR and inflammation .....	30
1.6.4 The PXR and liver fibrosis .....	31
<b>1.7 Nuclear factor-<math>\kappa</math>B (NF-<math>\kappa</math>B)</b> .....	<b>32</b>

1.7.1 NF- $\kappa$ B family members and signalling pathway .....	33
1.7.2 NF- $\kappa$ B and liver fibrosis.....	34
<b>1.8 Study objectives .....</b>	<b>34</b>
<b>Chapter 2.0 - Materials and Methods .....</b>	<b>37</b>
<b>2.1 Materials.....</b>	<b>38</b>
<b>2.2 Animals .....</b>	<b>38</b>
2.2.1 Ethics.....	38
2.2.2 Housing.....	38
2.2.3 C57B1/6 (wildtype) mice.....	38
2.2.4 3x- $\kappa$ B-luc C57BL/6J x CBA/J (NF- $\kappa$ B luciferase) mice.....	39
2.2.5 Sprague-Dawley rats .....	39
2.2.6 Dosing solutions .....	39
<b>2.3 Cell culture.....</b>	<b>40</b>
2.3.1 Primary human HSCs (hHSCs) .....	40
2.3.2 Primary mouse and rat HSCs .....	41
2.3.3 LX-2 cells (human myofibroblast cell line).....	41
2.3.4 Cos7 cells .....	42
2.3.5 U937-NF- $\kappa$ B cells (human monocytic cell line stably transfected with luciferase reporter gene under the control of 3 x NF- $\kappa$ B response elements).....	42
2.3.6 Cell passage.....	42
2.3.7 Cell storage.....	43
2.3.8 Cell revival .....	43
2.3.9 Cell viability and number.....	44
2.3.10 U937-NF- $\kappa$ B cells co-culture with LX-2 and hHSCs.....	44
2.3.11 LX-2 and hHSC conditioned media and its treatments .....	45
<b>2.4 Cell transfection .....</b>	<b>46</b>
2.4.1 Transfection using GeneJuice reagent (Merck) .....	46
2.4.2 Transfection using polyethylenimine (PEI) (Polysciences Inc.).....	47
2.4.3 Determination of transfection efficiency .....	47
<b>2.5 Plasmid DNA constructs.....</b>	<b>48</b>
2.5.1 Transformation of TOP10 competent cells (Invitrogen) .....	48
2.5.2 Storage of DNA plasmids.....	48
2.5.3 Miniprep purification of plasmid DNA.....	49
2.5.4 Maxiprep purification of plasmid DNA.....	49
2.5.5 3xNF- $\kappa$ B response element DNA insert construction.....	50
2.5.6 Restriction digests of plasmid DNA.....	50
2.5.7 Gel extraction of DNA samples.....	51
2.5.8 T4 DNA ligation of DNA plasmid and insert .....	51
<b>2.6 RNA and DNA isolation/ quantification .....</b>	<b>52</b>
2.6.1 RNA isolation .....	52
2.6.2 DNA isolation .....	53
2.6.3 RNA/ DNA quantification.....	53
2.6.4 DNase treatment of RNA .....	54
2.6.5 Reverse transcription.....	54
2.6.6 Polymerase Chain Reaction (PCR) .....	55

2.6.7 PCR primer design .....	56
2.6.8 Agarose gel electrophoresis .....	57
2.6.9 Quantitative real-time PCR (qRT-PCR) .....	58
<b>2.7 Protein isolation and quantification .....</b>	<b>59</b>
2.7.1 Preparation of whole tissue samples .....	59
2.7.2 Preparation of cell extracts .....	60
2.7.3 Lowry protein assay .....	60
2.7.4 Sodium-dodecyl sulphate polyacrylamide gel electrophoresis (SDS-PAGE) .....	61
2.7.5 Sample preparation and electrophoresis .....	62
2.7.6 Coomassie blue gel staining .....	62
2.7.7 Western blotting .....	63
<b>2.8 Immunohistochemistry (IHC) and immunocytochemistry (ICC) ...</b>	<b>64</b>
2.8.1 Immunohistochemistry (IHC) .....	64
2.8.2 Sodium citrate antigen retrieval .....	65
2.8.3 Proteinase K antigen retrieval .....	66
2.8.4 Haematoxylin and eosin staining (H&E) .....	66
2.8.5 Picro-sirius red staining .....	66
2.8.6 Fluorescent immunocytochemistry .....	67
<b>2.9 C1-3 production .....</b>	<b>67</b>
2.9.1 Bacterial culture and C1-3 protein expression .....	68
2.9.2 Protein isolation .....	68
2.9.3 C1-3 quantification and specificity .....	69
2.9.4 Binding ELISA .....	70
2.9.5 Capture ELISA .....	70
2.9.6 Detection of bound C1-3 .....	71
2.9.7 Conjugation of C1-3 to Fluorescein isothiocyanate (FITC) .....	71
2.9.8 Conjugation of C1-3 to Alexa-594 fluorophore .....	71
2.9.9 Conjugation of C1-3 to Xenolight™ XF750 .....	72
2.9.10 Conjugation of C1-3 to gliotoxin (GTX) .....	72
<b>2.10 Animal imaging .....</b>	<b>73</b>
2.10.1 Luminescence imaging .....	73
2.10.2 Fluorescent imaging .....	74
<b>2.11 Serum and tissue storage .....</b>	<b>74</b>
<b>2.12 Tissue homogenisation .....</b>	<b>75</b>
<b>2.13 Luciferase assay .....</b>	<b>75</b>
<b>2.14 Griess assay .....</b>	<b>75</b>
<b>Chapter 3.0 - The use of C1-3-750 as a non-invasive diagnostic imaging agent for hepatic fibrosis .....</b>	<b>77</b>
3.1 Introduction .....	78
3.2 Conjugation of C1-3-750 and its functioning <i>in vitro</i> .....	79
3.3 Pilot study of C1-3-750 functioning in an <i>in vivo</i> model of liver fibrosis .....	89

3.4 The effect of C1-3-750 injection route upon imaging outcome <i>in vivo</i> .....	93
3.5 Using C1-3-750 <i>in vivo</i> to distinguish between different fibrosis severities.....	98
3.6 C1-3-750 signal quenching by liver tissue – limitations of optical imaging .....	109
3.7 C1-3-750 functioning in an <i>in vivo</i> rat model of liver fibrosis.....	110
3.8 Chapter discussion .....	114
<b>Chapter 4.0 - C1-3 binding to synaptophysin and its' expression on hepatic myofibroblasts .....</b>	<b>119</b>
4.1 Introduction .....	120
4.2 Confirmation of C1-3's binding to synaptophysin .....	120
4.3 Variation in synaptophysin expression between species .....	122
4.3.1 Whole tissue synaptophysin expression .....	122
4.3.2 HSC synaptophysin expression .....	127
4.4 Variation in relative synaptophysin expression between quiescent and activated HSCs.....	128
4.5 Chapter discussion .....	133
<b>Chapter 5.0 - The anti-inflammatory potential of PXR activators in an <i>in vivo</i> model of liver fibrosis .....</b>	<b>135</b>
5.1 Introduction .....	136
5.2 Anti-inflammatory properties of PCN in an <i>in vivo</i> (chronic and acute) model of liver fibrosis.....	137
5.3 PCN administration does not influence CCl <sub>4</sub> hepatotoxicity and severity of fibrosis development .....	148
5.4 Chapter discussion .....	159
<b>Chapter 6.0 - Uncovering hepatic myofibroblasts inflammatory potential <i>in vitro</i> and <i>in vivo</i>.....</b>	<b>164</b>
6.1 Introduction .....	165
6.2 Generation of a NF- $\kappa$ B luciferase reporter construct and stable transfection of U937 cells .....	167
6.3 LX-2 and hHSCs are pro-inflammatory when co-cultured with U937-NF- $\kappa$ B cells.....	171
6.3.1 LX-2s and hHSCs release a pro-inflammatory soluble factor .....	173
6.3.2 The pro-inflammatory soluble factor released by LX-2 cells is a small (<1kDa) non peptide.....	178
6.4 Screening of potential inflammatory/ fibrotic agents with U937-NF- $\kappa$ B cells.....	180
6.4.1 Treatment of U937-NF- $\kappa$ B cells with inflammatory cytokines and fibrotic compounds.....	180

6.4.2 Increased production of nitric oxide (NO) and ROS does not induce NF- $\kappa$ B activity in U937-NF- $\kappa$ B cells .....	183
<b>6.5 <i>In vivo</i> studies investigating the inflammatory properties of hepatic myofibroblasts.....</b>	<b>186</b>
6.5.1 NF- $\kappa$ B luciferase mice genotyping .....	186
6.5.2 Pilot study of hepatic myofibroblast injection directly into NF- $\kappa$ B luciferase mice.....	187
6.5.3 <i>In vivo</i> study to determine if hepatic myofibroblasts inflammatory traits are unique or a property of other cell types.....	197
6.5.4 The effect of C1-3-GTX mediated hepatic myofibroblast depletion upon acute liver inflammation .....	205
<b>6.6 Chapter discussion .....</b>	<b>210</b>
<b>Chapter 7.0 – General discussion .....</b>	<b>216</b>
7.1 Results summary .....	217
7.2 Project limitations and future work .....	222
7.3 Conclusions.....	225
<b>Chapter 8.0 – References.....</b>	<b>227</b>
<b>Chapter 9.0 - Published abstracts and manuscripts.....</b>	<b>251</b>
<b>9.1 Abstracts.....</b>	<b>252</b>
9.1.1 British Toxicology Society (BTS) Annual Conference 2009 .....	252
9.1.2 International Society for Hepatic Sinusoidal Research (ISHSR) symposium 2010.....	253
9.1.3 North East Postgraduate Conference (NEPG) 2011 .....	254
<b>9.2 Published manuscripts .....</b>	<b>254</b>

**List of Figures**

	<b>Page</b>
<b>Chapter 1.0</b>	
<b>Figure 1.1</b> General liver anatomy	<b>2</b>
<b>Figure 1.2</b> Architecture of the hepatic sinusoids and location of specific hepatic cell types	<b>3</b>
<b>Figure 1.3</b> Schematic diagrams of Kiernan's lobule and Rappaport's acinus	<b>5</b>
<b>Figure 1.4</b> Major cellular morphological changes that occur during fibrosis development	<b>10</b>
<b>Figure 1.5</b> Schematic illustrating CCl <sub>4</sub> hepatotoxicity mode of action	<b>14</b>
<b>Figure 1.6</b> Outline of human synaptophysin protein	<b>21</b>
<b>Figure 1.7</b> Schematic diagram illustrating the domains present in all members of the NRS and sequence comparison across species illustrating PXR homology	<b>28</b>
<b>Figure 1.8</b> Canonical NF- $\kappa$ B signalling pathway	<b>33</b>
<b>Chapter 2.0</b>	
<b>Figure 2.1</b> Diagram of SYBR Green qRT-PCR reaction	<b>59</b>
<b>Figure 2.2</b> Schematic of C1-3-GTX conjugation reaction	<b>73</b>
<b>Figure 2.3</b> Griess assay chemical reaction	<b>76</b>
<b>Chapter 3.0</b>	
<b>Figure 3.1</b> SDS-PAGE analysis of C1-3 before and after conjugation with XF750 and comparison vs. BSA standards	<b>80</b>
<b>Figure 3.2</b> MALDI-TOF analyses of C1-3 and its conjugates	<b>81</b>

<b>Figure 3.3</b> Quantification of C1-3-750 concentration by capture ELISA versus human IgG standards	<b>83</b>
<b>Figure 3.4</b> Specificity ELISA of C1-3 and C1-3-750 to BSA synaptophysin peptide sequences 1 & 2	<b>84</b>
<b>Figure 3.5</b> BIACORE analyses of C1-3 and C1-3-750	<b>85</b>
<b>Figure 3.6</b> Fluorescence spectra of C1-3-750	<b>85</b>
<b>Figure 3.7</b> ICC of C1-3 conjugates in vitro with mHSCs and hHSCs	<b>87-88</b>
<b>Figure 3.8</b> Whole body fluorescent background scan prior to i.v. injection (and scan 4 hours after injection) of C1-3-750 into a control and CCl <sub>4</sub> treated mouse	<b>90</b>
<b>Figure 3.9</b> <i>Ex vivo</i> organ scan 4 hours after C1-3-750 administration	<b>91</b>
<b>Figure 3.10</b> Whole body (4 hour time point) and <i>ex vivo</i> organ scan + example ROIs used for total fluorescence calculations	<b>92</b>
<b>Figure 3.11</b> Total fluorescence values calculated for both the whole body and <i>ex vivo</i> organ scans	<b>93</b>
<b>Figure 3.12</b> Whole body fluorescent scans over two hour time course for i.p., i.v. and non inject C1-3-750 administered mice	<b>95</b>
<b>Figure 3.13</b> Whole body fluorescent scan + ROIs for the upper abdominal and bladder regions, and the total fluorescence values	<b>96</b>
<b>Figure 3.14</b> <i>Ex vivo</i> organ scan (with and without ROIs) and total fluorescence calculations for the individual organs from the i.p., i.v. and non inject C1-3-750 administered mice	<b>97</b>
<b>Figure 3.15</b> Schematic diagram outlining the dosing and imaging regimens for the animal study trying to differentiate fibrosis severity	<b>99</b>

<b>Figure 3.16</b> Whole body scan from the 12 week CCl <sub>4</sub> treated and control mice	<b>100</b>
<b>Figure 3.17</b> <i>Ex vivo</i> organ scan from the 12 week CCl <sub>4</sub> treated and control mice	<b>101</b>
<b>Figure 3.18</b> Example whole body and <i>ex vivo</i> organ images annotated with ROIs	<b>102</b>
<b>Figure 3.19</b> Total fluorescence values calculated for the upper abdominal and bladder regions of each treatment group	<b>103</b>
<b>Figure 3.20</b> Total fluorescence values for the major organs of each treatment group following their excision	<b>104</b>
<b>Figure 3.21</b> Total fluorescence of excised liver from each treatment group	<b>105</b>
<b>Figure 3.22</b> αSMA IHC analysis of liver tissue from each treatment group	<b>106</b>
<b>Figure 3.23</b> Sirius red IHC analysis of liver tissue from each treatment group	<b>107</b>
<b>Figure 3.24</b> αSMA and sirius red IHC quantification	<b>108</b>
<b>Figure 3.25</b> Quenching of C1-3-750 fluorescence by liver tissue	<b>110</b>
<b>Figure 3.26</b> Whole body fluorescent scans over two hour time course for 4 week CCl <sub>4</sub> treated and control C1-3-750 rats	<b>112</b>
<b>Figure 3.27</b> Total fluorescence values calculated for the upper abdominal and bladder regions	<b>113</b>
<b>Figure 3.28</b> <i>Ex vivo</i> organ scan from the 4 week CCl <sub>4</sub> treated and control rat and total fluorescence values calculated for individual organs	<b>113</b>

**Chapter 4.0**

**Figure 4.1** C1-3-594 and synaptophysin ICC staining of transfected Cos7 cells **121**

**Figure 4.2** Western blotting analysis of transfected Cos7 synaptophysin expression **122**

**Figure 4.3** Alignment of mouse, rat and human synaptophysin DNA sequences and synaptophysin primer locations **123**

**Figure 4.4** Synaptophysin expression of mouse, rat and human whole tissue samples **124**

**Figure 4.5** Western blotting analysis of mouse, rat and human whole tissue samples synaptophysin protein expression **125**

**Figure 4.6** C1-3-594,  $\alpha$ SMA and synaptophysin ICC staining of individual mouse, rat and human whole tissue samples **126**

**Figure 4.7** Synaptophysin expression of mouse, rat and human HSCs **127**

**Figure 4.8** Western blotting analysis of mouse, rat and human HSCs synaptophysin protein expression **128**

**Figure 4.9 A** Quantitative real-time PCR analysis of quiescent and activated HSCs synaptophysin expression. **B** Average cT values for each cell type **129**

**Figure 4.10** C1-3-594,  $\alpha$ SMA and synaptophysin ICC staining of quiescent mouse and human HSCs **131**

**Figure 4.11** C1-3-594,  $\alpha$ SMA and synaptophysin ICC staining of activated mouse and human HSCs **132**

**Chapter 5.0**

**Figure 5.1** Schematic diagram outlining the dosing and imaging regimen **137**

<b>Figure 5.2</b> Whole body luminescent background scan prior to PCN administration	<b>138</b>
<b>Figure 5.3</b> Acute CCl <sub>4</sub> & acute CCl <sub>4</sub> + PCN whole body luminescent scans 6 hours after PCN administration	<b>139</b>
<b>Figure 5.4</b> Example whole body image annotated with ROIs and accompanying 6 hour total fluorescence values	<b>140</b>
<b>Figure 5.5</b> Chronic CCl <sub>4</sub> & Chronic CCl <sub>4</sub> + PCN whole body luminescent scans 24 hours after PCN administration	<b>141</b>
<b>Figure 5.6</b> Example whole body image annotated with ROIs and accompanying 24 hour total fluorescence values	<b>142</b>
<b>Figure 5.7</b> Chronic CCl <sub>4</sub> & Chronic CCl <sub>4</sub> + PCN <i>ex vivo</i> organ luminescent scans 24 hours after PCN administration	<b>143</b>
<b>Figure 5.8</b> A Example <i>ex vivo</i> organ scan annotated with ROIs and B total fluorescence values calculated for each treatment group	<b>145</b>
<b>Figure 5.9</b> Mean total fluorescence of excised liver from each treatment group	<b>146</b>
<b>Figure 5.10</b> Mean luciferase activity of liver homogenates from each treatment group	<b>147</b>
<b>Figure 5.11</b> Serum ALT and ALP concentrations	<b>148</b>
<b>Figure 5.12</b> H&E IHC analysis of all treatment groups	<b>149</b>
<b>Figure 5.13</b> αSMA IHC analysis of liver tissue from each treatment group	<b>150</b>
<b>Figure 5.14</b> αSMA IHC quantification	<b>151</b>
<b>Figure 5.15</b> Sirius red IHC analysis of liver tissue from each treatment group	<b>153</b>

<b>Figure 5.16</b> Sirius red IHC quantification	<b>154</b>
<b>Figure 5.17</b> NIMP IHC analysis of liver tissue from each treatment group	<b>155</b>
<b>Figure 5.18</b> NIMP IHC quantification	<b>156</b>
<b>Figure 5.19 A</b> Optimisation of luciferase IHC analysis of liver tissue from each treatment group. <b>B</b> Repetition of 1/250 primary antibody dilution in non transgenic mice	<b>157</b>
<b>Figure 5.20 A</b> Luciferase western blot analysis of individual liver protein samples. <b>B</b> Luciferase activity of Cos7's transfected with pGL3 control plasmid	<b>158</b>
<b>Figure 5.21</b> Luciferase western blot analysis of individual liver protein samples and Cos7 + pGL3 control plasmid (positive control)	<b>159</b>
 <b>Chapter 6.0</b>	
<b>Figure 6.1</b> Schematic illustration showing HSC transdifferentiation to hepatic myofibroblasts during chronic liver injury	<b>165</b>
<b>Figure 6.2</b> General morphology of quiescent and activated HSCs, LX-2 and U937-NF- $\kappa$ B cell lines	<b>166</b>
<b>Figure 6.3</b> Generation of NF- $\kappa$ B luciferase reporter construct	<b>168</b>
<b>Figure 6.4</b> Restriction digests to confirm insertion of the 3xNF- $\kappa$ B insert	<b>169</b>
<b>Figure 6.5</b> pGL4.28-3xNF- $\kappa$ B luciferase reporter construct DNA sequencing	<b>170</b>
<b>Figure 6.6</b> Confirmation of NF- $\kappa$ B luciferase reporter construct functioning	<b>171</b>
<b>Figure 6.7</b> LX-2's are pro-inflammatory and induce NF- $\kappa$ B activity in U937-NF- $\kappa$ B cells	<b>172</b>

<b>Figure 6.8</b> hHSC co-culture induces NF- $\kappa$ B activity in U937-NF- $\kappa$ B cells	<b>173</b>
<b>Figure 6.9</b> LX-2's release a pro-inflammatory soluble factor that induces NF- $\kappa$ B activity in U937-NF- $\kappa$ B cells	<b>175</b>
<b>Figure 6.10</b> hHSCs release a pro-inflammatory soluble factor that induces NF- $\kappa$ B activity in U937-NF- $\kappa$ B cells	<b>176</b>
<b>Figure 6.11</b> Treatment of U937-NF- $\kappa$ B cells with IL-6 and IL-8 does not induce NF- $\kappa$ B activity in U937- NF- $\kappa$ Bs	<b>178</b>
<b>Figure 6.12</b> Range of treatments to uncover more about the pro-inflammatory soluble factor	<b>179</b>
<b>Figure 6.13</b> Incubation of U937-NF- $\kappa$ B cells with the pro-inflammatory cytokines IL-1 $\alpha$ and IL-1 $\beta$	<b>181</b>
<b>Figure 6.14</b> Incubation of U937-NF- $\kappa$ B cells with a range of pro-fibrogenic and/ or pro-inflammatory molecules	<b>183</b>
<b>Figure 6.15</b> Effect of increased ROS concentration on NF- $\kappa$ B activity in U937-NF- $\kappa$ B cells	<b>185</b>
<b>Figure 6.16</b> Genotyping NF- $\kappa$ B luciferase mice	<b>187</b>
<b>Figure 6.17</b> Whole body luminescent scans over 72 hour time course following hepatic myofibroblast injection	<b>188</b>
<b>Figure 6.18</b> Example whole body scan with ROIs overlaid and the calculated total luminescence values	<b>190</b>
<b>Figure 6.19</b> Example <i>ex vivo</i> organ scan with ROIs overlaid and the calculated total luminescence values	<b>191</b>
<b>Figure 6.20</b> $\alpha$ SMA IHC analysis of liver tissue from each treatment group	<b>192</b>
<b>Figure 6.21</b> Whole body luminescent scans over 48 hour time course following hepatic myofibroblast and 'trypsin dummy' injection	<b>193</b>
<b>Figure 6.22</b> Whole body scan with ROIs overlaid and the calculated total luminescence values	<b>194</b>

<b>Figure 6.23</b> <i>Ex vivo</i> organ scan with ROIs overlaid and the calculated total luminescence values	<b>196</b>
<b>Figure 6.24</b> Whole body luminescent scans over 48 hour time course following kidney fibroblast injection	<b>198</b>
<b>Figure 6.25</b> Whole body scan with ROIs overlaid and the calculated total luminescence values	<b>200</b>
<b>Figure 6.26</b> <i>Ex vivo</i> organ scan with ROIs overlaid and the calculated total luminescence values	<b>201</b>
<b>Figure 6.27</b> Whole body luminescent scans over 48 hour time course following hepatic myofibroblast, kidney fibroblast and latex bead injection	<b>202</b>
<b>Figure 6.28</b> Whole body scan with ROIs overlaid and the calculated total luminescence values	<b>204</b>
<b>Figure 6.29</b> Schematic diagram outlining the dosing and imaging regimen to determine the effect of hepatic myofibroblast depletion on NF- $\kappa$ B activity	<b>205</b>
<b>Figure 6.30</b> Whole body luminescent scans over 96 hour time course following acute liver damage and C1-3 or C1-3-GTX administration	<b>207</b>
<b>Figure 6.31</b> Whole body scan with ROIs overlaid and the calculated total luminescence values	<b>208</b>
<b>Figure 6.32</b> <i>Ex vivo</i> organ scan with ROIs overlaid and the calculated total luminescence values	<b>209</b>

**List of Tables****Page****Chapter 1.0****Table 1.1** Major liver biopsy scores**21****Table 1.2** Common non-invasive serum biomarker panels**24****Chapter 2.0****Table 2.1** *In vivo* dosing solutions**39****Table 2.2** U937-NF- $\kappa$ B cells *in vitro* treatments**45****Table 2.3** Treatments to 48 hour LX-2 conditioned media**46****Table 2.4** DNA oligonucleotide sequences for qRT-PCR and PCR genotyping**57****Table 2.5** Antibody dilutions**65****Chapter 6.0****Table 6.1** Cytokine profiles of major hepatic cell types**177**

**List of Abbreviations**

**1 x PBS** - Phosphate buffered saline

**1 x PLB** - Passive lysis buffer

**1 x TAE** - Tris acetate EDTA

**AF-1** - Activation function 1

**ATP** - Adenosine-5'-triphosphate

**ALD** - Alcoholic liver disease

**ALP** - Alkaline phosphatase

**ALT** - Alanine transaminase

**ANOVA** - Analysis of variance

**APRI** - AST to platelet ratio index

**αSMA** - Alpha smooth muscle actin

**AST** - Aspartate aminotransferase

**BAFF** - B-cell activating factor

**BDL** - Bile duct ligation

**BSA** - Bovine serum albumin

**CCl<sub>4</sub>** - Carbon tetrachloride

**cDNA** - complementary DNA

**CML** - chronic myeloid leukaemia

**CO** - Carbon monoxide

**CO<sub>2</sub>** - Carbon dioxide

**cT** - Cycle threshold

**CTGF** - Connective tissue growth factor

**CYP450** - Cytochrome P450

**DAB** - Diaminobenzidine

- DAPI** - 4', 6-diamidino-2-phenylindole
- DBD** - DNA binding domain
- DMN** - Dimethylnitrosamine
- DMSO** - Dimethyl sulfoxide
- dsDNA** - Double stranded DNA
- DSS** - Dextran sulphate sodium
- DMEM** - Dulbecco's Modified Eagle Media
- ECM** - Extracellular matrix
- EDTA** - Ethylenediaminetetraacetic acid
- ELISA** - Enzyme-linked immunosorbent assay
- EGF** - Epidermal growth factor
- eGFP** - Enhanced Green Fluorescent Protein
- EtBr** - Ethidium bromide
- FCS** - Fetal calf serum
- FITC** - Fluorescein isothiocyanate
- GAPDH** - Glyceraldehyde 3-phosphate dehydrogenase
- GFAP** - glial fibrillary acidic protein
- GGT** -  $\gamma$ -glutamyltransferase
- GR** - Glucocorticoid receptor
- GSTs** - Glutathione-S-transferases
- GTX** - Gliotoxin
- H<sub>2</sub>O<sub>2</sub>** - Hydrogen peroxide
- H&E** - Haematoxylin and eosin
- HGF** - Hepatocyte growth factor
- hHSCs** - Human HSCs
- HRP** - Horse-radish peroxidase

**HSCs** - Hepatic stellate cells

**i.p.** - Intraperitoneal

**i.v.** - Intravenous

**ICC** – Immunocytochemistry

**IgG** - Immunoglobulin G

**IHC** - Immunohistochemistry

**IBD** - Irritable bowel disorder

**IMAC** - Immobilised metal ion chromatography

**IκB** - Inhibitor of κB

**IKK** - Inhibitor of κB kinase

**IL-6** - Interleukin-6

**IPTG** - Isopropyl β-D-1-thiogalactopyranoside

**IVIS** - In vivo imaging system

**LBD** - Ligand binding domain

**LB media** - Luria-Bertani media

**LPS** - Bacterial lipopolysaccharide

**LqN<sub>2</sub>** - Liquid nitrogen

**MALDI-TOF** - Matrix-assisted laser desorption/ionization time of flight

**MCP-1** - Monocyte chemotactic protein-1

**MIP-1α** - Macrophage Inflammatory Protein 1 alpha

**mHSCs** - Mouse HSCs

**M-MLV RT** - Moloney Murine Leukemia Virus Reverse Transcriptase

**MMPs** - Matrix metalloproteinases

**MRI** - Magnetic resonance imaging

**mRNA** - Messenger RNA

**MW** - Molecular weight

- NAFLD** - Non-alcoholic fatty liver disease
- NASH** - Non-alcoholic steatohepatitis
- NF- $\kappa$ B** - Nuclear factor kappa beta
- NGF** - Nerve growth factor
- NIK** - NF- $\kappa$ B-inducing kinase
- NO** - Nitric oxide
- NRS** - Nuclear receptor superfamily
- PBC** - Primary biliary cirrhosis
- PCN** - Pregnenolone-16 $\alpha$ -carbonitrile
- PCR** - Polymerase Chain Reaction
- PDGF** - Platelet derived growth factor
- PEI** - Polyethylenimine
- PET** - Positron emission tomography
- PPAR $\gamma$**  - Peroxisome proliferator-activated receptor gamma
- PXR** - Pregnane X receptor
- qRT-PCR** - Quantitative real-time PCR
- rHSCs** - Rat HSCs
- ROI** - Region of interest
- ROS** - Reactive oxygen species
- RXR** - Retinoic acid receptor
- scAb** - Single chain antibody
- SD** - Standard deviation
- SDS-PAGE** - Sodium-dodecyl sulphate polyacrylamide gel electrophoresis
- SNP** - Sodium nitroprusside
- TGF- $\beta$**  - Transforming growth factor  $\beta$
- TIMPs** - Tissue inhibitors matrix metalloproteinases

**TLR** - Toll like receptor

**TNF $\alpha$**  - Tumour necrosis factor alpha

**TRAF1** - TNF $\alpha$  receptor-associated factor 1

**Total fluorescence units** - Total Radiant Efficiency ([p/s] / [ $\mu$ W/cm<sup>2</sup>])

**VEGF** - Vascular endothelial growth factor

## **Chapter 1.0 - Introduction**

## 1.1 The liver

### 1.1.1 General liver anatomy and physiology

The liver is the largest visceral organ, located within the upper right quadrant of the abdominal cavity weighing approximately 1.5kg (up to 2.5% of the total body weight in an average human adult). In man the liver is composed of two main anatomical lobes; the larger right lobe is separated from the left by the falciform ligament (a fold in the peritoneum). The smaller caudate and quadrate lobes are attached to the posterior inferior surface of the right lobe (Figure 1.1). The fibrous capsule of Glisson encases the entire liver, except one posterior region, where it is in direct contact with the diaphragm. The capsule of Glisson serves to reduce friction against the surrounding organs, whilst also protecting the hepatic blood vessels and bile duct.

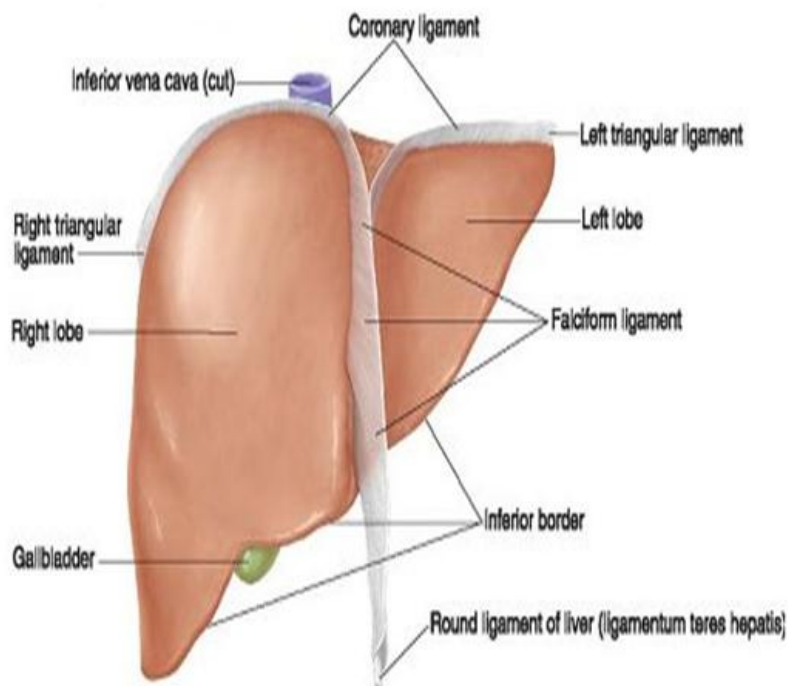
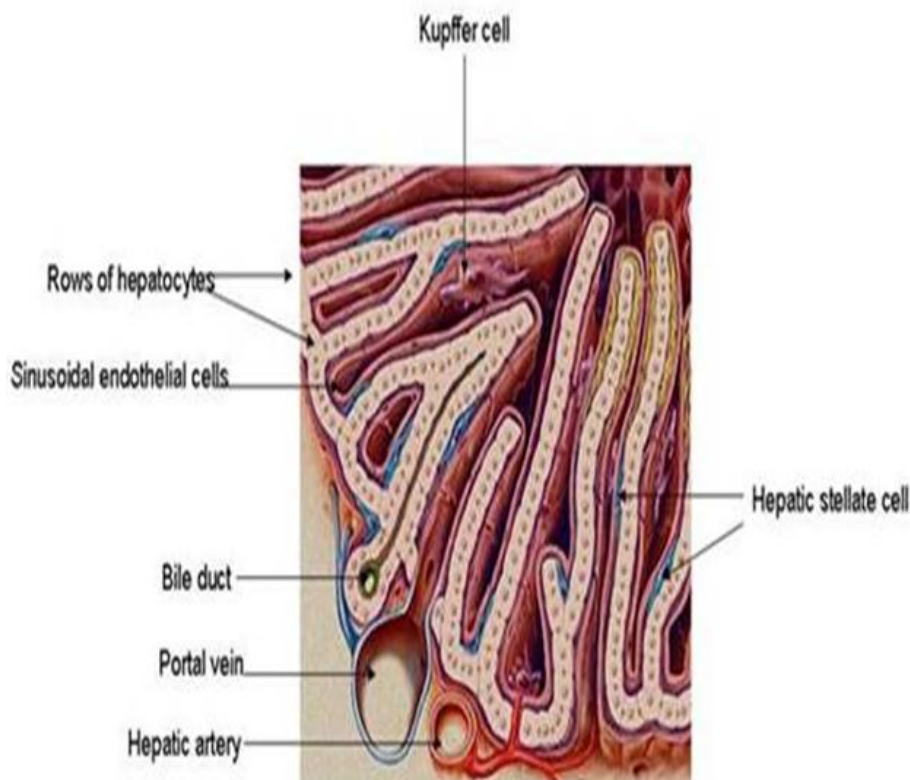


Figure 1.1 General liver anatomy (Image taken from [1])

The liver has a unique dual blood supply, arriving from the portal vein and hepatic artery, receiving approximately 75% and 25% from each respectively [2]. The blood from the portal vein is only partially oxygenated, but is rich in nutrients from the digestive tract, spleen, pancreas and gall bladder. Oxygenated blood arriving from the hepatic artery supplies the liver cells with the necessary oxygen for aerobic respiration and energy production. The two blood supplies mix at the edge of the portal tract before draining into the hepatic sinusoids.

Hepatic sinusoids are specialized blood vessels running between rows of hepatocytes, carrying blood from the portal tract to the central vein (before recirculation of the deoxygenated blood via the inferior vena cava). Bile produced by the hepatocytes is also transported to the bile duct via the sinusoids (Figure 1.2). Specialized fenestrated endothelial cells are found lining the hepatic sinusoid adapted to control the flow of macromolecules across the perisinusoidal area (Space of Disse) to the hepatocytes.



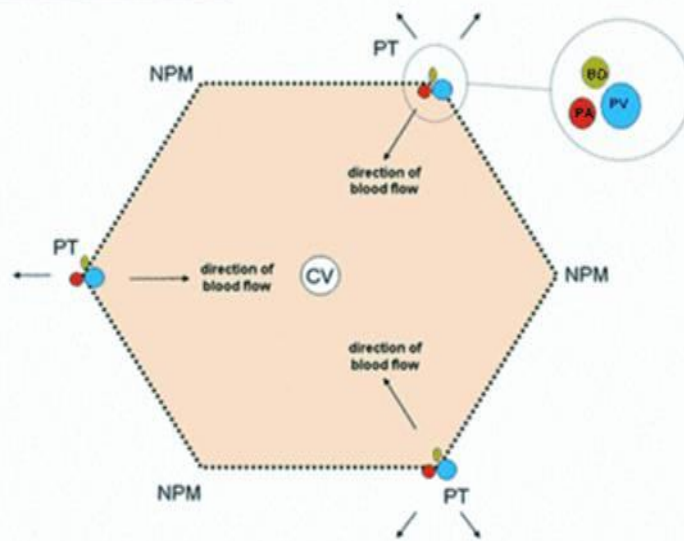
**Figure 1.2 Architecture of the hepatic sinusoids and location of specific hepatic cell types (Image taken from [3]).** Hepatic sinusoids are effectively the liver's capillaries and are found running between rows of hepatocytes. They are lined by specialized fenestrated endothelial cells to control the flow of materials between the sinusoids to the Space of Disse and hepatocytes. The space of Disse is where hepatic stellate cells (HSCs) are located; these cells are central in fibrosis development.

### **1.1.2 Functional units**

The structure of the liver has been well documented since Wepppler's initial description of liver lobules in 1665. The liver is known to be composed of tens of thousands of repeating functional units that are uniformly distributed around the portal tract (blood enters) and central vein (blood exits) [3, 4]. Many models have been proposed for these functional units, primarily due to the lack of a structural barrier between each functional unit making it difficult to define. The two most widely accepted are the liver lobule and liver acinus proposed by Kiernan [5] and Rappaport [6] respectively (Figure 1.3).

The hepatic lobule is based on a hexagonal unit with hepatocytes and sinusoids radiating out in branches [2, 5]. The central vein is found at the centre of the lobule and the portal triads (containing the bile canaliculi, portal venules and hepatic arterioles) are found at each corner of the hexagon defining the periphery of the lobule. The acinus of Rappaport is a smaller functional unit, consisting of an irregular shaped mass of hepatocytes aligned around the terminal afferent vessels (hepatic arterioles and distributing portal venules) just as they branch into the sinusoids [2, 6]. The blood flow from these branches is unidirectional as it flows along the sinusoids from the periportal to the centrilobular hepatocytes. The acinus can be divided into three functional zones (zone (1) periportal, (2) mediolobular, (3) centrilobular) governed by the difference in oxygen content in these areas decreasing from zone 1 – zone 3. Histopathologists favour the acinar model as it explains many pathological lesions in the liver. Another point of interest is the heterogeneous expression of genes along hepatic sinusoids, resulting in metabolic zonation across the lobule. Coupling the high expression of metabolic enzymes and the low levels of oxygen present, hepatocytes in zone 3 are most susceptible to both ischemic and drug-induced injury [7].

### The liver lobule



### The liver acinus

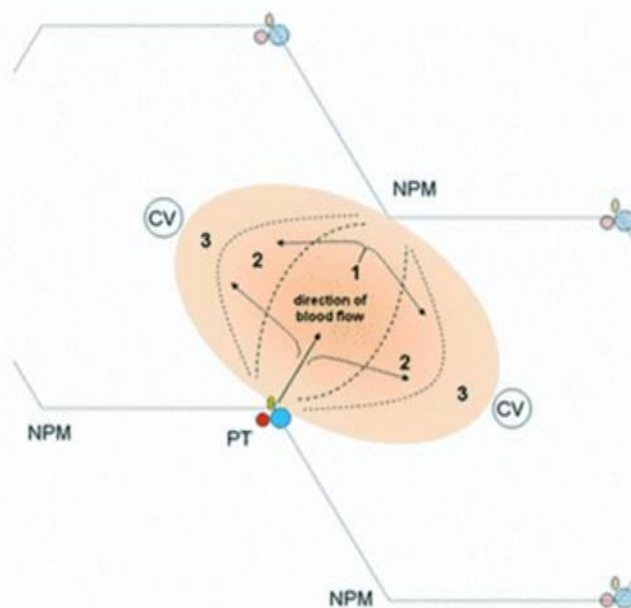


**Figure 1.3 Schematic diagrams of Kiernan's lobule (top) and Rappaport's acinus (bottom)** (Figure taken from [3]). The acinus has been overlaid onto the lobule schematic to aid in their comparison. In the lobule the portal tract (PT), which contains the periportal arteriole (PA – red dot), bile duct (BD – yellow dot) and periportal venule (PV – blue dot) mark the periphery of individual lobules and blood can flow in all directions including into surrounding lobules draining into the central vein (CV). However in the acinar model all blood entering from the portal tract is believed to stay in the acinus and the oxygen/ nutrient levels decrease as the blood diffuses from zone 1 – zone 3.

#### **1.1.3 Liver functions**

The major function of the liver is in intermediary metabolism and the metabolism/ clearance of xenobiotics absorbed from the environment and diet. It also performs a number of other critical roles essential in maintaining homeostasis throughout the body (including albumin production critical in maintenance of the blood volume and osmotic pressure). The bulk of these functions are carried out by the hepatocytes including [3, 8] : -

- Glycogenolysis and gluconeogenesis.
- Fatty acid metabolism.
- Amino acid metabolism and blood protein synthesis (e.g. coagulation and fibrinolysis factors, transport proteins and protease inhibitors).
- Ammonia metabolism and urea synthesis.
- Plasma lipid and lipoprotein metabolism (cholesterol, triglyceride and phospholipid homeostasis).
- Metabolism of bilirubin and bile acids prior to bile formation.
- Storage of metals (e.g. iron).

#### ***1.1.4 Hepatic cell types and their specific functions***

There are six major types of cell in the liver, each with an individual role critical to maintaining a healthy functional liver.

**Hepatocytes** account for over 60% of the total cell population of the liver and 80% of the liver volume [9]. They are highly specialized, containing a high number of mitochondria to provide the necessary ATP for the majority of the aforementioned functions (section 1.1.3). The hepatocyte's major function is intermediary metabolism and the metabolism of xenobiotics and compounds absorbed into the blood. They are specifically adapted for this by the presence of microvilli on the membrane in contact with the Space of Dissé, increasing the surface area available for uptake [2, 8]. The Space of Dissé (perisinusoidal space) represents a space between the sinusoidal endothelial

cells and hepatocytes which allows blood plasma to come into direct contact with the hepatocytes and improve absorption from the plasma.

**Kupffer cells** are liver resident macrophages, located in close proximity to the fenestrated endothelial cells lining the sinusoids. Their major function is to help remove any bacteria and cell debris from the blood as it flows along the sinusoids before reaching the central vein. When liver damage occurs, they are responsible for the release of a multitude of pro-inflammatory factors including cytokines interleukin-6 (IL-6), IL-1 $\beta$  and tumour necrosis factor alpha (TNF $\alpha$ ), interferons and reactive oxygen species (ROS) such as nitric oxide (NO) and superoxide [10]. If sufficiently high levels of these pro-inflammatory factors are released, circulating monocytes and macrophages in the blood can be activated, secreting their own pro-inflammatory cytokines. This results in an amplification of the inflammatory signal and increased fibrogenesis, although the different subsets of macrophages make it difficult to determine their exact function [11, 12]. Studies have also indicated these cytokines play a role in liver regeneration via priming hepatocytes for mitosis [13].

**Hepatic stellate cells (HSCs)** are the major storage location for retinoids and vitamin A in the body, residing within the Space of Disse (Figure 1.4). However, following liver damage, they lose their quiescent retinoid storing phenotype, becoming 'activated' and transdifferentiating to a myofibroblast-like phenotype characterised by the expression of alpha smooth muscle actin ( $\alpha$ SMA) [2, 14]. There are a range of inflammatory mediators associated with the activation of HSCs, the most common being transforming growth factor  $\beta$  (TGF- $\beta$ ) [15]. When activated to a hepatic myofibroblast phenotype they are the major fibrogenic cell in the liver, responsible for promoting the deposition of high levels of extracellular matrix (ECM) proteins including collagens by hepatic myofibroblasts (e.g. collagen type I), which are the main constituent of the fibrotic scars [14]. These scars are associated with a loss of tissue architecture and subsequent reduction in overall liver function. HSC transdifferentiation also affects other properties of the cells, including changes in their contractility, which contributes to the development of portal hypertension [16].

**Endothelial cells** line the liver sinusoid and are highly specialized for their function by the presence of fenestrae measuring 150 - 175nm in diameter, allowing macromolecules, solutes and water to reach the hepatocytes [17]. They have also been shown to endocytose a range of compounds via a membrane mediated method. This highlights their important role as a scavenger system, clearing macromolecular waste products, produced throughout the body in other tissues [18]. When inflammatory molecules are present in the blood, the endothelial cells upregulate adhesion molecules expression, which leads to the recruitment of neutrophils into the liver [19, 20]. Neutrophils are the hallmark cell in the acute inflammation response and their recruitment leads to further amplification of the inflammatory signal, often preceding liver damage.

**Oval cells** are bipotent progenitor cells located in the periportal regions of the liver, acting as a potential source of both hepatocytes and bile duct epithelial cells [21]. When hepatocytes fail to undergo mitosis after serious tissue damage, oval cells can migrate through the liver and repopulate hepatocytes [21, 22].

**Bile duct epithelial cells (cholangiocytes)** line the bile ducts and are important in the excretion of bile, dynamically controlling its excretion by alterations in their cellular electrolyte concentrations. They are also known to release a range of inflammatory mediators (e.g. TGF- $\beta$ , platelet derived growth factor (PDGF) and connective tissue growth factor (CTGF)) during liver injury, which prolongs the fibrotic response [23].

## 1.2 Liver disease

### 1.2.1 Epidemiology & background

The incidence of liver disease in the UK (and many other Western countries) has been rising for the past 50 years, shown by increasing liver cirrhosis mortality rates [24]. Liver disease is now one of the top five causes of death in

the UK, and is consequently an increasing burden on the healthcare system. Liver fibrosis and cirrhosis (end stage of liver fibrosis) represent the final pathway of nearly all major chronic liver insults/ diseases. The most common global cause of liver disease and fibrosis is viral infections (particularly hepatitis B and C viral infections) [25, 26].

In the Western world the increasing consumption of alcohol has led to a huge increase in alcoholic liver disease (ALD). Coupled with a more sedentary lifestyle and poor diet there has also been an increase in non-alcoholic forms of liver disease, including non-alcoholic fatty liver disease (NAFLD) and non-alcoholic steatohepatitis (NASH) [27, 28]. A range of autoimmune conditions exist, including autoimmune hepatitis and primary biliary cirrhosis (PBC), where autoimmune destruction of liver cells precedes fibrosis development [29]. There are also rarer genetic conditions that predispose fibrosis development, including haemochromatosis and Wilson's disease (which cause defective iron and copper metabolism respectively) leading to hepatic toxicity [30, 31].

### ***1.2.2 Liver fibrosis pathogenesis***

Liver fibrosis is defined as the excessive accumulation of ECM, rich in fibrillar collagens [32, 33]. It is a classical wound healing/ scarring response seen after acute liver injury, arising from multiple aetiologies including viral infections, adverse drug reactions and excessive alcohol consumption. Following an acute injury, hepatocytes are able to regenerate and replace the apoptotic and necrotic cells. The liver's remarkable regenerative properties are highlighted by its ability to return to its normal size and functioning capacity even after losing 70% of its parenchymal cells [21].

In chronic situations with continued insult there is repeated inflammation and ECM accumulation, leading to the increased replacement of the hepatic parenchyma with fibrotic scars, in an attempt to encapsulate the injury. Left untreated this culminates in liver fibrosis and eventually cirrhosis development, characterised by a disruption of liver architecture and

subsequent reduction in liver function [32, 34, 35]. Figure 1.4 illustrates the major cellular changes that occur as a result of liver fibrosis, including the accumulation of collagen scars and subsequent loss of hepatocyte microvilli and endothelial cell fenestrae reducing liver function.

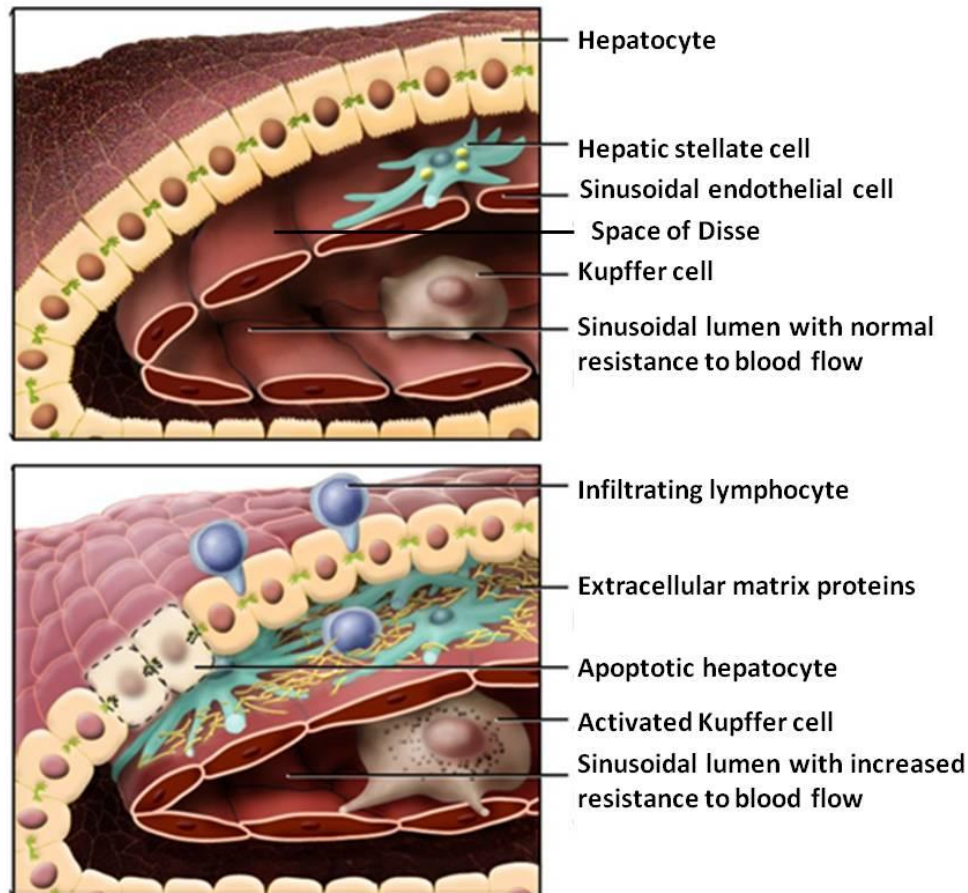


**Figure 1.4 Major cellular morphological changes that occur during fibrosis development (Figure taken from [32]).** Major cellular changes that occur as a result of HSC activation and liver fibrosis development include the accumulation of collagen scars, hepatocyte apoptosis and subsequent loss of hepatocyte microvilli and endothelial cell fenestrae.

### 1.2.3 HSCs and hepatic myofibroblast

The major fibrogenic cell in the liver is the hepatic myofibroblast, which is predominantly derived from the HSC. Hepatic myofibroblasts may also be derived from bone marrow mesenchymal cell progenitors [36], circulating fibrocytes and via an epithelial to mesenchymal transition route [37]. HSCs

are perisinusoidal cells located within the Space of Disse. In their quiescent state their major function is to store retinoids (e.g. Vitamin A) absorbed from the diet [38].

The activation of HSCs to hepatic myofibroblasts is divided into two major phases, firstly initiation, which describes the early changes in the gene expression of HSCs. Most prominent in this stage are the loss of Vitamin A and the increased expression of  $\alpha$ SMA from undetectable levels. There is coupled with increased expression of PDGF and TGF- $\beta$  receptors rendering HSCs more responsive to fibrogenic stimuli [14, 39].

Initiation is primarily induced by paracrine stimuli, such as fibrogenic ROS and pro-inflammatory cytokines including TGF- $\beta$  and IL-6 released by the neighbouring hepatic cells (hepatocytes, sinusoidal endothelial cells and Kupffer cells) when injury has occurred [40]. Hepatocyte apoptosis can also lead to the release of apoptotic fragments, which when phagocytosed by Kupffer cells leads to the expression of Fas and death ligands further perpetuating hepatocyte apoptosis and fibrosis development [41]. Endothelial cells are also known to produce a splice variant of fibronectin that plays a critical role in hepatic myofibroblast formation [42].

The second phase, perpetuation, results from the initiating stimuli and autocrine signals, which maintain the activated hepatic myofibroblast phenotype. Perpetuation is characterised by six changes in the cellular phenotype responsible for the increased deposition of ECM and subsequent loss of tissue architecture and liver function.

**Proliferation** – As outlined during initiation, increased levels of autocrine PDGF and the increased expression of PDGF receptors early in the activation process increases the HSCs responsiveness to the mitogen PDGF [43, 44]. There are also a range of other mitogens identified and known to promote myofibroblast proliferation including epidermal growth factor (EGF), thrombin and vascular endothelial growth factor (VEGF) [45].

**Chemotaxis** – Hepatic myofibroblasts migrate when exposed to cytokine chemoattractants, shown by their ability to align themselves in regions of

inflammation [46]. The major cytokines involved in chemotaxis are PDGF and monocyte chemoattractant protein-1 (MCP-1) [47].

**Fibrogenesis** – Fibrosis generation is accomplished by both an increase in hepatic myofibroblast number but also an increase in ECM production per individual cell [48]. The major component of hepatic scars is collagen type I, and the major stimulus for its production is TGF- $\beta$  arriving through both paracrine (activated Kupffer cells) and autocrine routes [49, 50]. A number of other signals are known to also contribute to fibrogenesis including lipid peroxide products and CTGF [51, 52].

**Contractility** – the increased levels of  $\alpha$ SMA bestow the cells with greater contractility properties [53]. This can result in increases in portal resistance, causing reduced blood flow along individual sinusoids. It is especially severe when cirrhosis develops and is a contributing factor in the development of portal hypertension [54].

**Matrix degradation** – Fibrosis development is significantly influenced by the relative activities of matrix metalloproteinases (MMPs) and tissue inhibitors of matrix metalloproteinases (TIMPs) [55]. Early alterations to basal MMP activity results in increased removal of ECM, therefore allowing its replacement with scar matrix. Hepatic myofibroblasts are known to express both MMPs (e.g. MMP-2) and TIMPs (e.g. TIMP-1, which is known to be anti-apoptotic to hepatic myofibroblasts) [56, 57].

**Retinoid loss** – Activation of HSCs is associated with the loss of the Vitamin A droplets. It is still not known whether this retinoid loss is necessary for HSC activation [33].

#### **1.2.4 *In vitro/ vivo models of liver fibrosis***

The most common *in vitro* model of liver fibrosis is the isolation of quiescent HSCs following collagenase and pronase digestion of liver tissue [53, 58]. When cultured on plastic in serum containing media the quiescent HSCs undergo a transdifferentiation to a myofibroblast phenotype cell type similar to

that seen in the liver during chronic injury. The cells can be sub-cultured by trypsinisation for approximately 5-6 passages, but often senesce around this passage number (varies between different species). An issue with their use is the different isolation protocols used between laboratories affecting the purity of HSCs isolated. They are a useful tool to assess potential anti-fibrotics for preventing initial HSC transdifferentiation.

Other important *in vitro* tools are the LX-1 and LX-2 cell lines. Both are human hepatic myofibroblast like cell lines derived by transfection and immortalisation with SV40 T antigen (LX-2s were further cultured in low serum conditions) [59]. Both cell lines express low levels of  $\alpha$ SMA and a number of receptors known to regulate fibrogenesis including the  $\beta$ -PDGF receptor. Microarray analysis confirmed similar gene expression to that of primary human HSCs (hHSCs) and LX-2 cells have the advantage of also being highly transfectable. The limited availability of human HSCs to investigate gene targets for anti-fibrotics makes the LX-1 and LX-2 cell lines a precious tool for advancements in hepatic fibrosis research [59].

*In vivo* models of liver fibrosis are invaluable in the search for novel anti-fibrotic agents, containing all the complex intracellular pathways present in the liver and extrahepatic sources that may contribute to liver fibrosis. The most common modes of inducing liver fibrosis *in vivo* are shown below: -

**Carbon tetrachloride (CCl<sub>4</sub>) administration** – The most commonly studied model, normally by intraperitoneal (i.p.) injection (1ml/kg body weight twice weekly for 4-12 weeks) [12]. CCl<sub>4</sub> hepatotoxicity results from the bioactivation of CCl<sub>4</sub> to a trichloromethyl radical by CYP2E1 metabolism; this radical reacts with oxygen forming the highly toxic trichloromethyl peroxy radical. This free radical is highly reactive and attacks polyunsaturated fatty acids commonly found in membrane lipids culminating in lipid peroxidation [60] (see Figure 1.5). The subsequent loss of membrane structure results in centrilobular hepatocyte death, with chronic administration leading to bridging fibrosis as fibrosis radiates out from the central veins.

**Dimethylnitrosamine (DMN)** – Most commonly induced by 10mg/kg i.p. injection for 3 consecutive days/ week for up to 4 weeks [61]. As with CCl<sub>4</sub>

CYP2E1 is responsible for metabolism of DMN [62], culminating in the production of formaldehyde and methanol. Alkylating intermediates are able to methylate nucleic acids and proteins of the hepatocytes, leading to severe hepatocyte necrosis [63]. In chronic treatments there is also destruction of sinusoidal endothelial cells in the centrilobular regions with increased coagulation [64, 65]. Induced macrophage activity can result in elevated iron concentrations and subsequent oxidative stress promoting fibrosis development [61].

**Bile duct ligation (BDL)** – A surgical procedure in which the bile duct is ligated with 2 pieces of suture for up to 3-4 weeks [66, 67]. Increased levels of bile acids in the liver result in hepatocyte apoptosis and at higher levels hepatocyte necrosis. The bile duct is located within the portal tract so fibrosis bridges out from the periportal regions [68].

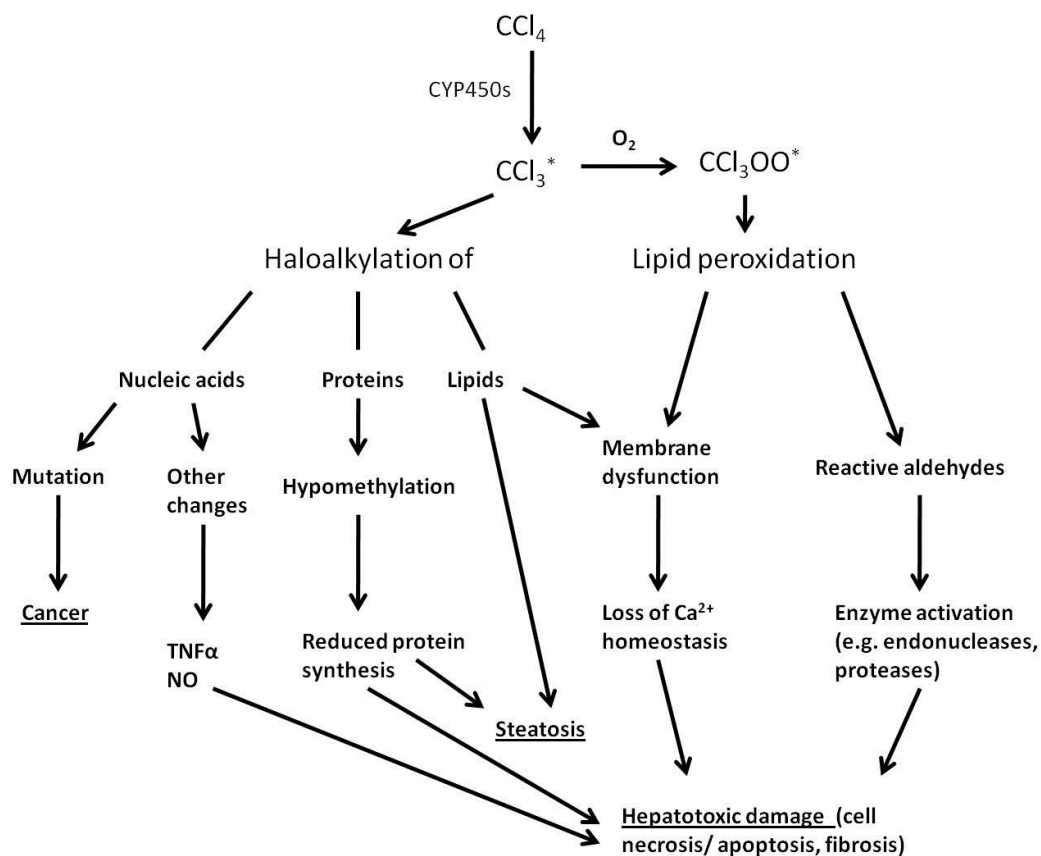


**Figure 1.5 Schematic illustrating CCl<sub>4</sub> hepatotoxicity mode of action (modified from [60]).** CCl<sub>4</sub> hepatotoxicity is a result of its metabolism by CYP2E1 to a trichloromethyl free radical. This radical reacts with oxygen to produce a highly reactive peroxytrichloromethyl free radical that culminates with a series of lipid peroxidation reactions and subsequent hepatotoxicity.

There are a number of other models available including the intragastric enteral feeding model of alcohol induced fibrosis and other alternative drug induced models (e.g. thioacetamide). Generally any potential anti-fibrotic agent should be tested in at least two of these models. It must be appreciated that all of these models exhibit some significant pathological differences to the severity of fibrosis seen in humans. Most notably the severity of fibrotic bands that develop in these models are not as severe as in humans and models do not exhibit the same alterations in vasculature that contribute to complications associated to fibrosis and cirrhosis in man [3].

### **1.3 Treatments of liver disease**

Despite enormous strides made over the past 30 years establishing the importance of the HSC in liver fibrosis and the multitude of signalling pathways involved in its initiation and perpetuation, an effective treatment regimen for liver fibrosis still eludes us. With the exception of transplantation, there is no recognised treatment; the increasing incidence of liver fibrosis coupled with the finite number of donors available reinforces the need for novel anti-fibrotic treatments. At present the most effective anti-fibrotic therapy is to treat the underlying cause of the disease, the most prominent example being the anti-viral (e.g. pegylated  $\alpha$ -interferon) treatment of hepatitis viral infections [69]. Alternatively in cases of NASH, educating the population so they know the severity of liver disease and encouraging weight loss is a good preventative measure.

There are a number of potential drug target sites/ pathways where anti-fibrotic agents are currently being targeted including:

#### ***1.3.1 Reducing the initial immune response/ inflammation to avoid HSC activation.***

Treatment of hepatitis C patients with a combination of ribavirin and pegylated  $\alpha$ -interferon has been able to reduce fibrosis severity as diagnosed by liver biopsy samples [69, 70]. It is believed their improvement is a result of viral clearance, but pegylated  $\alpha$ -interferon has also been shown to have anti-fibrotic benefits in biliary fibrosis suggesting it may have direct anti-fibrotic properties as well [71]. Corticosteroids have been employed in the treatment of numerous inflammatory diseases for decades (e.g. arthritis and irritable bowel syndrome). They also exhibit beneficial properties in autoimmune hepatitis with a reduction or abolition of fibrosis development when administered [72]. Other anti-inflammatory agents that may be beneficial in preventing initial HSC activation are inhibitors of the renin-angiotensin system [73]. This is a viable route as oxidative stress is known to be increased by this system. Finally novel compounds such as 'mimics' of hepatocyte growth factor (HGF) may decrease TGF- $\beta$  signalling and subsequent collagen deposition [74].

### **1.3.2 Directly prevent HSC activation.**

Activation of HSCs is the critical step in fibrosis development, therefore reducing the transdifferentiation of quiescent HSCs to hepatic myofibroblasts is an attractive anti-fibrotic route to pursue. Oxidative stress is one of the first stimuli to initiate HSC activation; experiments utilising the anti-oxidant  $\alpha$ -tocopherol have been successful in some animal models of liver fibrosis (specifically iron overload induced fibrosis) [75]. Peroxisome proliferator-activated receptor gamma (PPAR $\gamma$ ) is highly expressed in HSCs and synthetic PPAR $\gamma$  agonists reduced HSC activation *in vitro* [76]. These initial findings suggest anti-diabetic treatments such as thiazolidinediones may be an effective drug to treat liver fibrosis, which was later reinforced both *in vitro* and *vivo* by Galli *et al* [77]. Another anti-fibrotic target is leptin which is known to be released by HSCs and to be pro-inflammatory. When both leptin knockout and wildtype mice received liver insults the level of fibrosis development was significantly reduced in the knockout mice when compared

to the wildtype mice [78]. Therefore it is believed treatment of fibrosis with adiponectin, an important regulator of leptin, may reduce inflammation and HSC activation [79].

### ***1.3.3 Neutralise the proliferative, fibrogenic, contractile and pro-inflammatory responses of HSCs.***

The continued increase in knowledge of the growth factors (e.g. PDGF and TGF- $\beta$ ) involved in HSC initiation and perpetuation, including their intracellular signalling pathways and target receptors provide an array of anti-fibrotic targets. These intracellular signalling pathways are common to other disease states (e.g. chronic myeloid leukaemia (CML) and gastrointestinal stromal tumours) [80, 81], therefore a number of inhibitors are available and being tested in fibrosis models including Gleevec (a tyrosine kinase antagonist) used in leukaemia [82] and pentoxifylline (an inhibitor of PDGF signalling). Another major target is TGF- $\beta$  signalling, as this cytokine is prominent in fibrogenesis. A number of antagonists to TGF- $\beta$  have displayed the potential of this treatment route [83-85]. They are beneficial as they inhibit both matrix deposition whilst also simultaneously increasing its degradation [86]. There are also a number of other potential targets including relaxin [87], endothelin-1 and regulators of wound healing/ contraction whose antagonism is anti-fibrotic [88].

### ***1.3.4 Induction of hepatic myofibroblast apoptosis.***

Important work by the Iredale group ascertained that, following the removal of the causative stimuli, liver fibrosis naturally regresses, enforced by the increased apoptosis of hepatic myofibroblasts [89]. This discovery prompted the development of a number of targeted therapies, including gliotoxin (GTX) which was shown to induce HSC apoptosis *in vivo* and significantly reduce fibrosis severity [90]. A similar method to this was the inhibition of I $\kappa$ B, an

important factor in regulating NF- $\kappa$ B activation, responsible for preventing hepatic myofibroblast apoptosis and promoting fibrosis development [91]. A number of other apoptotic factors are expressed in hepatic myofibroblasts including nerve growth factor (NGF) [92], Fas ligands and Bcl providing alternative routes to induce hepatic myofibroblast apoptosis.

### **1.3.5 Increase MMP activity and fibrotic scar degradation.**

Matrix resorption and degradation are both essential in the resolution of liver fibrosis. Work by Issa *et al* [93] highlighted the importance of MMPs in fibrosis resolution, as mice expressing a mutated form of collagen type I were unable to resolve fibrosis. TIMP-1 is dramatically upregulated by several pro-inflammatory cytokines, including TNF $\alpha$  [94], and TGF- $\beta$  [95] inhibiting MMP activity and preventing collagen degradation. Novel methods to inhibit TIMP activity and restore MMP activity are ongoing. Examples include utilizing a mutant MMP-9 peptide to retain TIMP-1 bound in an inactive state [96], or alternatively antibodies antagonizing TIMP-1 result in a reduction in fibrosis severity in a rodent model of liver fibrosis [97].

## **1.4 Targeting hepatic myofibroblasts**

The major issue with potential treatments such as the fungal metabolite GTX is their lack of specificity to hepatic myofibroblasts. Although it preferentially induced the apoptosis of hepatic myofibroblasts, there was also increased apoptosis/ necrosis of Kupffer cells [90, 98]. The presence of Kupffer cells is known to be of benefit in both the development and the reversal of fibrosis from work carried out by Duffield *et al* [12], which shows they are required for successful degradation of the excess ECM. Also under inflammatory conditions hepatocytes may be more vulnerable to cell death if NF- $\kappa$ B has already been inhibited [90, 98]. It is well known that GTX has immunosuppressive effects, abrogating B and T cell stimulation and causing

leucocyte apoptosis [99]. These findings highlight the advantages in both efficacy and specificity of targeting apoptotic agents directly to hepatic myofibroblasts.

Initial research focused on identifying a target that was only present on hepatic myofibroblasts, it was discovered that the mannose 6 phosphate/insulin like growth factor II receptor (M6P/IGF-II) was highly expressed on the surface of hepatic myofibroblasts [100]. Further work involved the modification of human serum albumin (HSA) bound with M6P to target hepatic myofibroblasts directly [101]. When its functioning had been confirmed, it was conjugated with a range of anti-fibrotic agents including pentoxifylline, losartan, GTX and doxorubicin [102-105]. When administered to animal models of liver fibrosis they all showed a significant anti-fibrotic effect (e.g. decreased number of  $\alpha$ SMA positive cells).

#### ***1.4.1 Synaptophysin expression in the liver and the heterogeneity of hepatic myofibroblasts***

Synaptophysin is a transmembrane glycoprotein found within the presynaptic vesicles of neurons of the brain, spinal cord, and at neuromuscular junctions [106]. It is primarily involved in controlling neurotransmitter release and exocytosis at the nerve terminal although its specific function is yet to be established [107]. IHC analysis by Cassiman *et al* [108] revealed that synaptophysin is also expressed on the surface of quiescent and activated HSCs. Synaptophysin's external cellular location and cycling to internal locations made it an ideal target for anti-fibrotic therapeutics.

It is difficult to determine the origin of hepatic myofibroblasts due to the various populations (e.g. periportal fibroblasts and centrilobular myofibroblasts) [109], with a heterogeneous expression of various markers. As well as synaptophysin, quiescent HSCs and hepatic myofibroblasts express a range of other neural markers including glial fibrillary acidic protein (GFAP) and nestin [110]. This suggests that a proportion of hepatic myofibroblasts may derive from the neural crest, and would explain

synaptophysin's expression on hepatic myofibroblasts. However tests utilising transgenic mice encoded with fluorescent proteins (specific to neural crest cells) revealed that desmin-positive perisinusoidal cells of the liver did not express any fluorescent protein [111]. Further studies have highlighted alternative routes that may contribute to hepatic myofibroblast development including bone marrow derived HSCs [112, 113] and also directly from hepatocytes *via* an 'epithelial to mesenchymal' route during fibrosis [114].

#### **1.4.2 C1-3 a recombinant human single chain antibody fragment (scAb) and synaptophysin**

Phage display screening was used to generate a recombinant single chain antibody (scAb) specific to a conserved peptide sequence present on an extracellular domain of synaptophysin [115]. The scAb isolated could be rapidly produced in *E-coli* and subsequently purified via its terminal His tag; it was termed C1-3 and binds specifically to peptide sequence 2 of the synaptophysin protein (see Figure 1.6). Further *in vitro* work incubating fluorescently labelled C1-3 with both human hepatocytes and HSCs highlighted its specificity for HSCs [115]. The use of monensin to block scAb uptake and conjugation of the toxin tributyltin to test whether the scAb is taken up through the delivery of the toxin and subsequent cell death confirmed that the scAb is taken up intracellularly.

Work by Douglass *et al* [116] coupled the apoptosis inducing effects of GTX with the hepatic myofibroblast specificity of C1-3 in a CCl<sub>4</sub> model of liver fibrosis. This form of the scAb was named C1-3-GTX and shown to reduce the number of  $\alpha$ SMA positive hepatic myofibroblasts by up to 60%, and consequently fibrosis severity was significantly reduced [116]. In addition there was no effect on Kupffer cell numbers and no serious extrahepatic side effects associated with the administration of free GTX.

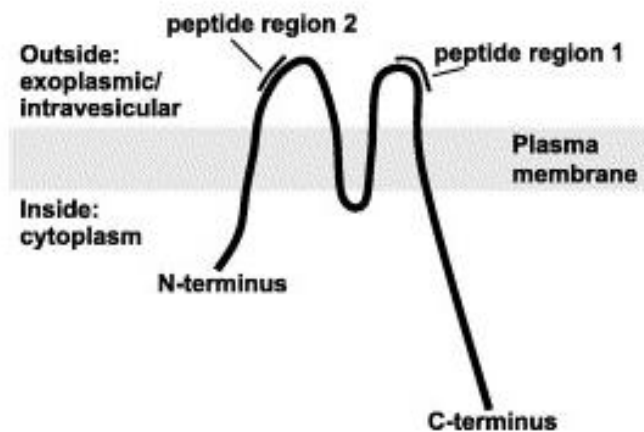


**Figure 1.6 Outline of human synaptophysin protein (taken from [115]).** Human synaptophysin is believed to span the plasma membrane as outlined; C1-3 is specific to the synaptophysin peptide region 2.

## 1.5 Diagnosis of liver fibrosis

Accurately assessing the severity of liver fibrosis is essential to determine the prognosis of the disease and ascertain whether a treatment may be beneficial for a specific patient, and also to determine the success of any treatment.

### 1.5.1 Liver biopsy

For fifty years since Menghini advocated the use of the percutaneous needle biopsy [117], it has been the 'gold standard' in the diagnosis of liver fibrosis. Histochemical analysis of the removed liver sample is in most instances achieved by staining with hematoxylin and eosin (H&E) and is graded by a pathologist, using the Ishak, METAVIR or Scheur scales [118-120] (Table 1.1).

Scoring system	Grade	Staging criteria
<b>METAVIR</b>	F0	No fibrosis
	F1	Fibrous portal expansion (stellate enlargement) but no septae formation
	F2	Enlargement portal tract with rare septae formation
	F3	Numerous septae without cirrhosis
	F4	Cirrhosis
<b>Ishak</b>	0	Normal (no fibrosis)
	1	Fibrous expansion of some portal areas, with or without short fibrous septa
	2	Fibrous expansion of most portal areas, with or without short fibrous septa
	3	Fibrous expansion of most portal areas, with or without portal-portal bridging
	4	Fibrous expansion of portal areas, with marked bridging (portal-portal and portal-central)
	5	Marked bridging (portal-portal &/or portal-central) with occasional nodules (incomplete cirrhosis)
	6	Cirrhosis, probable or definite
<b>Scheur</b>	0	None
	1	Enlarged, fibrotic portal tracts
	2	Periportal or portal-portal septa but intact architecture
	3	Fibrosis with architectural distortion but no obvious cirrhosis
	4	Probable or definite cirrhosis

**Table 1.1 – Major liver biopsy scores**

The limitations of the liver biopsy have become clear though; it is a highly invasive procedure. With significant medical complications ranging from excessive bleeding and pain (resulting in prolonged hospital admission in 1 - 5% of patients) to mortality (in 1 in 1000 – 10000 patients) [121]. Other potential complications include significant sampling variability due to the fact that on average, the size of the biopsy sample is approximately 1/50000<sup>th</sup> the total size of the liver. Regev *et al* [122] highlighted the sampling error associated with biopsies with a difference of at least one fibrosis stage recorded between the two major liver lobes. Interobserver variation is another issue due to the subjective nature of assessing fibrosis severity from liver biopsy samples, coupled with the number of scoring systems available

making it difficult to make comparisons between different studies as well [119].

### **1.5.2 Serum markers**

A range of common serum markers are used to assess the level of liver damage and they can be divided into two classes. An ideal serum marker should be specific to the liver, not impaired by biliary and urinary excretion, whilst being simple to assay and detectable in all classes of liver disease [34].

Class I (direct) biomarkers are generally derived from the increased ECM turnover seen during HSC activation or a mediator involved in fibrogenesis (e.g. TGF- $\beta$ ). Therefore many structural glycoproteins, pro-collagens and collagen fragments are used as biomarkers as well as MMPs and TIMPs, with N-terminal propeptide of type III procollagen (P III NP) being used in some clinical settings [123]. Hyaluronic acid (an essential component of ECM found at increased levels in fibrotic livers) [124] is currently considered the best class I biomarker due to its high sensitivity and specificity in a recent study of NAFLD [125] and its ability to exclude late fibrosis and cirrhosis.

Class II biomarkers are indirect markers estimating the degree of fibrosis, which do not necessarily involve ECM and fibrogenic cellular changes. They have however been statistically proven to be associated with fibrosis levels. They are composed of different 'biomarker panels' that are programmed into mathematical algorithms to stage fibrosis severity [126]. Parameters used in these tests include the Aspartate aminotransferase/ Alanine aminotransferase (AST/ ALT) ratio, with increased AST levels in the serum after liver injury. Another common parameter is the platelet count; thrombopoietin (the major enzyme responsible for platelet production) is produced in the liver and therefore its relative level is directly related to liver function [127]. To improve the accuracy of this test it can be combined with the AST levels to form the AST to platelet ratio index (APRI); this simple index is relatively easy to carry out and can potentially differentiate between individuals with severe fibrosis/ cirrhosis and those without [128].

There are over twenty scores that are currently used to stage fibrosis severity (the most widely employed are shown in table 1.2), the two most common being the Fibrotest™ (Fibro-Score) and the ActiTest™. The Fibrotest™ was developed by Imbert-Bismut *et al* [129]; it involves the detection of haptoglobin,  $\alpha$ 2-macroglobulin, apolipoprotein A1, bilirubin and  $\gamma$ -glutamyltransferase (GGT). The results of the Fibrotest™ are used to produce three categories of fibrosis – **mild** (METAVIR F0-F1), **significant** (METAVIR F2-F4) and **indeterminate** (removed from clinical reporting by making fibrosis score linear) [130]. The Actitest™ incorporates the same diagnostic criteria as the Fibrotest™ but also includes ALT, to reflect necro-inflammatory activity as well as fibrosis. Numerous studies have been performed to validate the accuracy of both these tests to suggest they could be used as an alternative to the liver biopsy in numerous models of liver disease preceding fibrosis development [131-133].

<b>Non invasive fibrosis test</b>	<b>Components</b>	<b>Theory</b>	<b>Pros</b>	<b>Cons</b>
<b>Actitest™</b>	$\alpha$ 2-macroglobulin Haptoglobin Apolipoprotein A1 Bilirubin GGT ALT	Identical to the Fibrotest™ but also assesses the necro-inflammatory activity.	Addition of ALT to criteria aids diagnosis of later stage fibrosis when there is increased necrosis and inflammation.	Only validated in HCV [132].
<b>APRI</b>	ALT Platelet count	Statistically significant +ve correlation between fibrosis severity & AST level, -ve correlation with platelet count.	Distinguishes between individuals with or without significant fibrosis [128].	Unable to differentiate between specific fibrosis stages [127, 128].
<b>Fibrotest™</b>	$\alpha$ 2-macroglobulin Haptoglobin Apolipoprotein A1 Bilirubin GGT	Mathematical formula combining 5 indirect markers of liver fibrosis that gives a fibrosis score.	Can distinguish between all stages of liver fibrosis [129, 134].	Discordant results with liver biopsy in HCV patients. False positives can result due to treatment regimens

				affecting bilirubin levels.
<b>Forns Index</b>	Platelet count GGT Age Cholesterol	4 variables developed in an attempt to differentiate between clinically significant fibrosis and less severe early stages.	Good at predicting early stage fibrosis [135].	Can't detect severe fibrosis, cholesterol parameter is a weakness and can vary according to HCV genotype. Only validated in HCV.
<b>Hepascore</b>	Bilirubin GGT Age Sex $\alpha$ 2-macroglobulin Hyaluronic acid	Bilirubin levels increase due to decreased liver function associated with fibrosis development, whilst hyaluronic acid and $\alpha$ 2-macroglobulin both increase as a result of HSC activation and fibrosis presence.	Use of hyaluronic acid improves the detection of significant and advanced fibrosis/ cirrhosis [136, 137].	Is not an effective model to determine early fibrosis stages.

Table 1.2 – Common non-invasive serum biomarker panels

### 1.5.3 Non-invasive imaging modalities

Radiologic assessment of hepatic fibrosis including ultrasonography and computed tomography has been trialled. However, they are limited to the detection of cirrhosis and complications associated with it (i.e. portal hypertension and ascites) [138]. These techniques are not sensitive enough to detect fibrosis during its developmental and early stages, which is a major limitation to their use when coupled with their high costs. Transient elastography (FibroScan) is a novel non-invasive imaging technique, incorporating a transducer which transmits vibrations through the liver producing a shear wave. Pulse-echo ultrasounds can detect the speed and velocity of the shear wave as it travels through the liver tissue. The velocity of the wave is directly proportional to the stiffness of the liver tissue, therefore as fibrosis and ECM deposition increase the relative stiffness of the liver also

increases. Consequently the velocity of a shear wave will be higher in a fibrotic liver when compared to a healthy liver [139]. The benefits of this technique focus on the fact it is non-invasive, whilst also being relatively cheap and having high reproducibility. Also it is able to measure a much larger region of the liver in comparison to a liver biopsy; normally a region of 1cm diameter and 5cm in length is measured in transient elastography over one hundred times that measured in a typical liver biopsy [140]. The major limitation of transient elastography is that it is not effective in determining liver stiffness in obese patients and those suffering with ascites. The presence of a fatty thoracic band attenuates the elastic wave and ultrasound waves making diagnosis impossible [141]. Transient elastography has been evaluated in a range of liver diseases including NAFLD, ALD and hepatitis B and C viral infections. Reproducibility of transient elastography is another important factor in its use in clinical practice; the level of inter-observer discrepancies is significantly reduced when compared to the liver biopsy. Fraquelli *et al* [142] amongst others have shown that its reproducibility is excellent for cirrhosis and severe fibrosis (>F2) but significantly reduced in milder forms of fibrosis (F0-F1). Continued research to develop probes that can penetrate thoracic fat and determine uniform cut-off points for all studies to improve the diagnosis of earlier types of fibrosis are ongoing [143].

Magnetic resonance imaging (MRI) has been investigated retrospectively by Aguirre *et al* [144] in over 100 patients using a double contrast agent to improve MRI resolution. It was found that this method could be used to detect severe fibrosis (F>3 using METAVIR scale) with a sensitivity/ specificity above 90%.

A major fundamental issue in diagnosing liver fibrosis is the fact that the liver biopsy, which is the 'gold standard' and reference for all novel hepatic imaging techniques has been shown to be limited (Section 1.5.1). Perhaps the most effective method to diagnose liver fibrosis as highlighted by numerous studies [145, 146] is the combination of multiple non invasive techniques (including more than one fibrosis test and/ or transient elastography). This non-invasive approach removes the need for liver biopsy unless absolutely necessary, whilst also reducing the incidence of misdiagnosis and subsequent treatment.

It is important to acknowledge the advancements being made with the use of imaging modalities in other diseases (e.g. positron emission tomography (PET) and MRI) that may be beneficial in non-invasively diagnosing hepatic fibrosis.

## **1.6 The pregnane X receptor (PXR)**

The PXR is an orphan nuclear receptor (~50 kDa in size) and a member of the nuclear receptor superfamily (NRS) of ligand activated transcription factors. It is named the PXR due to its activation by both natural and synthetic pregnanes (e.g. cortisone and progesterone). Other members of the NRS include the steroid, thyroid and retinoid hormone receptors [147-149]. The PXR is constitutively expressed at high levels in both the liver and intestines and has been shown to regulate drug and corticosteroid induction of important drug metabolising enzymes. This includes the glutathione-S-transferases (GST's) [150, 151], UDP-glucuronosyltransferases [152, 153] and numerous cytochrome P450 (CYP450) isoforms, including CYP3A4 [154]. This is of high significance as the CYP3A4 isoform is responsible for metabolising over 50% of clinically administered drugs [155, 156]. The PXR also mediates the expression of a number of drug efflux pumps and transporters, including the multidrug resistance 1 (MDR1) and organic anion transporter polypeptide-2 (OATP2) [157]. It is referred to as a 'xenosensor' [158], due to this wide variety of transcriptional impacts on the different processes central to the clearance and removal of drugs and toxins from the body.

### ***1.6.1 The PXR pathway***

The PXR protein, like all NRS members, is composed of a central DNA binding domain (DBD) containing two highly conserved zinc fingers, a variable amino-terminal domain and a carboxy-terminal ligand binding domain (LBD). In most cases there are two transcriptional activation domains, activation

function 1 (AF-1) located in the N-terminal domain and AF-2 found in the C-terminal region of the LBD [147, 159] (Figure 1.7A). Upon ligand binding to the LBD there is a conformational change in AF-2 resulting in disruption of the interactions normally seen with transcriptional co-repressor proteins such as N-CoR and SMRT. This now allows transcriptional co-activator proteins including SRC-1 and TIF-2 to bind to the AF-2 domain facilitating heterodimer formation with the 9-cis retinoic acid receptor (RXR) [160]. This PXR/ RXR heterodimer is able to bind to DNA response elements found in the promoter regions of target genes, stimulating their expression i.e. CYP3A4.

The PXR has been identified in other species including the mouse, rat, rabbit and dog with there being very close homology between the orthologues. The mammalian PXR shares approximately 95% homology in the DBD, but there is more variation with regards to the LBD (see Figure 1.7B). This may be the reason for the differences seen in ligand binding between species to the PXR, with pregnenolone-16 $\alpha$ -carbonitrile (PCN) demonstrating high affinity for the rodent PXR but none for the human PXR [161, 162].

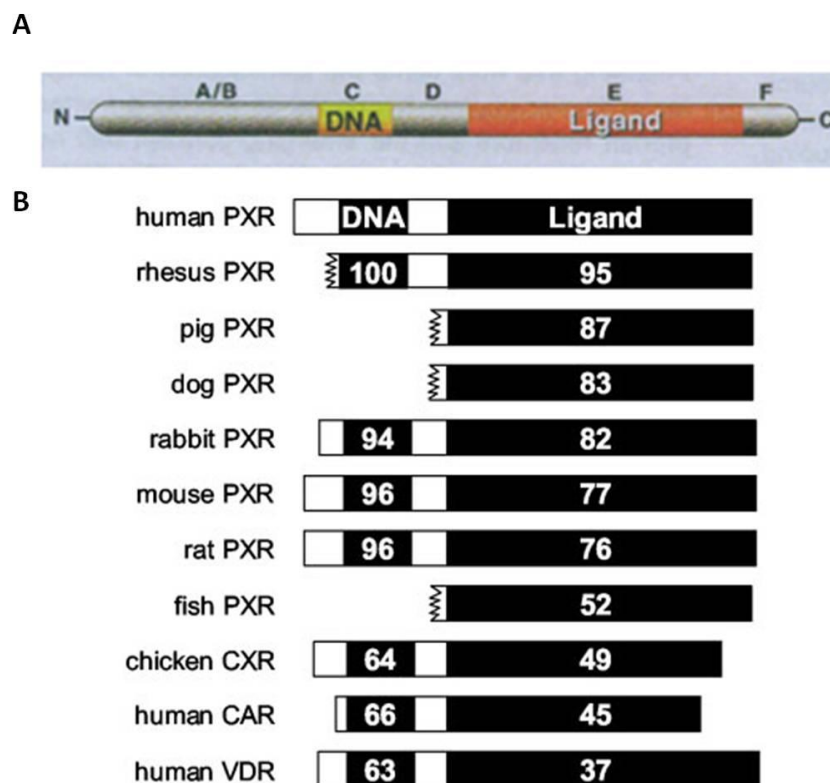


**Figure 1.7 A:** Schematic diagram illustrating the domains present in all members of the NRS and **B:** Sequence comparison across species illustrating PXR similarity (taken from [147] and [155])

**respectively**). A/B = variable N-terminal region. C = highly conserved DBD. D = variable hinge region. E = conserved LBD. F = variable C-terminal domain.

### **1.6.2 PXR ligands and drug-drug interactions**

What separates the PXR from its counterparts in the NRS is its ability to bind such a broad spectrum of xenobiotics. Research utilising X-ray crystallography gave a greater insight into the architecture of the LBD region of the PXR [155]. It showed that the hydrophobic pocket of the PXR was much larger than other members of the NRS, and had a unique smooth elliptical shape [155, 163].

The hydrophobicity of the ligand binding site means that the receptor is ideal for binding lipophilic ligands that are able to diffuse into the cells. Chief examples include rifampicin, hyperforin, taxol and ritonavir. The issue involving these compounds is their induction of the CYP3A4 isoform and potential drug-drug interactions. Consequently if polypharmacy is being employed there can be increased CYP3A4 metabolism of the compound, sometimes resulting in ineffective treatment outcome or formation of life threatening levels toxic metabolites. The detrimental drug-drug interaction effects of St. John's Wort (hyperforin) on the anti-cancer agent irinotecan is a recent example [164]. Commonly encountered PXR activators: -

**Rifampicin** is a macrocyclic antibiotic used as a component of a multidrug regimen to treat tuberculosis, and now commonly used to treat a range of bacterial and fungal infections. Extensive research in humans has also outlined its immunosuppressive effects in the liver, in some instances depressing IgG antibody response [165, 166]. Rifampicin functions by inhibiting DNA dependent RNA polymerase in bacterial cells, it binds to the  $\beta$ -subunit preventing gene transcription and subsequent protein formation.

**St. John's Wort** is an herb derived from the *Hypericum perforatum* plant used to treat mild depression. Normally a prescription is required to obtain St. John's Wort but this is not the case in the USA. The mode of action of St. John's Wort is not fully understood but is believed to be similar to the

conventional selective serotonin reuptake inhibitor class of anti-depressants, by preventing the reuptake of serotonin. Hyperforin, a major constituent of St. John's Wort was found to be the most active chemical present activating the PXR, responsible for numerous drug-drug interactions between St. John Wort, and prescription drugs cited in medical literature in the 1990's in the USA [164, 166].

### **1.6.3 PXR and inflammation**

It has long been known that there is a correlation between increased levels of inflammation and infection with decreased hepatic expression of CYP450 isoforms, yet the mechanism of this CYP downregulation remained unclear [167]. Other nuclear receptors, most notably the glucocorticoid receptor (GR) have been shown to inhibit the nuclear factor  $\kappa$ B (NF- $\kappa$ B) signalling pathway, which is a major pro-inflammatory transcription factor important in the inflammation/ apoptosis cascade [168, 169].

Work by Zhou *et al* [166] demonstrated that activation of the PXR by rifampicin administration antagonised the activity of NF- $\kappa$ B in both *in vitro* and *in vivo* models of irritable bowel disorder (IBD), suggesting there is an important link between xenobiotic metabolism and the immune system. The major findings of this report were that PXR agonists (e.g. rifampicin and phenytoin) reduce expression of NF- $\kappa$ B regulated pro-inflammatory genes such as TNF $\alpha$ , and rifampicin inhibits NF- $\kappa$ B by a PXR dependent manner not *via* the GR as postulated [166].

These findings were reinforced by Shah *et al* [170], whilst investigating the effects of PXR activation on IBD again *via* NF- $\kappa$ B inhibition. They induced IBD by administration of dextran sulphate sodium (DSS) in both PXR wildtype and PXR null mice. Administration of the rodent PXR activator PCN resulted in reduced colitis in PXR wildtype mice, but had no effect on PXR null mice indicating that PXR activation reduced the severity of IBD and this effect was mediated by the PXR. Relative mRNA levels highlighted that this was

mediated by decreased expression of several important NF- $\kappa$ B target genes (including TNF $\alpha$ ) [170].

The PXR is constitutively expressed in the liver, in combination with the knowledge that the immune and inflammatory cascades are central to liver fibrosis development following liver injury. This suggests that PXR activation may be a viable route to ameliorate liver fibrosis.

#### **1.6.4 The PXR and liver fibrosis**

**Rodents** - Initial studies within this group focussed on investigating the potential of utilising liver regeneration as a method of alleviating liver fibrosis, as demonstrated previously by other groups [171]. This was investigated by administering PCN to rodents with CCl<sub>4</sub> induced liver fibrosis. Administration of PCN to rodents treated with CCl<sub>4</sub> did not affect the hepatotoxicity of CCl<sub>4</sub>, but did reduce the severity of liver fibrosis that developed, gauged by  $\alpha$ SMA levels and sirius red IHC [172]. *In vitro* treatment of quiescent rat HSCs (rHSCs) with PCN prevented their transdifferentiation to an activated myofibroblast phenotype, suggesting it would be an effective anti-fibrogenic agent. PXR mRNA was not detected at significant levels in rHSCs implying that PCN's mode of action was independent of the PXR. Further studies *in vivo* in both PXR wildtype and PXR null mice highlighted that PCN's anti-fibrotic action was dependent on the presence of a functional PXR [172].

**Humans** - Further studies from within the group focussed on the effects of PXR activation in humans to reinforce the earlier work carried out in rodent models of liver fibrosis [172]. Firstly freshly isolated human HSCs (hHSCs) were shown to express PXR mRNA at all stages (quiescent to activated HSC transdifferentiation), displayed by increased levels of collagen I, TGF- $\beta$  and an induction of  $\alpha$ SMA mRNA. Transfection of hHSCs with a PXR responsive luciferase construct demonstrated that the PXR was constitutively expressed, and treatment with rifampicin (a PXR specific agonist) further increased the luciferase response of the reporter construct [173]. GeneChip analysis highlighted that rifampicin treatment modulated the expression of TGF $\beta$ , a

cytokine central to increased ECM deposition in liver fibrosis. Further qRT-PCR data showed that TIMP-1 expression was also significantly decreased following rifampicin treatment and a variety of genes important in the cell cycle were also repressed (e.g. cyclins and WNT signalling). This suggests that PXR activation could prevent HSC transdifferentiation/ proliferation supporting the data from the earlier rodent studies [173, 174].

Later work aimed to ascertain whether the anti-fibrogenic effects displayed by the PXR were due to inhibition of NF- $\kappa$ B activity [175], trying to build upon the work carried out by other groups in similar inflammatory situations (DSS induced model of IBD [170]). The importance of NF- $\kappa$ B during the development and maintenance of liver fibrosis has been shown; it plays a key role in preventing the inhibition of hepatic myofibroblast apoptosis [90, 91, 176]. The effect of PXR activation on NF- $\kappa$ B activity was investigated using the U937-NF- $\kappa$ B cell line (stably transfected with firefly-luciferase gene under the control of a concatamer of NF- $\kappa$ B response elements) [175, 177]. Treatment of the U937-NF- $\kappa$ B cells with the pro-inflammatory cytokine TNF $\alpha$  or bacterial lipopolysaccharide (LPS) induced luciferase expression. Addition of the PXR activators rifampicin, hyperforin and metyrapone in turn all inhibited this luciferase induction, when induced by LPS but not with TNF $\alpha$ . Multiple cell lines (THP-1, HepG2 and LX-2) were transfected with a luciferase reporter gene under the control of a TNF $\alpha$  promoter (as U937-NF- $\kappa$ B cells are not very amenable to transfection). Administration of PXR activators as above inhibited the constitutive luciferase expression seen previously. To verify these findings to the conditions seen in liver fibrosis and inflammation, Kupffer cells were isolated from human patients (confirmed by their expression of CD68 – a recognised monocyte/ macrophage marker). Kupffer cells express TNF $\alpha$  in response to LPS treatment, and this response was abrogated upon treatment with PXR activators. It was confirmed this was mediated via a PXR dependent mode of action by identical studies carried out in Kupffer cells isolated from both PXR wild type and null mice [177].

## **1.7 Nuclear factor- $\kappa$ B (NF- $\kappa$ B)**

### 1.7.1 NF- $\kappa$ B family members and signalling pathway

NF- $\kappa$ B is a family of transcription factors (made up of dimers) central to the regulation of the inflammatory, immune, wound healing and cell fate cycles. It functions by binding to  $\kappa$ B binding domains present in the regulatory regions of target genes (e.g. TNF $\alpha$  receptor-associated factor 1 (TRAF1) and pro-inflammatory cytokines) and inducing their transcription. The NF- $\kappa$ B dimers consist of either homodimers or heterodimers. There are five members of the NF- $\kappa$ B family in mammals – p50, p52, p65, RelB and c-Rel. Each member has distinct biological activities; consequently all dimers have different effects/targets on gene transcription. NF- $\kappa$ B is known as a ‘rapid-acting’ primary transcription factor, as a result of its presence in cells at all times. In resting cells NF- $\kappa$ B is held in an inactive state within the cytoplasm by inhibitor of  $\kappa$ B (I $\kappa$ B) proteins. Upon activation I $\kappa$ B is phosphorylated at specific sites ultimately resulting in its ubiquitination and degradation (catalysed by I $\kappa$ B kinase (IKK)). Following its release the NF- $\kappa$ B dimer is able to cross the nuclear membrane and bind to the DNA binding domain of target genes initiating their transcription [178] (See figure 1.8).

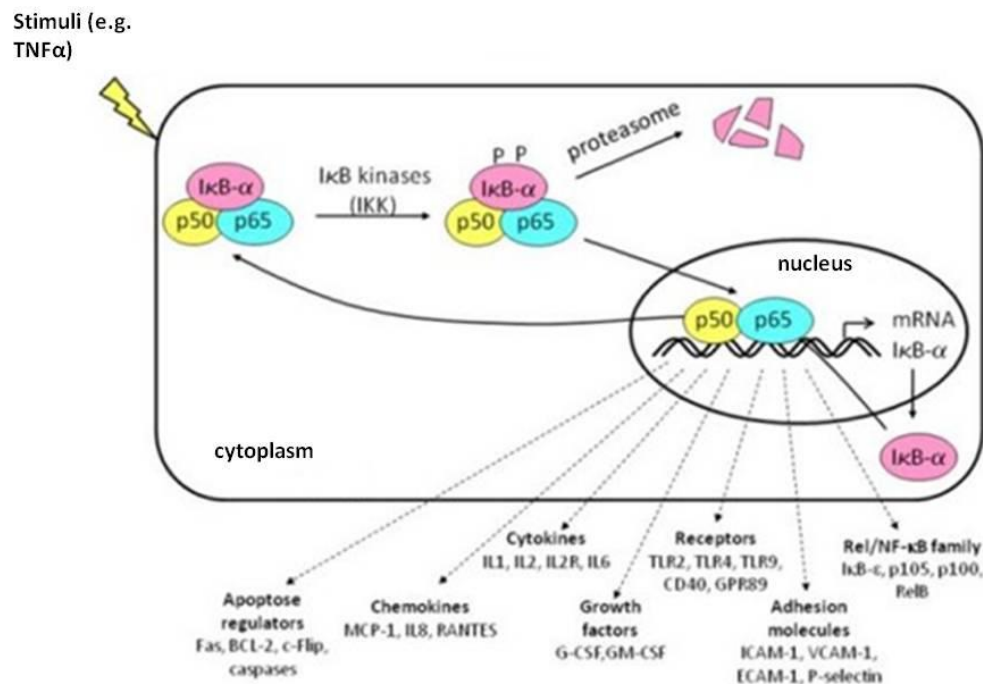


**Figure 1.8 Canonical NF- $\kappa$ B signalling pathway.** Illustrates cytoplasmic location of NF- $\kappa$ B heterodimer (p50/p65) until I $\kappa$ B degradation by IKK allowing NF- $\kappa$ B translocation to the nucleus and subsequent gene transcription.

The NF- $\kappa$ B pathway is controlled by two major signal transduction routes called the canonical and non-canonical pathways. The canonical pathway (Figure 1.8) is activated by a wide range of stimuli including bacterial antigens that activate Toll like receptors (TLR) (e.g. LPS) and pro-inflammatory cytokines including TNF $\alpha$  and IL-1. It functions as outlined above with IKK mediated degradation of the I $\kappa$ B protein allowing NF- $\kappa$ B translocation to the nucleus and gene transcription. The non-canonical pathway has a smaller set of activating stimuli (e.g. CD40, lymphotoxin  $\beta$  and B-cell activating factor (BAFF)), and is involved specifically in activation of p52/ RelB heterodimer activation (which is central in B- and T-cell organ development). Upon stimuli binding NF- $\kappa$ B-inducing kinase (NIK) is activated, which phosphorylates specific serine residues on IKK $\alpha$ . Specific serine residues present on p52's precursor p100 are phosphorylated leading to release of the mature p52/ RelB heterodimer and subsequent gene transcription [179].

### **1.7.2 NF- $\kappa$ B and liver fibrosis**

As highlighted earlier liver fibrosis development is a result of chronic inflammation and the wound healing response, experimental models have shown that elevated NF- $\kappa$ B levels are found in a variety of hepatic cell types [180, 181]. Kupffer cells exhibit high levels of NF- $\kappa$ B activity in response to continued liver insult and as a result secrete a range of pro-inflammatory cytokines including TNF $\alpha$  and IL-6 that perpetuate fibrosis development [182]. NF- $\kappa$ B activation is also important in HSC transdifferentiation to hepatic myofibroblasts (central in fibrosis development). Specifically NF- $\kappa$ B is associated with promoting hepatic myofibroblast survival and preventing their apoptosis [183, 184].

## **1.8 Study objectives**

Research over the previous thirty years has recognised the central role of the HSC in hepatic fibrosis development and perpetuation [185, 186]. A number of routes and pathways have been identified to target potential anti-fibrotic agents to (e.g. inducing hepatic myofibroblast apoptosis and preventing initial HSC activation) [72, 76, 90, 93]. A relatively unstudied target except for work within this laboratory is the PXR, whose anti-inflammatory potential has been highlighted in other chronic diseases including IBD [166, 170].

A fundamental issue in the development of a clinically available anti-fibrotic agent is the lack of a suitable non-invasive imaging modality to accurately quantify hepatic fibrosis at all stages of disease progression.

Another area of interest is that the stimulus responsible for activation and transdifferentiation of HSCs remains elusive. This may be due to the complex interaction between wound healing and inflammatory pathways after liver injury, highlighted by the numerous inflammatory cytokines and mediators released after initial liver injury [39, 40]. It has been suggested the stimulus may arise from a subset of hepatic myofibroblasts themselves, which I intend to investigate further [3].

Recognising the central role of hepatic myofibroblasts in the development of liver fibrosis, the first hypothesis is that their number is an indicator of fibrosis severity. Secondly we hypothesise that hepatic myofibroblasts are pro-inflammatory and will therefore perpetuate fibrosis development following hepatic myofibroblast formation. Finally in addition to their anti-fibrotic traits we hypothesise that PXR agonists also possess beneficial anti-inflammatory properties decreasing NF- $\kappa$ B activity.

The specific initial aims of this study are to: -

- Determine whether the hepatic myofibroblast specific scAb C1-3 can be used as a non-invasive imaging agent for liver fibrosis *in vivo* when conjugated to a fluorescent tag.

- Investigate synaptophysin expression of both quiescent and activated HSCs and to confirm C1-3's affinity for synaptophysin expressed on their surface.
- Investigate the anti-inflammatory potential of the PXR agonist PCN in both an acute and chronic animal model of liver fibrosis.
- Determine whether hepatic myofibroblasts are pro-inflammatory *in vitro* by co-culturing them with a NF- $\kappa$ B luciferase responsive monocyte cell line. Secondly *in vivo*, inject hepatic myofibroblasts directly into NF- $\kappa$ B luciferase mice and calculate their inflammatory properties from the optical images.

## **Chapter 2.0 - Materials and Methods**

## **2.1 Materials**

Materials were purchased from Sigma-Aldrich (Poole, Dorset) unless stated otherwise.

## **2.2 Animals**

### **2.2.1 Ethics**

All animal work was carried out adhering to Home Office regulations as outlined in both the project license (PPL 60/3907) and personal license (PIL 60/12677). Protocols were individually designed for each study and the senior animal technician consulted before the study commenced.

### **2.2.2 Housing**

Rats and mice were housed separately in the Comparative Biology Centre (CBC) at Newcastle University. Specifically they were housed in an air conditioned environment with a 12 hour light dark cycle, regulated temperature ( $20\text{ }^{\circ}\text{C} \pm 3\text{ }^{\circ}\text{C}$ ) and humidity ( $50\% \pm 10\%$ ).

3x- $\kappa\text{B-luc}$  C57BL/6J x CBA/J (NF- $\kappa\text{B}$  luciferase) mice were also housed in regulated conditions in the animal unit at the University of Oslo or in the CBC, and all experiments were performed according to the national guidelines for animal welfare.

### **2.2.3 C57B1/6 (wildtype) mice**

Mice were purchased from Charles-River (Margate, UK) and housed as outlined in 2.2.2 and cared for as outlined in the Home Office licenses. All mice were at least 8 weeks of age before use in any studies.

#### **2.2.4 3x- $\kappa$ B-luc C57BL/6J x CBA/J (NF- $\kappa$ B luciferase) mice**

In the PXR study, NF- $\kappa$ B luciferase mice [187] were kindly provided by Dr Harald Carlsen (University of Oslo, Norway). In the later C1-3/ C1-3-GTX and hepatic myofibroblast studies carried out at the CBC in Newcastle (section 6.5), NF- $\kappa$ B luciferase mice were bred in house after revival and fertilisation of zygotes purchased from Charles-River. All mice were a minimum of 8 weeks of age before use in any studies.

#### **2.2.5 Sprague-Dawley rats**

Male Sprague-Dawley rats were purchased from Charles-River and housed as outlined in 2.2.2, rats were approximately 250-300g in bodyweight when studies began.

#### **2.2.6 Dosing solutions**

The concentration, volumes and administration routes of all compounds administered to mice and rats are listed in Table 2.1.

<b>Solution</b>	<b>Concentration</b>	<b>Amount dosed</b>	<b>Route</b>
<b>CCl<sub>4</sub></b>	1:3 (CCl <sub>4</sub> : olive oil)	1.5ml/kg bodyweight	i.p. injection
<b>Olive oil</b>	Olive oil only (control)	1.5ml/kg bodyweight	i.p. injection
<b>PCN</b>	50mg/ml in 1:3 (CCl <sub>4</sub> : olive oil)	2ml/kg bodyweight	i.p. injection
<b>PCN</b>	50mg/ml in olive oil	2ml/kg bodyweight	i.p. injection

<b>C1-3</b>	1mg/ml in 1 xPBS	20ml/kg bodyweight	i.p. injection
<b>C1-3-GTX</b>	0.5mg/ml in 1 xPBS	40ml/kg bodyweight	i.p. injection
<b>C1-3-750</b>	1mg/ml in 1 x PBS	20ml/kg bodyweight	i.p. & i.v. injection
<b>D-luciferin</b>	15mg/ml in 1 xPBS	10ml/kg bodyweight	i.p. injection
<b>Hepatic myofibroblasts</b>	1 x10 <sup>6</sup> (NF-κB luciferase) cells/ml in 1 x PBS	10ml/kg bodyweight	i.v. injection (tailvein)
<b>Kidney fibroblasts</b>	1 x10 <sup>6</sup> (NF-κB luciferase) cells/ml in 1 x PBS	10ml/kg bodyweight	i.v. injection (tailvein)
<b>Latex beads</b>	Sigma (1.0μM, L2778)	2.5ml/kg bodyweight	i.v. injection (tailvein)

Table 2.1 – *In vivo* dosing solutions

## 2.3 Cell culture

### 2.3.1 Primary human HSCs (hHSCs)

Cells were isolated from human liver resection tissue samples following a collagenase/ pronase digestion method as outlined previously [90, 188]. Ethical approval for the use of human tissue was obtained from the Newcastle and North Tyneside Local Regional Ethical Committee 2, and was subject to informed patient consent.

Briefly the liver was perfused with calcium free Hanks Balanced Salt Solution (HBSS-) (NaCl, 80 g/L; KCl, 4 g/L; glucose, 10 g/L; KH<sub>2</sub>PO<sub>4</sub> 600 mg/L; Na<sub>2</sub>HPO<sub>4</sub> 475 mg/L and phenol red, 170 mg/L) supplemented with 6mM Hepes and 0.035% (w/v) NaHCO<sub>3</sub> manually to flush blood out of the liver. The liver was then perfused with HBSS+ (composed as above but with the addition of 1mM CaCl<sub>2</sub>) supplemented with 235mg of pronase (Roche) and 30mg of Collagenase B (Roche) until it was malleable to touch. At this point the tissue was diced and filtered through 125μm nybolt mesh with HBSS+ washes and the flowthrough aliquoted into 50ml falcons. 1mg of DNase was added per falcon prior to centrifugation at 2000rpm for 7 minutes. The cell pellet was resuspended in 50ml of HBSS+ containing 1mg of DNase and washed a further two times in the same way. Following the final wash the cell

pellet was resuspended in 13ml of optiprep, 2mg of DNase and 60ml of HBSS+. 2ml of HBSS+ was carefully overlaid onto the mixture prior to density gradient centrifugation at 4000rpm for 20 minutes. The lipid rich HSC phase was visible at the top of the falcon and was removed prior to mixing with an excess of HBSS+ (at least 3:1 excess) before centrifugation at 2000rpm for 7 minutes. The HSC cell pellet was resuspended in HSC media and seeded out in 6 well plates as desired.

HSCs were grown in Dulbecco's Modified Eagle Media (DMEM) with 4.5g/L glucose, 110mg/L sodium pyruvate, and 110mg/L sodium bicarbonate, supplemented with 20% (v/v) fetal calf serum (FCS), 10mg/L penicillin/streptomycin and 2mM L-glutamine. Cells were incubated in a humidified atmosphere at 37 °C and 5% CO<sub>2</sub>.

### ***2.3.2 Primary mouse and rat HSCs***

Mouse and rat HSCs were isolated by an essentially identical method to that used in 2.3.1 for hHSC isolation. The only difference being the scaling down of the pronase and collagenase B as necessary, determined on the number of mice/ rat livers to be digested. The cells were cultured in identical media and conditions to that of hHSCs.

### ***2.3.3 LX-2 cells (human myofibroblast cell line)***

LX-2 cells were kindly provided by Professor Scott Friedman (Mount Sinai School of Medicine, New York) and were grown in DMEM with 4.5g/L glucose, 110mg/L sodium pyruvate, and 110mg/L sodium bicarbonate, supplemented with 10% (v/v) FCS, 10mg/L penicillin/ streptomycin and 2mM L-glutamine. Cells were incubated at 37 °C and 5% CO<sub>2</sub>.

#### **2.3.4 Cos7 cells**

Cos7 cells were grown in DMEM with 4.5g/L glucose, 110mg/L sodium pyruvate, and 110mg/L sodium bicarbonate, supplemented with 10% (v/v) FCS, 10mg/L penicillin/ streptomycin and 2mM L-glutamine. Cells were incubated at 37 °C and 5% CO<sub>2</sub>.

#### **2.3.5 U937-NF-κB cells (human monocytic cell line stably transfected with luciferase reporter gene under the control of 3 x NF-κB response elements)**

U937-NF-κB cells are stably transfected with 3 copies of NF-κB response elements and were generously donated by Dr Harald Carlsen (University of Oslo, Norway) and grown in RPMI-1640 media (25mM Hepes and 25mM sodium bicarbonate) (Sigma) supplemented with 10% (v/v) FCS, 10mg/L penicillin/ streptomycin, 2mM L-glutamine and 150µg/ml *Hygromycin B*. Incubated at 37 °C with 5% CO<sub>2</sub>, U937-NF-κB cells are a non-adherent cell line so trypsination was not required when passaging.

Untransfected U937 cells were also purchased from the European Collection of Cell Cultures (ECACC). They were cultured in identical media except the lack of selective antibiotic *Hygromycin B*.

#### **2.3.6 Cell passage**

All the cell lines cultured with the exception of the U937 and U937-NF-κB cells were adherent and were routinely grown as a monolayer to approximately 75-100% confluence before passaging. Initially the media was aspirated from the cells prior to two brief washes in 1 x PBS (approximately 10mls – T75 and 1ml per well of a 6 well plate). Cells were then incubated with Trypsin-EDTA diluted accordingly (dependent upon cell type) in 1 x PBS (approximately 3mls

– T75 and 0.5ml per well of a 6 well plate) in identical conditions listed in 2.3.1 for between 5-15 minutes. At random intervals during this incubation the detachment of the cells from the culture vessel was encouraged by gentle tapping. Once detachment was confirmed by light microscopy, Trypsin-EDTA activity was inhibited by the addition of an excess of serum containing media. The Trypsin-EDTA/ cell mixture was then transferred to a sterile 50ml falcon tube prior to centrifugation (typically at 2000rpm for most cell types) for 5 minutes. The supernatant was aspirated off prior to resuspension of the cell pellet in fresh media, before seeding the cells as desired for experiments or cell maintenance.

### **2.3.7 Cell storage**

Cell lines were routinely frozen down both in liquid nitrogen (LqN<sub>2</sub>) and at – 80 °C when no longer required or for stock lines. Cells were detached as outlined in 2.3.6, but the cell pellet was resuspended in a small volume of media (typically 1-2ml for a T75 flask). This was then diluted 1:1 with freezing media (90% (v/v) FCS/ 10% (v/v) DMSO) before aliquoting into sterile cryovials (approximately 1.5ml per cryovial). The cryovials were then placed into a Nalgene® Mr. Frosty® Cryo 1°C Freezing Container containing isopropanol and left at – 80 °C overnight. This cools the cells at a rate of approximately 1 °C per hour. The following day some cryovials were placed in LqN<sub>2</sub> whilst the rest were left at – 80 °C.

### **2.3.8 Cell revival**

Cell lines were removed from the – 80 °C or LqN<sub>2</sub> and rapidly thawed at 37 °C in a waterbath, resuspended in 30ml freshly warmed media and centrifuged at 600rpm for 5 minutes. The supernatant was then discarded and the cell pellet resuspended in 5mls of fresh media, which was aliquoted between 2 wells of

a 6 well plate. The cells were left to attach overnight and the following morning the media was replaced.

### ***2.3.9 Cell viability and number***

The viability of cells was determined by their ability to exclude trypan blue. This was particularly important for counting the non adherent U937 and U937-NF- $\kappa$ B cells. Typically a fixed volume of cells (normally 50 $\mu$ l) was added to an equal volume of 0.4% (w/v) trypan blue solution. This mixture was then pipetted into a haemocytometer and the number of viable live cells was determined by those that had not excluded the trypan blue. As the area of the haemocytometer and the volume of cell suspension are known, the number and percentage of viable cells can be calculated.

### ***2.3.10 U937-NF- $\kappa$ B cells co-culture with LX-2 and hHSCs***

hHSCs or LX-2 cells were grown to approximately 50% confluence in 6 well plates. The media was then aspirated and the cells washed three times with 1 x PBS, prior to addition of  $1 \times 10^5$  U937-NF- $\kappa$ B cells in 1.5ml of RPMI-1640 media per well.  $1 \times 10^5$  U937-NF- $\kappa$ B cells were also added to wells not containing any cells, which acted as controls. At this point any treatments were also added (e.g. LPS 300ng/ $\mu$ l, see table 2.2 for a full list of treatments and final concentrations). The co-culture was incubated as outlined in 2.3.1 for 6 hours, before centrifugation of the U937-NF- $\kappa$ B cells at 13,000rpm for 5 minutes to isolate the cell pellet. Each individual cell pellet was resuspended in 100 $\mu$ l of 1 x passive lysis buffer (1 x PLB) (Promega) diluted in distilled water, prior to luciferase activity determination.

**2.3.11 LX-2 and hHSC conditioned media and its treatments**

LX-2 cells or hHSCs were washed three times in sterile 1 x PBS before being cultured in U937 media (RPMI-1640) for 48 hours, typically the LX-2/ hHSC cells were approximately 50% confluent at the start of the 48 hour incubation. The media was removed and centrifuged at 2000rpm to remove any cell debris and the supernatant was stored at 4 °C short term or -20 °C long term before the incubation with U937-NF- $\kappa$ B cells with further treatment when required.

To determine the identity of the soluble factor present in the LX-2/ hHSC conditioned media, a number of treatments were performed prior to the resuspension of U937-NF- $\kappa$ B cells. A full list of these treatments is shown in table 2.3.

<b>Treatment (final concentration)</b>	<b>Theory (reference)</b>
<b>LPS 055:B5 (300ng/<math>\mu</math>l)</b>	Positive control known to induce NF- $\kappa$ B activity in U937-NF- $\kappa$ B cells ([175])
<b>TNF<math>\alpha</math> (10ng/<math>\mu</math>l)</b>	Pro-inflammatory cytokine - positive control shown to induce NF- $\kappa$ B activity in U937-NF- $\kappa$ B cells ([175])
<b>IL-6 (10ng/<math>\mu</math>l)</b>	Pro-inflammatory cytokine produced by hepatic myofibroblasts ([189] and Table 6.1)
<b>IL-8 (10ng/<math>\mu</math>l)</b>	Pro-inflammatory cytokine produced by hepatic myofibroblasts (Table 6.1)
<b>IL-1<math>\alpha</math> (10ng/<math>\mu</math>l)</b>	Expressed at high levels following liver injury and known to be pro-inflammatory ([190, 191])
<b>IL-1<math>\beta</math> (10ng/<math>\mu</math>l)</b>	Expressed at high levels following liver injury and known to be pro-inflammatory ([190, 191])
<b>IL-1RA (10ng/<math>\mu</math>l)</b>	Expressed at high levels following liver injury and known to be pro-inflammatory ([190, 191])
<b>Serotonin (1<math>\mu</math>M)</b>	hHSCs express serotonin receptors and treatment with serotonin antagonists anti-fibrogenic ([192])
<b>TIMP-1 (10ng/<math>\mu</math>l)</b>	Important regulator of ECM deposition & prevention of myofibroblast apoptosis ([57, 193])
<b>Angiotensin II (10ng/<math>\mu</math>l)</b>	Known to promote hepatic myofibroblast survival by inhibition of NF- $\kappa$ B degradation ([194])
<b>Leptin (1<math>\mu</math>g/ml)</b>	Leptin expression confined to activated HSCs & has a pro-fibrogenic effect ([195, 196])
<b>IP-10 (50ng/<math>\mu</math>l)</b>	IP-10 levels correlate with liver inflammation

	and fibrosis ([197])
<b>MCP-1 (10ng/μl)</b>	MCP-1 important in monocyte recruitment during liver fibrosis development ([198, 199])
<b>MIP-1α (100ng/μl)</b>	MIP-1α is pro-inflammatory chemokine involved in T-cell recruitment and fibrosis progression ([200])
<b>CXCL12 (10ng/μl)</b>	CXCL12 chemokine is up-regulated in regions of liver fibrosis in HCV patients ([201])
<b>Hydrogen peroxide (10mM - 1μM)</b>	Oxidation of fatty acids is a source of ROS including H <sub>2</sub> O <sub>2</sub> ([202, 203])
<b>Sodium nitroprusside (1mM)</b>	Increased nitric oxide production found during hepatic inflammation ([204, 205])
<b>OxPAPC (1μg/ml)</b>	TLR4 antagonist to inhibit LPS induced inflammation to show LPS isn't being stored and re-released by LX-2s ([206])

Table 2.2 – U937-NF-κB cells *in vitro* treatments

<b>Treatment</b>	<b>Theory</b>
<b>90 °C incubation</b>	Break dipole and Van der Waal bonds - disrupting 2 <sup>o</sup> / 3 <sup>o</sup> protein structure
<b>10 x trypsin-EDTA treatment</b>	Protease treatment to hydrolyse proteins and peptides present
<b>Charcoal/ dextran media stripping</b>	Adsorb small organic molecules from the media (e.g. steroid hormones and prostaglandins)
<b>Separation organic/ aqueous phases</b>	Separate organic (e.g. phospholipids, lipids) and aqueous phase to see if soluble factor is retained specifically in a phase
<b>pH 1/ 13 incubation</b>	Determine the effect of extreme variation in pH on soluble factor function
<b>PD-10 filtration</b>	Sepharose gel column so larger molecules are eluted earlier as they can't diffuse into the column bed

Table 2.3 – Treatments to 48 hour LX-2 conditioned media

## 2.4 Cell transfection

### 2.4.1 Transfection using GeneJuice reagent (Merck)

Cos7 and U937 cells were transfected as outlined in the manufacturers' guidelines, under the standard conditions listed in 2.3.1. Typically adherent cells were approximately 60-70% confluent (non adherent cells were seeded

at  $1 \times 10^6$  cells/ml) to ensure the cells were undergoing cell division at the time of transfection. In all instances the cells were suspended in 3ml of serum containing media per well, and for each well to be transfected 100 $\mu$ l of serum free media was mixed with 3 $\mu$ l of GeneJuice (Merck) and incubated at room temperature for 5 minutes. 1 $\mu$ g of plasmid DNA for each well was subsequently added and mixed by gentle pipetting, before further incubation at room temperature for 15 minutes. The GeneJuice/ DNA mixture (approximately 105 $\mu$ l per well) was added dropwise to the centre of the well and mixed by gentle rocking. The cell transfection mixture was incubated overnight and replaced with fresh media the following morning. The cells were left for a further 24 hours before harvesting for analysis or addition of antibiotics to select for transfected cells.

#### ***2.4.2 Transfection using polyethylenimine (PEI) (Polysciences Inc.)***

Cell lines were seeded at the same densities as outlined in 2.4.1, containing a total of 1ml of serum containing media per well. For each well of a 6 well plate, 10 $\mu$ l of PEI (1mg/ml in 20 mM HEPES, pH 7.5) and 1 $\mu$ g of plasmid DNA was added to 1ml of serum free media prior to vortexing and incubation for 30 minutes at room temperature. The whole mixture (approximately 111 $\mu$ l) was then added dropwise to the centre of each well before incubation as outlined in 2.4.1 and subsequent harvesting or treatment.

#### ***2.4.3 Determination of transfection efficiency***

Alongside the transfection of the desired plasmid DNA, control cells were also transfected with varying concentrations of enhanced Green Fluorescent Protein (eGFP) peGFP-N1 plasmid DNA. The number of GFP positive cells was determined by fluorescent microscopy and expressed as a percentage of the total number of cells per field of view (normally at least 10 fields of view were counted per well).

## **2.5 Plasmid DNA constructs**

### ***2.5.1 Transformation of TOP10 competent cells (Invitrogen)***

Upon thawing on ice, 2µl of plasmid DNA was added to the TOP10 cells and mixed by gentle pipetting. The plasmid cell mixture was left to incubate on ice for 30 minutes; following this the cells were heat shocked at 42 °C for thirty seconds before a second incubation on ice for five minutes. 250µl of SOC media (2% tryptone, 0.5% yeast extract, 10 mM sodium chloride, 2.5 mM potassium chloride, 10 mM magnesium chloride, 10 mM magnesium sulphate and 20 mM glucose) was added prior to incubation at 37 °C and 250rpm for one hour. Finally a small volume (i.e. 10-50µl of each plasmid was streaked out on selective agar plates (e.g. 100µg/ml ampicillin) and grown overnight at 37 °C.

The following morning a single colony was selected and incubated in 5ml of Luria-Bertani media (LB media) (5g/L yeast extract, 10g/L tryptone and 10g/L sodium chloride) containing the desired selective antibiotic and grown up at 37 °C and 250rpm for 8 hours. The culture could then be further used for large scale plasmid expression or frozen down for storage as described in 2.5.2.

### ***2.5.2 Storage of DNA plasmids***

All constructs were stored long-term as bacterial glycerol stocks by mixing 500µl of the final culture from 2.5.1 with an equal volume of LB media (containing 30% (v/v) glycerol) in a cryovial followed by freezing at – 80 °C. The stocks could be streaked out directly onto selective agar plates as described in 2.5.1 when further plasmid DNA was required. The plasmid DNA could then be purified by either a miniprep (2.5.3) or maxiprep (2.5.4) procedure dependent upon the bacterial scale of expression.

### ***2.5.3 Miniprep purification of plasmid DNA***

The QIAprep® Miniprep system (Qiagen) is designed to rapidly purify plasmid DNA in small quantities (up to 20µg of DNA). The principle is based upon the alkaline lysis of bacterial cells followed by the adsorption of the DNA onto the silica columns at high salt concentrations [207].

The manufacturer's guidelines were followed; briefly the bacterial pellet was isolated by centrifugation at 13,000rpm for 5 minutes, this pellet was resuspended in 250µl of Buffer P1 (containing RNase) and transferred to an RNase free eppendorf. 250µl of Buffer P2 (high salt) was added and mixed by inverting the tube six times, 350µl of Buffer N3 was added and again mixed immediately by inversion. This solution was centrifuged at 13,000rpm for 10 minutes; the supernatant is applied to the QIAprep spin column which was centrifuged for a further minute. After discarding the flow-through the column was washed with 750µl of Buffer PE and centrifuged for one minute, the flow-through was discarded once more and the column was centrifuged for a further minute to remove any residual buffer. Finally the QIAprep spin column was placed in an RNase free eppendorf, to elute the plasmid DNA 50µl sterile water was added to the column. This was allowed to stand for a minute prior to centrifugation for a final minute; the eluted DNA was quantified as outlined in 2.6.3.

### ***2.5.4 Maxiprep purification of plasmid DNA***

The Qiagen Maxiprep kit purification of plasmid DNA is based upon the same principle as that of the Miniprep kit, but is simply manufactured to purify larger amounts of plasmid DNA (up to a maximum of 500µg). Initially the bacterial cell pellet was isolated by centrifuging the bacterial culture at 3500rpm for 10 minutes at 4 °C. The cell pellet was resuspended in 10ml of Buffer P1 (containing RNase) by repeated pipetting, 10ml Buffer P2 was added and

mixed by inverting the sealed tube 4-6 times and incubated at room temperature for 5 minutes. 10ml of chilled Buffer P3 was subsequently added and the whole mixture was mixed by 4-6 vigorous inversions prior to incubation on ice for 20 minutes. The mixture was then centrifuged at 6000rpm and 4 °C for 30 minutes. During the centrifugation step a QIAGEN-tip 500 was equilibrated by the addition of 10ml Buffer QBT. Upon completion of the centrifugation step the supernatant was applied to the column and allowed to enter the resin by gravity flow. The column was then washed twice in 30ml of Buffer QC; all the flow-through was discarded. The DNA was eluted from the column by the addition of 15ml of Buffer QF, which was collected in a 50ml falcon. The DNA was precipitated by the addition of 0.7 volumes (10.5ml) of sterile isopropanol, mixed and centrifuged at 6000rpm for 30 minutes. The supernatant was discarded and the pellet washed in 5ml of sterile 100% ethanol and the DNA pelleted by centrifugation at 6000rpm for 15 minutes. Finally the ethanol was removed and the pellet dried briefly for 5 minutes before resuspension of the DNA in a suitable volume of RNase free water (dependent upon the size of the pellet). The DNA was quantified as outlined in 2.6.3.

### ***2.5.5 3xNF-κB response element DNA insert construction***

The complementary sequences containing the coding sequence for three copies of a NF-κB response element were firstly denatured by heating at 95 °C for 10 minutes. The temperature was then reduced by 1 °C every minute from 95 °C down to 50 °C to ensure the complementary sequences annealed successfully (see results 3.4.3 for the complete 3xNF-κB insert sequence).

### ***2.5.6 Restriction digests of plasmid DNA***

Restriction digests were performed following the manufacturers' guidelines (Promega, UK) typically using 1µg (1µl) of plasmid DNA. The reaction mixture

was composed of 16.3 $\mu$ l of sterile water, 2 $\mu$ l of 10 x reaction buffer (dependent on compatibility with specific restriction enzyme), 0.2 $\mu$ l of acetylated BSA (10 $\mu$ g/ $\mu$ l) and 1 $\mu$ l of plasmid DNA (1 $\mu$ g/ $\mu$ l). 0.5 $\mu$ l restriction enzyme was added at the last instance and mixed by gentle pipetting before incubation at 37 °C for 4 hours. A sample in which no restriction enzyme was added was also incubated as a negative control; both samples were run out on an agarose gel as described in 2.6.8 to determine if the restriction digest had generated DNA fragments of the desired size.

### ***2.5.7 Gel extraction of DNA samples***

The DNA fragment of interest was excised from the gel using a clean sharp scalpel and placed in a DNase/ RNase free eppendorf. The DNA was purified using a gel extraction kit (Qiagen). Firstly the gel fragment was resuspended in 3 volumes of Buffer QG (i.e. 100mg gel = 300 $\mu$ l of buffer QG), this was heated at 50 °C for 10 minutes until the agarose was fully dissolved. One volume of sterile isopropanol was added (100mg gel = 100 $\mu$ l isopropanol). The sample was applied to the QIAquick spin column, and centrifuged for one minute at 13,000rpm, discarding the flow through. 0.75ml of Buffer PE was added to the QIAquick spin column and centrifuged for a further minute to wash the bound DNA. The flow through was discarded once more and the column centrifuged for another minute to remove any residual Buffer PE. Finally the column was placed into a sterile DNase/ RNase free eppendorf and the DNA eluted by adding 30 $\mu$ l sterile water to the centre of the QIAquick membrane. The column was left to stand for one minute before centrifuging for a final minute at 13,000rpm.

The amount of DNA collected in the eppendorf was quantified as before in 2.6.3.

### ***2.5.8 T4 DNA ligation of DNA plasmid and insert***

T4 DNA ligase (Promega) was used to ligate the NF- $\kappa$ B insert (section 2.5.5) into the linearised plasmid DNA. The insert encodes the same 'sticky ends' (restriction site sequences) at its ends as those used to restrict the plasmid DNA. A range of molar ratios (1:1, 3:1 and 1:3) of plasmid to insert DNA were used in the ligation reaction using 100ng of plasmid DNA. A 10 $\mu$ l reaction volume was used composed of 100ng plasmid DNA, a calculated volume of insert DNA (dependent on the molar ratio used), 1 $\mu$ l of 10 x ligase buffer, and 0.5 $\mu$ l of T4 DNA ligase made up to 10 $\mu$ l with sterile water. The reaction was incubated at 15 °C for at least 4 hours.

## **2.6 RNA and DNA isolation/ quantification**

### ***2.6.1 RNA isolation***

Total RNA was isolated following a guanidium thiocyanate-phenol-chloroform extraction protocol using TRIzol reagent (Invitrogen, UK) [208]. A tissue sample was resuspended in 1ml of TRIzol and homogenised manually in an RNase/ DNase free eppendorf. Alternatively cells were washed in sterile 1 x PBS and 1ml of TRIzol was added per well of a 6 well plate and placed on a rotating plate mixer at 250rpm for 5 minutes before being transferred to an RNase/ DNase free eppendorf. 200 $\mu$ l of chloroform was added to the TRIzol and vortexed briefly prior to centrifugation at 13,000rpm and 4 °C for 15 minutes. The upper aqueous layer containing the RNA was removed and transferred to a fresh eppendorf, then 500 $\mu$ l chilled sterile isopropanol was added and the mixture incubated on ice for 20 minutes; before centrifugation at 13,000rpm and 4 °C for 10 minutes. The supernatant was discarded and the RNA pellet washed in 500 $\mu$ l 70% (v/v) ethanol (diluted in sterile water) before a final ten minute centrifugation step at 13,000rpm and 4 °C. Finally following removal of the 70% ethanol the RNA pellet was resuspended in a small volume (typically 10-30 $\mu$ l) of nuclease free water dependent upon the pellet size. The purified RNA was quantified as outlined in 2.6.3.

### **2.6.2 DNA isolation**

Cells were washed in sterile 1 x PBS, before detachment by scraping into sterile 1 x PBS. The cell pellet (typically  $5\text{-}20 \times 10^6$  cells) was isolated by centrifugation and the 1 x PBS was discarded and the pellet resuspended in 200 $\mu$ l of genomic DNA preparation buffer (50mM Tris, 10mM sodium chloride, 10mM EDTA and 0.5% NP-40, pH 8). For genotyping, ear notches from mice were collected in an RNase/ DNase free eppendorf and resuspended in 200 $\mu$ l of genomic DNA preparation buffer as above. 20 $\mu$ l of Proteinase K solution (20mg/ml) (Qiagen) was added and the mixture was incubated at 55 °C for a minimum of 4 hours – overnight with occasional mixing. The following morning 50 $\mu$ g of RNase A was added to each sample and incubated at room temperature for 20 minutes. 1 volume (200 $\mu$ l) of phenol/ chloroform/ isoamyl alcohol (25/24/1 v/v/v) was added, vortexed and centrifuged briefly. The upper aqueous phase was carefully removed (~200 $\mu$ l) to a fresh RNase/ DNase free eppendorf, prior to the addition 0.1 volumes (20 $\mu$ l) of 3M sodium acetate, pH 5.2. 2 volumes (500 $\mu$ l) of chilled 100% ethanol was added prior to incubation at – 80 °C for one hour; following this, the DNA was isolated by centrifugation at 13,000rpm for 10 minutes and 4 °C. The supernatant was discarded and the pellet dislodged and washed in 500 $\mu$ l of chilled 70% ethanol before incubation at – 80 °C for a further hour. After a final centrifugation step at 13,000rpm and 4 °C for 10 minutes the supernatant was discarded and the pellet air dried briefly before resuspension in a suitable volume of sterile water (typically 10-50 $\mu$ l dependent on pellet size). The purified DNA was quantified as outlined in 2.6.3.

### **2.6.3 RNA/ DNA quantification**

RNA and DNA were both quantified at 260nm. The relative purity of RNA/ DNA was determined by calculating the 260/ 280 ratio. 2 $\mu$ l of RNA/ DNA was

diluted in 198µl sterile water and transferred to a quartz cuvette, the absorbance of samples was measured at both 260 and 280nm, using 200µl of sterile water as a control to account for the background absorbance. The DNA concentration was calculated knowing an absorbance of 1.0 at 260nm was equivalent to a DNA concentration of 20µg/ml; for RNA an absorbance of 1.0 at 260nm was equivalent to an RNA concentration of 25µg/ml.

The purity of DNA was assessed with pure DNA having a 260/ 280 ratio of approximately 1.80, ratios nearer 1.60 indicate protein contamination whilst nearer 2.0 indicate RNA contamination. Pure RNA has a 260/ 280 ratio of 2.1 so any reading significantly lower than 2.0 suggests DNA and protein contamination [209, 210].

#### ***2.6.4 DNase treatment of RNA***

RNA was treated with RQ1 (RNA-Qualified) RNase-Free DNase, which is a DNase I endonuclease (Promega) that degrades both double-stranded and single-stranded DNA whilst not affecting RNA integrity. Typically RNA was resuspended in 30-50µl sterile water; if 30µl was used, 0.1 volumes of RQ1 10x DNase I and 0.1 volumes of DNase I were added to each RNA sample (i.e. 3µl of each). The sample was mixed by gentle pipetting and incubated at 37 °C for 30 minutes; the reaction was terminated by the addition of 0.1 volumes (3µl) of RQ1 DNase stop solution and incubation at 65 °C for a further 10 minutes. An aliquot of the RNA was quantified as outlined in 2.6.3 to determine sufficient purity for future use.

#### ***2.6.5 Reverse transcription***

Moloney Murine Leukemia Virus Reverse Transcriptase (M-MLV RT) is an RNA-dependent DNA polymerase (Promega) that can be used in complementary DNA (cDNA) synthesis with long messenger RNA templates.

RNA samples were diluted to 200ng/ $\mu$ l with nuclease free water; 1 $\mu$ l of 50ng/ $\mu$ l Random Primers (Promega) was added to 800ng of RNA (i.e. 4 $\mu$ l of 200ng/ $\mu$ l RNA) and incubated at 90 °C for three minutes before reducing the temperature to 42 °C, and placing the samples on ice. 15 $\mu$ l of reverse transcription mastermix was then added to each sample (containing 8 $\mu$ l nuclease free water, 2 $\mu$ l 10mM dNTPs, 4 $\mu$ l 5 x M-MLV buffer (50mM Tris-HCl, 75mM KCl, 3mM MgCl<sub>2</sub> and 10mM DTT, pH 8.3) and 1 $\mu$ l M-MLV enzyme). The samples were then incubated for a further hour at 42 °C to produce 1st strand cDNA and stored at – 20 °C prior to further use.

### **2.6.6 Polymerase Chain Reaction (PCR)**

PCR is a universal technique in molecular biology and is used to amplify specific DNA sequences. Generally Go-Taq Green master mix (Promega) containing a Taq DNA polymerase was used to amplify DNA; however Pfu DNA polymerase (Promega) was also used. Pfu was chosen instead of Go-Taq in some instances as it has enhanced proofreading capabilities and will result in fewer base misinsertions and more accurate DNA amplification.

PCR reaction conditions were optimised for each individual primer set (see table 2.4), always with the same reaction volume, as follows: -

**Go-Taq Green** – the PCR mastermix was composed of 10 $\mu$ l 2 x Go-Taq green master mix, 6 $\mu$ l of nuclease free water and 2 $\mu$ l of each upstream (US) and downstream (DS) primer (diluted to 10 $\mu$ M) giving a final concentration of 1 $\mu$ M per individual sample. 1 $\mu$ l of cDNA was added giving a total volume of 21 $\mu$ l in each PCR tube.

**Pfu** – the PCR mastermix was composed of 5 $\mu$ l of 10 x Pfu buffer (200mM Tris-HCl, 100mM KCl, 100mM (NH<sub>4</sub>)<sub>2</sub>SO<sub>4</sub>, 20mM MgSO<sub>4</sub>, 1.0% Triton® X-100 and 1mg/ml nuclease-free BSA, pH 8.8), 1 $\mu$ l of 10mM dNTPs, 4 $\mu$ l of each US and DS primer (10 $\mu$ M), 30.3 $\mu$ l of nuclease free water and finally 0.7 $\mu$ l of Pfu

enzyme. 5µl of cDNA was added giving a total volume of 50µl in each reaction.

Each PCR reaction was performed using a programmed benchtop thermocycler (Px2 Thermal Cycler, Thermo Scientific).

Typically a PCR run consisted of: -

**Initial denaturation** step at 90 °C for 3 minutes.

35 cycles consisting of

**Denature** – 90 °C for 1 minute.

**Anneal** – X °C for 1 minute. (Optimised for each primer set ~55 °C)

**Elongate** – 73 °C for 1 minute 30 seconds.

**Final elongation** step at 73 °C for 8 minutes.

PCR products were stored at 4 °C for short term periods or – 20 °C long term.

### ***2.6.7 PCR primer design***

As shown in table 2.4 multiple primer sequences were designed to specifically amplify desired DNA sequences. DNA sequences were obtained from the NCBI database ([www.ncbi.nlm.nih.gov](http://www.ncbi.nlm.nih.gov)). The Primer-BLAST program was then used to derive the primer sequences specific for the transcript and avoid the likelihood of primer dimer formation. The general rules for primer design

are that the G & C content of each primer should be similar to ensure the  $T_m$  values are also similar and that they should contain 40-60% G & C. Primers were 18 – 25 bases in length and were not complementary to avoid dimer formation. The optimal annealing temperature was determined for each primer pair, generally starting around 5 °C below the  $T_m$ .

<b>Oligo ID</b>	<b>5' - 3' sequence</b>	<b>Annealing temperature (°C)</b>	<b>Amplicon size (bp)</b>
<b>LUCIF (US)</b>	CCGGAAGCGACCAACGCCTT	58	221
<b>LUCIF (DS)</b>	CCGGCGTCATCGTCGGGAAG		
<b>GAPDH (US)</b>	TGACATCAAGAAGGTGGTGAAG	42	234
<b>GAPDH (DS)</b>	TCTTACTCCTTGGAGGCCATGT		
<b>SYN1 (US)</b>	ATGGACGTGGTGAATCAGCTGGT	62	347
<b>SYN2 (DS)</b>	GCCCCATGGAGTAGAGGAA		
<b>SYN3 (DS)</b>	CATCTGATTGGAGAAGGAGGTGGG	63	924
<b>SYN4 (DS)</b>	GGGTGCATCAAAGTACACTTGG	63	237

**Table 2.4 – DNA oligonucleotide sequences for RT-PCR and PCR genotyping**

### **2.6.8 Agarose gel electrophoresis**

This method can be used to separate both DNA and RNA when a charge is applied across the gel in an appropriate conducting buffer. The nucleic acids will migrate towards the positive electrode due to the negative charge of their sugar-phosphate backbone; the distance migrated is governed by the size of the fragment, with smaller nucleic acids fragments migrating further. Samples were compared against a DNA ladder (New England Biolabs) containing DNA fragments of known size, so the size and specificity of bands could be determined easily.

The percentage of agarose used in the gel was dependent on the size of the PCR product with a higher percentage gels being used for smaller fragments. Typically 1.5% (w/v) agarose in 1 x TAE (Tris acetate EDTA) was heated in the microwave until the agarose was fully melted. When it had cooled sufficiently, ethidium bromide (EtBr) (2µl EtBr (10mg/ml) per 100ml of agarose) was added and mixed. EtBr is an intercalating agent binding to nucleic acids, and upon exposure to UV light fluoresces allowing the visualisation of both DNA and RNA. The gel was poured into a casting stand

with the well comb in the place to form the wells for sample loading. When the gel had set it was placed into the gel tank and submerged in 1 x TAE. 10µl of each amplified PCR product (diluted 1:0.5 with 6 x loading dye) was loaded alongside 6µl of 100bp DNA ladder (New England Biolabs). The gel was typically run at 80V for an hour, approximately 4-5V/cm agarose gel, and was visualised by UV transillumination using an Alpha Innotech fluorescent imaging system and the supplied Fluorchem software.

### **2.6.9 Quantitative real-time PCR (qRT-PCR)**

cDNA samples were diluted 1:4 to 10ng/µl, 1µl was then added to each well of a 96 well plate (Applied Biosystems, Warrington, UK), and each sample was loaded in triplicate. 12µl of SYBR green mastermix was added to each well in turn (consisting of 3.5µl DNase free water, 6.5µl 2x SYBR green mastermix and 2µl US and DS primers (250nm)). The plate was run on an Applied Biosystems 7500 Fast Real-Time PCR system machine, after the initial denaturation step there were 40 cycles consisting of –

- 95 °C for 5 seconds
- 62 °C for 30 seconds
- 72 °C for 1 minute

The level of SYBR Green detected was measured during the cycling step of each cycle and the cycle threshold ( $C_T$ ) values were calculated by manually applying a threshold limit to represent the exponential phase of amplification. SYBR Green binds to double stranded DNA (dsDNA) and fluoresces, this was detected at the end of each elongation step giving a value to the amount of dsDNA present (demonstrated in Figure 2.1).

Quantitation of gene expression (e.g. synaptophysin) was calculated relative to the endogenous control 18s using the comparative  $C_T$  method as described

in the manufacturer's RT-PCR guide and as validated by Yuan *et al* [211]. Briefly, the mean and standard deviation (SD) of the  $C_T$  values were calculated for 18s and the target gene. The  $\Delta C_T$  was calculated by subtracting the 18s  $C_T$  from the target gene  $C_T$ . The SD for the  $\Delta C_T$  was calculated as follows:  $SD = (SD_1^2 + SD_2^2)^{1/2}$  where  $SD_{1/2}$  is the SD of 18S and the target gene. The  $\Delta\Delta C_T$  was calculated by subtracting the average  $\Delta C_T$  of the designated control (e.g. mouse brain) from the  $\Delta C_T$  of the remaining values. The fold change relative to the designated control was calculated using the following equation:  $\text{fold change} = 2^{-\Delta\Delta C_T}$  with SD range calculated by SD plus =  $(2^{-\Delta\Delta C_T - SD})$  – Fold change and SD minus =  $(2^{-\Delta\Delta C_T + SD})$ .

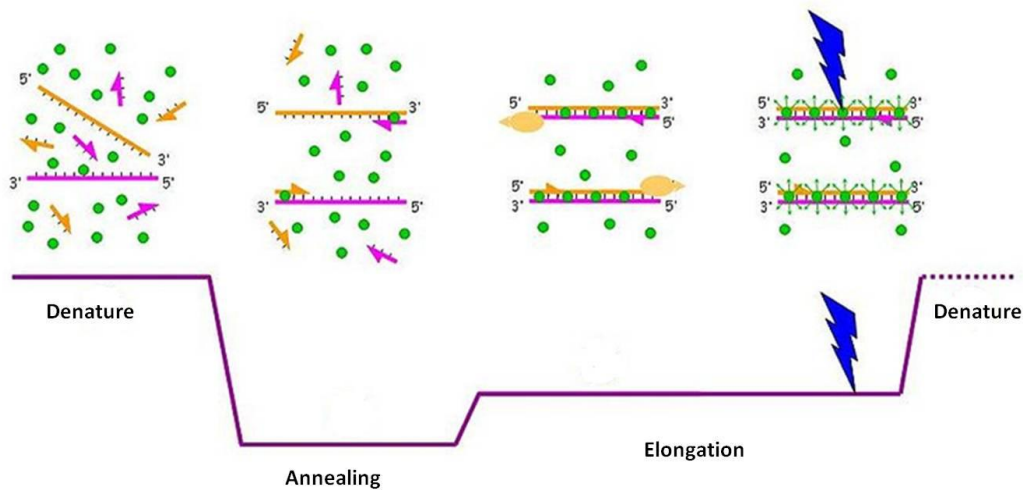


**Figure 2.1 Diagram of SYBR Green qRT-PCR reaction.** Firstly the DNA was denatured by heating at 90 °C; the primers were annealed and result in production of complementary dsDNA. SYBR green dye binds to freshly produced dsDNA and fluoresces. The level of fluorescence is detected at the end of each cycling stage and can be used to calculate variations in the level of target gene present.

## 2.7 Protein isolation and quantification

### 2.7.1 Preparation of whole tissue samples

Tissue samples from mice and rats were snap frozen in  $LqN_2$ , each sample was subsequently resuspended in 20% (w/v) TKMS buffer (50mM Tris, 25mM potassium chloride, 5mM magnesium chloride and 250mM sucrose). If necessary the sample was also sonicated briefly. The homogenised samples were aliquoted and stored at -20 °C short term or -80 °C long term. 5 $\mu$ l of

protein sample was required for quantification of total protein by the Lowry method (2.7.3).

### **2.7.2 Preparation of cell extracts**

Media was aspirated off the cells before two quick washes in 1 x PBS, the cells were then scraped into 1ml of 1 x PBS. This 1ml of 1 x PBS was transferred from each well of a 6 well plate in turn to maximise the amount of protein collected. Once transferred to a clean eppendorf the cell pellet was isolated by centrifugation at 13,000rpm for 5 minutes. The supernatant was removed and the cell pellet resuspended in a suitable volume of 20mM Tris, pH 7.4 (typically 30 – 100µl dependent on pellet size). Samples were stored as described in 2.7.1; 5µl of protein sample was required for quantification of total protein by the Lowry method (2.7.3).

### **2.7.3 Lowry protein assay**

Protein concentration was determined using a version of Lowry protocol originally described by Lowry in 1951 [212]. The principle is that under alkaline conditions copper complexes with any protein present; when Folin-phenol reagent is added this copper-protein complex is reduced. The resultant colour change can be measured spectrophotometrically at 750nm to determine the protein concentration. Therefore unknown protein concentrations can be easily determined when measured in parallel with samples of known protein concentration (e.g. bovine serum albumin (BSA)). This can be extrapolated on a simple graph of protein concentration versus absorbance, utilising the equation  $y = mx + c$ .

BSA protein standards were prepared ranging from 0 - 20µg/ml, Buffer ABC was prepared fresh each time, composed of 1 x Lowry A (2% (w/v)  $\text{Na}_2\text{CO}_3$ /4% (w/v) NaOH), B (2% (w/v) sodium tartrate), C (1% (w/v) copper sulphate)

mixed at a ratio of 100:1:1 (v/v/v). 5µl of each BSA standard or unknown protein sample was placed into an individually labelled eppendorf and further diluted with 50µl of distilled water and 1ml of buffer ABC. After incubation for 10 minutes at room temperature 100µl of Folin's reagent (diluted 1:1 with distilled water) was added and incubated for a minimum of 25 minutes to allow colour development. Samples were transferred to individual plastic cuvettes prior to absorbance determination at 750nm by spectrophotometric analysis using the 0µg/ml BSA standard as the background absorbance. A calibration curve was generated using the BSA standards.

#### ***2.7.4 Sodium-dodecyl sulphate polyacrylamide gel electrophoresis (SDS-PAGE)***

SDS-PAGE analysis is an invaluable technique first described by Laemmli in 1970 [213], for analysing proteins based upon their molecular weight. The fundamental principle involves the denaturation of proteins by heating in the presence of both DL-Dithiothreitol (DTT) (a thiol reducing agent) and SDS (a detergent). The combination of all three ensures that the proteins lose all their secondary, tertiary and quaternary structures and are linear, with a negative charge. Therefore when loaded onto a gel with fixed pore sizes and a current is applied they will migrate towards the positive electrode, governed by their molecular weight. When run against markers of known molecular weight (Colorburst™, Sigma) the molecular weight of unknown protein sample bands could be determined.

Briefly the acrylamide gels were set between glass plates clamped together and sealed at the bottom with Vaseline to prevent leaking. The separating gel was typically composed of 9% acrylamide (determined by the size of the protein of interest), 375mM Tris buffer, pH 8.8, 0.05% (w/v) ammonium persulphate (APS), 0.1% (w/v) SDS and 0.05% (v/v) TEMED. A thin layer of isopropanol was applied to remove air bubbles and ensure a level interface between the stacking and separating gels. The gels generally take 30-45 minutes to polymerise; upon polymerisation the isopropanol was removed and

the gel washed briefly with deionised water before the stacking gel was cast on top. The stacking gel was composed of 4% (w/v) acrylamide; 125mM Tris buffer, pH 6.8, 0.05% (w/v) APS, 0.1% (w/v) SDS and 0.1% (v/v) TEMED. Combs were carefully placed into the stacking gel to form the wells for the samples to be loaded into. When polymerisation was complete the combs were removed and the gels were fastened into the gel tank, which was then filled with electrode running buffer (1 x ERB) (20mM Tris, 160mM glycine and 0.08% (w/v) SDS, pH 8.3).

### ***2.7.5 Sample preparation and electrophoresis***

Protein samples were quantified as outlined in 2.7.3 prior to dilution to 1-2µg/ml in reducing loading buffer (62.5mM Tris buffer, pH 6.8, 10% (v/v) glycerol, 2% (w/v) SDS, 100mM DTT and 0.02% (w/v) bromophenol blue). Samples were denatured by heating at 90 °C for 5 minutes, routinely 10-20µg total protein was loaded per well (governed by the relative expression of the protein of interest). Electrophoresis was carried out at 100V initially till the dye front had crossed the interface of the stacking and separating gel, then at 150V until the dye front had reached the end of the gel. At this point the gels were removed and either stained using coomassie blue (2.7.6) or the proteins transferred onto a nitrocellulose membrane to detect specific proteins (2.7.7).

### ***2.7.6 Coomassie blue gel staining***

Once removed from the electrophoresis tank the gels were briefly washed in distilled water, prior to staining with coomassie blue (0.5% (w/v) coomassie blue in 25% (v/v) isopropanol / 10% (v/v) acetic acid) for one hour. The gel was then destained in 10% (v/v) methanol and 10% (v/v) acetic acid in deionised water, (the length of destaining was governed by the frequency of washes). The gel was imaged using white light on an Alpha Innotech fluorescent imaging system and image processed using Fluorchem software.

### **2.7.7 Western blotting**

Following removal from the gel tank the gels were removed from between the plates and the stacking gel was discarded whilst the separating gel was placed in chilled transfer buffer (25mM Tris, 192mM glycine and 20% (v/v) methanol, pH 8.3) to equilibrate for 10 minutes. Gels were loaded into the Western transfer cassettes overlaid with the nitrocellulose membrane between both filter paper and pads, and placed in the tanks with an ice pack before being submerged in chilled transfer buffer. The negatively charged proteins were transferred onto the positively charged nitrocellulose membrane by running the tank at 100V for an hour. Afterwards the nitrocellulose membrane was removed and washed in 1 x TBS-T (0.2M NaCl, 20mM Tris and 0.05% (v/v) Tween 20, pH 7.4) to remove any traces of methanol. The nitrocellulose membrane was then blocked in 3% (w/v) marvel milk powder in 1 x TBS-T buffer for one hour at room temperature to prevent non-specific protein binding. The nitrocellulose membrane was then washed three times in 1 x TBS-T, prior to incubation with the primary antibody for a further hour at room temperature or overnight at 4 °C. Both primary and secondary antibodies were diluted in incubation buffer (0.3% (w/v) milk powder in 1 x TBS-T). Following another three 1 x TBS-T washes the membrane was incubated in the appropriate secondary (horse radish peroxidase (HRP) conjugated) antibody for an hour at room temperature (see Table 2.5 for specific antibody dilutions). Finally the membrane was washed for a minimum of 30 minutes with multiple TBS-T changes prior to chemiluminescent detection.

Pierce ECL reagent (Thermo Scientific) was used for chemiluminescent detection of the HRP activity of the intended protein. Following the guidelines provided equal volumes of reagents 1 and 2 (~750µl) were mixed and pipetted onto the membrane, ensuring that it was covered equally for one minute. Excess ECL reagent was removed by blotting with tissue paper and then the membrane was wrapped in saran wrap and all air bubbles were

removed. The membrane was fixed into a cassette and exposed to x-ray film (CL-Xposure Film, Thermo Scientific) in a dark room followed by development of x-ray film with an X-omat developer (Kodak).

## **2.8 Immunohistochemistry (IHC) and immunocytochemistry (ICC)**

### **2.8.1 Immunohistochemistry (IHC)**

Tissue sections (typically liver or pancreas) fixed in 10% formalin (in 1 x PBS) for a minimum of 24 hours were processed (sequential ethanol washes) before embedding in paraffin blocks. Sequential 5µM sections were cut and subsequently mounted onto superfrost plus slides (Thermo, UK). Before individual staining procedures were undertaken, the slides were dewaxed in xylene for 10 minutes and washed in 100% and 95% ethanol for one minute before a final wash in deionised water. Tissue sections were then incubated in 3% (v/v) hydrogen peroxide in methanol for 15 minutes to quench endogenous peroxidase activity. 3 x 5 minute 1 x PBS washes were performed prior to antigen retrieval. The predominant methods used for antigen retrieval were sodium citrate incubation (2.8.2) or by digestion with 10µg/ml proteinase K (2.8.3). Non specific binding of the antibody was blocked by performing a 20 minute incubation with 15% (v/v) FCS in 1 x PBS at room temperature. The primary antibody (diluted in 0.05% (v/v) FCS in 1 x PBS) was incubated for a minimum of an hour at room temperature or overnight at 4 °C, see table 2.5 for individual antibody dilutions. The sections were then washed 3 x 5 minute in 1 x PBS to remove any residual primary antibody, before incubation with the desired secondary (HRP conjugated) antibody; again for an hour at room temperature. Following the 3 x 5 minute 1 x PBS washes, HRP activity was determined using diaminobenzidine (DAB) chromogen (Dako), which develops a dark brown colour when oxidized by bound HRP. The length of the DAB incubation was optimised for each individual antibody; following this step the sections were briefly washed in deionised water before the nuclei were counterstained with haematoxylin for

15 seconds. Finally the sections were dehydrated sequentially through a number of ethanol washes (50%, 75%, 90%, and 2 x 100% ethanol) before two xylene washes and mounting in Depex.

Antigen (raised in)	Dilution	Molecular weight (kDa)	Supplier (product code)
Firefly-luciferase (goat)	WB - 1/100 IHC - 1/50 - 1/500	62	Abcam (AB81823)
Firefly-luciferase (chicken)	WB - 1/400 IHC - 1/500	61	Abcam (AB18595)
$\beta$ -actin (mouse)	WB - 1/3000	44	Sigma (A1978)
Synaptophysin (mouse)	WB - 1/1000	37	Dako (M0776)
Synaptophysin (rabbit)	IHC - 1/200 ICC - 1/200	34	Millipore (AB9272)
Amylase (goat)	WB - 1/1000	52	Abcam (AB21156)
$\alpha$ SMA-FITC (mouse)	IHC - 1/200 ICC - 1/200	42	Sigma (F3777)
NIMP (rat)	IHC - 1/200	40	Serotec (MCA771G)
anti-FITC-HRP 2 <sup>o</sup> (rabbit)	IHC - 1/200	N/A	Dako (P5100)
anti-chicken-HRP 2 <sup>o</sup> (rabbit)	WB - 1/5000 IHC - 1/200	N/A	Abcam (AB6753)
anti-rabbit-FITC 2 <sup>o</sup> (sheep)	ICC - 1/160	N/A	Sigma (F7512)
anti-rabbit-TRITC 2 <sup>o</sup> (swine)	ICC - 1/400	N/A	Dako (R0156)
anti-rabbit-HRP 2 <sup>o</sup> (goat)	WB - 1/3000 IHC - 1/200	N/A	Dako (P0448)
anti-goat-HRP 2 <sup>o</sup> (rabbit)	WB - 1/6000 IHC - 1/300	N/A	Sigma (A5420)
anti-mouse-HRP 2 <sup>o</sup> (goat)	WB - 1/6000	N/A	Dako (P0447)
anti-rat-HRP 2 <sup>o</sup> (chicken)	IHC - 1/300	N/A	Abcam (AB6836)

Table 2.5 – Antibody dilutions (IHC – immunohistochemistry, ICC – immunocytochemistry, WB – western blot)

### 2.8.2 Sodium citrate antigen retrieval

Tissue sections were placed in a microwaveable rack and submerged in 0.01M sodium citrate buffer, pH 6. The lid of the rack was placed loosely on top and the sections were heated at full power for 20 minutes in a microwave.

It was necessary to regularly keep topping up the level of citrate buffer to prevent the sections from drying out; the sections were then allowed to cool down at room temperature before recommencing the IHC protocol.

### ***2.8.3 Proteinase K antigen retrieval***

Tissue sections were digested for 25 minutes at 37 °C in 10µg/ml proteinase K (diluted in 1 x PBS) before continuing with the IHC protocol.

### ***2.8.4 Haematoxylin and eosin staining (H&E)***

H&E is one of the most common stains performed in IHC, staining the nucleus and cytoplasm respectively. The sections were dewaxed and rehydrated as outlined in 2.8.1, before staining in haematoxylin for 1 minute and subsequent washing in deionised water. This was followed by a thirty second incubation in Scott's water before further washing in deionised water. Sections were finally counterstained in eosin for 30 seconds before deionised water washing and dehydration and mounting as outlined in 2.8.1.

### ***2.8.5 Picro-sirius red staining***

Picro-sirius red stain is known to specifically bind to collagens due to its sulphonic groups reacting strongly with the basic groups present in collagen molecules [214]. This makes it an ideal stain for determining fibrosis severity as collagen is deposited by hepatic myofibroblasts. Slides were dewaxed and rehydrated as outlined in 2.8.1 before incubation in picro-sirius red stain (0.036mM in saturated picric acid) for two hours at room temperature. Any excess stain was removed by three brief washes in acidified water (0.5% (v/v)

acetic acid in deionised water). As previously slides were dehydrated and mounted in depex as outlined in 2.8.1.

### **2.8.6 Fluorescent immunocytochemistry**

Typically all ICC analyses were performed with cells seeded in chamber slides (Merck) or 6 and 24 well plates. Plates were removed from the incubator and media aspirated off before three washes in HBSS/ Hepes, pH 7.4 (0.14M NaCl, 5.4mM KCl, 0.34mM Na<sub>2</sub>HPO<sub>4</sub>12H<sub>2</sub>O, 0.44mM KH<sub>2</sub>PO<sub>4</sub>, 5.6mM glucose, 1mM CaCl<sub>2</sub>, 6mM Hepes and 4mM NaHCO<sub>3</sub>), they were left coated in 1ml of HBSS/ Hepes before addition of 60µg/ml fluorescent C1-3 scAb. The cells and scAb were wrapped in foil and incubated for two hours at 37 °C and 5% CO<sub>2</sub>. Following two brief washes in 1 x PBS the cells were fixed by incubation with 1ml of fixative per well (2% (v/v) formaldehyde and 0.2% (v/v) glutaraldehyde in 1 x PBS, pH 7.4) for 15 minutes at room temperature. Fixative was removed and the cells subsequently washed three times in 1 x PBS, at this point a 20 minute blocking step was performed by incubating with 20% (v/v) FCS in 1 x PBS. Primary and secondary antibodies were added and incubated in turn for an hour at room temperature (see Table 2.5 for dilutions). After a further three 1 x PBS washes the cells were coated in 500µl of DAPI (4', 6-diamidino-2-phenylindole) (6µg/ml in 1 x PBS) and incubated for 10 minutes at room temperature. DAPI is a cell permeable fluorescent dye that binds specifically to AT rich regions of double stranded DNA and is therefore ideal for visualizing cell nuclei. The DAPI was removed and the cells washed a further three times in 1 x PBS (five minutes each wash) before mounting in vectashield anti fade (Vector Labs) and storage (protected from light) at 4 °C prior to fluorescent microscopy analysis.

### **2.9 C1-3 production**

### **2.9.1 Bacterial culture and C1-3 protein expression**

*E-coli* XL-1 blue cells were transfected with the pIMS147-C1-3 plasmid and cultured in baffled flasks containing LB media, with the addition of glucose (1% (w/v)) and selective antibiotics (50µg/ml ampicillin and 50µg/ml tetracycline) to select cells that had been successfully transfected. Following culture of the cells initially in LB and then TB media (24% (w/v) yeast, 12% (w/v) tryptone and 5% (v/v) glycerol) over a few days to encourage bacterial growth at 37 °C and 250rpm C1-3 expression was induced by the addition of 0.5M Isopropyl β-D-1-thiogalactopyranoside (IPTG). Following culture for a further 4 hours the cell pellet was isolated by centrifugation at 6000g for 20 minutes. The supernatant was discarded and cell pellet resuspended in 10ml of fractionation buffer (200mM Tris-HCl, 20% sucrose, 1mM EDTA, pH 7.5) supplemented with 50mg/L lysozyme and lysed on ice for 15 minutes. Afterwards an equal volume of 5mM magnesium sulphate was added to the solution and incubated on ice for a further 15 minutes. The cells were pelleted by centrifugation at 6000g for 30 minutes at 4 °C, but the supernatant was retained as it now contains the C1-3 scAb.

### **2.9.2 Protein isolation**

C1-3 was isolated from the supernatant by Ni<sup>2+</sup> charged immobilised metal ion affinity chromatography (IMAC), using a fast flow sepharose resin (Amersham Biosciences). IMAC exploits the interaction between the side chains located on histidine amino acids found on the C-terminal tag of C1-3 and the chelated transition metal ions within the column resin. The ethanol was removed from the sepharose resin and washed in deionised water prior to resuspension in binding buffer (10mM imidazole), 1ml of binding buffer was added for every 40ml of supernatant, the nickel sepharose was resuspended in supernatant and added to the rest of the supernatant and incubated overnight at 4 °C. The following morning the whole mixture was passed through the column twice, before a wash in binding buffer to remove any non-specifically bound proteins.

Two 10ml washes of elution buffer (400mM imidazole) were performed to remove the bound C1-3 scAb from the column, then the solution was dialyzed with 1 x PBS overnight (approximately 1L of 1 x PBS per mg of C1-3 produced) to remove any imidazole.

If C1-3 was being used in animal studies it was also necessary to remove all traces of endotoxin (ETX), which was accomplished using Q maxi H columns (Sartorius Vivascience). The column was prepared by sequential washes with: (each time the column was centrifuged at 2200rpm for 5 minutes before discarding the flowthrough): -

- 17ml Pharmacy water
- 17ml 0.5M NaOH
- 17ml Pharmacy water
- 17ml Pharmacy water
- 17ml Pharmacy water
- 17ml 1x sterile PBS

Finally the C1-3 scAb was loaded onto the column and centrifuged at 2200rpm for 10 minutes. The flowthrough containing C1-3 was collected and sterile filtered through a 0.45µM syringe filter (VWR International) prior to storage at - 20 °C.

### ***2.9.3 C1-3 quantification and specificity***

Enzyme linked immunosorbant assays (ELISAs) are utilised to determine the binding of a protein to specific antibody or antigen when coated on plastic. A binding ELISA was performed using synaptophysin peptide sequences 1 and 2 (see figure 1.4.1) to display C1-3's specificity to peptide sequence 2. Secondly a capture ELISA was performed alongside IgG controls to determine the C1-3 protein concentration.

#### **2.9.4 Binding ELISA**

Initially flat bottomed 96 well microtitre plates (Dynex, Sussex) were coated with 100µl BSA as a negative control, or synaptophysin peptide 1 or 2 conjugated to BSA (all 20µg/ml) and incubated at room temperature for 2 hours (all steps were performed at 300rpm on a rocker to ensure homogenous coating of the wells). Afterwards 3 x PBS-T washes (1 x PBS + 0.05% (v/v) Tween) were carried out, non specific binding was blocked by incubation with blocking buffer (2% (w/v) marvel milk protein in 1 x PBS) overnight at 4 °C. Following a further 3 x PBS-T washes both C1-3 and human IgG (Sigma) (negative control) samples were serially diluted across the plate before incubation for an hour at room temperature. After 5 x PBS-T washes the secondary antibody (goat anti human Ck light chain-HRP (diluted 1:1000 in 2% (w/v) marvel milk protein in 1 x PBS)) was added, this was incubated for an hour at room temperature before a final set of PBS-T washes prior to detection as outlined in 2.9.6.

#### **2.9.5 Capture ELISA**

Flat bottomed 96 well microtitre plates were coated with goat anti-human Ck light chain (bound and free) for two hours at room temperature, prior to 2 x PBS-T washes and blocking of non specific protein binding by overnight incubation with 2% (w/v) BSA in 1 x PBS. The next morning after 3 x PBS-T washes, human IgG was serially diluted across the plate (from an initial concentration of 1250ng/ml to a final concentration of 0.61ng/ml) as calibration standards. Alongside this, C1-3 of unknown concentration was diluted 1 in 10 prior to serial dilution across the plate and both were incubated at room temperature for 90 minutes. The plate was then washed five times with PBS-T before addition of the secondary antibody goat anti human Ck light chain-HRP (diluted 1/1000 in 1 x PBS). Following the final set of PBS-T washes, the plate was ready for detection (2.9.6).

### **2.9.6 Detection of bound C1-3**

The amount of bound antibody was determined by incubation for 10 minutes with 100µl 3, 3', 5, 5'-Tetramethylbenzidine dihydrochloride monohydrate (TMB) per well, 1 tablet of TMB was dissolved in 10ml of 0.05M phosphate citrate buffer, pH 5 and 2µl of 30% (v/v) hydrogen peroxide. The reaction was ended by the addition of 50µl of 1M sulphuric acid, which results in a colour change from yellow to blue that can be detected spectrophotometrically at 450nm.

### **2.9.7 Conjugation of C1-3 to Fluorescein isothiocyanate (FITC)**

C1-3 was conjugated to FITC using a kit purchased from Molecular probes, briefly 200µl of C1-3 (~ 1mg/ml) was added to 20µl of 1M bicarbonate solution. 12.6µl of FITC dye solution (10mg/ml diluted in DMSO) was added and the reaction stirred for an hour at room temperature, protected from light. The C1-3-FITC conjugate was separated from free dye by centrifugation with sepharose gel columns equilibrated with 1 x PBS. The fluorescently labelled C1-3 was stored in aliquots at 4 °C short term or – 20 °C long term (protected from light).

### **2.9.8 Conjugation of C1-3 to Alexa-594 fluorophore**

C1-3 was conjugated to Alexa-594 using a kit purchased from Molecular probes, briefly 50µl of 1M bicarbonate solution was added to 500µl of C1-3 (~ 1mg/ml). This C1-3 solution was then added to a vial of Alexa-594 dye and vortexed briefly to mix completely, before it was stirred for an hour at room temperature, protected from light. The C1-3-594 conjugate was separated

from free dye by centrifugation with sepharose gel columns equilibrated with 1 x PBS. The fluorescently labelled C1-3 was stored as aliquots at 4 °C short term or – 20 °C long term (protected from light).

### **2.9.9 Conjugation of C1-3 to Xenolight™ XF750**

C1-3 was conjugated to the XF750 fluorophore following the guidelines provided by the manufacturer (Caliper biosciences), initially 100µl of 1M sodium bicarbonate, pH 8.3 was added to 900µl of C1-3 (~ 1mg/ml). 1 vial of XF750 dye was resuspended in 25µl of DMSO and 12µl of this was added to the C1-3-bicarbonate solution and mixed at room temperature for 1 hour protected from light. The free dye was removed by centrifugation using a Nanosep® exclusion vial (MW 10,000) (Pall), so free dye will be lost in the flowthrough and the fluorescently conjugated C1-3 retained in the vial. After three washes with 1 x PBS the C1-3-750 was resuspended in 1ml of 1 x PBS to give approximately 1mg/ml of C1-3-750, which was stored at 4 °C short term or – 20 °C long term (protected from light).

### **2.9.10 Conjugation of C1-3 to gliotoxin (GTX)**

The conjugation of C1-3 and GTX was optimized previously within this laboratory (see Figure 2.2) based on the method described by *Fox et al* [215]. Briefly, 750nmoles of C1-3 was reacted with 22µmoles of S-acetyl thioglycolic acid N-hydroxysuccinimide (SATA) and 1mM EDTA for an hour at room temperature. The GTX was prepared as a 2mg/ml stock in DMSO; 12µmoles was activated by reaction for an hour with 60µmoles of N-p-maleimidophenyl isocyanate (PMPI) at room temperature. Afterwards the GTX-PMPI was added to the C1-3-SATA and incubated for a further 2 hours, the unreacted components were removed by gel filtration using a PD-10 column and 1 x PBS washes. C1-3-GTX was aliquoted out and stored at – 20 °C until required.

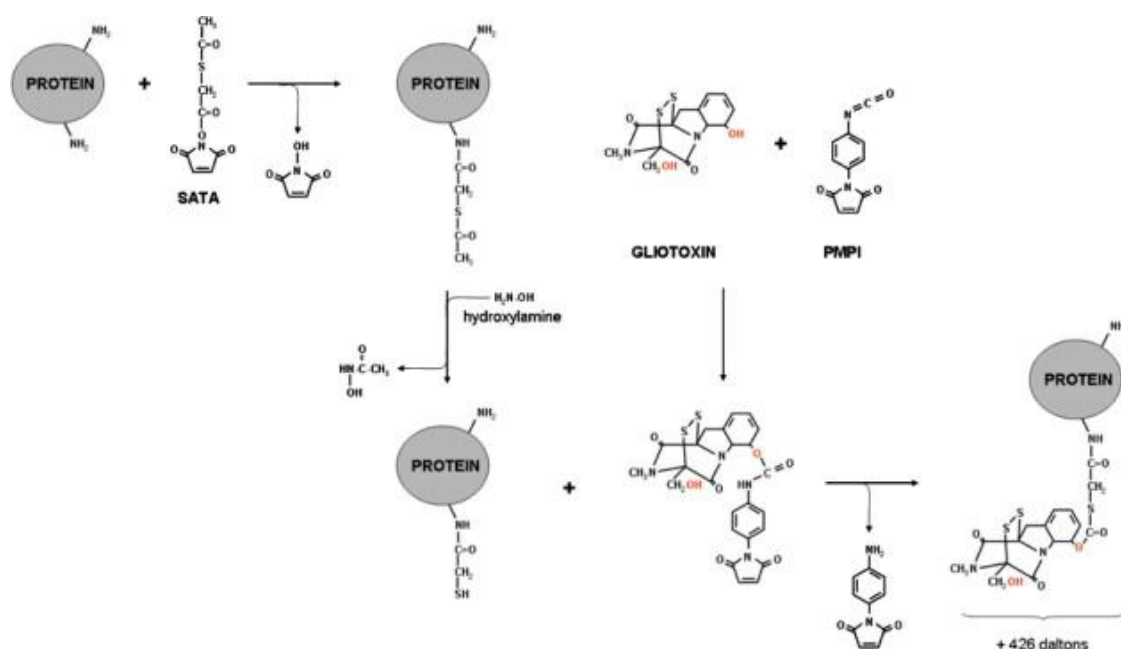


**Figure 2.2 Schematic of C1-3-GTX conjugation reaction (taken from [116]).** Initially the primary amine groups on C1-3 were thiolated by reaction with SATA for 1 hour at room temperature (RTP), at the same time GTX was conjugated for 1 hour with PMPI at RTP. Excess reagents were removed from each reaction by PD-10 filtration. Upon completion C1-3-SATA was reacted with GTX-PMPI for 2 hours at RTP, excess compounds were once again removed by PD-10 filtration. Successful conjugation was confirmed by SDS-PAGE and western blotting with a GTX specific antibody.

## 2.10 Animal imaging

An in vivo imaging system (IVIS) ultrasensitive camera (Xenogen) was used to image the mice and determine luminescent and fluorescent levels. Prior to imaging mice were anaesthetized with isoflurane and the fur was removed from their abdominal region by shaving.

### 2.10.1 Luminescence imaging

Mice were placed in the IVIS imaging chamber under anaesthesia before i.p. injection of 200µl D-Luciferin (15 mg/kg) purchased from Caliper (Hopkinton, MA, United States) diluted in 1 x PBS, pH 7.8. A background luminescence reading over 60 seconds was recorded just prior to injection; following D-Luciferin injection luminescence readings were taken every 5 minutes for a total of 15 minutes (each lasting 60 seconds). Mice were either placed back in

their housing prior to future studies or at the culmination of a study mice were terminated by cervical dislocation, and blood was collected for serum analysis by cardiac puncture. The major organs (liver, brain, kidney, stomach, spleen, lung and heart) were excised and placed in the IVIS imaging chamber and imaged using identical settings.

### **2.10.2 Fluorescent imaging**

Mice were placed in the IVIS imaging chamber under isoflurane anesthesia, before a fluorescence background scan was performed using the auto exposure settings at the desired wavelengths ( $\lambda_{\text{abs}}/\lambda_{\text{em}} = 755/775\text{nm}$ ). The C1-3-750 fluorophore was administered by either an intravenous (i.v.) or i.p. injection (10mg/kg bodyweight) as outlined the in individual protocols. Fluorescent scans were performed at designated timepoints. On completion of the study, the mice were culled by cervical dislocation and the major organs excised and scanned by an identical method.

All images taken were analyzed using Image-Pro plus 4.0 (Media Cybernetics, Silver Spring, MD) software integrated with the HPD-LIS module as developed by Hamamatsu.

### **2.11 Serum and tissue storage**

The blood samples harvested were allowed to clot before centrifuging at 13,000rpm for at least 20 minutes. The serum layer was pipetted off into individual eppendorfs and stored at  $-20\text{ }^{\circ}\text{C}$  until analysis by the Clinical Biochemistry Department at the Royal Victoria Infirmary, Newcastle.

Following imaging the liver tissue samples were dissected and either fixed in 10% formalin solution in 1 x PBS, snap frozen in TRIzol or snap frozen directly in LqN<sub>2</sub> prior to RNA and protein isolation at a later date. All the other major organs collected were snap frozen in LqN<sub>2</sub> and stored at  $-20\text{ }^{\circ}\text{C}$  prior to future analysis where required.

### **2.12 Tissue homogenisation**

A small sample was removed from each snap frozen liver section and weighed before resuspension in five times that volume of homogenisation buffer (20mM Tris, 100mM KCl, pH 7.4). For example a sample weighing 100mg was resuspended in 500µl of homogenisation buffer, the sample was then homogenised using a small pestle and where necessary sonicated in short bursts to further disrupt the tissue. This ensured that all samples contained approximately the same amount of liver tissue.

### **2.13 Luciferase assay**

The same general protocol was followed for both luciferase assays involving the U937-NF-κB cells and the homogenised tissue from the PXR animal study using a Dual-glo luciferase assay kit (Promega). A fixed volume (typically 100µl) of 1 x PLB was mixed 1:1 with 100µl liver homogenate or the U937-NF-κB cell pellet was resuspended in 100µl of 1 x PLB. 50µl of this was then added to an equal volume of the supplied Dual-glo luciferin substrate (Promega), and mixed vigorously before a 10 second luminescent detection was performed using a Junior LB 9509 benchtop luminometer detector (Berthold technologies).

### **2.14 Griess assay.**

The levels of nitric oxide (NO) produced by cells (both U937-NF-κB cells on their own and in co-culture with LX-2 cells and hHSCs) could be determined by the nitrite (NO<sup>2-</sup>) levels present in the culture media. NO<sup>2-</sup> is one of the major stable and non-volatile breakdown products of NO present in the media. Culture media was removed at designated time points (0, 2, 4, 8, 24, 48 and 72 hours) and if necessary centrifuged to remove U937s, before 100µl

aliquots were reacted with 100 $\mu$ l of Griess reagent (1% sulfanilamide in 0.1 mol/l HCl and 0.1% *N*-(1-naphthyl)ethylenediamine dihydrochloride) in triplicate. The reaction of nitrite present in the culture media with sulfanilamide results in the formation of diazonium salts. When this is coupled with *N*-(1-naphthyl)ethylenediamine an azo dye forms, and the resultant colour change can be detected spectrophotometrically at 540nm (Figure 2.3). Therefore the level of NO<sup>2-</sup> produced can be determined when the samples are extrapolated against a plot generated from sodium nitrite standards of known concentrations [216].

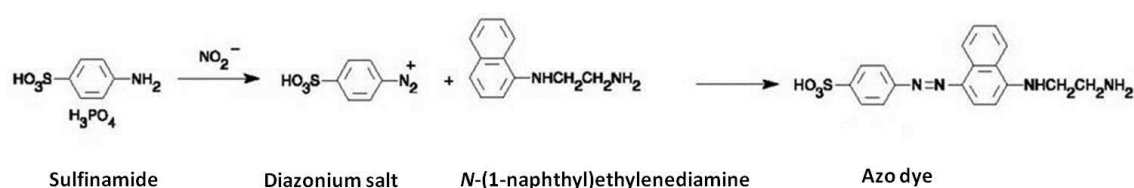


**Figure 2.3 Griess assay chemical reaction.** The level of NO can be detected by measuring the nitrite (NO<sub>2</sub><sup>-</sup>) formation in the culture media. When Griess reagent is added the sulfanilamide it contains leads to the formation of a diazonium salt, which in turn reacts with *N*-(1-naphthyl)ethylenediamine present in the Griess reagent leading to the formation of an azo dye that can be detected spectrophotometrically at 540nm. The nitrite concentration is determined against a standard curve of known sodium nitrite concentrations.

**Chapter 3.0 - The use of C1-3-750 as a non-invasive  
diagnostic imaging agent for hepatic fibrosis**

### 3.1 Introduction

The continuing escalation in the incidence of liver fibrosis and its endpoint cirrhosis [24], coupled with the lack of a recognised treatment regimen explain why liver disease is an ever increasing healthcare issue and major burden on the National Health Service (NHS). Despite the significant advances in our understanding of the pathogenesis of liver fibrosis over the past thirty years, principally the ‘activation’ of HSCs to hepatic myofibroblasts - the primary fibrogenic cell in the liver, relatively little progress has been made in developing an effective anti-fibrotic treatment regimen [32, 186, 217]. Accurate diagnosis and staging of hepatic fibrosis at all stages of disease progression is critical to the development and assessment of the functioning of new potential anti-fibrotic agents. The methods currently available to diagnose liver fibrosis including the ‘gold standard’ percutaneous liver biopsy are listed in section 1.5, which outlines some of the major problems of the liver biopsy (e.g. sampling errors) [122]. Sections 1.5.2 and 1.5.3 highlight the limitations when using alternative diagnosis techniques such as serum biomarker panels and non invasive imaging modalities. Primarily these difficulties are differentiating between the various stages of fibrosis severity, and detecting early developmental fibrosis [132, 142].

The development of a non-invasive imaging modality to accurately quantify liver fibrosis severity at all stages of fibrosis development would aid the discovery of novel anti-fibrotic agents because it would allow rapid diagnosis and could be used to determine the effect of treatment outcome for individual patients. Obviously there would also be a significant reduction in the number of side effects associated with the liver biopsy. With that in mind we intend to utilize the hepatic myofibroblast specific properties of the scAb C1-3 as an imaging agent, when conjugated with a long wavelength fluorophore (approximately 780 nm peak emission). Previous work within this laboratory [115] highlighted C1-3’s ability *in vitro* to target hepatic myofibroblasts. *In vivo* it was predominantly used as a potential anti-fibrotic agent when conjugated with GTX, inducing hepatic myofibroblast apoptosis and a significant reduction in liver fibrosis severity *in vivo* [116].

We hypothesised that there was a relationship between the number of hepatic myofibroblasts and the severity of hepatic fibrosis (i.e. level of collagen scar deposition). Using an *in vivo* model of liver fibrosis (CCl<sub>4</sub> treated mice) we aimed to test this hypothesis, specifically if the C1-3-750 signal is an indicator of fibrosis severity there should be an increase in liver fluorescence. Both whole body scans and *ex vivo* organ scans will be performed to determine if C1-3-750 liver fluorescence was an appropriate indicator of fibrosis severity, and can be used to quantify and differentiate between different stages of liver fibrosis non invasively.

### **3.2 Conjugation of C1-3-750 and its functioning *in vitro***

C1-3 was conjugated with the XF750 dye as outlined in methods 2.9.8. Successful conjugation was confirmed by SDS-PAGE analysis alongside unconjugated C1-3. The SDS-PAGE gel in figure 3.1 indicates an increase in molecular weight (MW) seen when XF750 was conjugated. C1-3 has a MW of approximately 37 kDa (lane 2 figure 3.1); the C1-3-750 scAb (lane 3 figure 3.1) has not migrated as far along the SDS gel, indicative of its increased MW. The blurry appearance of the band was due to the variation in the number of dye molecules bound to the scAb, which cannot be controlled during the conjugation process.

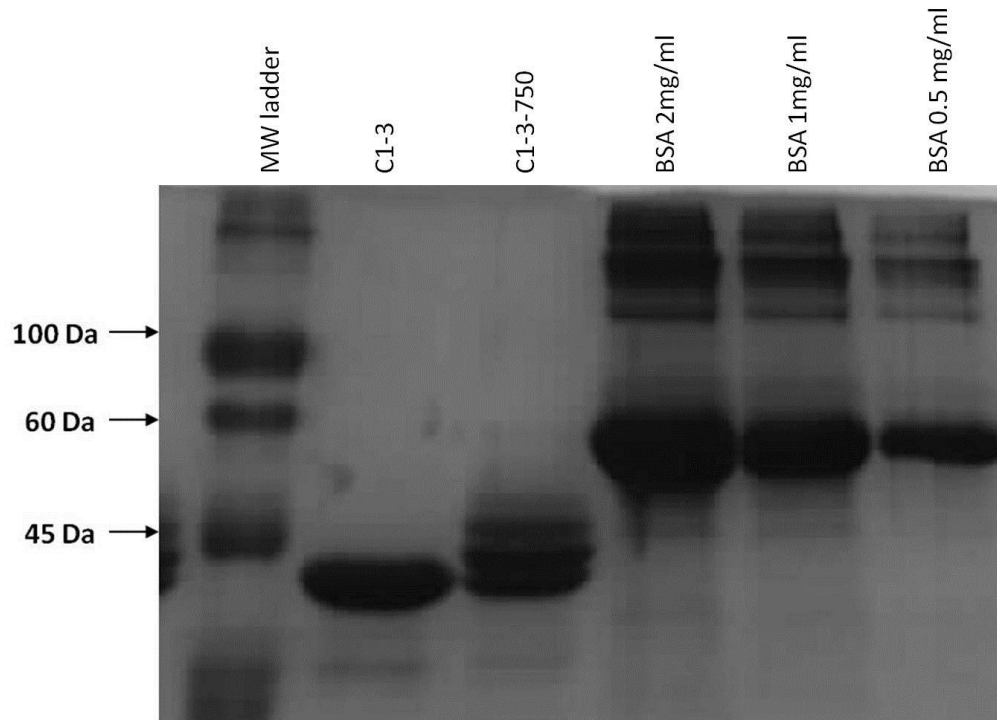


**Figure 3.1 SDS-PAGE analysis of C1-3 before and after conjugation with XF750 and comparison vs. BSA standards.** C1-3 and C1-3-750 were diluted 1:1 in loading buffer, whilst BSA standards were diluted directly into loading buffer from a 20mg/ml stock; following electrophoresis the gel was stained with coomassie blue for one hour and destained with multiple washes in 10% (v/v) acetic acid and methanol in deionised water. The gel was imaged using a Syngene GBox gel imaging system; C1-3 has a MW of approximately 37 kDa, presence of XF750 is shown by the increased MW and reduced migration along the gel. The size of each band is directly proportional to the concentration of the protein sample. Therefore comparing the unknown C1-3 & C1-3-750 bands with the BSA standards (68 kDa) we can estimate their protein concentration – C1-3 = ~ 1mg/ml, C1-3-750 = ~ 1mg/ml.

Successful conjugation of XF750 was also confirmed by MALDI-TOF analysis of the C1-3-750 conjugated scAb versus unconjugated C1-3 and also C1-3-FITC. The results of these analyses are shown in figure 3.2, the findings confirm the SDS-PAGE results (Figure 3.1); firstly unconjugated C1-3 has a MW of 37.5 kDa [116] shown by the single distinct peak. There was an increase in C1-3's MW when conjugated to either XF750 or FITC. There was also a difference in binding efficiency between the XF750 and FITC binding reactions, shown by the presence of multiple peaks in the C1-3-750 MALDI-TOF (peaks of approximately 37.5, 37.6, 40.5 and 43.4kDa). This indicates that there was a variation in the number of XF750 dye molecules bound to the scAb, in contrast there was 100% binding efficiency in the C1-3-FITC reaction shown by the presence of a single peak, larger than that seen in the unlabelled C1-3 sample (37.9kDa versus 37.5kDa). The presence of an

identical peak at 37.5kDa in the C1-3-750 sample suggests that there was still unbound C1-3 present that was not conjugated during the labelling reaction.

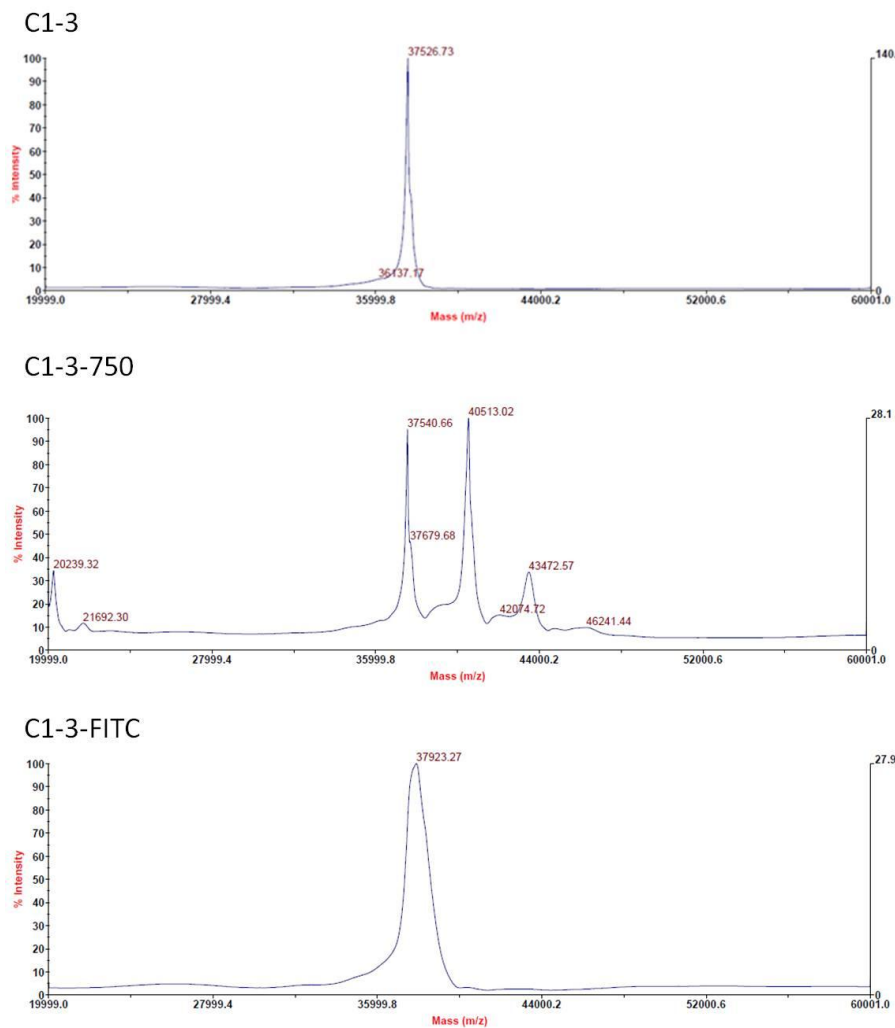


**Figure 3.2 MALDI-TOF analyses of C1-3 and its conjugates.** C1-3 run out confirms the SDS-PAGE findings (Figure 3.1) as C1-3 has a MW of 37.5 kDa shown by the single clear peak. C1-3-750 reinforces the SDS-PAGE further as there are multiple peaks around 37 kDa as a result of varying numbers of dye molecules being conjugated to the C1-3 scAb. C1-3-FITC is conjugated via an identical protocol to C1-3-750, however it's MALDI-TOF has a single slightly larger peak than C1-3, indicating that the labelling procedure is 100% successful, unlike the C1-3-750.

The C1-3-750 concentration was estimated by SDS-PAGE analysis; in this instance the conjugated scAb was compared against BSA standards of known concentration (Figure 3.1). The concentration of the protein was directly proportional to the intensity of the band it produces on the SDS gel. Therefore it was possible to estimate the concentration of C1-3 or C1-3-750 when it was compared to the BSA standards, C1-3-750 was at a concentration of

approximately 1mg/ml, when corrected for the 1:1 dilution in loading buffer (i.e. multiply by 2).

The C1-3-750 concentration was also quantified by a capture ELISA using human IgG as standards; the freshly conjugated C1-3-750 was serially diluted (1:2) across a 96 well plate (initial dilution 1 in 10) alongside the IgG samples (initial concentration 1250ng/μl). Figure 3.3A is a typical plot of the absorbance versus protein concentration generated for both C1-3-750 and the IgG standards; the unknown C1-3-750 protein concentration was calculated from the linear segment of the curve. It was necessary to correct for both the initial dilution and the presence of a second human kappa light chain domain on the human IgG antibody; this calculation is shown in figure 3.3B. A second binding ELISA using 96 well plates coated in both synaptophysin peptide sequences 1 and 2 (Figure 1.6) was performed to confirm that the conjugation process had not adversely affected C1-3's affinity for synaptophysin peptide sequence 2. Figure 3.4 shows that C1-3-750 retains the unique binding characteristics of unconjugated C1-3, only binding to synaptophysin peptide sequence 2. This was also reaffirmed by BIACORE analysis (Figure 3.5) when synaptophysin peptide sequence 2 was immobilised onto a CM5 BIACORE chip (synaptophysin peptide 1 was also immobilised separately as a negative control – Figure 3.5C). Varying concentrations of both C1-3 and C1-3-750 (50, 25, 12.5 and 6.25μM) were passed across the CM5 BIACORE chip in turn and the affinity of the antibody for the peptide sequence determined by surface plasmon resonance. It is clear in figures 3.5A and 3.5B that the association and dissociation characteristics of C1-3 and C1-3-750 are almost identical for synaptophysin peptide 2 following the PBS washes. This was confirmed when you compare the affinity (binding constant) values calculated from the dissociation and association rate values in figure 3.5D.

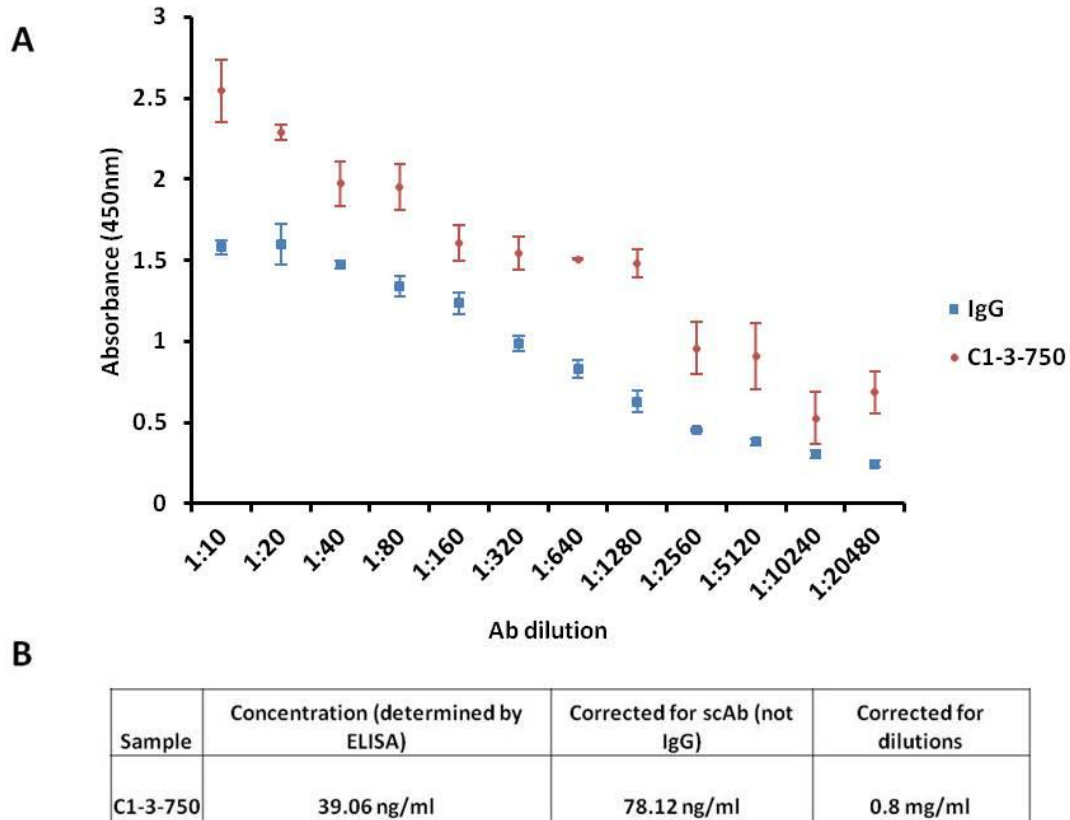


**Figure 3.3 Quantification of C1-3-750 concentration by capture ELISA versus human IgG standards.** **A** 96 well plates were coated with ck light chain, prior to serial dilution of C1-3-750 and human IgG across the plate. Following incubation with the secondary antibody (ck light chain-HRP), the level of bound antibody was detected by spectrophotometric analysis at 450nm after TMB addition. A standard curve was then produced of protein concentration versus absorbance. **B** Using the standard curve the unknown C1-3-750 concentration is calculated by extrapolating against an IgG dilution of similar absorbance in the linear phase of the curve. C1-3-750 concentration was corrected for the dilutions factor and for the presence of an extra human kappa light chain domain on the human IgG antibody by multiplying by 2. In this instance dilution 9 of C1-3-750 is equal to dilution 6 of IgG with a concentration of 39.06ng/ml. To correct for dilution this number is multiplied by 27 and finally by 10 to account for the initial 1:10 dilution.

Fluorescent spectroscopy was performed to determine the fluorphores peak absorbance at approximately 750nm, and also its emission/ excitation characteristics. Figure 3.6 highlights the fluorescence spectra of C1-3-750, with peak absorption at 755nm and peak emission at approximately 780nm. These findings correlate with the manufacturers' predicted absorption peak at 755nm and emission peak at 777nm. When performing the *in vivo* studies and imaging mice following C1-3-750 injection, the XF750 filter settings programmed into the IVIS software will ensure maximum fluorescence detection of the C1-3-750 scAb.

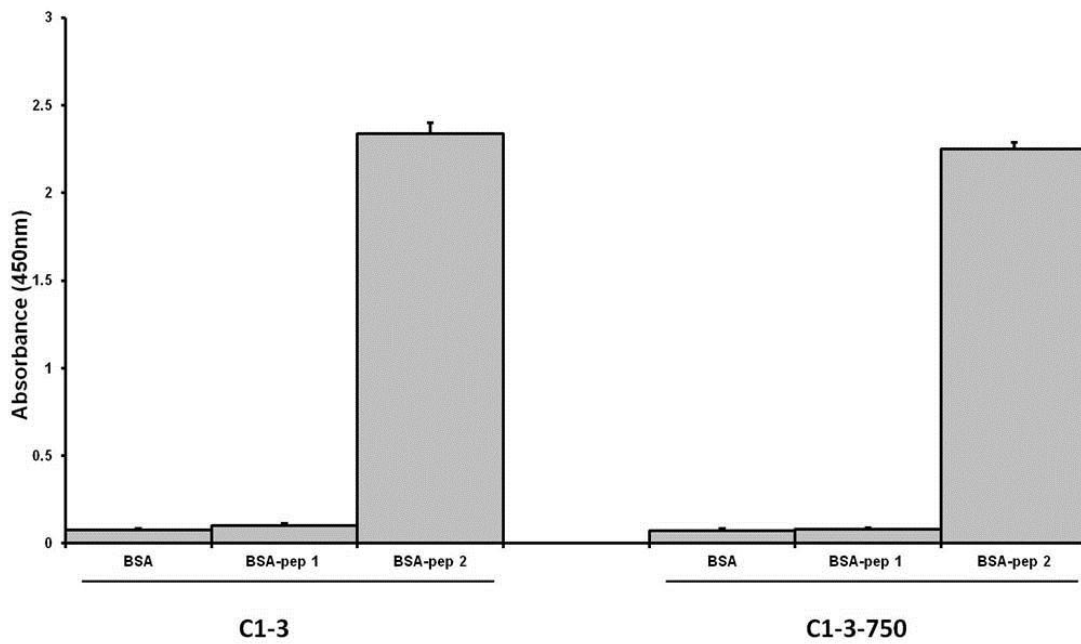


**Figure 3.4 Specificity ELISA of C1-3 and C1-3-750 to BSA synaptophysin peptide sequences 1 & 2.** 96 well plates were coated with BSA conjugated synaptophysin peptide 1 and 2 (see figure 1.6) or BSA (negative control). C1-3 and C1-3-750 were serially diluted across the plate and the level of bound antibody was detected as outlined in section 2.9.6. Dilution 5 (1/160) is shown above; highlighting that conjugation of XF750 to the C1-3 scAb has not altered its binding to synaptophysin peptide sequence 2.

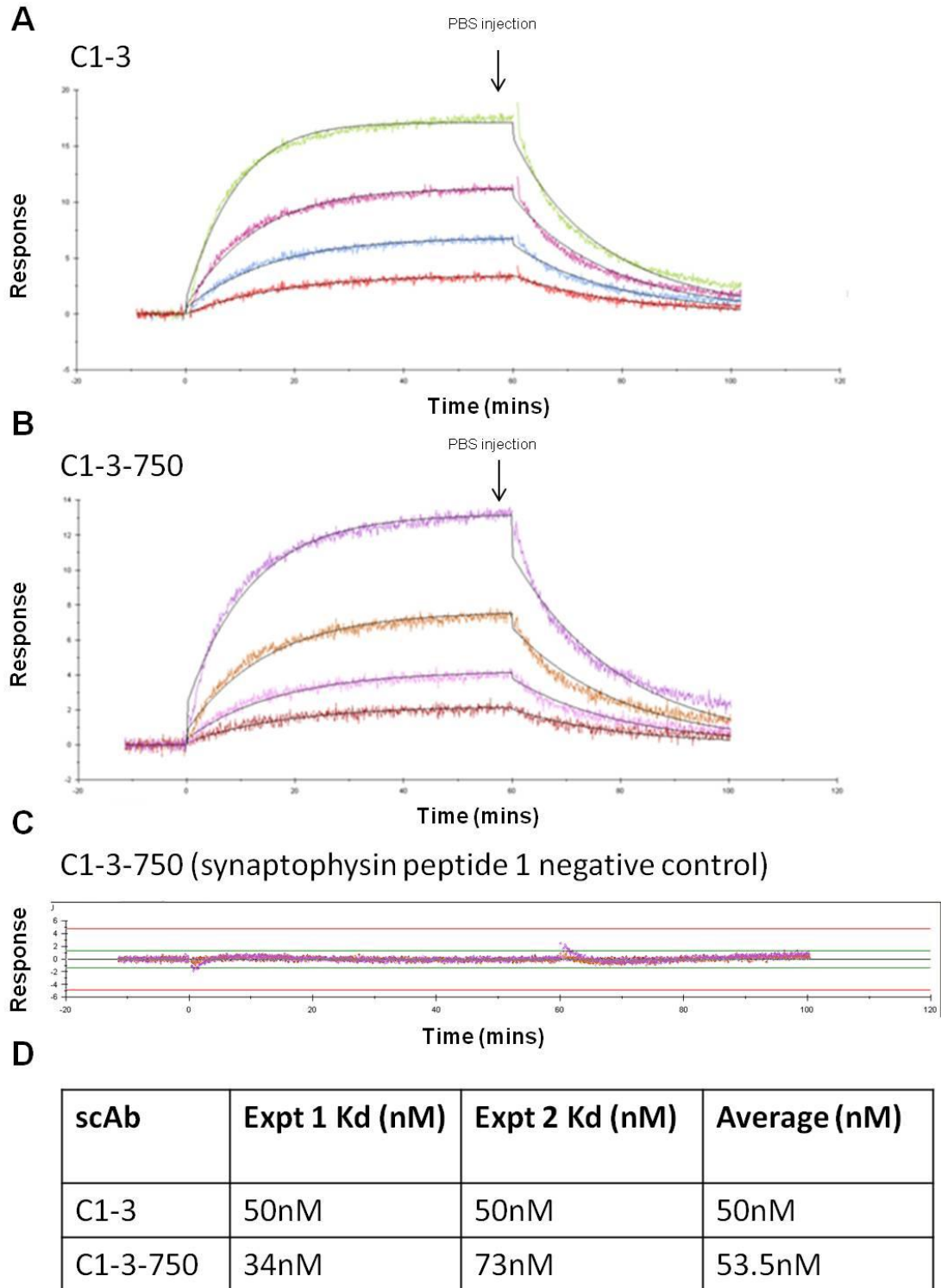
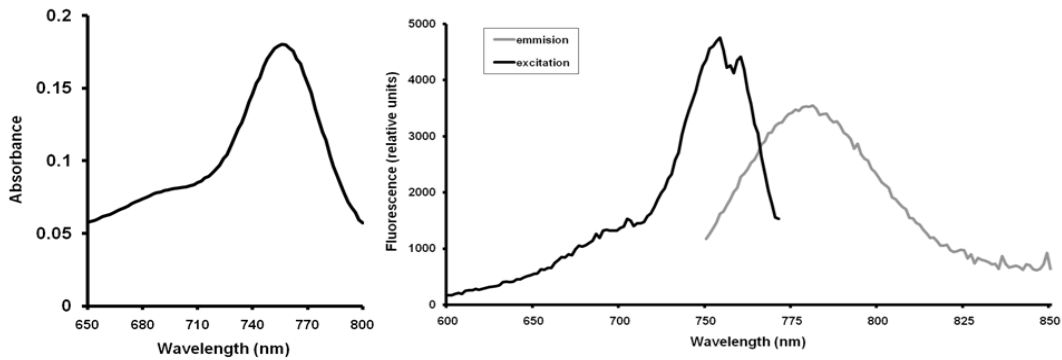


**Figure 3.5 BIACORE analyses of C1-3 and C1-3-750.** In the BIACORE flow hood synaptophysin peptide 2 was immobilised onto a CM5 BIACORE chip. **A** C1-3 and **B** C1-3-750 were separately flowed across the chip at a constant rate for 1 hour. After 1 hour PBS washes were performed to remove the bound scAb from the peptide, the level of bound scAb was detected by surface plasmon resonance. **C** C1-3-750 was also flowed across a chip with synaptophysin peptide 1 immobilised onto it, to highlight it is binding specifically to the peptide coated onto the chip. **D** The Kd and relative affinity

of the scAb for the peptide sequence were calculated, revealing that conjugation of XF750 onto the C1-3 scAb does not alter its binding kinetics with synaptophysin peptide sequence 2.



**3.6 Fluorescence spectra of C1-3-750.** C1-3-750 (diluted 1:10 in 1 x PBS) was exposed to a range of excitation wavelengths to determine firstly its optimum absorbance at approximately 755nm. Secondly its excitation and emission characteristics were confirmed peaking at 755nm and 777nm respectively as outlined in the manufacturers' predicted values.

Prior to *in vivo* experimentation utilising C1-3-750, ICC was performed *in vitro* using both mouse and human hepatic myofibroblasts to confirm C1-3-750's affinity for them. 60µg/ml C1-3-750 (C1-3-594 and C1-3-FITC were also incubated separately as controls) was incubated with hepatic myofibroblasts as outlined in 2.8.6. To confirm the cells myofibroblast phenotype αSMA dual staining was included. Typical fluorescent microscopy images from both the human and mouse hepatic myofibroblasts performed upon completion of the ICC protocol are shown in figure 3.7. It was clear from the representative images that whilst there was co-localization of both the C1-3-FITC and C1-3-594 conjugates with the αSMA positive cells, there was no C1-3-750 signal detected. This could be due to the large MW of the 750 dye molecules altering its kinetics or a result of competitive inhibition due to the presence of unbound C1-3 (Figure 3.2). These findings are in contrast to the positive findings of the binding ELISA and BIACORE analyses (Figures 3.4 and 3.5) that indicated the XF750 labelled scAb still functions. Due to these positive findings a pilot study utilising an *in vivo* model of liver fibrosis was designed to determine whether the C1-3-750 scAb functioned *in vivo*.

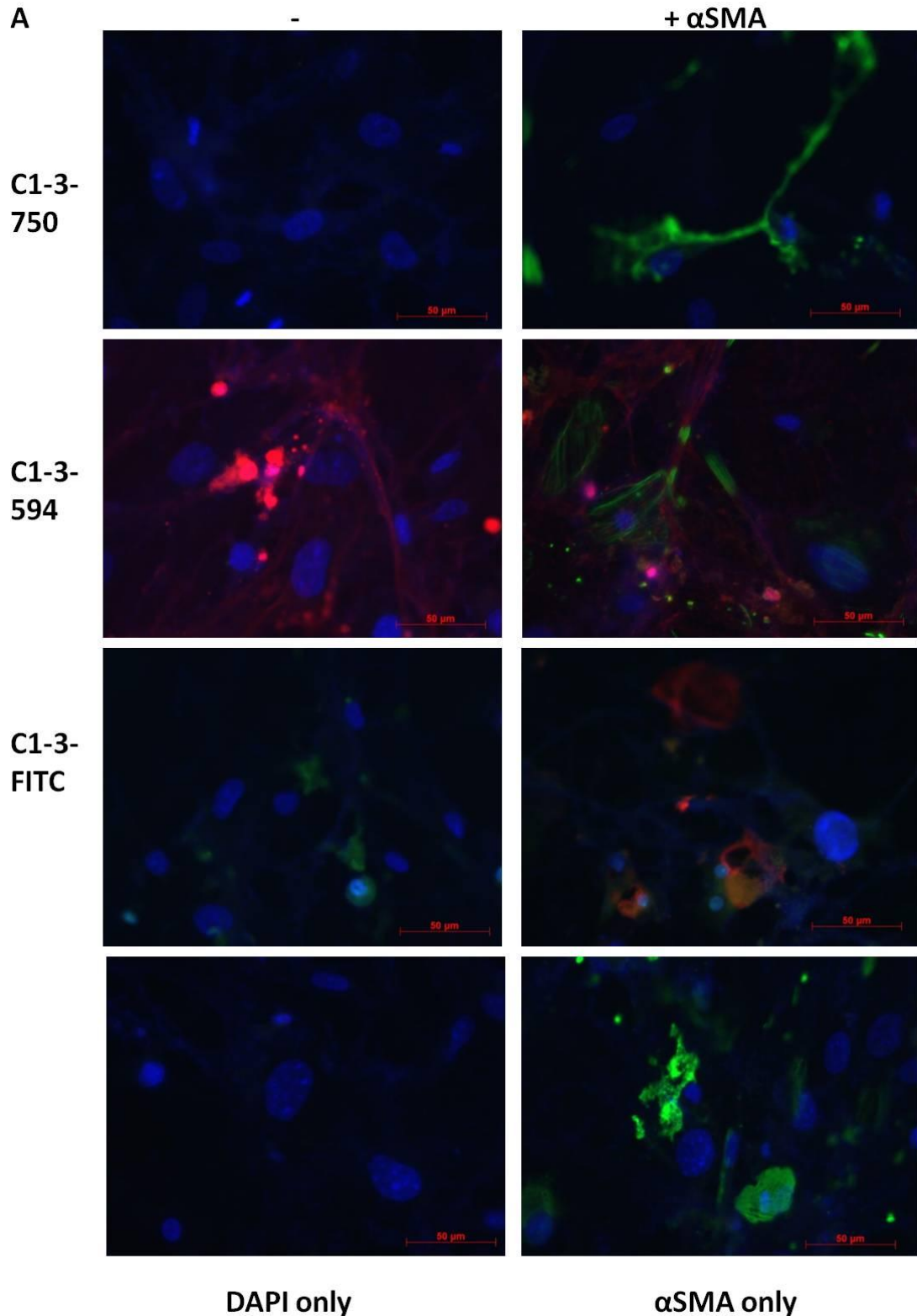


**Figure 3.7 ICC of C1-3 conjugates *in vitro* with mHSCs and hHSCs.** Both activated **A** mHSCs and **B** hHSCs isolated from C57B1/6 mice and human resected liver tissue respectively were cultured in chamber slides. Briefly the media was aspirated off and replaced with HBSS/ Hepes, 60 $\mu$ g/ml C1-3-FITC/ 594/ 750 was added and incubated for 2 hours at 37 °C and 5% CO<sub>2</sub>. The HSCs were fixed with 2% formaldehyde/ 0.2% glutaraldehyde in 1 x PBS prior to co-staining with  $\alpha$ SMA for a further hour; after PBS washes a complementary secondary fluorescent antibody was used FITC conjugated for C1-3-750 and C1-3-594, but TRITC conjugated for C1-3-FITC incubations. Finally a 10 minute incubation

with DAPI was performed to stain the cell nuclei and were visualised using a Zeiss fluorescent microscope (all images shown are x40 magnification).

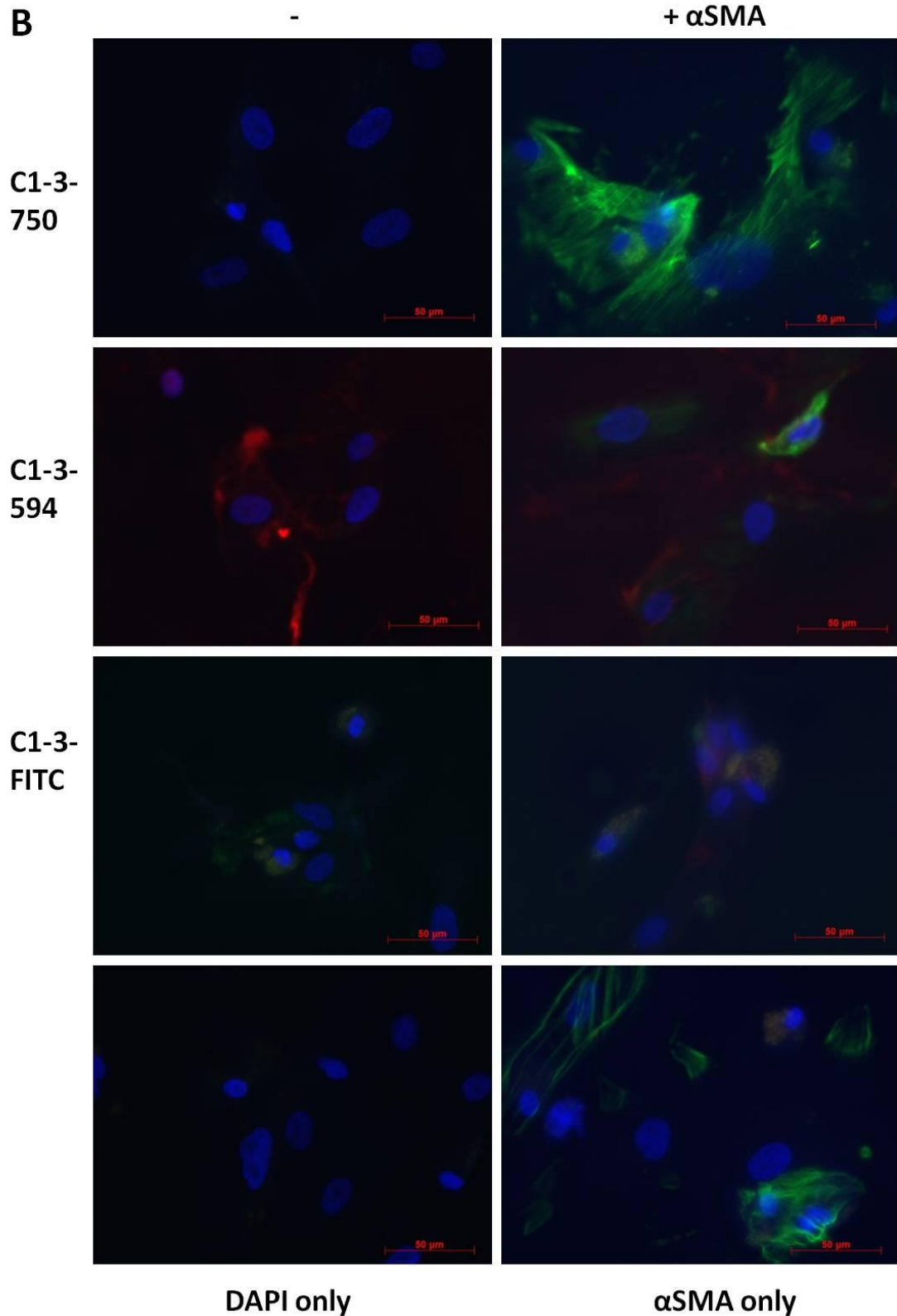


**Figure 3.7 ICC of C1-3 conjugates *in vitro* with mHSCs and hHSCs.** Both activated **A** mHSCs and **B** hHSCs isolated from C57B1/6 mice and human resected liver tissue respectively were cultured in chamber slides. Briefly the media was aspirated off and replaced with HBSS/ HEPES, 60 $\mu$ g/ml C1-3-FITC/ 594/ 750 was added and incubated for 2 hours at 37 °C and 5% CO<sub>2</sub>. The HSCs were fixed with

2% formaldehyde/ 0.2% glutaraldehyde in 1 x PBS prior to co-staining with  $\alpha$ SMA for a further hour; after PBS washes a complementary secondary fluorescent antibody was used FITC conjugated for C1-3-750 and C1-3-594, but TRITC conjugated for C1-3-FITC incubations. Finally a 10 minute incubation with DAPI was performed to stain the cell nuclei and were visualised using a Zeiss fluorescent microscope (all images shown are x40 magnification).

### **3.3 Pilot study of C1-3-750 functioning in an *in vivo* model of liver fibrosis**

In the initial pilot study to minimise the number of mice used a single C57B1/6 mouse was administered with CCl<sub>4</sub> twice weekly (see Table 2.1) for a total of 3 weeks, together with a control mouse which received olive oil. Upon completion of these treatments the mice were anaesthetised with isoflurane and had their ventral side shaved before being placed in the IVIS imaging chamber. Prior to injection of C1-3-750, background fluorescent scans were performed (Figure 3.8A), using the XF750 filter settings and both the auto exposure and a manual 5 second exposure setting. 10 mg/kg C1-3-750 was injected by i.v. injection and fluorescence scans using the same exposure settings were performed at regular time intervals; the final 4 hour time point whole body scan is shown in figure 3.8B. Upon completion of the final 4 hour time point the mice were terminated by a schedule I method and the major organs excised.

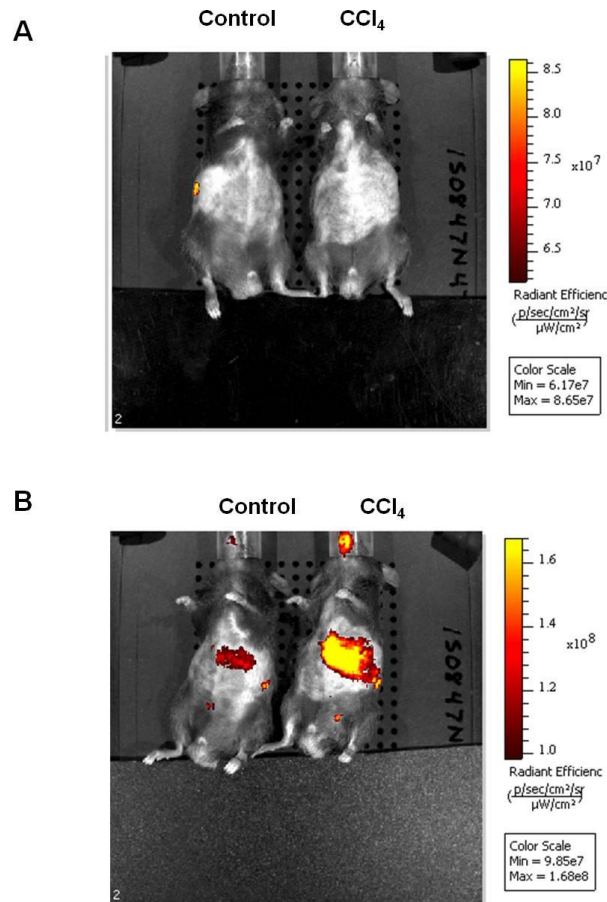


**Figure 3.8 A Whole body fluorescent background scan prior to i.v. injection of C1-3-750 into a control and CCl<sub>4</sub> treated mouse.** Mice were anaesthetised with isoflurane and shaved ventrally prior to placing in the IVIS chamber. All scans were performed using the XF750 filter settings and initially performed with both the auto and a manual 5 second exposure settings separately. **B Whole body fluorescent scan 4 hours post C1-3-750 injection.** The scan was performed as outlined in figure 3.8A using both the auto and 5 second exposure setting following i.v. injection of 10mg/kg bodyweight C1-3-750. (All following IVIS images utilised the auto settings, as the 5 second exposure resulted in saturated pixels).

The organs were placed inside the IVIS imaging chamber and *ex vivo* fluorescent scans were performed to determine the fluorescence signal of each individual organ (Figure 3.9). The successful targeting of C1-3-750 to the liver was displayed by the high fluorescent signal from the liver of the fibrotic mouse. There was no signal from any other organ and there was only a weak signal from the liver of the control mouse, this was due to the presence of quiescent HSCs in the liver that also express synaptophysin [108].

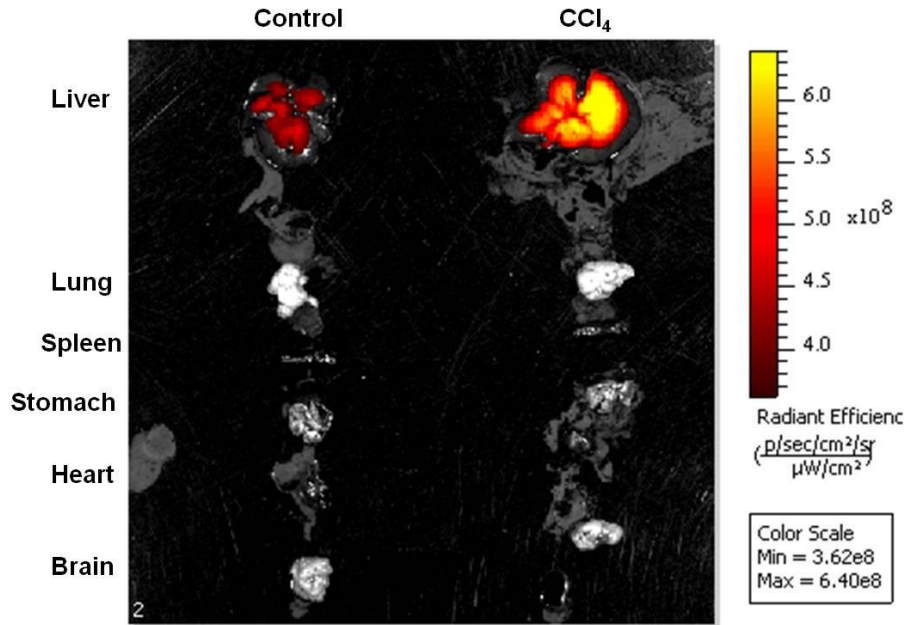


**Figure 3.9** *Ex vivo* organ scan 4 hours after C1-3-750 administration. Mice were terminated by a schedule I method and the major organs excised and placed in the IVIS imaging chamber prior to IVIS imaging.

All images measured on the IVIS were analysed using the accompanying Living Image 4.0 software; regions of interest (ROI) could be overlaid onto images as shown in figure 3.10. It was possible to detect the total fluorescence within these ROIs and therefore the total fluorescence of individual body regions and specific organs when they had been excised. The Total Radiant Efficiency ( $[\text{p/s}] / [\mu\text{W}/\text{cm}^2]$ ) (Total fluorescence) is shown in figure 3.11 for both the liver ROI and excised livers (Figure 3.10) of the  $\text{CCl}_4$  and control mice 4 hours after C1-3-750 administration. The total fluorescence calculations (Figure 3.11) support the initial images, indicating that there was approximately a two fold increase in the level of fluorescence seen in both the whole body liver ROI and excised liver of the  $\text{CCl}_4$  fibrotic mouse when compared to the control mouse. These initial findings suggest that C1-3-750 was a viable route to image liver fibrosis non invasively, although larger scale studies are required to confirm this.

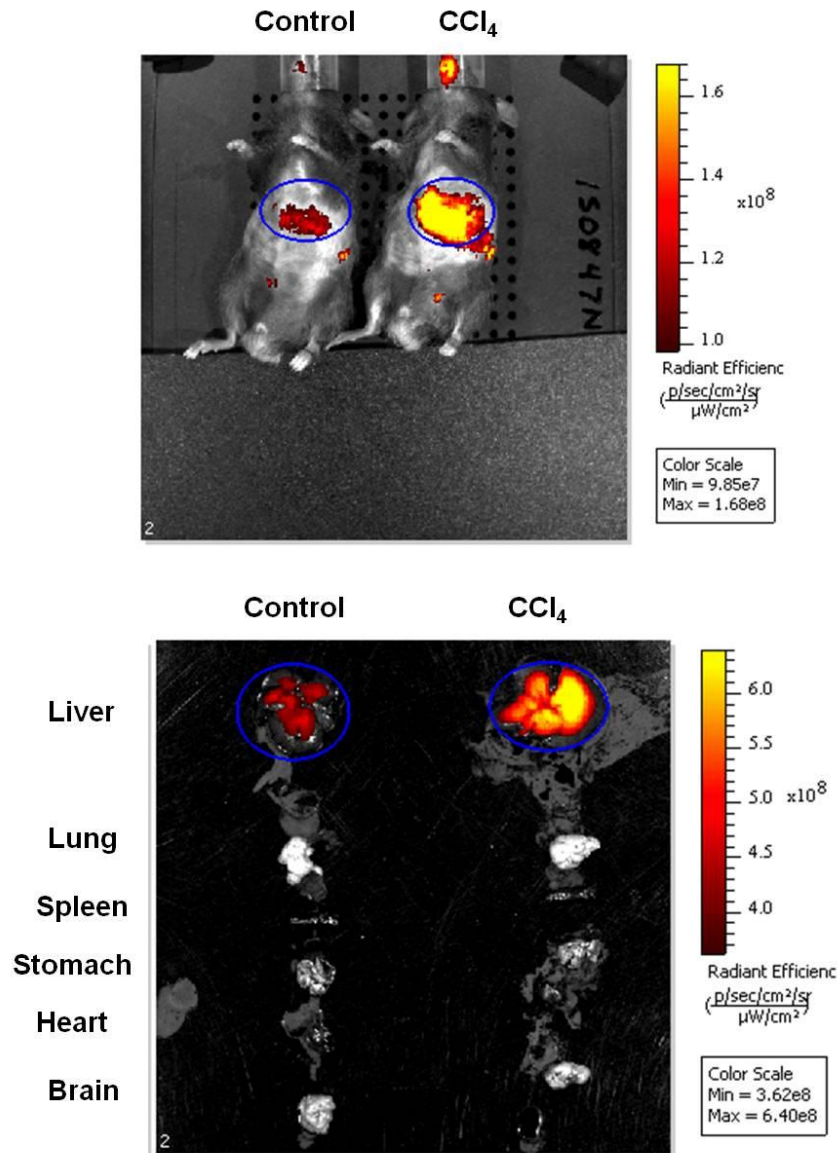


**Figure 3.10 Whole body (4 hour time point) and *ex vivo* organ scan + example ROIs used for total fluorescence calculations.** ROIs could be overlaid onto images with the Image Pro Plus 4.0 software, allowing the calculation of total fluorescence values for specific regions and excised organs.

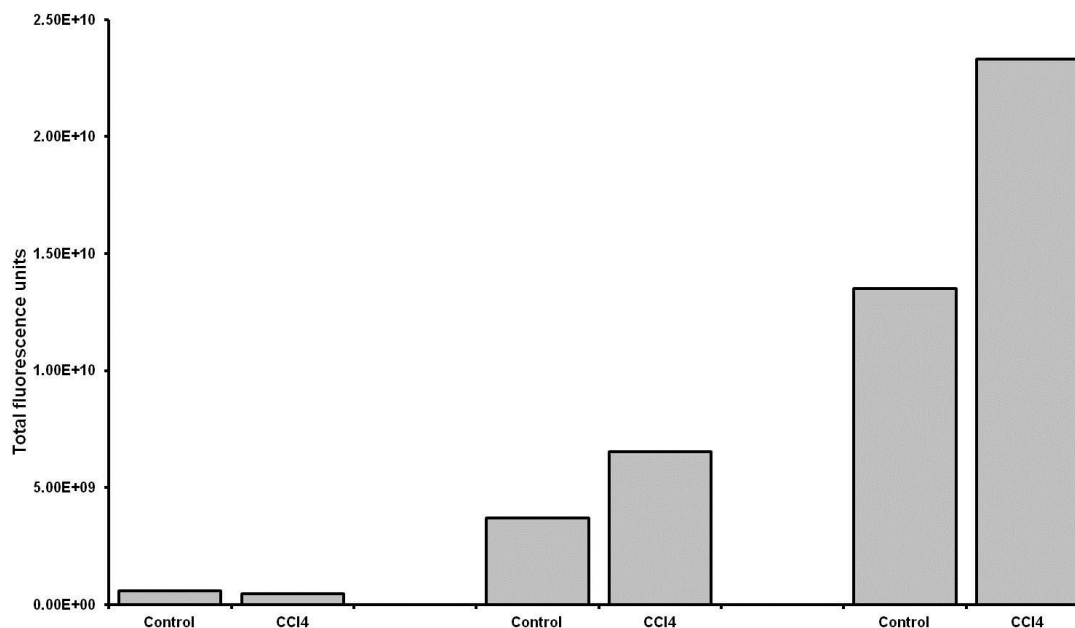


**Figure 3.11 Total fluorescence values calculated for both the whole body and *ex vivo* organ scans.** Numerical fluorescence values (total fluorescence) calculated from the individual ROIs shown in figure 3.10, allowing quantification of the difference in C1-3-750 binding between the control and CCl<sub>4</sub> treated mice (n=1).

### 3.4 The effect of C1-3-750 injection route upon imaging outcome *in vivo*

Another area of concern before undertaking the larger study was determining the best route to inject C1-3-750; an i.v. injection route was used in the initial study upon consultation with the IVIS technicians, as this is the route used in clinical imaging settings. However, all previous *in vivo* work with C1-3 and its conjugates (e.g. C1-3-GTX) was performed using an i.p. injection route. This was an essential consideration as the planned future study will involve multiple imaging time points and repeated injections of C1-3-750. To determine if i.p. was a suitable route to administer C1-3-750 the initial pilot study was repeated with an i.p injection route alongside the recommended i.v. injection route. In particular we wished to ascertain whether this had any detrimental effects on the imaging outcome, such as retention of the dose in the tail sheath.

Three C57B1/6 mice received CCl<sub>4</sub> twice weekly for 4 weeks before commencement of the imaging aspect of the study; following a background scan (Figure 3.12) one received C1-3-750 by an i.p. injection, one via an i.v.

injection and a control mouse received no C1-3-750 injection. The mice were subsequently imaged at regular intervals for 2 hours prior to termination by a schedule I method and *ex vivo* imaging of the major organs. Figure 3.12 shows the variation in fluorescence detected over the 2 hour time course between the i.p., i.v. and non inject mice. When ROIs were overlaid (Figure 3.13A) the level of fluorescence was quantified for specific body regions, such as the upper abdominal (liver) region and the bladder region (Figure 3.13B). The bladder region was measured as it also emits a strong fluorescent signal as there will be continual excretion of C1-3-750 from the body. Figure 3.14A is the *ex vivo* organ scan 2 hours after C1-3-750 administration highlighting the variation in fluorescence resulting from the route of C1-3-750 injection. Total fluorescence calculations (Figure 3.14B) from the ROI surrounding the individual organs suggest that both i.p. and i.v. injection routes are suitable to dose C1-3-750.

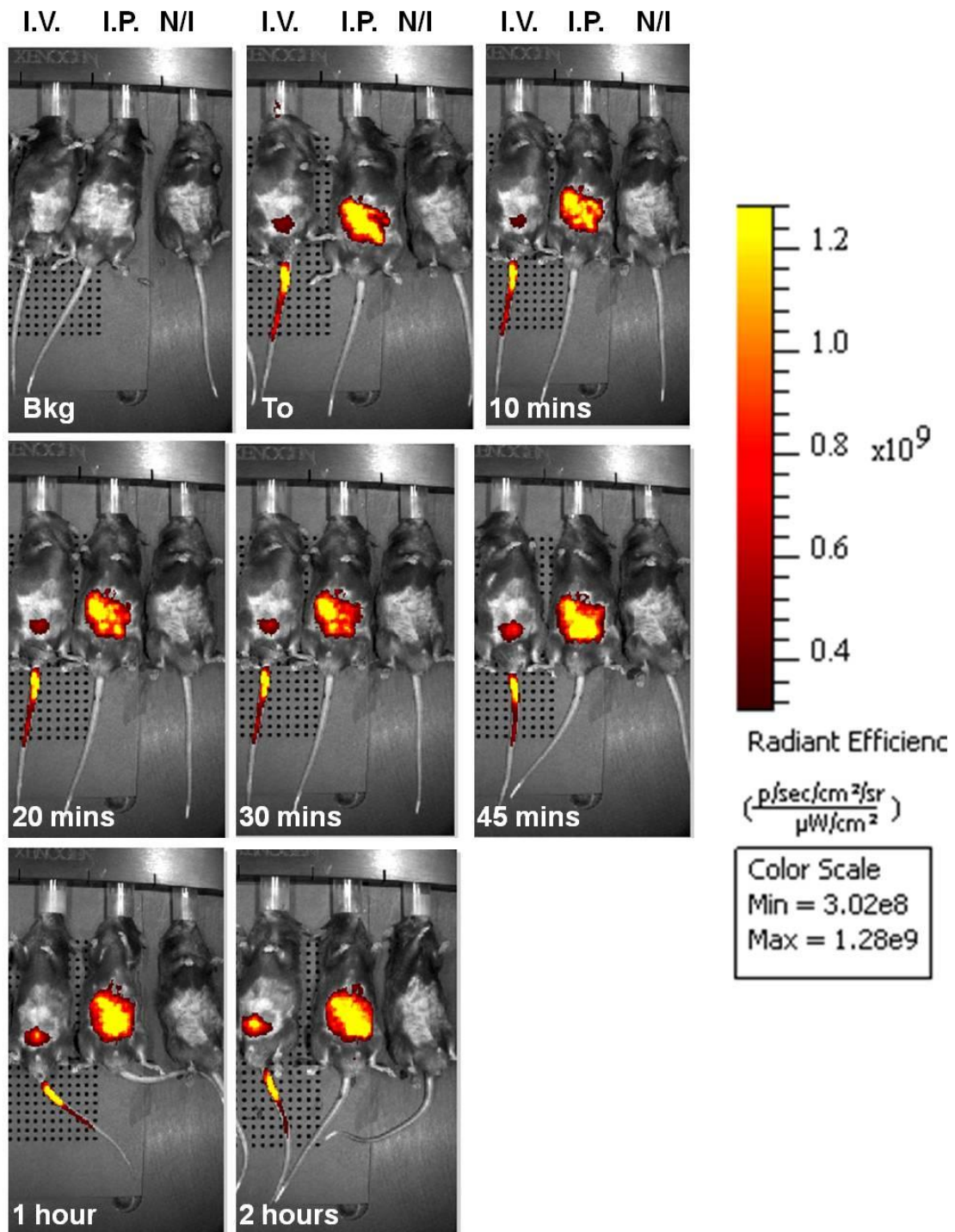


**Figure 3.12 Whole body fluorescent scans over two hour time course for i.p., i.v. and non inject C1-3-750 administered mice.** Individual fluorescent scans at designated time points from before and after C1-3-750 administration, highlighting the variation in fluorescent signal dependent upon the route of C1-3-750 injection. (Bkg – background scan prior to C1-3-750 administration,  $T_0$  – Time zero immediately after C1-3-750 administration, and the rest are hourly (h) time points).

The initial whole body scan (Figure 3.12) highlights the major problem associated with i.v. injection, displayed by the high fluorescent signal emitted

from the tail (injection site) of the i.v. mouse due to the retention of the C1-3-750 dose in the tail sheath. This was counteracted in the initial pilot work by covering the tails (injection site) of the mice, although this will just mask the fluorescence signal and does not impact upon the amount of C1-3-750 dosed. Therefore doubts about the success of injection and potential variations in the dose of C1-3-750 administered by i.v. injection will always persist. Secondly there was a strong signal emitted from the upper abdominal/ liver region of the i.p. mouse when compared to the i.v. mouse throughout the 2 hour time course (Figure 3.12), these findings were reinforced by the total fluorescence calculations in figure 3.13B. However the *ex vivo* organs scan (Figure 3.14A) and the total fluorescence calculations (Figure 3.14B) generated from the ROI reveal that there was a greater fluorescence from the liver of the i.v. injected mouse than the i.p. injected mouse. However there was still a significantly higher level of fluorescence from the liver of the i.p. mouse when compared to the non inject mouse.

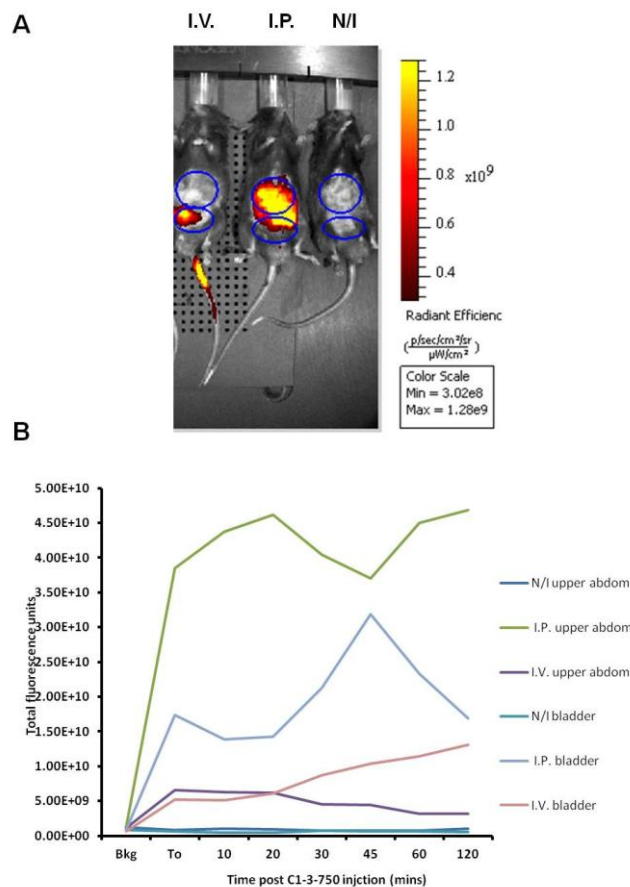


**Figure 3.13 Whole body fluorescent scan + ROIs for the upper abdominal and bladder regions, and the total fluorescence values. A** Example image post scanning with ROIs overlaid using the Image Pro Plus 4.0 software. **B** Total fluorescence values calculated for each individual mouse (n=1).

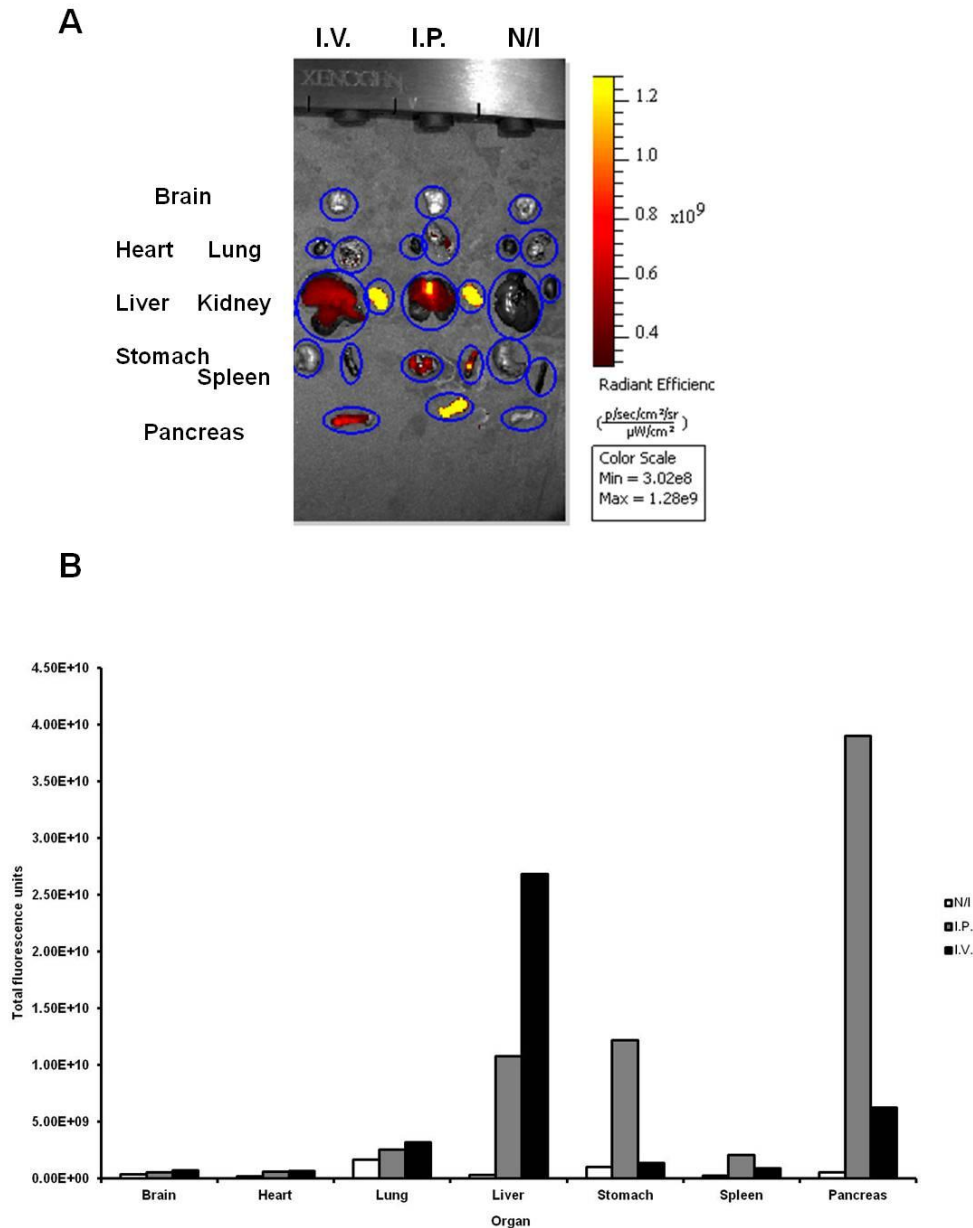


**Figure 3.14 Ex vivo organ scan (with ROIs) and total fluorescence calculations for the individual organs from the i.p., i.v. and non inject C1-3-750 administered mice. A** The *ex vivo* organ scan performed upon completion of the final (2 hour) whole body scans and schedule I termination of the mice. **B** The total fluorescence data generated shows both i.p. and i.v. are viable routes to administer C1-3-750 demonstrated by the high fluorescent signals emitted from the liver. There was also a high non specific signal emitted from the kidney (data not shown) as the scAb was being excreted from the body, there is also a strong pancreas signal especially in the i.p. injected mouse due to the presence of the target synaptophysin in the Islet cells (n=1).

Considering the size of the planned study and the findings in section 3.1.4, in particular the need for repeated dosing and imaging of the same mice with C1-3-750, it was concluded that administering C1-3-750 by i.p. injection would

be the most easily reproduced and effective way of dosing C1-3-750 in the chronic study. There was no evidence of fluorescent antibodies previously being administered by an i.p. route in the literature; the general consensus is that i.v. gives a better distribution of the imaging agent [218] and is obviously more applicable clinically. However as the major aim of this study was the development of a non invasive imaging agent, an i.v. injection route cannot be used after the poor whole body findings in the pilot study (Figures 3.12 and 3.13). This was reinforced by the need for repeated C1-3-750 injections, which can result in scarring of the injection site and subsequent problems when performing later injections.

Another point of interest from this study was the high level of fluorescent signal emitted from the pancreas, particularly of the i.p. injected but also the i.v. injected mouse. This was not a result of non specific binding of the C1-3 scAb, but due to the expression of high levels of synaptophysin in the Islet cells of the pancreas [219].

### **3.5 Using C1-3-750 *in vivo* to distinguish between different fibrosis severities**

To determine C1-3-750's potential to differentiate between the various stages of hepatic fibrosis and to provide a quantitative value of fibrosis, a final *in vivo* study was performed with increased numbers of C57B1/6 mice with varying degrees of CCl<sub>4</sub> induced liver fibrosis. Figure 3.15 is a schematic diagram illustrating the different treatment groups, alongside the dosing and imaging schedule.

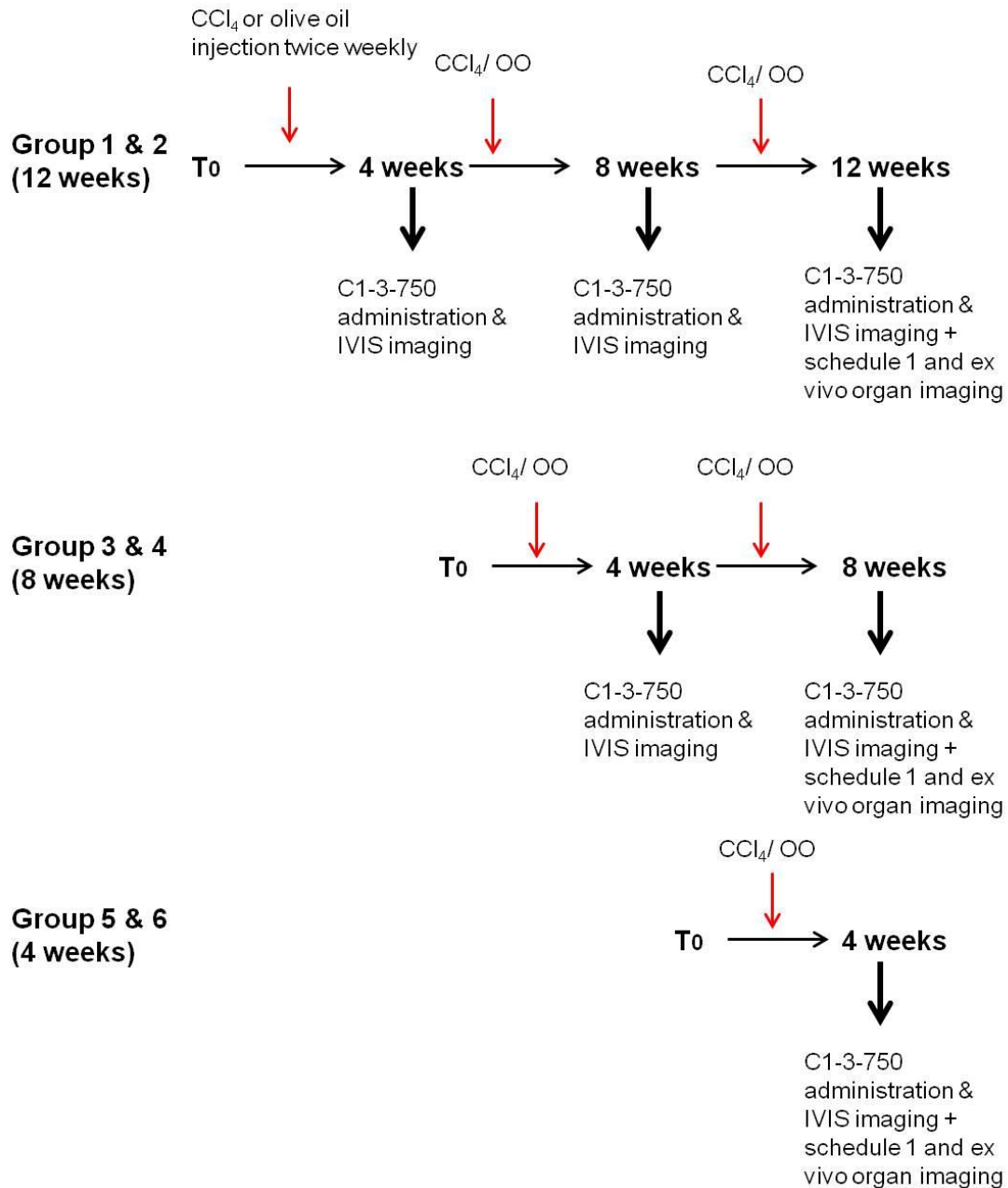


**Figure 3.15 Schematic diagram outlining the dosing and imaging regimens for the animal study trying to differentiate fibrosis severity.** Each mouse received CCl<sub>4</sub> twice weekly to induce centrilobular fibrosis (whilst controls received olive oil); the groups were staggered so the final CCl<sub>4</sub> doses were administered on the same day. Each group was imaged in the IVIS at 4 week intervals following anaesthetic and i.p. injection of 10mg/kg C1-3-750. After the final dose of CCl<sub>4</sub> and subsequent IVIS imaging the following day all mice were terminated by a schedule I method. The major organs were excised and placed in the IVIS chamber and imaged using the same settings, prior to retention for subsequent IHC and biochemical analysis.

Briefly, group 1 received CCl<sub>4</sub> for 12 weeks whilst group 2 received olive oil, and they were imaged at 4, 8 and 12 weeks following C1-3-750 injection. Group 3 received CCl<sub>4</sub> for 8 weeks, whilst group 4 received olive oil for the same time period (and were imaged at 4 and 8 weeks of treatment); finally

group 5 received  $\text{CCl}_4$  for 4 weeks and group 6 received olive oil for the same period and both were imaged after 4 weeks of treatment. Whole body fluorescence scans following C1-3-750 i.p injection were performed and the 12 weeks of  $\text{CCl}_4$  and olive oil treatment group scan is shown as an example in figure 3.16 (all images shown are from the two hour time point). The final imaging point for all treatment groups coincided on the same day and at this point all the mice were terminated by a schedule I method prior to *ex vivo* imaging of the major organs (Figure 3.17, 12 week treatment group example). The i.p. injection route is not infallible though as highlighted in figures 3.16 and 3.17, where the final 12 week olive oil mouse does not emit any C1-3-750 fluorescent signal from any excised organ. This was due to a poor i.p. injection, with the dose being accidentally administered subcutaneously and being trapped under the skin and unable to distribute to any of the major organs as seen in the other animals.

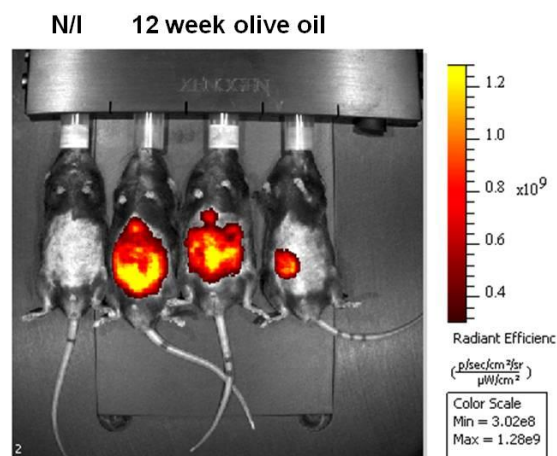
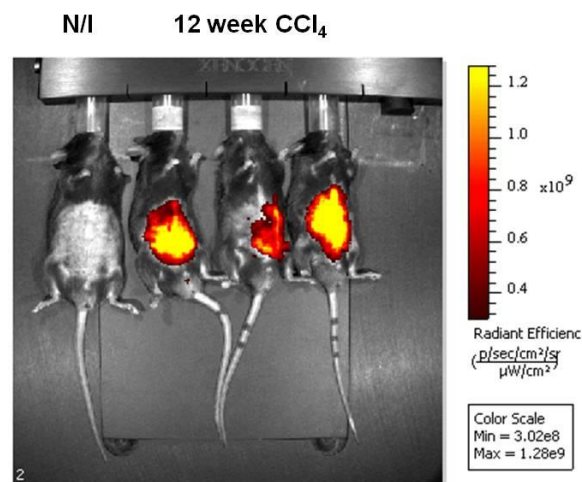


**Figure 3.16 Whole body scan from the 12 week CCl<sub>4</sub> treated and control mice.** Image shown is the 4 hour time point after C1-3-750 i.p. injection, all images were analysed using the Image Pro Plus 4.0 software and the same total fluorescence scale was applied so they can be directly compared to each other.

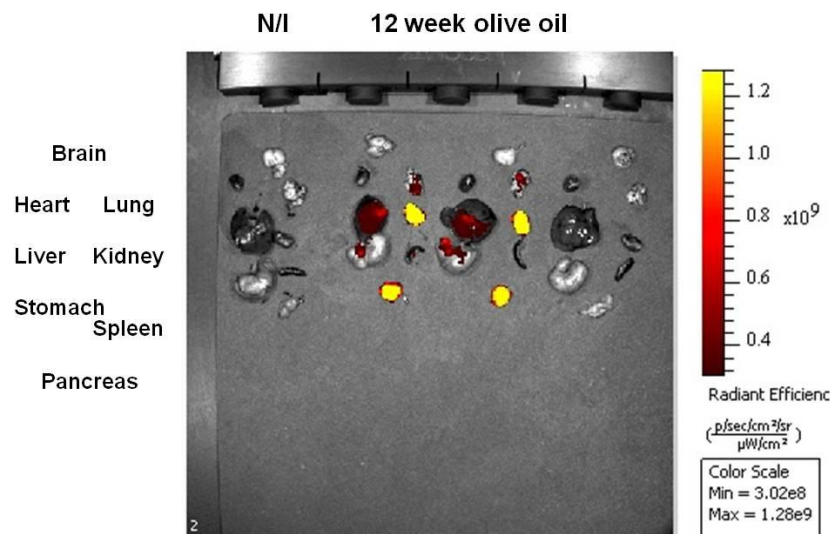
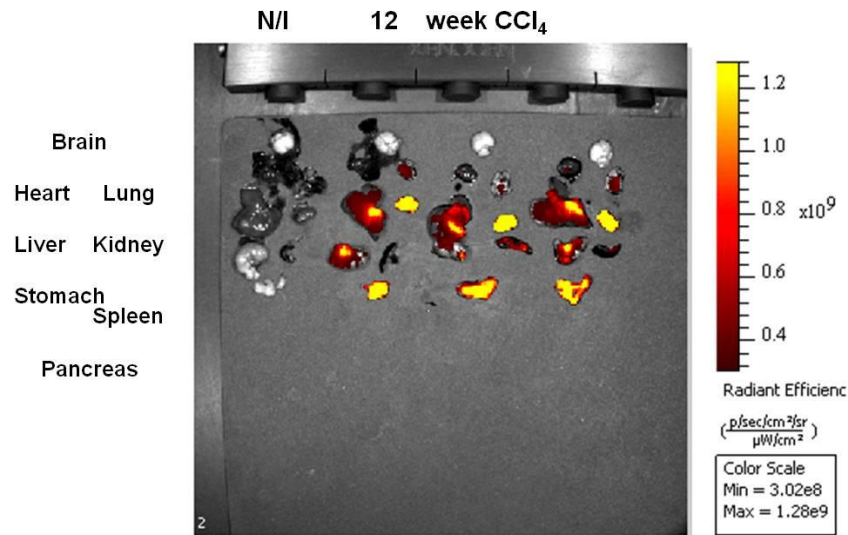


**Figure 3.17 Ex vivo organ scan from the 12 week CCl<sub>4</sub> treated and control mice.** Upon completion of the 4 hour time point the mice were culled by a schedule I method and the major organs excised and imaged using the same settings. All images were analysed using the Image Pro Plus 4.0 software and the same total fluorescence scale was applied so they can be directly compared to each other.

Using ROIs (Figure 3.18) as described in section 3.1.3 the total fluorescence could be calculated for both the upper abdominal and bladder regions as displayed in figure 3.19. The values shown are the mean for each treatment group (each group had a minimum of 3 animals). There was no difference in the total fluorescence values for the upper abdominal (liver) region of all the

CCl<sub>4</sub> treatment groups and the olive oil control groups. These findings indicate that C1-3-750 cannot be used non-invasively as intended. The reason for the high upper abdominal fluorescence signals in the whole body scans of both the CCl<sub>4</sub> and olive oil mice (Figure 3.16) and total fluorescence calculations (Figure 3.19) was a result of the C1-3-750 i.p. injection route. It appears that C1-3-750 pools in the peritoneal cavity for the duration of the time course and cannot distribute evenly throughout the body. It was saturating the upper abdominal region and masking any potential liver region signal, making it impossible to non-invasively image liver fibrosis.

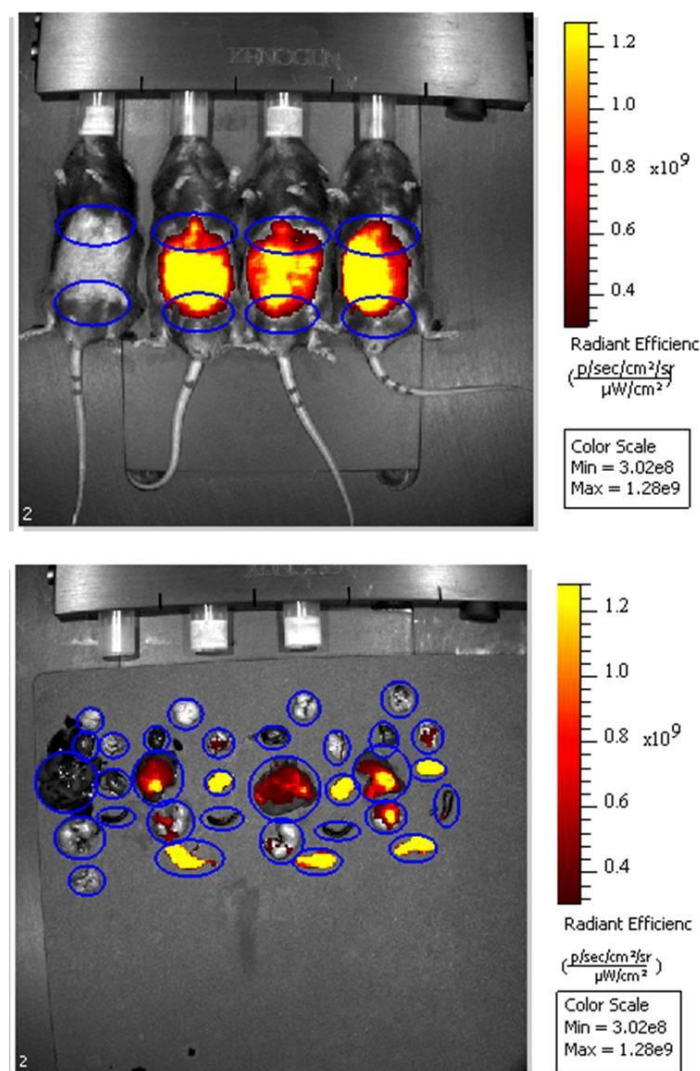


**Figure 3.18 Example whole body and *ex vivo* organ images annotated with ROIs.** When analysing images with Image Pro Plus 4.0 software ROIs could be overlaid the images to allow quantification of total fluorescence values for specific body regions – (upper abdominal/ liver region and bladder/ C1-3-750 excretion) and organs.

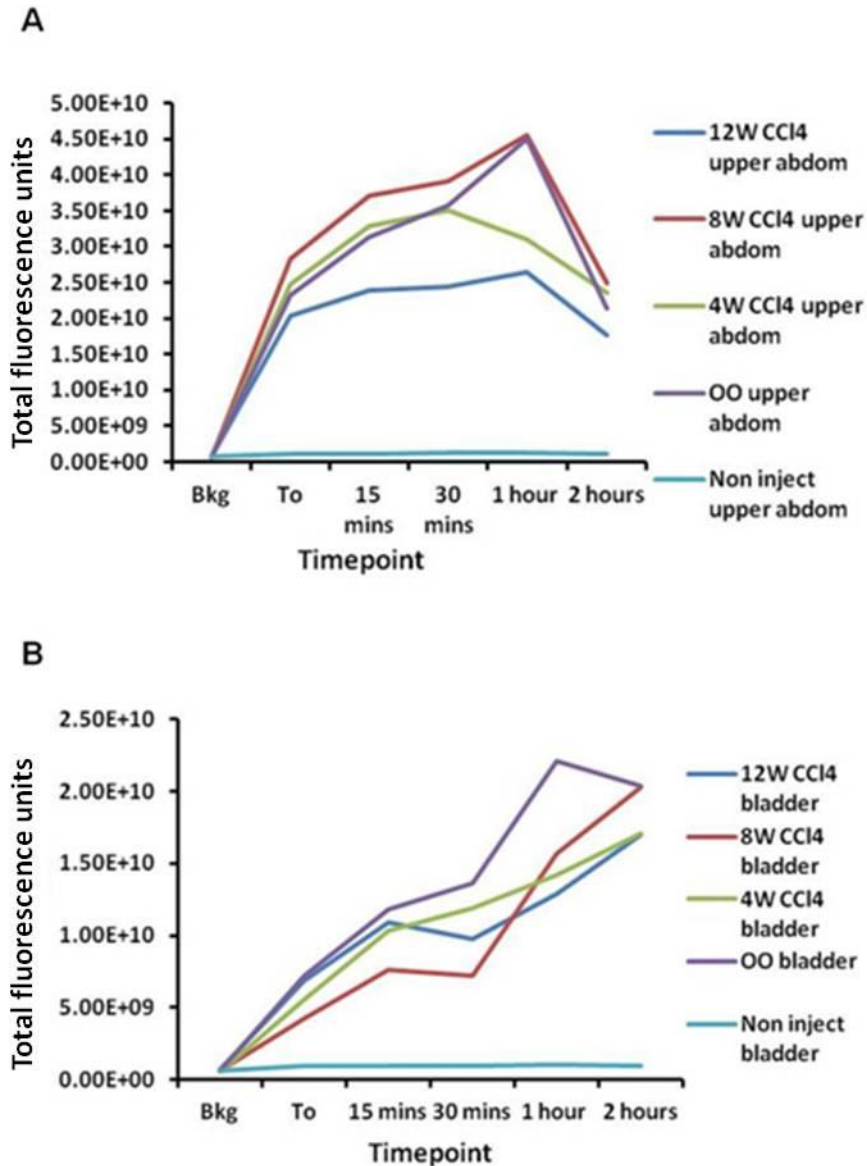


**Figure 3.19 Total fluorescence values calculated for the upper abdominal and bladder regions of each treatment group.** A upper abdominal and B bladder total fluorescence values calculated from the ROIs used during analysis of each individual treatment group. Data shown is the mean for each treatment group (Data are the mean,  $n=3$  for each treatment group, Bkg – background scan prior to C1-3-750 administration,  $T_0$  – Time zero immediately after C1-3-750 administration.)

Total fluorescence calculations were also performed for the *ex vivo* organ scans (Figure 3.17) and the data generated is shown in figure 3.20A. Figure 3.20B shows the mean total organ fluorescence of the brain, lung and liver when all the olive oil control animals have been combined, making it easier to distinguish between the treatment groups. The brain and lung have been included as they show very little fluorescence regardless of the treatment

group and help highlight the variation in liver signal between the treatment groups. Figure 3.21 shows the mean total fluorescence values for the excised livers of each treatment group, highlighting that there was no significant difference in fluorescence between the 12, 8 and 4 week CCl<sub>4</sub> treatment groups. However there was a statistically significant (increased) level of liver fluorescence between the CCl<sub>4</sub> treatment groups when compared to the controls and analysed using an ANOVA ( $p < 0.009$ ). In this instance C1-3-750 can distinguish between *ex vivo* fibrotic and non fibrotic livers, but was not sensitive enough to distinguish between the varying degrees of fibrosis.

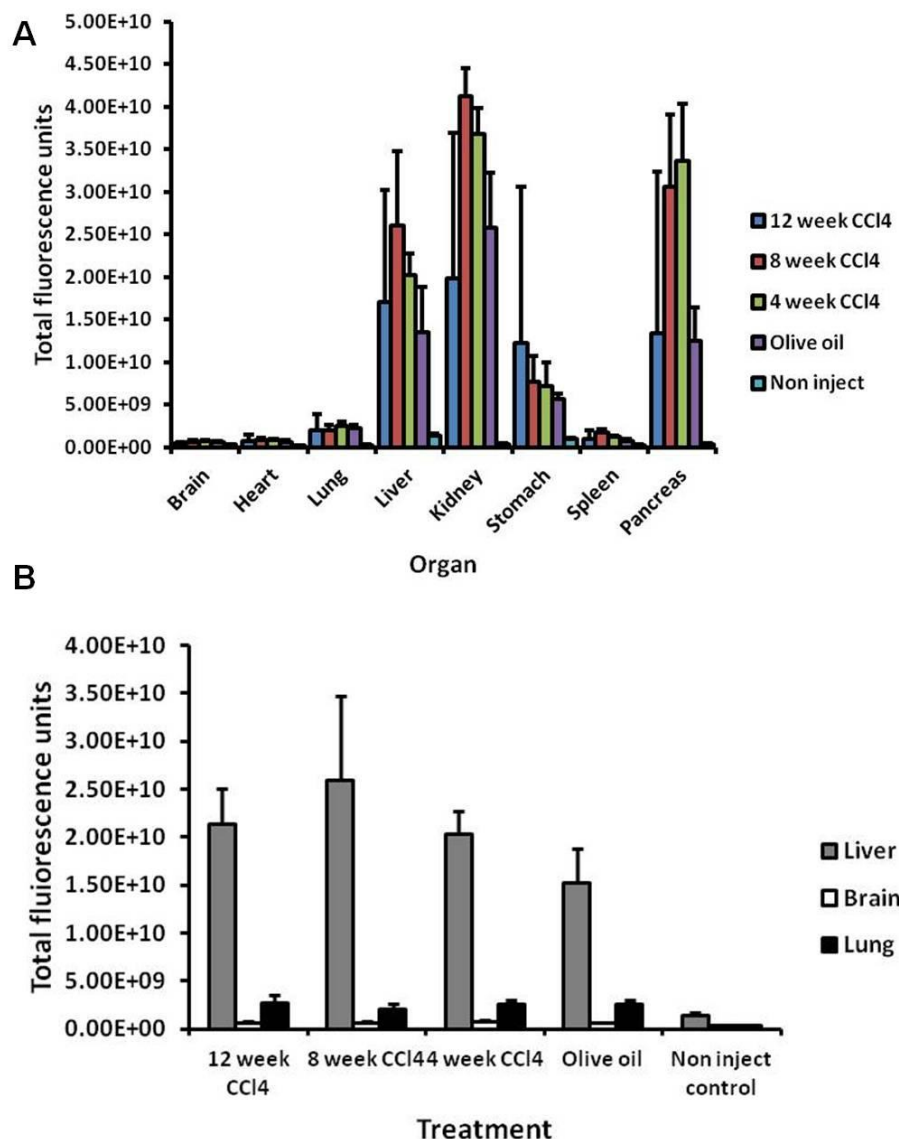


**Figure 3.20 Total fluorescence values for the major organs of each treatment group following their excision. A** all excised organs **B** brain, lung and liver fluorescence only. Individual organ total fluorescence values calculated from ROIs drawn around each organ, the data shown is the mean and

standard deviation (SD) for each treatment group (Mean and SD n=3 for non inject and CCl<sub>4</sub> treatment groups, n=9 olive oil controls).

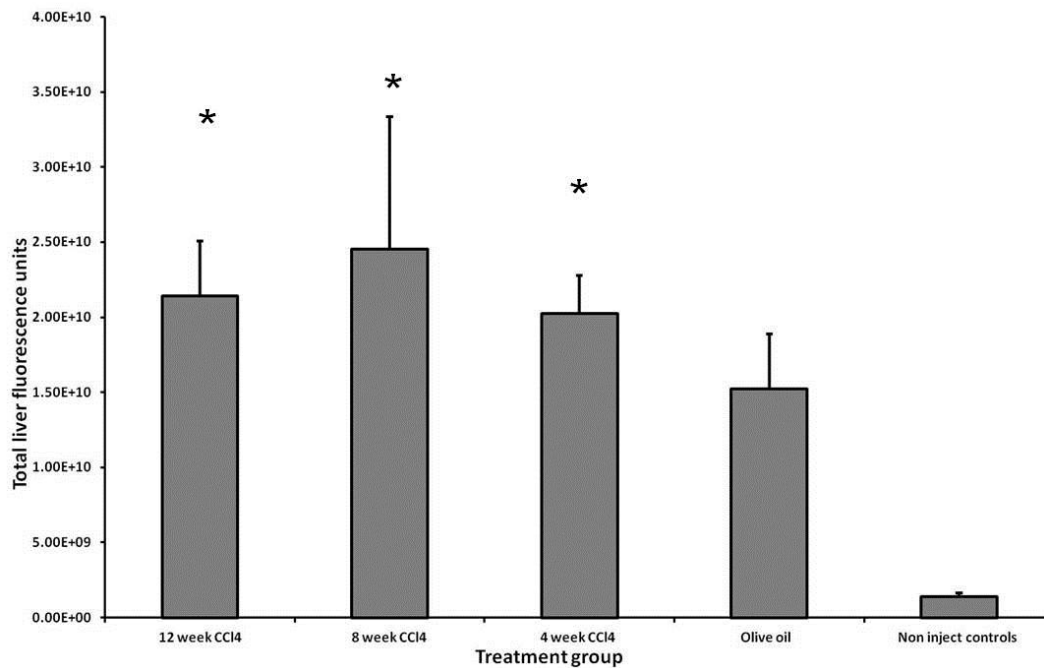


**Figure 3.21 Total fluorescence of excised liver from each treatment group.** The individual total liver fluorescence values calculated for each treatment group from the ROIs drawn using the Image Pro Plus 4.0 software. (Mean and SD n=3 for non inject and CCl<sub>4</sub> treatment groups, n=9 olive oil controls), \* denotes that a group is significantly different to the olive oil control when analysed using an ANOVA ( $p < 0.009$ ).

To confirm that the level of liver fluorescence coincided with liver damage and fibrosis development, a range of IHC analyses were performed to confirm both fibrosis development and the presence of hepatic myofibroblasts. Firstly, IHC analysis of the formalin fixed liver sections was performed to determine if there was, as hypothesised, a correlation between the number of hepatic myofibroblasts and the level of liver fluorescence.  $\alpha$ SMA IHC was performed as this is a direct marker of hepatic myofibroblasts following HSC activation [220]. Typical images taken on the light microscope from each individual treatment group are shown in figure 3.22, showing the increased number of  $\alpha$ SMA positive cells with CCl<sub>4</sub> treatment. The number of  $\alpha$ SMA positive cells was quantified blindly using Qwin software (Leica Microsystems) with a minimum of 10 random fields of view per image and 9 images per treatment group. As expected there was a statistically significant increase ( $p < 0.0001$ , analysed using an ANOVA) in the number of  $\alpha$ SMA positive cells with CCl<sub>4</sub>

treatment, when compared to the olive oil and non inject control mice (Figure 3.24A).

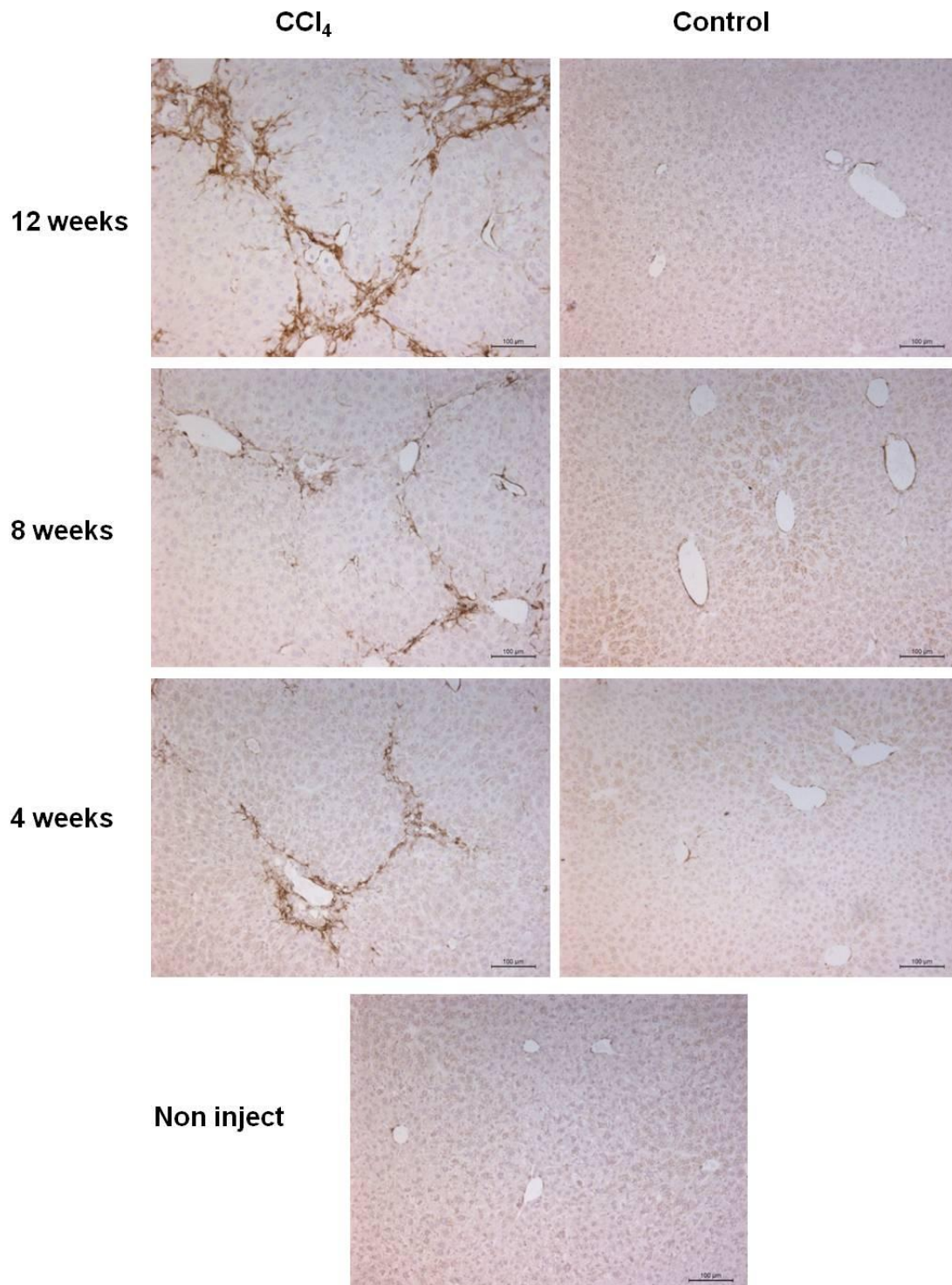


**Figure 3.22  $\alpha$ SMA IHC analysis of liver tissue from each treatment group.** Liver tissue was fixed in 10% formalin prior to paraffin embedding, 5 $\mu$ M sections were cut from each animal. Sections were dewaxed prior to blocking of endogenous peroxidase activity and heat induced antigen retrieval. Followed by serum blocking and incubation for an hour at RTP with  $\alpha$ SMA primary antibody, after PBS washing and addition of the complementary secondary antibody the level of bound antibody was detected by DAB incubation. The sections were counterstained with haematoxylin and dehydrated prior to mounting and analysis with a Leica upright microscope. (All images shown are x20 magnification).

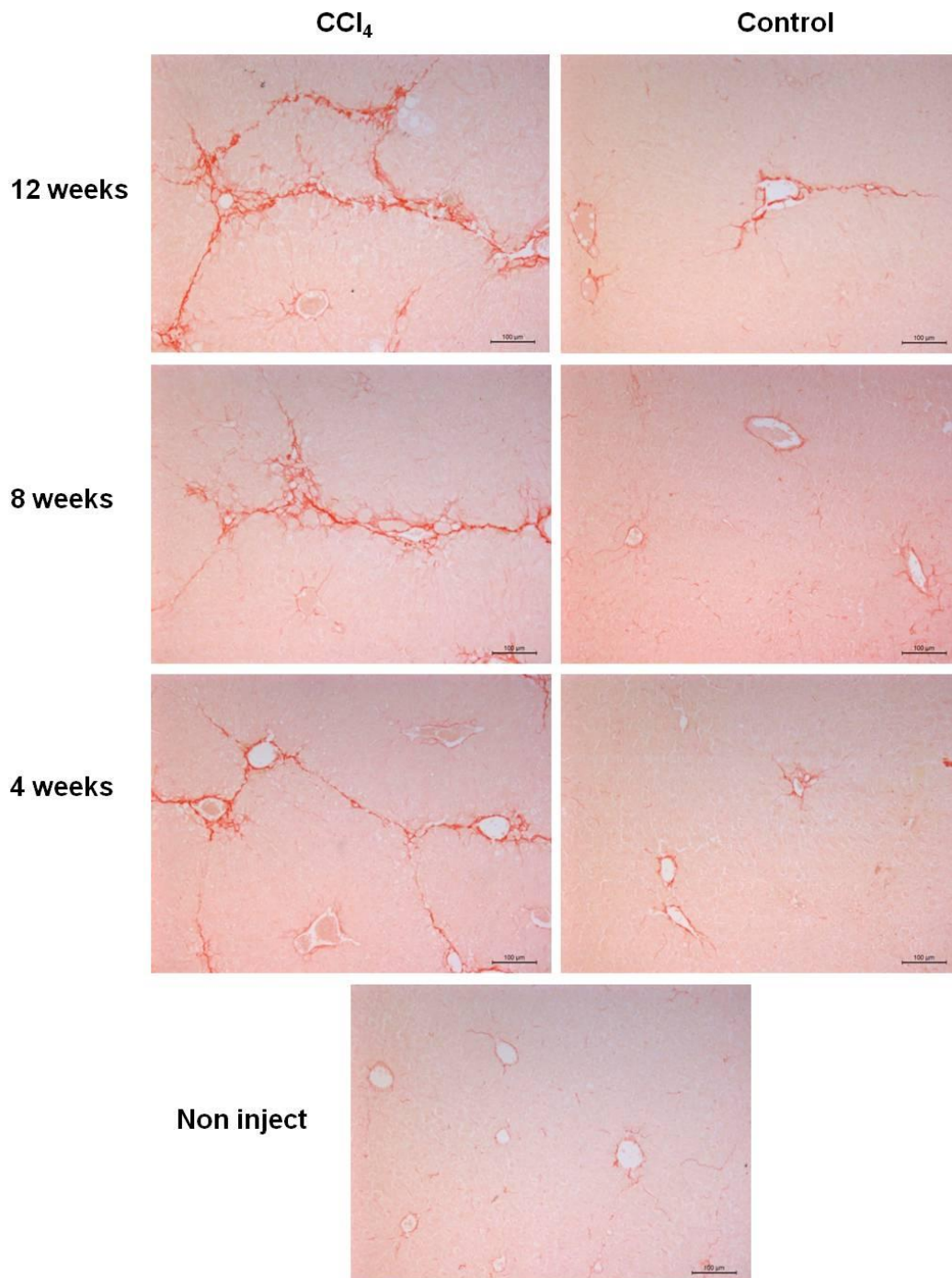


**Figure 3.23 Sirius red IHC analysis of liver tissue from each treatment group.** Liver tissue was fixed in 10% formalin prior to paraffin embedding, 5 $\mu$ M sections were cut from each animal. Sections were dewaxed prior to incubation in sirius red stain (0.036mM in saturated picric acid) for 2 hours, after 3 brief washes in acidified H<sub>2</sub>O the sections were dehydrated prior to mounting and analysis with a Leica upright microscope. (All images shown are x20 magnification).

Picro-sirius red IHC staining was performed, as sirius red binds strongly to collagens, and therefore it is an excellent indicator of fibrosis severity [214].

As with the  $\alpha$ SMA images there was an increase in collagen deposition with increased  $\text{CCl}_4$  administration (Figure 3.23). Quantification using the Qwin software (minimum of 10 random fields of view per image and 9 images per treatment group) confirmed that there was a statistically significant increase in collagen deposition proportional to the level of liver damage when compared to the olive oil and non inject control groups ( $p < 0.0001$ , analysed using an ANOVA) (Figure 3.24B).

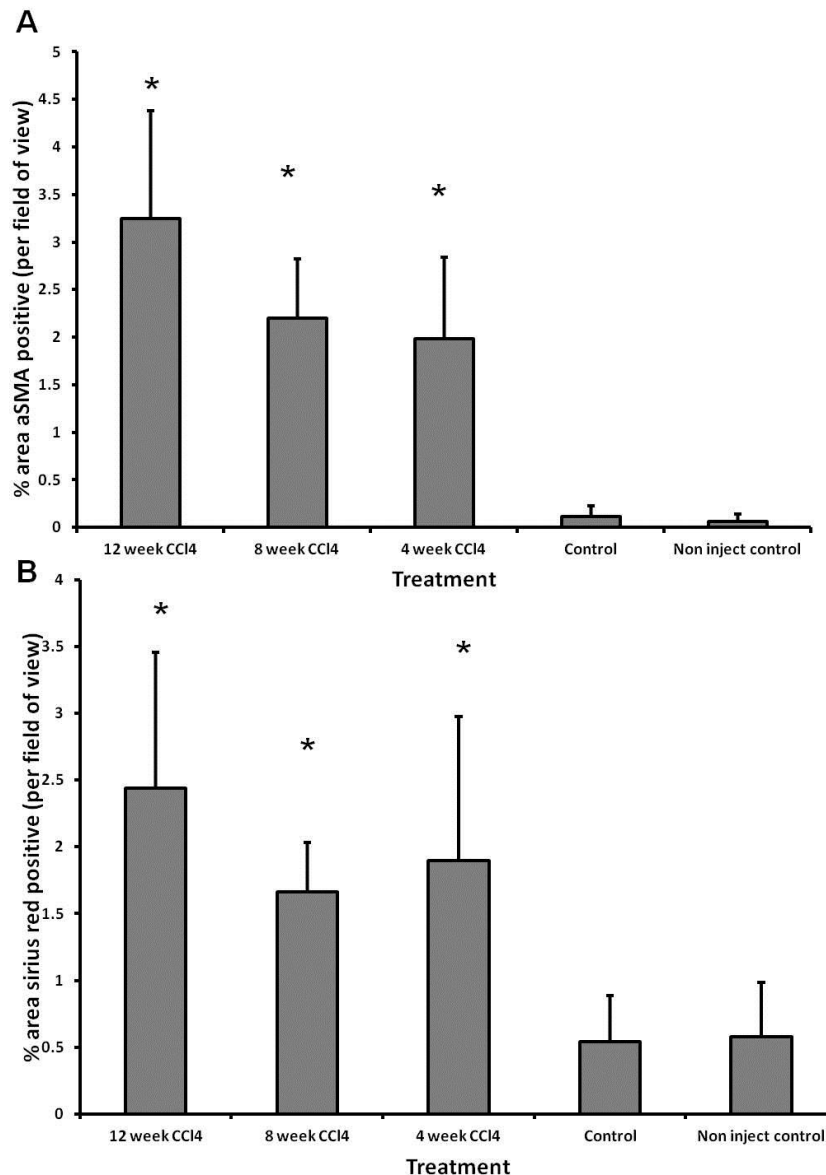


**Figure 3.24  $\alpha$ SMA and sirius red IHC quantification.** **A**  $\alpha$ SMA and **B** sirius red positive staining was quantified using Qwin software (Leica), briefly 10 random images were captured for each section and blindly quantified to determine the positive  $\alpha$ SMA and sirius red stain per field of view. (Mean and SD  $n=30$ ) of percentage area of the stain for each treatment group and were tested for statistical significance using an ANOVA. (\* denotes significance  $p < 0.0001$  when compared to the olive oil and non inject control).

### 3.6 C1-3-750 signal quenching by liver tissue – limitations of optical imaging

The long wavelength fluorophore XF750 was chosen for these imaging studies as the major issue with optical imaging techniques is the penetration of light to deep tissue locations and the high auto fluorescence associated with mouse tissue. Tissue depth issues are due to absorption by haemoglobin at lower wavelengths (below 650nm) and the absorption by water at higher wavelengths (above 900nm) [221, 222]. Auto fluorescence is predominantly due to the presence of chlorophyll and other natural flavins in the mice's diet, which absorbs at approximately 640nm and fluoresces at approximately 675nm [218, 222]. Therefore by selecting XF750 as our fluorophore the amount of background fluorescence will be reduced. The effect of tissue penetration on imaging outcome was another limitation I wished to determine. To assess this, a simple experiment was performed where a single dose of C1-3-750 in an eppendorf was imaged, and this was repeated when a mouse liver was placed over the C1-3-750 containing eppendorf (Figure 3.25A). Total fluorescence values were calculated with the aid of ROIs (Figure 3.25B) and the level of C1-3-750 fluorescence that was quenched by the liver tissue was calculated. In this instance 75% of the fluorescent signal had been lost, highlighting a major issue associated with optical imaging techniques [218, 223]. This loss of signal will be increased when having to penetrate other tissues/ organs and the skin. Previous imaging work utilising C1-3 conjugated to an Alexa Fluor 594 dye (Molecular Probes) had signal quenching values of up to 99% by the liver tissue, showing the use of the long wavelength fluorophore XF750 improves tissue imaging.

These findings confirm that poor tissue penetration and signal loss (Figure 3.25) may explain the earlier results of the i.p. versus i.v. injection route pilot study, with improved *ex vivo* liver signal from the i.v. injected mouse, but very little upper abdominal (liver) signal detected in the whole body scans. In contrast the i.p. injected mouse exhibited a much higher upper abdominal (liver) fluorescent signal and still a relatively strong *ex vivo* liver signal, however this upper abdominal (liver) fluorescent signal was due to pooling of

the C1-3-750 dose in the i.p. cavity. This was confirmed in the later study when there was no difference in liver fluorescence detected between the  $\text{CCl}_4$  treated and control mice in the whole body scans (Figure 3.16), whilst a statistically significant difference ( $p < 0.009$ , ANOVA) was detected in the *ex vivo* liver scans (Figure 3.21).

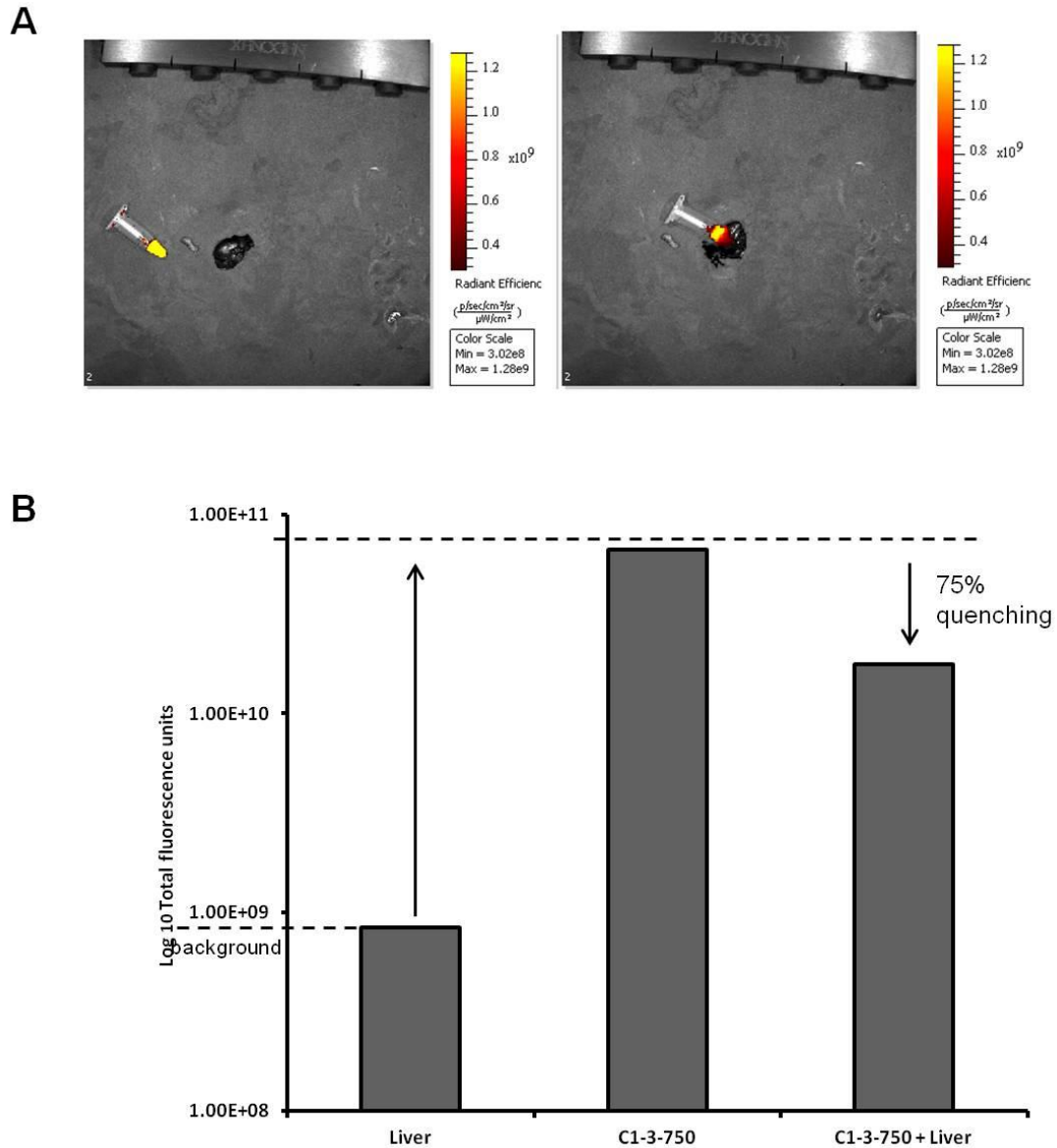


**Figure 3.25 Quenching of C1-3-750 fluorescence by liver tissue.** **A** Single C1-3-750 dose and a single C1-3-750 covered by an *ex vivo* liver scans **B** Total fluorescence calculations for single C1-3-750 dose and liver covered C1-3-750 dose. The arrows highlight the background fluorescence of the liver tissue and the degree of quenching (loss of fluorescence) of the C1-3-750 signal when covered with the mouse liver (n=1).

### 3.7 C1-3-750 functioning in an *in vivo* rat model of liver fibrosis

To build upon the initial findings of the mouse study (Section 3.1.3), an identical study was performed in two Sprague-Dawley rats, where one received CCl<sub>4</sub> twice weekly for four weeks (Table 2.1) whilst a control received olive oil. Upon completion of the CCl<sub>4</sub> dosing regimen, both rats were anaesthetised using isoflurane and had their ventral side shaved. A background fluorescence scan was performed (Figure 3.26), prior to the i.p. injection of 10mg/kg C1-3-750. Whole body fluorescence scans were performed at regular time intervals as shown in figure 3.26. These initial whole body images coupled with the total fluorescence calculations for the upper abdominal/ liver region (Figure 3.27) suggest that the C1-3-750 conjugate was not functioning as seen previously in the mouse model. The signal appears to be originating more from the bladder region than the upper abdominal region, although it was greater in the CCl<sub>4</sub> treated rat than the control rat. The *ex vivo* organ scans (Figure 3.28A) showed little fluorescence from both the control and CCl<sub>4</sub> treated livers, and the total fluorescence calculations (Figure 3.28B) from the *ex vivo* organ scan confirm this.

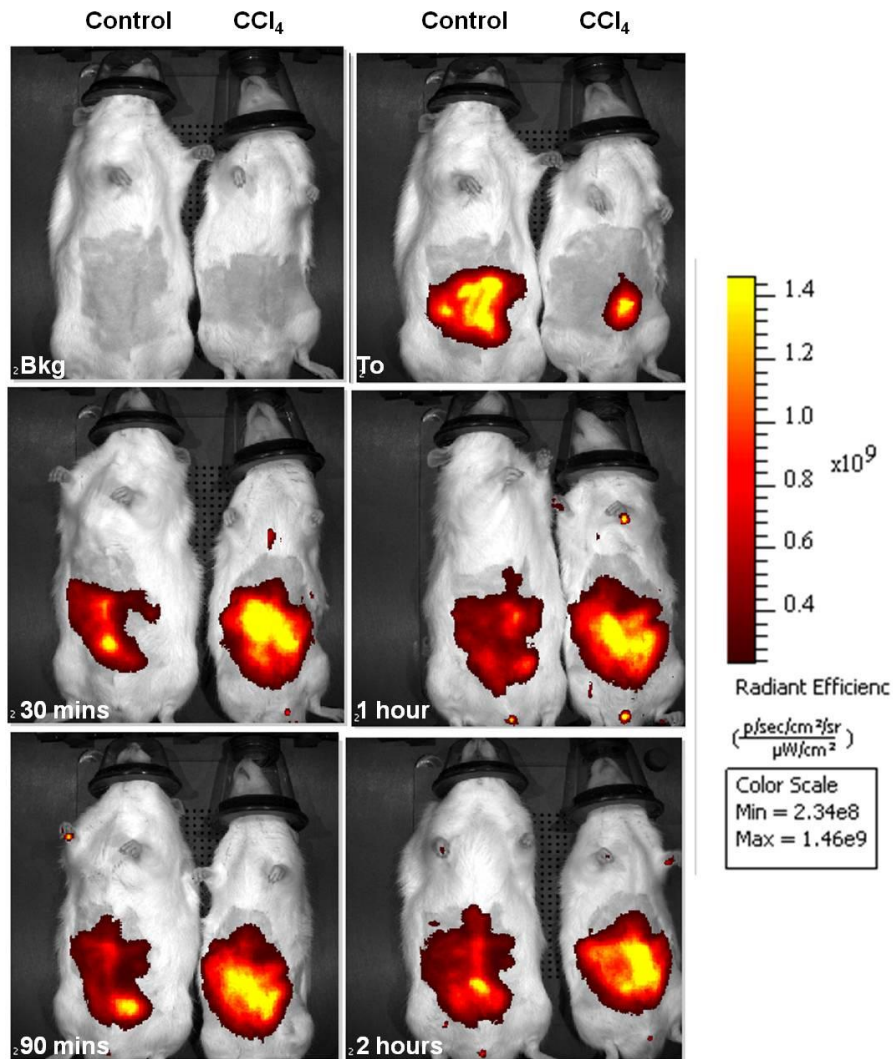


**Figure 3.26 Whole body fluorescent scans over two hour time course for 4 week  $\text{CCl}_4$  treated and control C1-3-750 rats.** Individual fluorescent scans at designated time points from before and after C1-3-750 administration, highlighting the variation in fluorescent signal between the control and fibrotic rats. ( Bkg – background scan prior to C1-3-750 administration,  $T_0$  – Time zero immediately after C1-3-750 administration, and the rest are hourly (h) time points).

There was negligible difference in the fluorescent signal emitted from the control and fibrotic rat livers, suggesting that C1-3-750 was not able to bind to synaptophysin present in the rat liver. The reason for this lack of binding is unknown, but could involve the presence of splice variants of synaptophysin or a variation in post translational modifications between species. This was particularly interesting as C1-3-750 was still binding strongly to the synaptophysin positive Islet cells in the rat pancreas (Figure 3.28). These findings are not totally unexpected, as previous unpublished *in vitro* work

within the laboratory found that C1-3-FITC does not bind rHSCs with the same affinity as it does mHSCs and hHSCs.

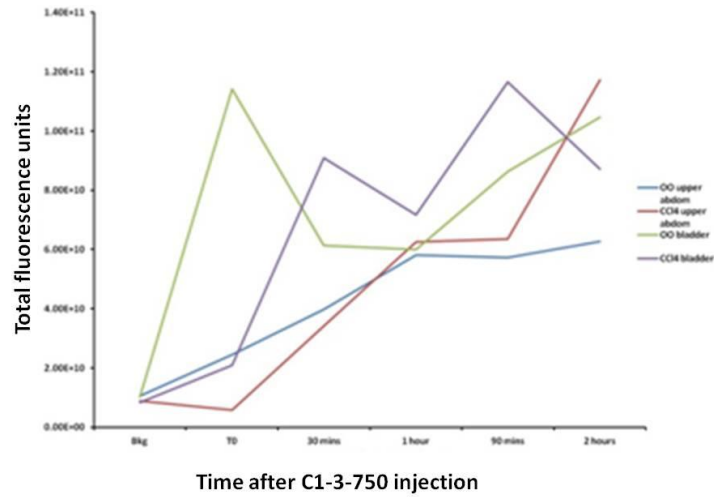


**Figure 3.27 Total fluorescence values calculated for the upper abdominal and bladder regions.** Upper abdominal and bladder total fluorescence values calculated from the ROIs used during the analysis of each rat (n=1).

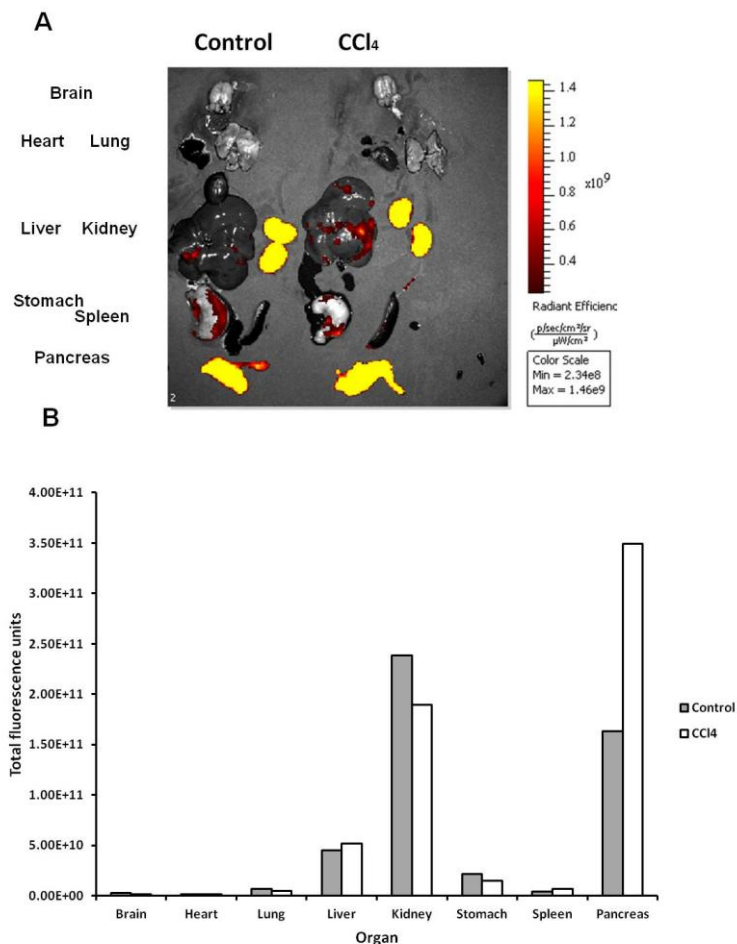


**Figure 3.28 *Ex vivo* organ scan from the 4 week CCl<sub>4</sub> treated and control rat and total fluorescence values calculated for individual organs.** **A** Upon completion of the 2 hour time point the rats were culled by a schedule I method and the major organs excised and imaged using the same settings. **B** Total fluorescence values for individual organs calculated following analysis using ROIs available in the Living Image 4.0 software (n=1).

### 3.8 Chapter discussion

Liver fibrosis is caused by a wide variety of aetiologies (viral infections, autoimmune conditions and genetic disorders) and the current lack of a recognised anti-fibrotic treatment regimen, with the exception of transplantation, means its incidence is only expected to increase [24]. Commonly liver fibrosis is not diagnosed until its later stages (i.e. cirrhosis) [224]; this is primarily due to the compensatory ability of the hepatocytes to replace damaged liver tissue and the overcapacity of the liver. Despite recent advances in our knowledge of the fundamental steps involved in the pathogenesis of liver fibrosis [32, 186], we are still without a recognised anti-fibrotic treatment regimen.

Critical to the development of the novel anti-fibrotic regimes is the accurate diagnosis and quantification of fibrosis during therapeutic testing. At present the percutaneous liver biopsy remains the 'gold standard' and first choice in the diagnosis of liver fibrosis, despite its widely recognised limitations. These include issues of sample size and subsequent sampling errors [122], as well as medical complications associated with the procedure itself [121] and finally problems associated with the scoring of fibrosis/ interobserver variation. Other non invasive techniques, such as serum marker panels and transient elastography have been developed to diagnose liver fibrosis but are only able to successfully diagnose later stages of fibrosis [126, 139].

The C1-3 scAb developed by the Wright group in 2005 [115], was shown to be specific to synaptophysin peptide sequence 2, expressed on the surface of hepatic myofibroblasts. As hepatic myofibroblasts are the major fibrogenic cell type in the liver, the ability of C1-3 to target them is of great use. C1-3 has been previously conjugated with GTX as a potential anti-fibrotic agent inducing the apoptosis of hepatic myofibroblasts and significantly reducing the severity of fibrosis [116]. In this chapter we hypothesised that the number of

hepatic myofibroblasts was an indicator of fibrosis severity and therefore C1-3 when conjugated with a long wavelength fluorophore (XF750) could act as an effective imaging agent to quantify fibrosis severity in an *in vivo* model of liver fibrosis.

Firstly the C1-3 scAb was successfully conjugated with the XF750 fluorescent dye, which was confirmed by SDS-PAGE analysis and its functioning confirmed by an ELISA to its target peptide (synaptophysin peptide sequence 2). However, unlike the controls (C1-3-FITC and C1-3-594) C1-3-750 could not be detected *in vitro* co-localising with  $\alpha$ SMA positive hepatic myofibroblasts. It was most likely this was a result of the large MW of the XF750 dye molecules, despite the fact all the other analyses suggested the C1-3-750 scAb retained C1-3's unique properties. The functioning of the long wavelength filter on the microscope was confirmed as it could detect C1-3-750 when a drop was placed directly under a coverslip. Potentially unbound C1-3 from the conjugation process detected in the MALDI-TOF analysis may have been competing with the C1-3-750 and inhibiting its binding to hepatic myofibroblasts *in vitro*; this was unavoidable as there was no effective viable way to separate the two samples. The size of the peaks also revealed how large the XF750 dye was, with an increase in MW from 37.5 kDa to 40.5 kDa. 3 kDa is a large increase in MW and may sterically hinder C1-3's interaction with its target antigen, whilst in contrast conjugation of FITC only increased the MW by less than 0.5 kDa.

*In vivo* a single CCl<sub>4</sub> and a single control mouse were administered C1-3-750 by i.v. injection (as used in clinical settings) and optically imaged utilising the IVIS. The initial findings from the whole body scans were encouraging, with a clear increase in fluorescent signal from the upper abdominal (liver) region of the fibrotic mouse. This was reinforced by the *ex vivo* organ scan and total fluorescence calculations that confirmed there was an approximate two fold increase in fluorescent signal in the fibrotic mouse liver when compared to the control mouse. These results indicate that C1-3-750 was an effective method to non invasively image liver fibrosis, although a larger study with varying degrees of fibrosis severity was needed to confirm this.

Prior to undertaking this study a second pilot study was performed to determine whether C1-3-750 could be injected via an i.p. injection route without any significant detrimental effects on the imaging outcome. To assess this CCl<sub>4</sub> treated mice were administered C1-3-750 by an i.p. and i.v. injection route together; the initial whole body scans suggested that i.p. injection would be an acceptable route. There was a much higher level of fluorescent signal from the upper abdominal (liver) region of the i.p. mouse when compared to the i.v. mouse on the whole body scans. Another point of interest is the high fluorescent signal emitted from the tail of the i.v. injected mouse, indicating that the C1-3-750 dose was retained in the tail sheath. Therefore the exact amount of the C1-3-750 dose administered cannot be known and could vary significantly between individual animals influencing the imaging outcome. However, the *ex vivo* organ scans revealed that there was a greater fluorescent signal from the liver of the i.v. mouse than the i.p. mouse, suggesting dosing via this route was more effective at reaching the liver. Potentially this could be due to the increased supply of venous blood to the liver from the portal vein, coupled with the slower distribution from the i.p. injection route [218]. There was also a strong fluorescent signal emitted from the liver of the i.p. mouse when compared to the other major organs indicating that this was also a viable route to dose C1-3-750. Due to the high numbers of mice and the need for repeated C1-3-750 dosing of the same mice, an i.p. injection route was chosen for the chronic study with varying degrees of fibrosis severity (12, 8 and 4 week CCl<sub>4</sub> dosing). This decision was predominantly due to the difficulty associated with consistently performing effective i.v. injections (ensuring identical dosing) as there was the need for repeated injections to the same mice (issues with scarring via the i.v. route). Also the lack of detection of upper abdominal fluorescence in the liver region of i.v. pilot mouse in the whole body images suggests C1-3-750 administration by this route does not generate a signal that can be detected non invasively as desired unlike following i.p. injection.

The whole body scans from the chronic study revealed the major limitation of employing an i.p. injection route, which was not encountered in the preliminary pilot studies. There was no difference in the fluorescent signal

between the upper abdominal (liver) and bladder regions of the CCl<sub>4</sub> and olive oil groups; this was confirmed by the total fluorescence calculations. This was unavoidable especially when during the injection route pilot study; the i.v. injected mouse exhibited very little fluorescent signal until the liver was excised from the body, therefore this injection route could not be used non invasively. In hindsight it was a major oversight when performing the injection route pilot to not administer C1-3-750 to control mice. Alternatively taking into account the short biological half life of scAbs [225] the severity of the C1-3-750 pooling/ signal from the i.p. cavity may have dropped significantly after a longer time period (e.g. 24 or 48 hours) to allow the diagnosis of the liver specific signals and determine any difference between the fibrotic and control animals.

The *ex vivo* organ scans show that there was a statistically significant increase in liver fluorescence of all the CCl<sub>4</sub> treatment groups when compared to olive oil and non inject controls ( $p < 0.009$ , ANOVA). These findings were reinforced by the IHC analysis, in particular the number of  $\alpha$ SMA positive myofibroblasts and sirius red positive collagen scars being significantly higher in all CCl<sub>4</sub> treatment groups when compared to the olive oil and non inject controls ( $p < 0.0001$ , ANOVA). Another point of interest is the increase in fluorescence of the olive oil livers, when compared against the non inject controls. This increase may be due to the expression of synaptophysin on the surface of quiescent HSCs that are also present in the liver as well as the hepatic myofibroblasts (activated HSCs) [108].

The potential of C1-3 as a diagnostic imaging agent for liver fibrosis is clear, highlighted by the significant increase in liver fluorescence between the excised livers of the CCl<sub>4</sub> treated and olive oil control groups. However there are major limitations to its use that need to be addressed, primarily the route of C1-3-750 injection. The findings from these pilot studies suggest that administration of C1-3-750 by i.p. injection results in pooling of the scAb in the peritoneal cavity. When coupled with C1-3's short biological half-life this makes it impossible to diagnose fibrosis severity non invasively, which was the intended benefit of this novel technique. Secondly the deep tissue location of the liver and high level of fluorescence quenching (75% of the signal) by

the liver tissue result in a high loss of signal, illustrated when a free C1-3-750 dose was covered by an uninjected mouse liver.

The lack of functioning of C1-3-750 in a rat model of CCl<sub>4</sub> induced liver fibrosis whilst still binding to the rat pancreas as seen in the mouse model indicates there is some variation in synaptophysin expression between species, which need to be investigated further. These pancreas findings suggest that C1-3-750 may be of benefit in measuring Islet cell numbers in pancreatic conditions such as pancreatitis, and the relative Islet mass in conditions including type II diabetes [226]. Although the significance of the pancreas signal upon the level detected in whole body scans is unclear due to the pooling of the C1-3-750 dose in the i.p. cavity. If a repeat study is performed in the future employing an i.v. injection route it is possible to generate a 3D composite image of the mice using the IVIS software, which may reveal the contribution of the pancreas fluorescence on that detected in the upper abdominal (liver) region of the whole body scans.

C1-3-750 provides proof of concept findings that the C1-3 scAb can be used to target hepatic myofibroblasts *in vivo* and that their number is an indicator of fibrosis severity. Although in this instance C1-3 could not determine fibrosis severity non invasively, predominantly due to the issues with the injection route of C1-3-750 and the high quenching of the fluorescent signal by the liver tissue. The combination of C1-3 with a high power technique such as PET scanning is a future route to investigate. The conjugation of C1-3 with a radioisotope, such as <sup>18</sup>F-SFB and PET scanning will remove the issues of tissue penetration and signal loss associated with optical imaging. PET centres on the beta decay of the radioisotope, generating a positron which upon collision with an electron releases two gamma rays that can be detected by a scanner and reconstructed into a 3D image [227].

**Chapter 4.0 - C1-3 binding to synaptophysin and its'  
expression on hepatic myofibroblasts**

## 4.1 Introduction

The expression of synaptophysin by quiescent HSCs and activated hepatic myofibroblasts was first reported by Cassiman *et al* [108], its use as a target for anti-fibrotics was pioneered within this research laboratory with the development of the C1-3 scAb (Section 1.4). The results in chapter 3 highlight C1-3's ability to bind to fibrotic livers *in vivo* when conjugated with a long wavelength fluorophore. There was a statistically significant increase in the *ex vivo* liver fluorescence of fibrotic mice when compared to the control mice ( $p < 0.009$ , analysed using an ANOVA). Interestingly there was also an increase in fluorescent signal emitted from the non-fibrotic mice livers when administered C1-3-750, supporting Cassiman's initial work that synaptophysin is also expressed by quiescent HSCs. The presence of quiescent HSCs in the non-fibrotic mice livers explaining this signal detected.

There was also a disparity in C1-3's functioning between species highlighted by its lack of functioning in a rat model of liver fibrosis (Section 3.7), in contrast to the positive findings when employing a mouse model of liver fibrosis (Sections 3.3 - 3.6). Surprisingly C1-3 was still able to bind to the Islet cells in the rat pancreas with high affinity, suggesting there was also a variation in synaptophysin expression between cells from different organs.

Since the binding of synaptophysin in cells had not been formally tested, this was examined. Secondly ICC analysis was performed to investigate C1-3's binding to quiescent as well as activated HSCs *in vitro* and to uncover more about the variation in synaptophysin expression of both quiescent and activated HSCs.

## 4.2 Confirmation of C1-3's binding to synaptophysin

Following successful transfection of Cos7 cells with plasmids encoding either mouse or human synaptophysin under the control of tetracycline, C1-3-594 and a commercially available C-terminal synaptophysin specific primary antibody (Dako, see Table 2.5) were individually added to the culture media,

as outlined in the ICC protocol (Section 2.8.6) prior to fluorescent microscopy. The fluorescent microscopy images shown in figure 4.1 firstly highlight the successful transfection of the synaptophysin plasmids into the Cos7 cells by the binding of the synaptophysin specific antibody. Secondly the co-localisation of C1-3-594 only to the Cos7 cells transfected with the synaptophysin plasmids confirm its affinity for synaptophysin, their target present on the surface of hepatic myofibroblasts.

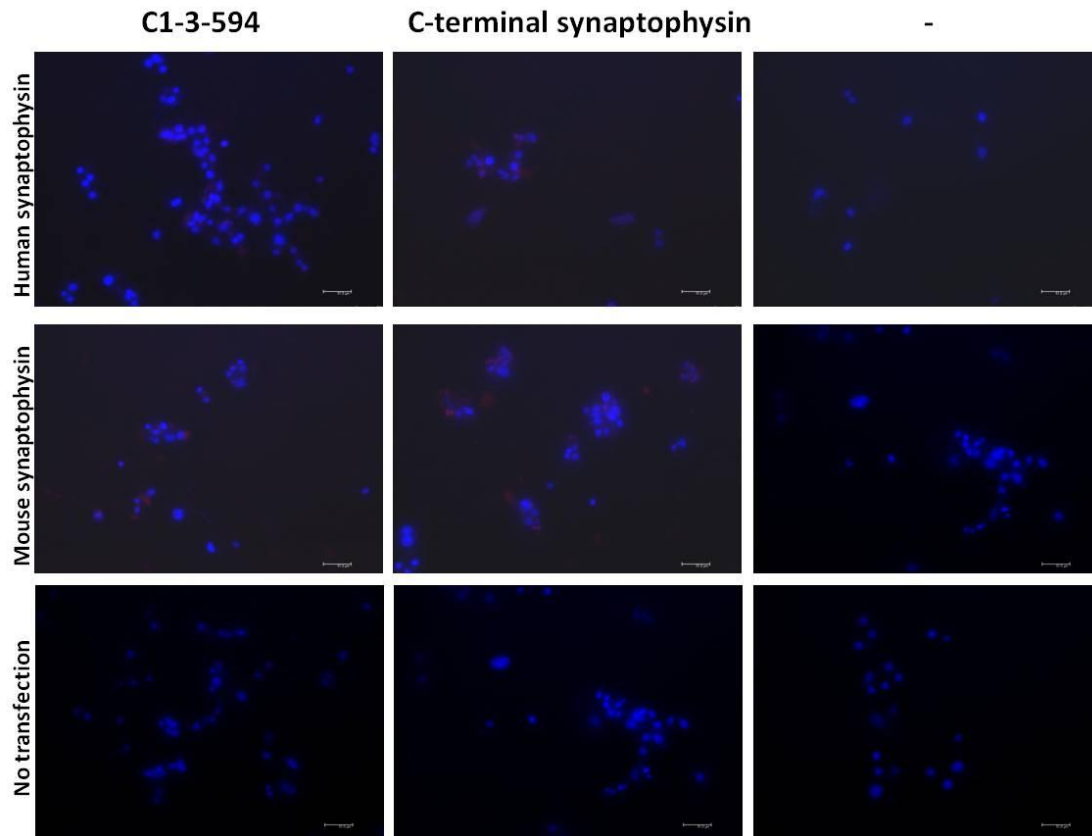


**Figure 4.1 C1-3-594 and synaptophysin ICC staining of transfected Cos7 cells.** Cos7 cells grown in chamber slides (Merck) were transfected with either mouse or human synaptophysin plasmids overnight at 37 °C and 5% CO<sub>2</sub>. C1-3-594 or a synaptophysin primary antibody was added to the cells for 2 hours at 37 °C and 5% CO<sub>2</sub> before subsequent 1 x PBS washing and addition of complementary fluorescent secondary antibody. The nuclei were visualised by a 10 minute DAPI incubation and subsequent fluorescent microscopy. Images shown are at x40 magnification.

Western blotting analysis of protein samples isolated from these cell types (using mouse brain protein as a positive control) only detected the presence of synaptophysin protein in the transfected Cos7 protein samples (Figure 4.2). These findings prove that C1-3 specifically targets synaptophysin and the binding seen was not a property of the Cos7 cells.

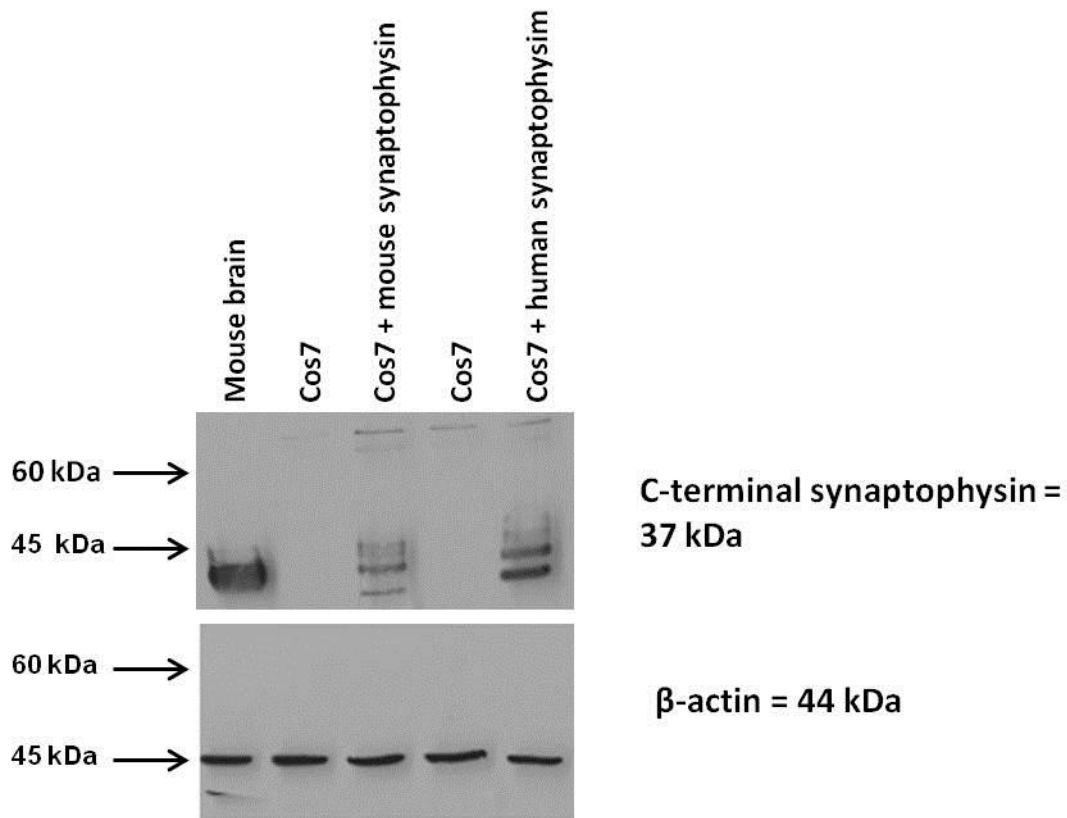


**Figure 4.2 Western blotting analysis of transfected Cos7 synaptophysin expression.** Protein samples were isolated from the transfected cells and diluted to  $2\mu\text{g}/\mu\text{l}$  in loading buffer,  $20\mu\text{g}$  protein per sample was loaded onto a 9% acrylamide SDS gel. Following electrophoresis the protein was transferred onto a nitrocellulose membrane, blocked with 3% marvel protein prior to detection of C-terminal synaptophysin and  $\beta$ -actin protein levels.

### 4.3 Variation in synaptophysin expression between species

#### 4.3.1 Whole tissue synaptophysin expression

To investigate the variation in synaptophysin expression between individual species further, three sets of primers were designed to conserved regions of synaptophysin cDNA (human, mouse and rat sequences) (Figure 4.3 and Table 2.4).

```

rSYNAP      -----GCATTGCTGCTGCTGCTGGCAGACAATGAGCGTGGTGAATCAGCTGGTGGC 53
mSYNAP      -----ATGCTGATGCTGCTGCTGGCAGACATGGAOCGTGGTGAATCAGCTGGTGGC 51
hSYNAP      GCOCCCTGCATTGCTGATGCTGCTGCTGGCGACATGGACGTGGTGAATCAGCTGGTGGC 60
          *****

rSYNAP      TGGGGTTCAGTTCOCGGTGGTCAAGGAGCCCTTGGCTTCGTGAAGGTGCTGCAGTGGGT 113
mSYNAP      TGGGGTTCAGTTCOCGGTGGTCAAGGAGCCCTTGGCTTCGTGAAGGTGCTGCAGTGGGT 111
hSYNAP      TGGGGTTCAGTTCOCGGTGGTCAAGGAGCCCTTGGCTTCGTGAAGGTGCTGCAGTGGGT 120
          *****

rSYNAP      CTTTGCCATCTTCGCCTTTGCTACGTGTGGCAGTACACCGGGAGCTTCGGCTGAGCGT 173
mSYNAP      CTTTGCCATCTTCGCCTTTGCTACGTGTGGCAGTACACCGGGAGCTTCGGCTGAGCGT 171
hSYNAP      CTTTGCCATCTTCGCCTTTGCTACGTGTGGCAGTACAGTGGGAGCTTCAGCTGAGCGT 180
          ***

rSYNAP      GGAGTGTGCCAACAAAGACGGAGAGTGCCTCAACATCGAAGTGAATTCAGTACCCCTT 233
mSYNAP      GGAGTGTGCCAACAAAGACGGAGAGTGCCTCAACATCGAAGTGAATTCAGTACCCATT 231
hSYNAP      GGATTGTGCCAACAAAGACGGAGAGTGAACCTCAGACTCGAGGTGCAGTTCAGTACCCCTT 240
          ***

          peptide 2 encoding region
rSYNAP      CAGGCTGCACCAAGTGTACTTTGATGCACCCTCCTGCCTCAAAGGGGGACTACCAAGAT 293
mSYNAP      CAGGCTGCACCAAGTGTACTTTGATGCACCCTCCTGCCTTAAAGGGGGACTACCAAGAT 291
hSYNAP      CAGGCTGCACCAAGTGTACTTTGATGCACCCTCCTGCCT---GAGGGGGACCAACCAAGT 297
          *****

rSYNAP      CTTCCGTGGTGGGACTACTCCTCGTCGGTGAATTCCTTGTACACGTGGCTGTGTTTGC 353
mSYNAP      CTTCCGTAGTGGTACTACTCCTCCTCGCTGAATTCCTTGTACACGTGGCTGTGTTTGC 351
hSYNAP      CTTCTTAGTGGGACTACTCCTCGTCAGCGAATTCCTTGTACACGTGGCGTGTGTTGC 357
          *****

rSYNAP      TTCCCTACTCCATGGGGCCCTGGCCACCTACATCTTCCGCAAGAACAGTACCGAGA 413
mSYNAP      TTCCCTACTCCATGGGGCCCTGGCCACCTACATCTTCCGCAAGAACAGTACCGAGA 411
hSYNAP      CTTCCCTACTCCATGGGGCCCTGGCCACCTACATCTTCCGCAAGAACAGTACCGAGA 417
          *****

rSYNAP      GAACAAACAAAGGGCCATGATGGACTTTCGGCTACAGCGTGTTCGCTTTCATGTGGCT 473
mSYNAP      GAACAAACAAAGGGCCATGATGGACTTTCGGCTACAGCGTGTTCGCTTTCATGTGGCT 471
hSYNAP      GAATAACAAAGGGCCATGCTGACTTTCGGCCACGGCTGTGTTGCTTTCATGTGGCT 477
          ***

rSYNAP      AGTTAGTTCATCAGCCTGGCCAAAGGCTGTCCGATGTGAAGATGGCCACGGACCCAGA 533
mSYNAP      AGTTAGTTCATCAGCCTGGCCAAAGGCTGTCCGATGTGAAGATGGCCACGGACCCAGA 531
hSYNAP      AGTTAGTTCATCAGCCTGGCCAAAGGCTGTCCGATGTGAAGATGGCCACGGACCCAGA 537
          *****

rSYNAP      GAACATTATCAAGGAGATGCCATGTGCCCCAGACAGGAACACATGCAAGGAAGTGA 593
mSYNAP      GAACATTATCAAGGAGATGCCATGTGCCCCAGACAGGAACACATGCAAGGAAGTGA 591
hSYNAP      GAACATTATCAAGGAGATGCCATGTGCCCCAGACAGGAACACATGCAAGGAAGTGA 597
          *****

rSYNAP      GGACCCGTGACTCAGGACTCAACACCTCAGTGGTGTGGCTTCCGAACTGGTGTCT 653
mSYNAP      GGACCCGTGACTCAGGACTCAACACCTCAGTGGTGTGGCTTCCGAACTGGTGTCT 651
hSYNAP      AGACCCGTGACTCAGGACTCAACACCTCAGTGGTGTGGCTTCCGAACTGGTGTCT 657
          *****

rSYNAP      CTGGGTTGGCAACTTATGGTTCGTGTTCAAGGAGACAGGCTGGCCGCCCCATTCATGCG 713
mSYNAP      CTGGGTTGGCAACTTATGGTTCGTGTTCAAGGAGACAGGCTGGCCGCCCCATTCATGCG 711
hSYNAP      CTGGGTTGGCAACTTATGGTTCGTGTTTAAGGAGACAGGCTGGCCGCCCCATTCATGCG 717
          *****

rSYNAP      CGCACCTCCAGGCGCCCGGAAAAGCAACAGCACCTGGCGATGCCTACGGCGATGCGGG 773
mSYNAP      CGCACCTCCAGGCGCCCGGAAAAGCAACAGCACCTGGCGATGCCTACGGCGATGCGGG 771
hSYNAP      CGCGCTCCCGGCGCCCGGAAAAGCAACAGCACCTGGCGATGCCTACGGCGATGCGGG 777
          ***

rSYNAP      CTACGGGCAGGGCCCGGAGGCTATGGGCCCAAGACTCCTACGGGCTCAGGGTGGTTA 833
mSYNAP      CTATGGGCAGGGCCCGGAGGCTATGGGCCCAAGACTCCTACGGGCTCAGGGTGGTTA 831
hSYNAP      CTACGGGCAGGGCCCGGAGGCTACGGGCCCAAGACTCCTACGGGCTCAGGGGCGSCTA 837
          ***

rSYNAP      TCAACCCGATTACGGGAGCCAGCCAGCGG---TGGGGTGGCTACGGGCTCAGGGCGA 890
mSYNAP      TCAACCCGATTACGGGAGCCAGCCAGCGGCGGTGGCGTGGCTACGGGCTCAGGGCGA 891
hSYNAP      CCAGCCTGACTATGGTCAACCGCCAGCGGCGGTGGCGTGGCTACGGGCTCAGGGCGA 897
          *****

rSYNAP      CTATGGGCAGCAAGGCTATGGCCAAAGGGTGGCCACCTCCTCTCCAAATCAGATGTA 950
mSYNAP      CTATGGGCAGCAAGGCTACGGCCCAAGGGTGGCCACCTCCTCTCCAAATCAGATGTA 951
hSYNAP      CTATGGGCAGCAAGGCTACGGCCCAAGGGTGGCCACCTCCTCTCCAAATCAGATGTA 957
          *****

rSYNAP      ATCTGGTCAAGTGAAGTCCATGAAGATCCACGGGTGGGCAAGAGCTCAAAGAGAAGCCCT 1010
mSYNAP      ATCTGGTCAAGTGAAGTCCATGAAGATCCACGGGTGGGCAAGAGCTCAAAGAGAAGCCCT 1011
hSYNAP      GCTGGTCAAGTGAAGTCCATGAAGATCCACGGGTGGGCAAGAGCTCAAAGAGAAGCCCT 1015
          *****

```

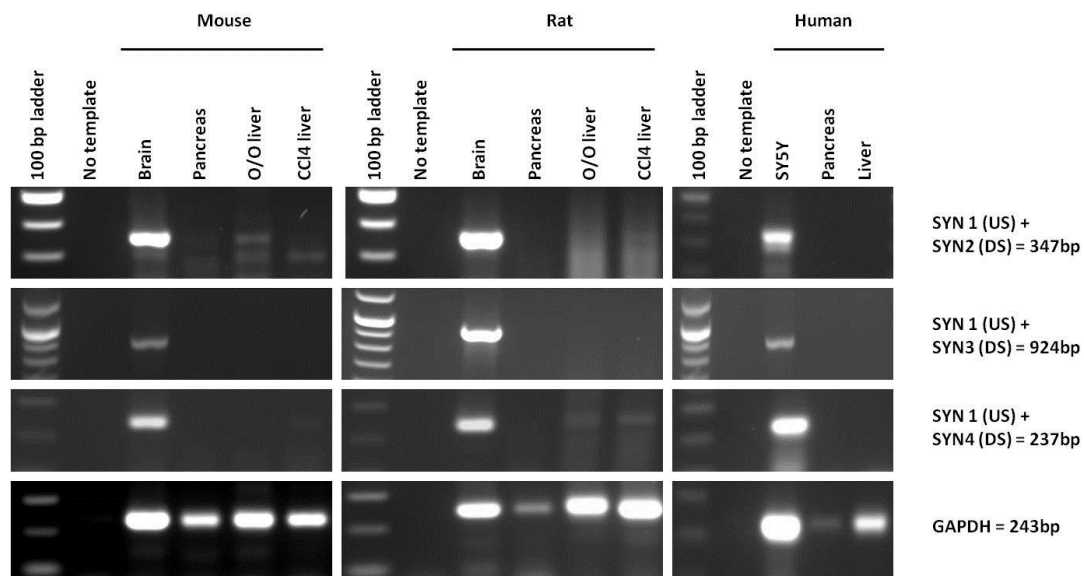
**Figure 4.3 Alignment of mouse, rat and human synaptophysin DNA sequences and synaptophysin primer locations.** Synaptophysin DNA sequences were obtained from the NCBI database ([www.ncbi.nlm.nih.gov](http://www.ncbi.nlm.nih.gov)) and were aligned using ClustalW software (found on <http://www.ebi.ac.uk/>). Primers (shown by the underlined coloured sequences) were subsequently designed using the Primer-BLAST programme from the NCBI database to conserved regions present in all species.

As discussed in section 3.8 when utilising C1-3-750 as an in vivo imaging agent there was a variation in C1-3-750's ability to bind to synaptophysin present in both the rat and mouse liver, with minimal efficacy seen in a rat fibrotic liver (Figure 3.28).

Total RNA was isolated from the liver, pancreas and brain tissue of rats, mice and human (no human brain sample was available, so the SY5Y neuroblastoma cell line was used) and cDNA generated. Identical PCRs were

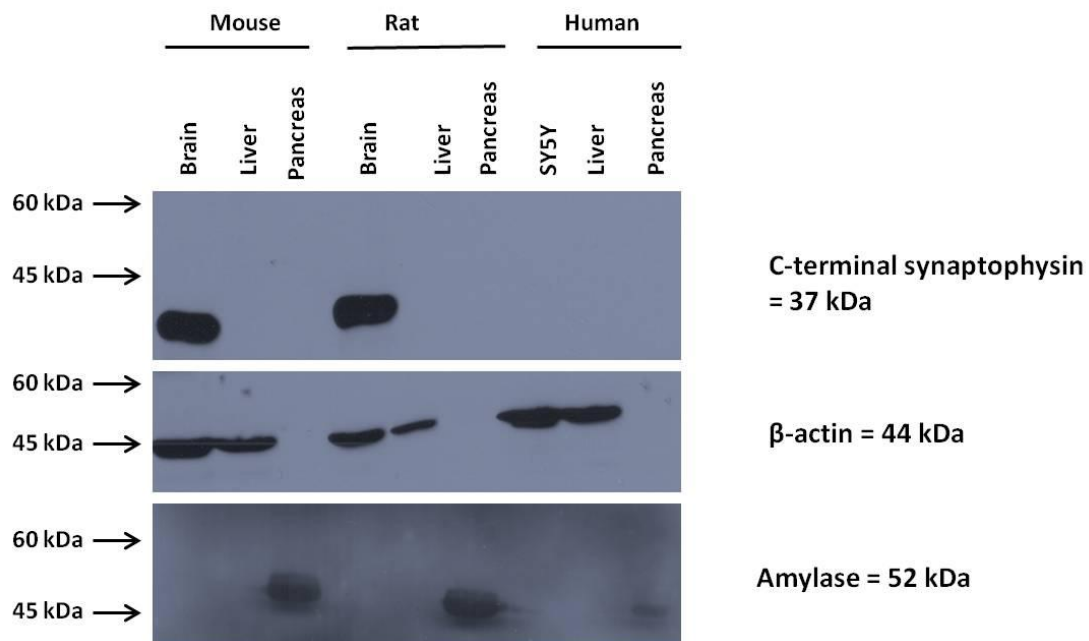
carried out using the three separate synaptophysin primer sets (1 upstream primer and 3 downstream primers (Table 2.4)) to detect the presence of synaptophysin in each tissue sample.

Figure 4.4 shows that both mouse, rat brain and the SY5Y cell line express high levels of synaptophysin with all primer sets, however no synaptophysin could be detected in any tissue samples using the SYN1 and SYN3 primer set (which amplifies the whole translated cDNA sequence). When using SYN1 and SYN2 a weak band of the correct size (347bp) was detected in the mouse olive oil liver but not in the mouse CCl<sub>4</sub> liver. There are no visible bands in the rat liver samples, however the opposite is found when using the SYN1 and SYN4 primer set (DS4 is part of the synaptophysin peptide 2 cDNA sequence, Figure 1.6) as there were bands of the correct size in both the rat fibrotic and control liver samples, whilst there was only a very weak band in the fibrotic liver from the mouse samples. GAPDH was included as a housekeeping gene to confirm the integrity of the cDNA. Synaptophysin was only detected in the SY5Y positive control and could not be detected in any of the human tissue samples or the pancreas in all species.



**Figure 4.4 Synaptophysin expression of mouse, rat and human whole tissue samples.** Total RNA was isolated from tissue samples using Trizol and quantified prior to reverse transcription to produce 40ng/ $\mu$ l cDNA. 40ng was added to the PCR mastermix (see section 2.6.6). Following completion of the PCR cycle the products were run out on a 1.5% agarose gel (containing EtBr) to separate them according to their size and visualised by UV light exposure.

Figure 4.5 is an identical Western blot analysis on all tissue samples using a C-terminal synaptophysin specific primary antibody. Synaptophysin protein was only detected in the mouse and rat brain samples, suggesting that the level of synaptophysin protein expression was not high enough to be detected in any of the liver and pancreas samples by this method unlike the earlier PCR (Figure 4.4).  $\beta$ -actin is an internal housekeeping gene like GAPDH in the PCRs and serves as a loading control for Western blots, although its expression is minimal in the pancreas samples. Therefore the level of amylase was also detected as it is a pancreatic marker, simply confirming the presence of protein in the pancreas samples.



**Figure 4.5 Western blotting analysis of mouse, rat and human whole tissue samples synaptophysin protein expression.** Protein samples were isolated from the tissue samples and diluted to  $2\mu\text{g}/\mu\text{l}$  in loading buffer,  $20\mu\text{g}$  protein per sample was loaded onto a 9% acrylamide SDS gel. Following electrophoresis the protein was transferred onto a nitrocellulose membrane, blocked with 3% marvel milk protein prior to detection of C-terminal synaptophysin, amylase and  $\beta$ -actin protein levels.

Dual ICC analysis using  $\alpha$ SMA and synaptophysin specific primary antibodies was also performed on fixed tissue samples to confirm the variation in synaptophysin expression between the organs of various species (Figure 4.6).  $\alpha$ SMA was probed to confirm the presence of hepatic myofibroblasts in the  $\text{CCl}_4$  damaged rodent liver samples. Once again no synaptophysin was detected in any of the liver samples irrespective of the presence of hepatic

myofibroblasts. The presence of synaptophysin positive Islet cells in the pancreas samples firstly confirm the functioning of the synaptophysin antibody, although again only low levels of synaptophysin could be detected. Secondly it highlights the variation in synaptophysin expression between the organ samples.

The variation in synaptophysin expression between the liver samples detected when utilising PCR, Western blotting and ICC analysis techniques suggest that synaptophysin may potentially be modified post-transcriptionally in the liver (e.g. glycosylation) preventing successful antibody detection by these methods.

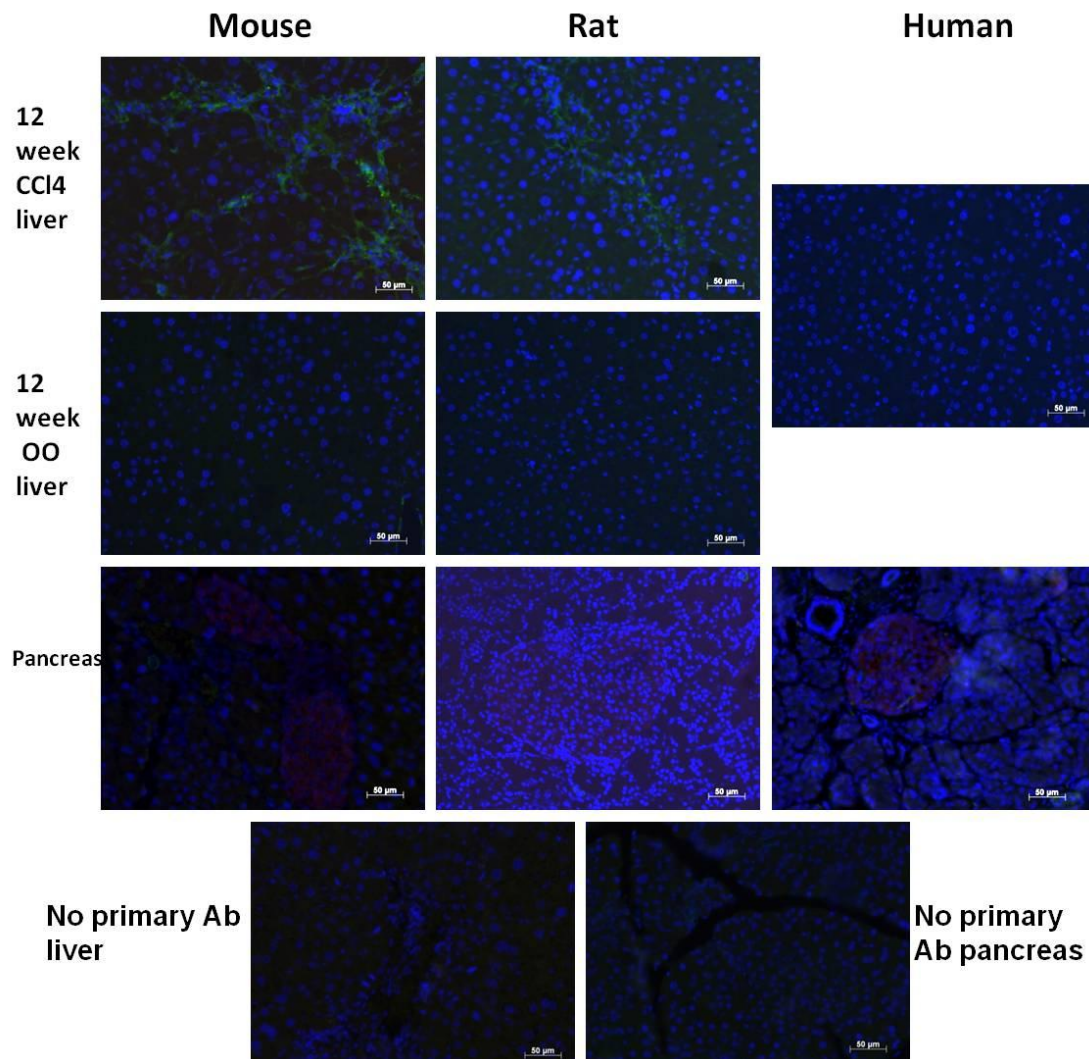


**Figure 4.6 C1-3-594,  $\alpha$ SMA and synaptophysin ICC staining of individual mouse, rat and human whole tissue samples.** Tissue samples were fixed in 10% formalin prior to paraffin embedding, 5 $\mu$ M sections were cut from each animal. Sections were dewaxed prior to serum blocking and incubation for

an hour at room temperature with either C1-3-594, or the  $\alpha$ SMA and synaptophysin primary antibodies, after PBS washing and addition of the complementary fluorescent secondary antibody. The sections were counterstained with DAPI prior to mounting and analysis with a Zeiss fluorescent microscope. (All images shown are x20 magnification).

### 4.3.2 HSC synaptophysin expression

The level of synaptophysin was also examined in cDNA isolated from activated mouse, rat and human HSCs utilising the same synaptophysin primer sets. Figure 4.7 highlights that synaptophysin can be detected in all HSC samples, with every primer set. Although the levels of synaptophysin detected are very low in comparison to the level detected in the mouse brain cDNA sample (positive control).

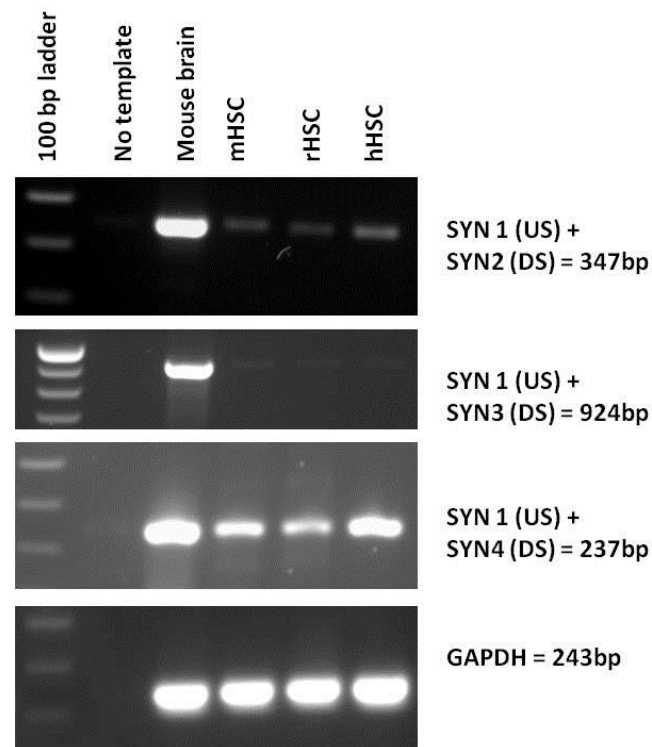


**Figure 4.7 Synaptophysin expression of mouse, rat and human HSCs.** Total RNA was isolated from cultured HSCs using Trizol and quantified prior to reverse transcription to produce 40ng/ $\mu$ l cDNA. 40ng was added to the PCR mastermix (see section 2.6.6). Following completion of the PCR cycle the products were run out on a 1.5% agarose gel (containing ethidium bromide) to separate them according to their size and visualised by UV light exposure.

Figure 4.8 is an identical Western blot on HSC protein samples using the same C-terminal synaptophysin primary antibody (Table 2.5). Once again full length synaptophysin protein was only detected in the mouse brain sample, suggesting that the level of synaptophysin protein expression was not high enough to be detected using this method. These data reaffirms our earlier observation (found when analysing the tissue samples) that there was a post-transcriptional modification of synaptophysin preventing its detection by this method.

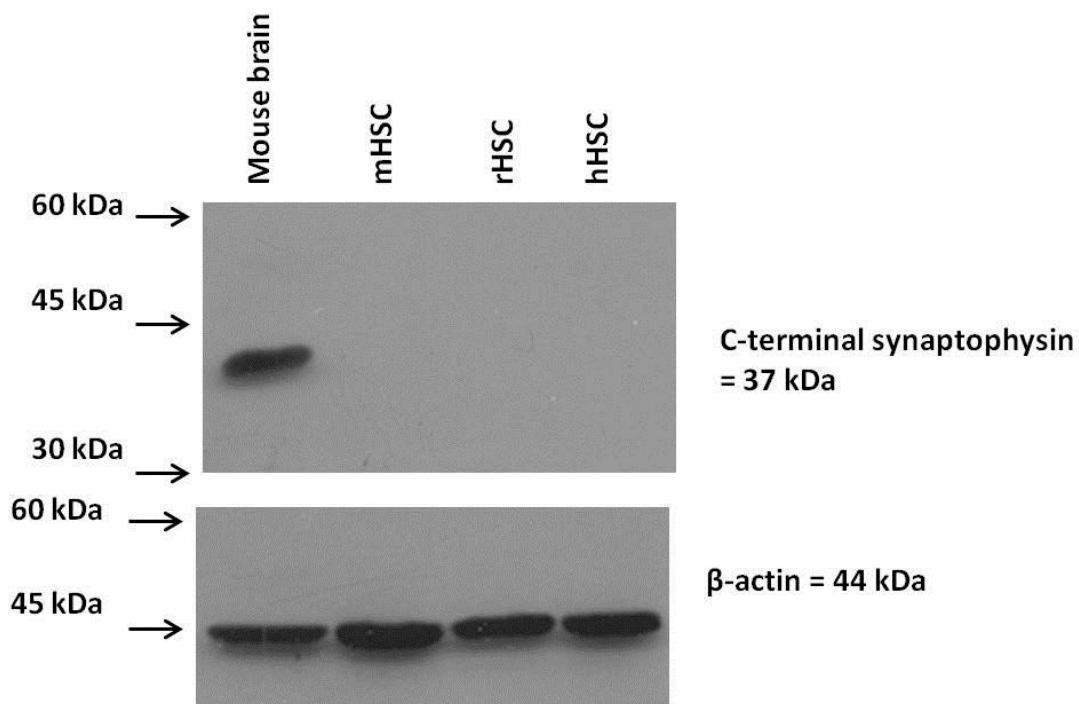


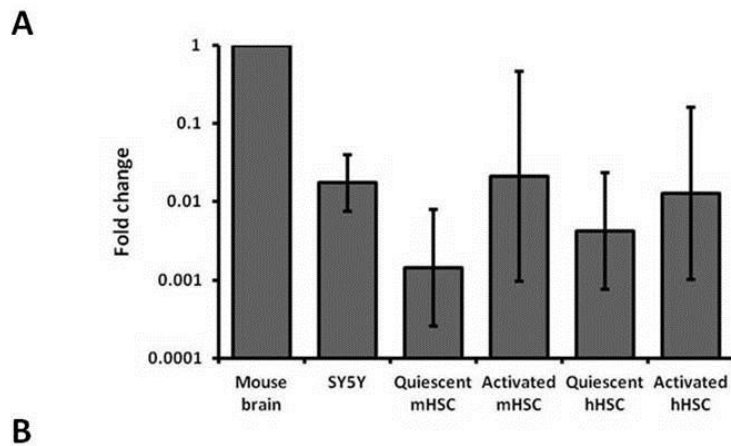
**Figure 4.8 Western blotting analysis of mouse, rat and human HSCs synaptophysin protein expression.** Protein samples were isolated from HSCs and diluted to  $2\mu\text{g}/\mu\text{l}$  in loading buffer,  $20\mu\text{g}$  protein per sample was loaded onto a 9% acrylamide SDS gel. Following electrophoresis the protein was transferred onto a nitrocellulose membrane, blocked with 3% marvel protein prior to detection of C-terminal synaptophysin and  $\beta$ -actin protein levels.

#### 4.4 Variation in relative synaptophysin expression between quiescent and activated HSCs

As highlighted in chapter 3, there was increased liver fluorescence in the control mice when compared to the non inject controls, suggesting that C1-3-750 targets quiescent HSCs as well as the intended hepatic myofibroblasts (activated HSCs) present in the  $\text{CCl}_4$  treated mice. Despite its use previously,

little work has been carried out to determine the relative synaptophysin expression of both quiescent and activated HSCs, and C1-3's affinity to both.

qRT-PCR utilising SYBR Green and the SYN1 (US) and SYN4 (DS) primer set was performed to determine synaptophysin expression in both mice and human quiescent and activated HSCs. All data was calculated relative to the endogenous control 18s and the fold change calculated against the level of mouse brain synaptophysin expression. Figure 4.9A shows that both (mouse and human) quiescent and activated HSCs express synaptophysin at a level similar to that detected in the neuroblastoma SY5Y cell line. Activated HSCs express more synaptophysin than quiescent HSCs although both were approximately 100 fold lower than that detected in the mouse brain sample. The average  $\Delta C_T$  values calculated for each cell type are shown in figure 4.9B, highlighting the lower  $\Delta C_T$  value in comparison to the mouse brain sample. Secondly it shows the similarity in  $\Delta C_T$  between the various HSC cell types and SY5Y cell line.



Average $\Delta C_T$ value						
Sample/ cell type	Mouse brain	SY5Y	quiescent mHSC	mHSC	quiescent hHSC	hHSC
1	16.18	21.18	22.40	18.10	20.81	15.65
2	11.42	18.11	28.63	23.82	19.87	12.96
3	12.41	18.80	27.53	18.05	18.28	18.98
4			24.47	26.81	15.99	11.48
5			25.09	17.27	15.95	19.33
6				26.46	21.74	17.31
7					21.53	21.99
8						16.78
9						22.99
10						19.57
<b>Average <math>\Delta C_T</math></b>	<b>13.34</b>	<b>19.36</b>	<b>25.63</b>	<b>21.75</b>	<b>19.17</b>	<b>17.70</b>

**Figure 4.9 A Quantitative real-time PCR analysis of quiescent and activated HSCs synaptophysin expression. B Average cT values for each cell type.** Total RNA was isolated from quiescent HSCs (48 hours after isolation) and activated HSCs (after one passage) using Trizol and quantified prior to reverse transcription to produce 40ng/μl cDNA. 10ng was added to the PCR mastermix in triplicate (see section 2.6.9). Quantitation of synaptophysin gene expression was calculated relative to the endogenous control 18s; the fold change was calculated against the mouse brain cDNA (high synaptophysin expression). (Data plotted is the mean and SD, minimum n=3 for each cell type). **B** Average  $\Delta C_T$  values for each cell type following subtraction of equivalent 18s cT value.

To confirm C1-3's affinity for both cell types C1-3-594 was added to both quiescent (48 hours after isolation) and activated (after one passage) mouse and human HSCs, antibodies specific to both synaptophysin and  $\alpha$ SMA were also detected (Table 2.5). Figure 4.10 is a typical image from both the ICC stained mouse and human quiescent HSCs, the binding of C1-3-594 (red) to some of the DAPI stained quiescent HSCs is apparent. As expected no  $\alpha$ SMA could be detected whilst the cells were still in their quiescent state and synaptophysin was also undetectable.

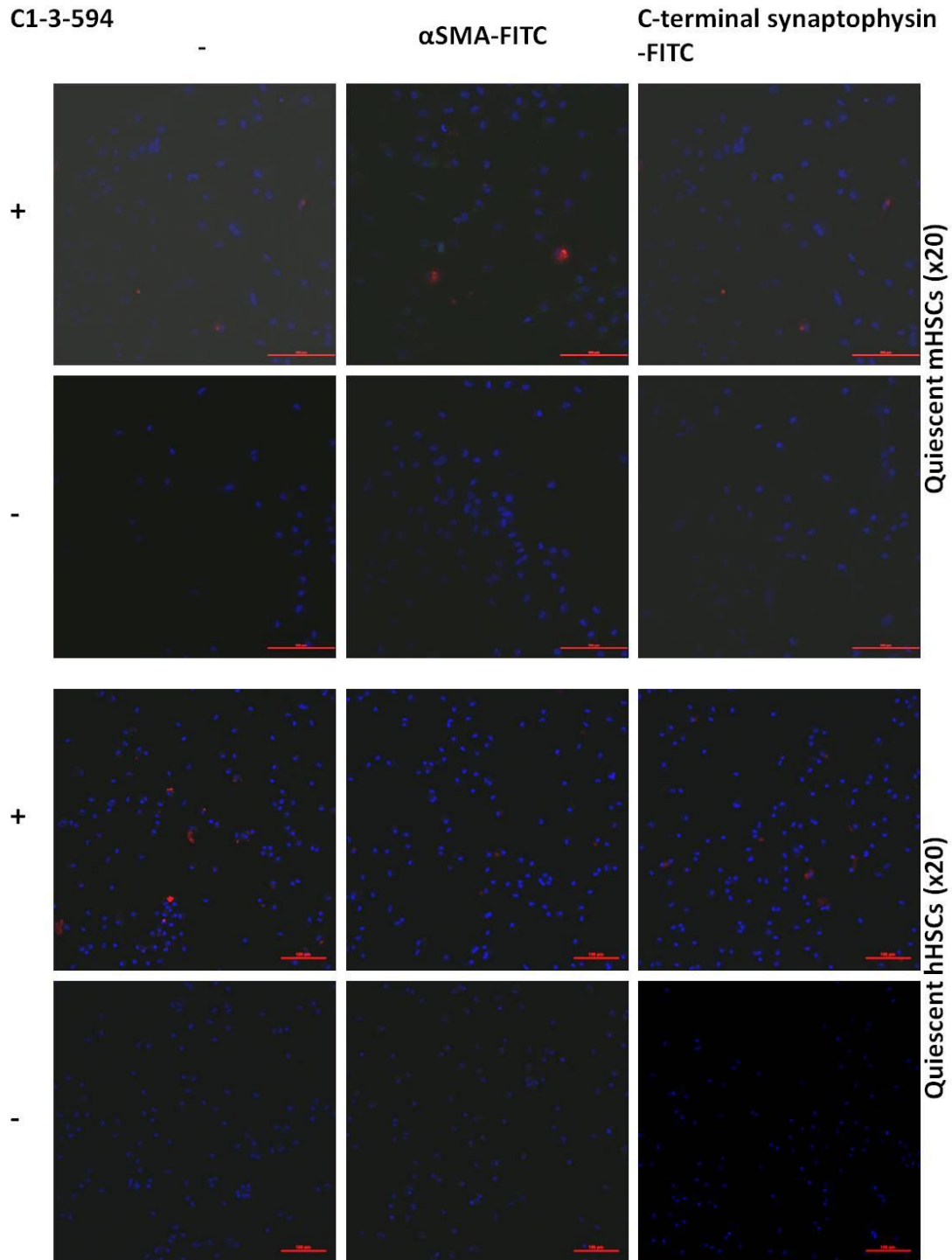


**Figure 4.10 C1-3-594,  $\alpha$ SMA and synaptophysin ICC staining of quiescent mouse and human HSCs.** 48 hours after isolation quiescent mouse and human HSCs were serum blocked with 20% FCS in 1 x PBS before incubation for an hour at room temperature with either C1-3-594, or the  $\alpha$ SMA and synaptophysin primary antibodies, after PBS washing and addition of the complementary FITC secondary antibody. The cells were counterstained with DAPI prior to analysis with a Leica fluorescent microscope. (All images shown are x20 magnification).

Figure 4.11 is a typical image from both the mouse and human activated HSCs following C1-3-594 incubation. There is strong binding of C1-3-594

(red) to some of the DAPI stained HSCs and co-localisation with  $\alpha$ SMA. Synaptophysin was also detected, although the level of synaptophysin and number of synaptophysin positive myofibroblasts was very low in comparison to  $\alpha$ SMA levels detected. The co-localisation of C1-3-594 with synaptophysin supports our initial hypothesis that C1-3 is binding to synaptophysin on the surface of hepatic myofibroblasts.

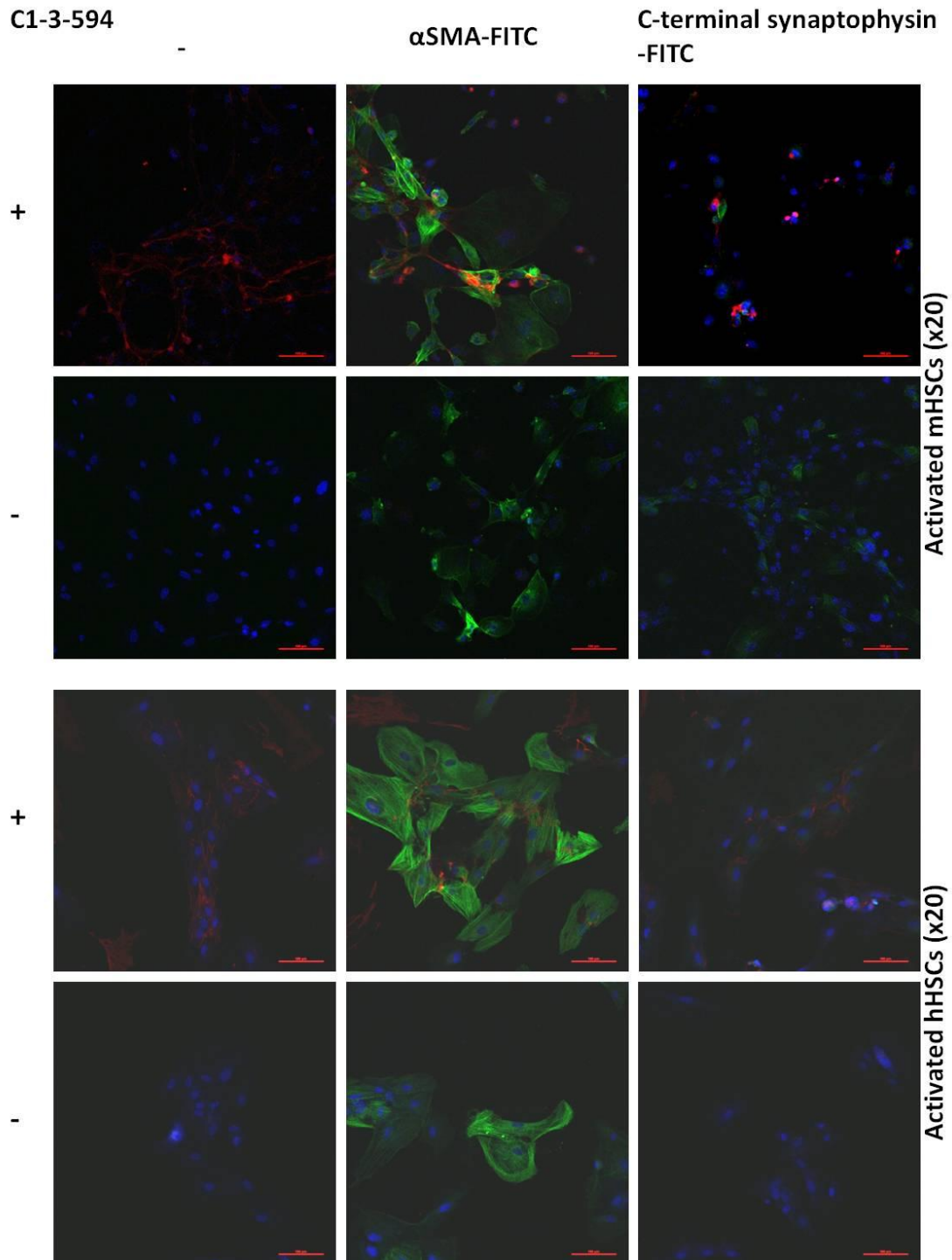


**Figure 4.11 C1-3-594,  $\alpha$ SMA and synaptophysin ICC staining of activated mouse and human HSCs.** Activated mouse and human HSCs (following one passage) were serum blocked with 20% FCS in 1 x PBS before incubation for an hour at room temperature with either C1-3-594, or the  $\alpha$ SMA and synaptophysin primary antibodies, after PBS washing and addition of the complementary FITC secondary antibody. The cells were counterstained with DAPI prior to analysis with a Leica fluorescent microscope. (All images shown are x20 magnification).

## 4.5 Chapter discussion

The data presented in this chapter confirm our previous findings that C1-3 is specific to hepatic myofibroblasts, due to the presence of synaptophysin on their surface (Figure 1.6). This was confirmed by fluorescent microscopy when fluorescently labelled C1-3 (C1-3-594) was shown to bind specifically to Cos7 cells *in vitro* (transfected with plasmids encoding the over expression of mouse or human synaptophysin). C1-3-594 displayed no affinity for untransfected Cos7 cells, indicating that it was binding as a result of their synaptophysin expression (Figure 4.1). Western analysis of protein samples isolated from these transfected cells confirmed the successful transfection of synaptophysin plasmids into the cells (Figure 4.2).

In the future further confirmation of C1-3's binding to synaptophysin positive Cos7 cells could be performed by Western blotting following C1-3 culture with synaptophysin transfected Cos7s. Using a Ck light chain specific primary antibody that will bind any C1-3 present, any bands detected will confirm C1-3's binding to synaptophysin positive Cos7 cells.

The variation in synaptophysin expression between species and the various organs (i.e. liver and pancreas) was investigated employing PCR, Western blotting and ICC techniques. These findings (Figures 4.4 and 4.5) highlight the difficulty of detecting synaptophysin protein in the liver using commercially available antibodies with only very low levels detected by fluorescent ICC and none by a Western blotting method. The detection of synaptophysin by PCR but not by Western blotting suggests that the protein is post-transcriptionally modified, and the transcript may be truncated in myofibroblasts as the antibody was unable to detect it. The synaptophysin PCR products could be purified from the agarose gels and cloned into a plasmid vector for sequencing analysis (e.g. Zero Blunt TOPO vector, Invitrogen). The

sequencing data would highlight any variations in synaptophysin expression between the rat and mouse livers and also between quiescent and activated HSCs.

It was also shown by qRT-PCR that quiescent HSCs express a similar level of synaptophysin to hepatic myofibroblasts (Figure 4.9), as initially reported by Cassiman *et al* [108] and suspected from the data presented in chapter 3. The binding of C1-3 to both quiescent HSCs and hepatic myofibroblasts was confirmed *in vitro* (Figures 4.10 and 4.11). A future study is required to determine the significance of C1-3 binding to quiescent HSCs upon the imaging outcome *in vivo*. Initially addition of both free GTX and C1-3-GTX to quiescent HSCs *in vitro* could shed light on their susceptibility to its toxicity and give an indication of what may occur when C1-3-GTX is administered *in vivo* to deplete hepatic myofibroblasts. If C1-3-GTX induces quiescent HSC apoptosis *in vitro* it could be possible to treat non-fibrotic mice with C1-3-GTX to determine the effect of qHSC loss in a normal healthy liver setting. This could in turn be repeated prior to administration of CCl<sub>4</sub> and see the downstream effects of quiescent HSC loss upon liver fibrosis development.

The data presented in this chapter confirms that C1-3 is able to target both quiescent and activated HSCs (hepatic myofibroblasts), and that both express similar levels of synaptophysin. Performing these future studies will reveal the impact of C1-3 targeting quiescent HSCs when it is used as either an imaging or anti-fibrotic agent. Finally the difficulties encountered in detecting synaptophysin expression by both Western blotting, IHC and ICC analysis techniques, indicates there may be post-transcriptional modification of the protein that also requires further investigation.

**Chapter 5.0 - The anti-inflammatory potential of PXR  
activators in an *in vivo* model of liver fibrosis**

## 5.1 Introduction

The correlation between decreased CYP450 activity and increased levels of inflammation is well documented, although initially the mechanism of this CYP450 down regulation was unknown [167]. The glucocorticoid receptor (GR) (another major member of the NRS) has been shown to inhibit NF- $\kappa$ B activity and inflammation [169]. A number of groups then highlighted the beneficial anti-inflammatory properties of pregnane X receptor (PXR) agonists, most notably in gastrointestinal inflammatory disorders (e.g. IBD) [166, 170]. With the knowledge that the inflammatory cascade is central in liver fibrosis development and that the PXR is constitutively expressed in the liver [154], the potential benefits of employing PXR activators are clear. Previous work within this laboratory (both *in vitro* and *in vivo*) demonstrated the anti-fibrotic properties of PXR agonists in combating liver fibrosis development [172, 173].

The importance of NF- $\kappa$ B in the maintenance and development of liver fibrosis has been shown; it is expressed in hepatic myofibroblasts [91, 92, 183]. Novel anti-fibrotic agents such as C1-3-GTX and sulfasalazine, which are known to target NF- $\kappa$ B, have been used *in vivo* to induce hepatic myofibroblast apoptosis and reduce fibrosis severity [90, 91]. *In vitro* work, utilising the monocytic U937-NF- $\kappa$ B cell line (stably transfected with the luciferase gene under the control of a concatemer of NF- $\kappa$ B response elements) also showed that PXR activators inhibit NF- $\kappa$ B activity. Addition of PXR agonists (e.g. rifampicin, hyperforin and metyrapone) inhibited the luciferase response normally seen after addition of pro-inflammatory mediators including TNF $\alpha$  and LPS [175].

The generation of transgenic mice (NF- $\kappa$ B luciferase mice) that contain the firefly-luciferase gene under the control of NF- $\kappa$ B response elements [187], provide a live animal model for examining inflammation *in vivo*.

Using both an acute and chronic *in vivo* model of liver fibrosis (CCl<sub>4</sub> treated NF- $\kappa$ B luciferase mice) we hypothesised that administration of the rodent specific PXR activator PCN would have beneficial anti-inflammatory properties. Upon completion of the designated CCl<sub>4</sub> treatment regimen, PCN

was administered prior to  $\beta$ -luciferin injection and IVIS imaging to generate both whole body and *ex vivo* organ images. The level of luciferase activity and luminescence detected is directly related to the level of inflammation, governed by NF- $\kappa$ B induction. It will be possible to locate and quantify the level of NF- $\kappa$ B activity (and inflammation) from both the whole body and *ex vivo* luminescent scans. If PXR activators exhibit beneficial anti-inflammatory properties as hypothesised, there would be a reduction in the level of luminescence (i.e. NF- $\kappa$ B activity) in the upper abdominal (liver) region of  $\text{CCl}_4$  treated mice and *ex vivo* liver when also administered with PCN.

## 5.2 Anti-inflammatory properties of PCN in an *in vivo* (chronic and acute) model of liver fibrosis

Figure 5.1 is a schematic diagram illustrating the different treatment groups, alongside the dosing and imaging schedule. Briefly the chronic groups were treated for four weeks with  $\text{CCl}_4$  (see table 2.1 for dosing solutions), whilst controls received olive oil for four weeks. The acute groups received a single dose of  $\text{CCl}_4$  when the chronic groups received their final dose of  $\text{CCl}_4$  (the day before imaging). PCN was administered with these final doses where designated, dissolved in the olive oil vehicle solution.

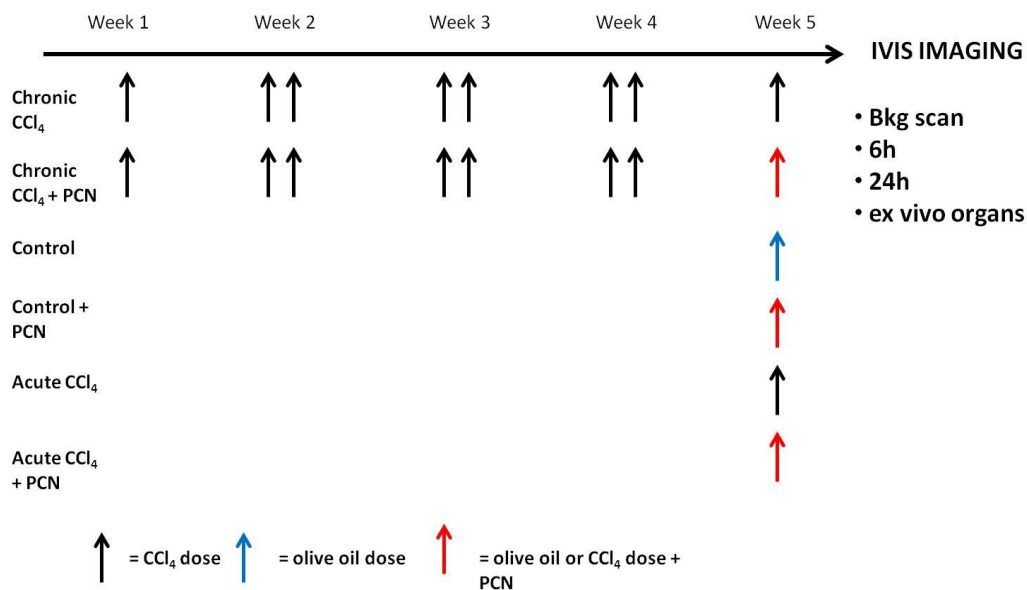


**Figure 5.1 Schematic diagram outlining the dosing and imaging regimen.** Chronic  $\text{CCl}_4$  mice received  $\text{CCl}_4$  twice weekly to induce centrilobular fibrosis (whilst controls received olive oil); acute

CCl<sub>4</sub> mice received a single dose on the same day of the chronic groups' final dose. Where required PCN was co-administered in the vehicle solution (olive oil) with the final dose, at this point mice were returned to their cages prior to IVIS imaging at the desired timepoints.

The mice were anaesthetised with isoflurane and had their ventral side shaved before being placed in the IVIS imaging chamber. Whole body bioluminescent scans were performed before the acute dose of CCl<sub>4</sub> to confirm firstly that every mouse in the study contained the luciferase transgene and also to demonstrate basal levels of luciferase activity. Figure 5.2 is an example basal whole body scan performed 10 minutes after i.p. injection of 200µl D-luciferin (15mg/kg) using a 2 minute exposure setting (these settings were retained for each subsequent scan performed).

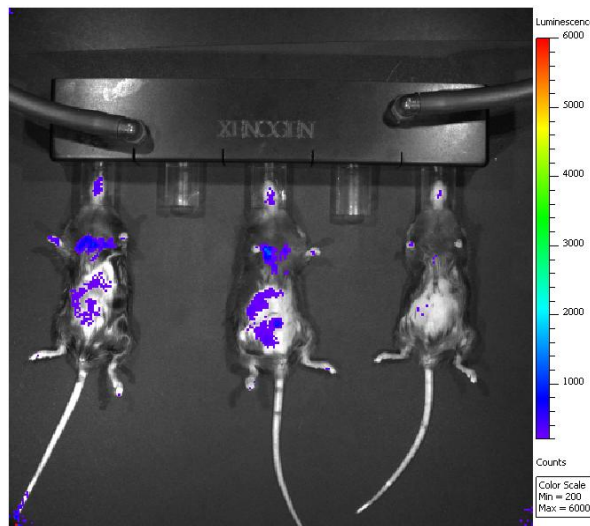


**Figure 5.2 Whole body luminescent background scan prior to PCN administration.** Control mice were anaesthetised with isoflurane and had their ventral side shaved, prior to placement in the IVIS chamber and i.p. injection of 15mg/kg D-luciferin. All scans were performed using the same luminescent filter settings and a manual 2 minute exposure settings. The images were analysed using the Image Pro Plus 4.0 software and the total luminescence scale bar set to the same levels so they could be directly compared.

Figure 5.3 is an example individual whole body scan, as performed for each treatment group 6 hours after the final CCl<sub>4</sub>/ PCN administration using the same imaging settings as outlined for the background scan.

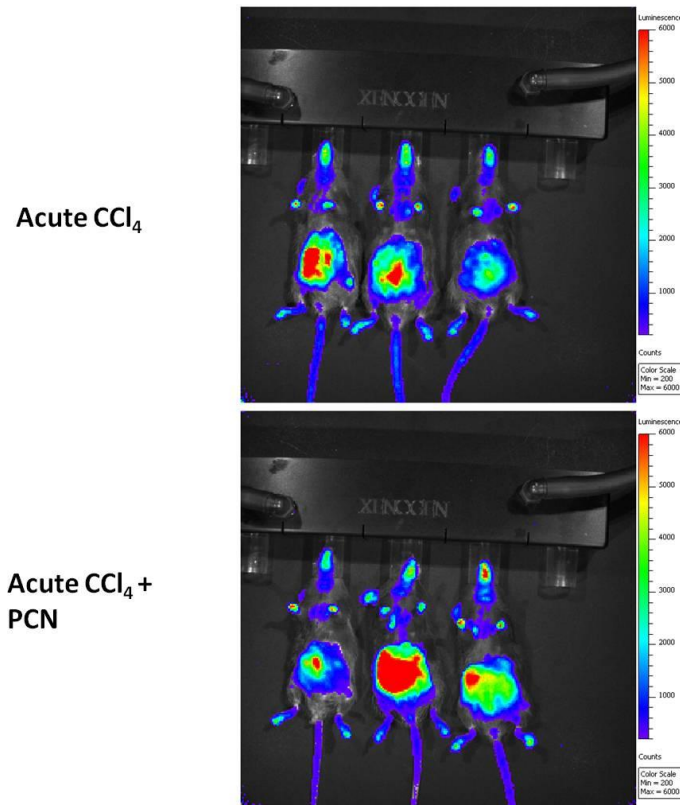
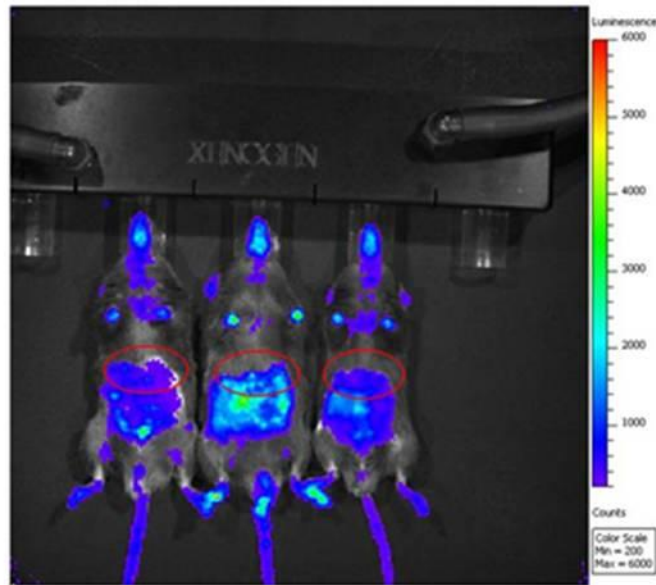


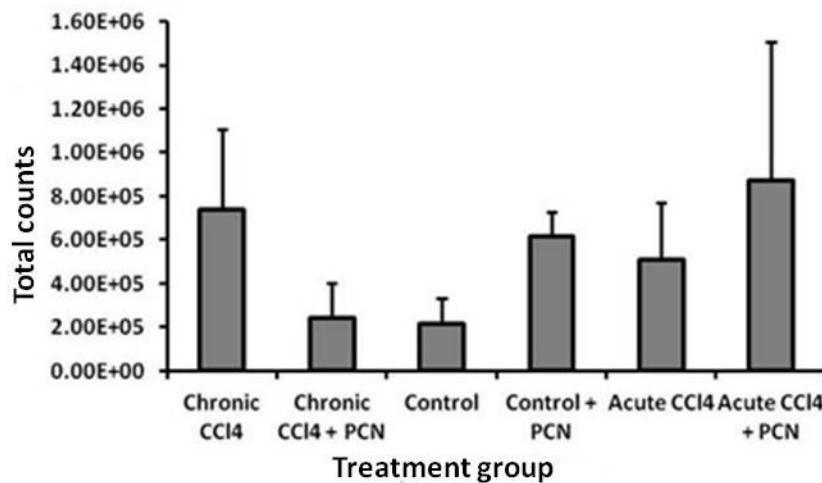
**Figure 5.3 Acute CCl<sub>4</sub> & acute CCl<sub>4</sub> + PCN whole body luminescent scans 6 hours after PCN administration.** Image shown was captured 10 minutes after <sup>125</sup>I-luciferin injection using the same filter and exposure settings. All images were analysed using the Image Pro Plus 4.0 software and the same total luminescence scale applied so they can be directly compared to each other.

It was difficult to discern much from the images themselves, however using ROIs as shown earlier in section 3.3, and it was possible to quantify the level of luminescence of specific body regions seen in the whole body scans (Figure 5.4A). Figure 5.4B is the mean and SD total luminescence calculated for the upper abdominal (liver) region of each treatment group, the findings reinforce the observations from the whole body scans. The chronic CCl<sub>4</sub> group was the only group where PCN appeared to act as hypothesised, with a decrease in luminescence of the liver region although this decrease was not statistically significant ( $p < 0.056$ , ANOVA). PCN administration has had no effect on the level of luminescence in the liver region of either the control or acute CCl<sub>4</sub> treatment groups. In this instance PCN appears to be pro-inflammatory demonstrated by the increased levels of luminescence detected in the acute and control groups when they also received PCN.

A



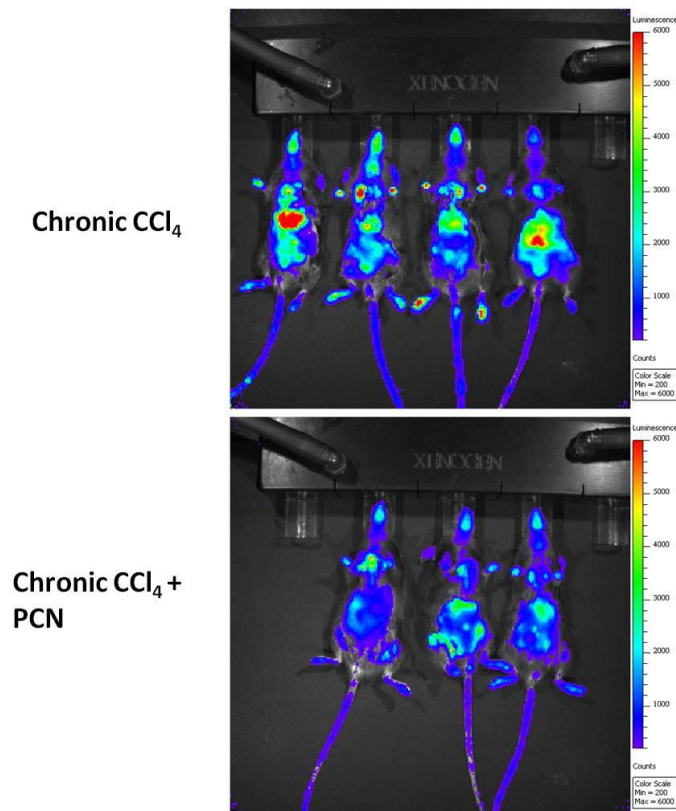
B



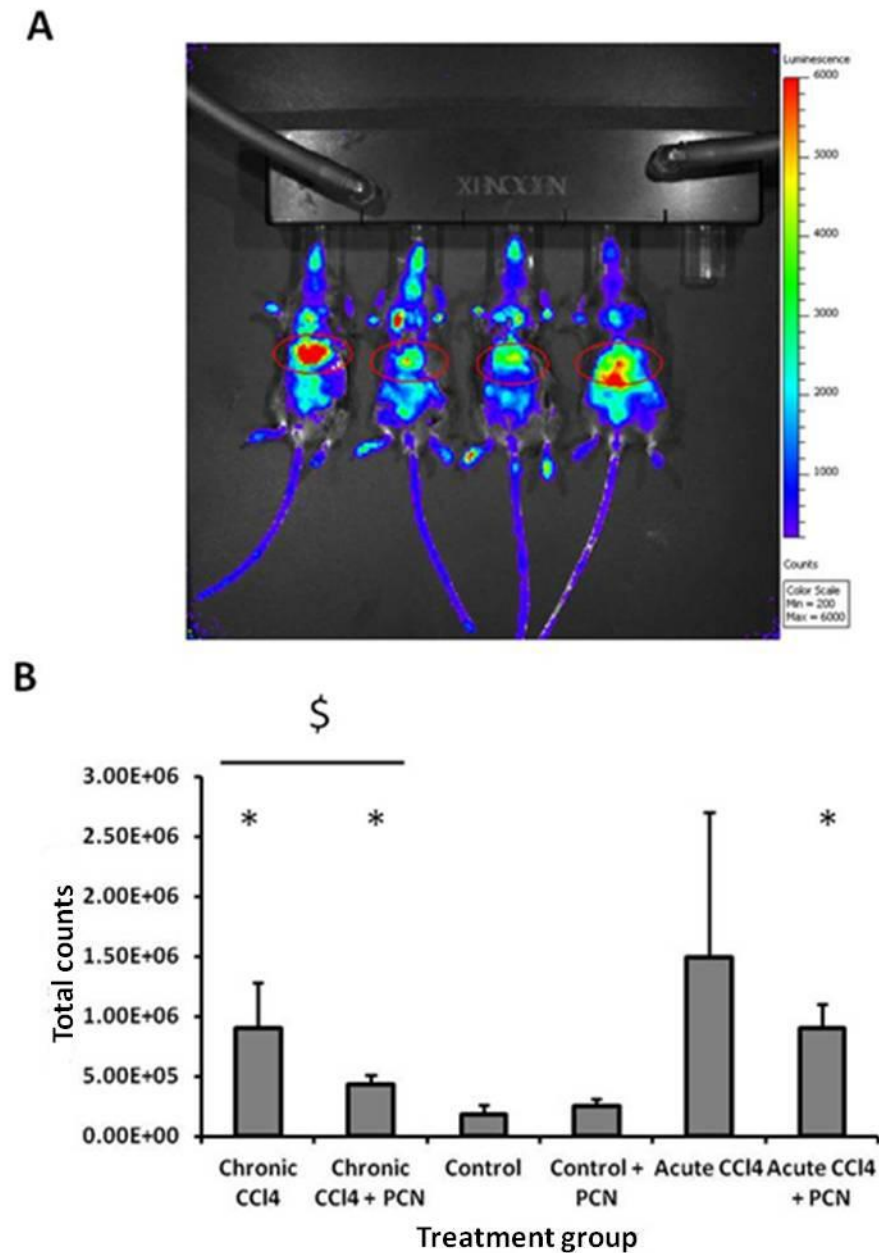
**Figure 5.4 Example whole body image annotated with ROIs and accompanying 6 hour total luminescence values.** **A** When analysing images with Image Pro Plus 4.0 software ROIs could be overlaid onto the images to allow quantification of total luminescence values for specific body regions e.g. upper abdominal/ liver region. **B** upper abdominal/ liver total luminescence values calculated for each individual treatment group. (Data shown is the mean and SD n=3 for each treatment group). Data was analysed for any statistically significant differences between treatment groups although none were found.

Figure 5.5 is an example individual whole body scan performed for each treatment group performed 24 hours after the final CCl<sub>4</sub>/ PCN dose, using the same exposure settings and captured 10 minutes after D-luciferin injection. There was a much greater level of luminescence in all CCl<sub>4</sub> treatment groups when compared to the control groups, and PCN administration had reduced

the level of luminescence in both CCl<sub>4</sub> treatment groups. Figure 5.6A is an example of the ROI used to calculate the mean total luminescence counts for the upper abdominal (liver) region of each treatment group. The data shown in figure 5.6B confirm the initial observations from the whole body scans (Figure 5.5), firstly all CCl<sub>4</sub> treatment groups (except acute CCl<sub>4</sub> only, due to one anomalous reading) exhibited significantly higher levels of upper abdominal (liver) luminescence when compared to the control groups ( $p < 0.016$ , ANOVA). More importantly there was a reduction in the level of upper abdominal (liver) region luminescence in both the chronic and acute CCl<sub>4</sub> mice when also treated with PCN, with the greatest effect seen in the chronic CCl<sub>4</sub> mice treated with PCN. Analysis of the chronic CCl<sub>4</sub> mean total luminescence using an ANOVA revealed this difference was statistically significant ( $p < 0.0087$ ). Therefore it is highly plausible that PCN does have beneficial anti-inflammatory properties mediated via NF- $\kappa$ B, especially when taken together with the previous findings of this laboratory [172, 173].



**Figure 5.5 Chronic CCl<sub>4</sub> & Chronic CCl<sub>4</sub> + PCN whole body luminescent scans 24 hours after PCN administration.** Image shown was captured 10 minutes after <sup>125</sup>I-luciferin injection using the same filter and exposure settings (these were retained for all subsequent images). All images were analysed using the Image Pro Plus 4.0 software and the same total luminescence scale applied so they can be directly compared to each other.



**Figure 5.6 Example whole body image annotated with ROIs and accompanying 24 hour total luminescence values.** **A** When analysing images with Image Pro Plus 4.0 software ROIs could be overlaid onto the images to allow quantification of total luminescence values for specific body regions e.g. upper abdominal/ liver region. **B** upper abdominal/ liver total luminescence values calculated for each individual treatment group. (Data shown is the mean and SD n=3 for each treatment group, \* denotes a statistically significant difference between CCl<sub>4</sub> treatment group and controls, analysed by ANOVA ( $p < 0.016$ ) and \$ denotes a significant decrease in upper abdominal luminescence following PCN treatment, analysed using an ANOVA ( $p < 0.0087$ ).

Upon completion of whole body scans 24 hours after PCN administration the mice were terminated by cervical dislocation and the major organs excised

and placed in the IVIS imaging chamber prior to detection of their individual luminescence. Figure 5.7 is an example *ex vivo* organ scan from the chronic CCl<sub>4</sub> treatment group; it was clear from all the scans that there was a marked increase in luminescence of the liver compared to the other excised organs (kidney, spleen and stomach). This indicates that CCl<sub>4</sub> treatment has resulted in liver damage/ inflammation as expected; the other organs exhibit minimal luminescence with the exception of a single anomalous stomach signal in the acute CCl<sub>4</sub> + PCN treatment group (data not shown).

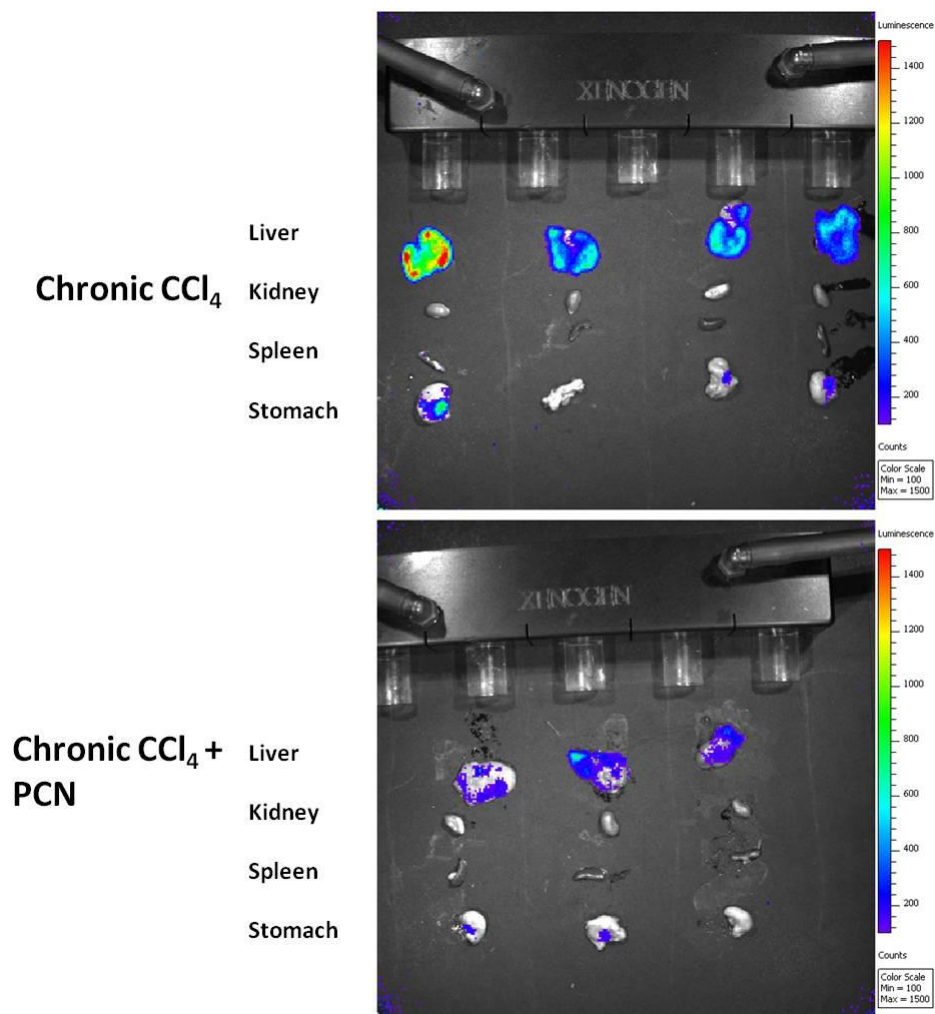


**Figure 5.7 Chronic CCl<sub>4</sub> & Chronic CCl<sub>4</sub> + PCN *ex vivo* organ luminescent scans 24 hours after PCN administration.** Upon completion of the 24 hour whole body scans mice were culled by a schedule I method the major organs were excised (liver, kidney, spleen and stomach) and placed in the IVIS imaging chamber. The same filter and exposure settings were used and all images were analysed using the Image Pro Plus 4.0 software and the same total luminescence scale applied so they can be directly compared to each other.

As found in the 24 hour whole body scans the livers of chronic and acute CCl<sub>4</sub> mice display significantly higher luminescence than the control groups. This difference in luminescence was statistically significant in the 24 hour whole body scans for the liver regions of chronic CCl<sub>4</sub> mice versus those that also received PCN ( $p < 0.0087$ , ANOVA), whilst no difference was detected in the acute CCl<sub>4</sub> treatment groups. To determine the accuracy of these observations ROIs were overlaid onto the images around each individual organ, as shown in figure 5.8A. The mean total luminescence for each organ of a treatment group was calculated and is shown in figure 5.8B. As reported earlier there was no luminescence detected from the kidney or spleen in all the treatment groups and the stomach was only detected at low levels in a couple of groups, which could be a result of localised inflammation unrelated to CCl<sub>4</sub> administration.

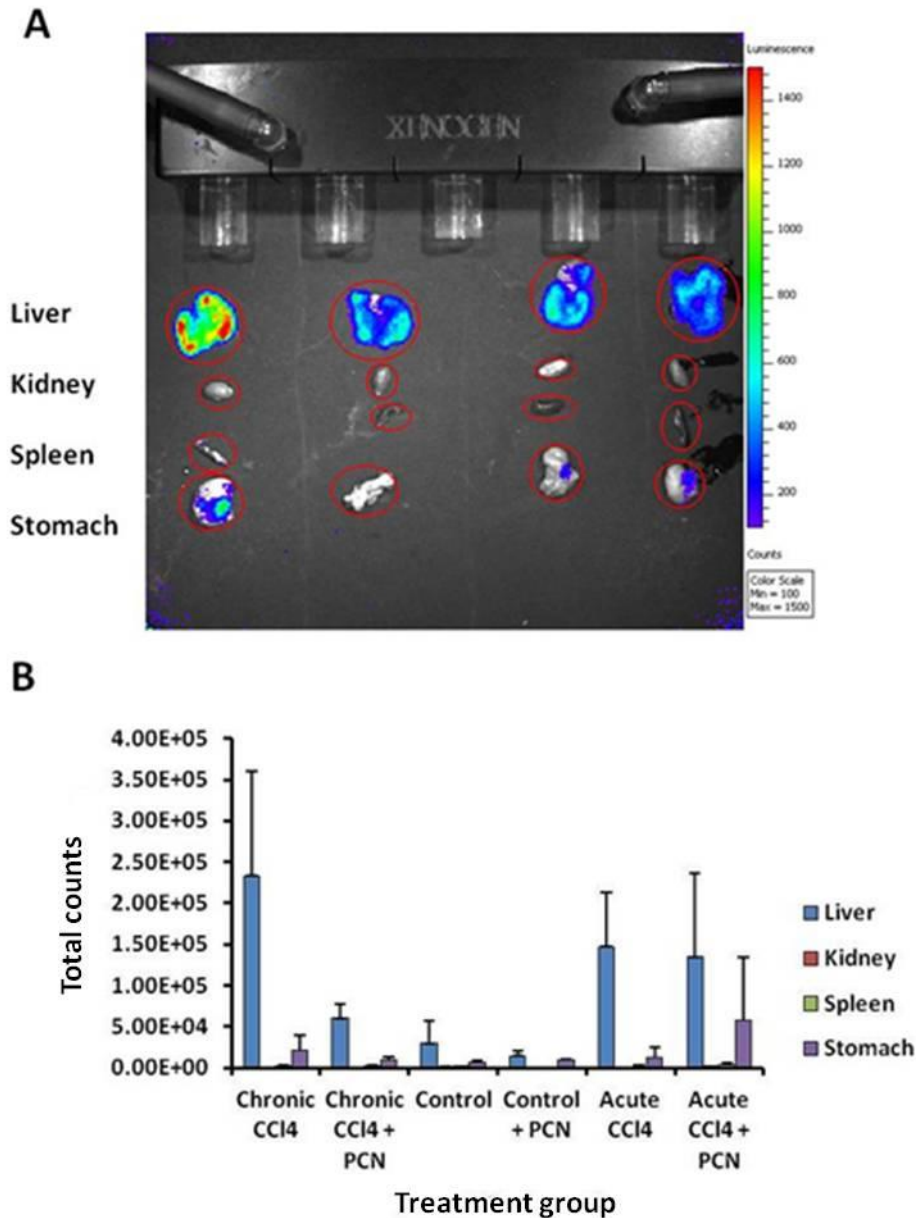


**Figure 5.8 A Example *ex vivo* organ scan annotated with ROIs and B total luminescence values calculated for each treatment group.** When analysing images with Image Pro Plus 4.0 software ROIs could be overlaid to allow quantification of total luminescence values for specific organs. The data shown is the mean and SD n=3 for each treatment group.

Figure 5.9 is the mean and SD total liver luminescence calculated for each treatment group. As expected there was a statistically significant increase in the total liver luminescence of both the chronic and acute CCl<sub>4</sub> treated mice when compared to the control mice ( $p < 0.019$ , ANOVA). More importantly the treatment of chronic CCl<sub>4</sub> mice with PCN has reduced the level of luminescence to a level similar to that of the control mice; when analysed

employing an ANOVA these findings were statistically significant ( $p < 0.012$ ). In contrast there was negligible difference in total liver luminescence between the acute CCl<sub>4</sub> mice regardless of PCN administration, suggesting that PCN has no effect in an acute model of liver damage. This could be due to the lack of hepatic myofibroblasts, as they take longer than 24 hours to develop following CCl<sub>4</sub> administration.

These data confirms that PCN has beneficial anti-inflammatory properties mediated via NF- $\kappa$ B, and may be a potential route to alleviate inflammation in chronic liver disease and form part of a treatment regimen to combat liver fibrosis.

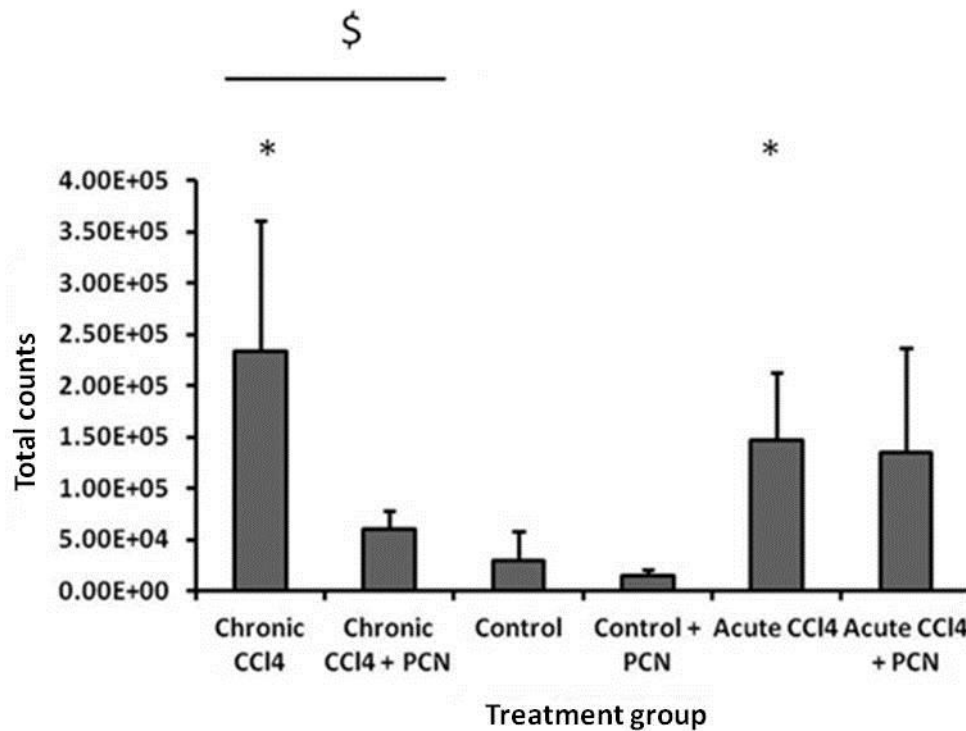


**Figure 5.9 Mean total luminescence of excised liver from each treatment group.** The individual total liver luminescence values calculated for each treatment group from the ROIs drawn using the Image Pro Plus 4.0 software. The data shown is the mean and SD  $n=3$  for each treatment group, \* denotes a statistically significant increase in total liver luminescence in comparison to the olive oil control when analysed using an ANOVA ( $p < 0.019$ ). \$ denotes that there was a significant difference in liver luminescence following PCN treatment, analysed using an ANOVA ( $p < 0.012$ ).

Following completion of the *ex vivo* organ scans the liver tissue was both snap frozen in LqN<sub>2</sub> for further biochemical analyses and fixed in 10% formalin for IHC analysis. Luciferase assays were performed on liver tissue homogenates (see methods 2.12 and 2.13), providing another route to

ascertain whether PCN treatment had reduced the level of inflammation induced by CCl<sub>4</sub> administration. Figure 5.10 shows the mean and SD luciferase activity of each treatment group. The data mirrors the total luminescence calculations from the whole body scans and *ex vivo* liver scans as PCN administration has reduced the level of transgene expression (i.e. inflammation). In this instance PCN administration has had a greater effect in the acute CCl<sub>4</sub> treated mice when compared to the chronic CCl<sub>4</sub> treated mice as found previously. There was a statistically significant increase in the luciferase activity of the liver homogenate of both the chronic and acute CCl<sub>4</sub> treatment groups in comparison to the control groups ( $p < 0.043$ ). However the difference between the chronic CCl<sub>4</sub> treatment group and those that also received PCN was outside the range of significance ( $p < 0.16$ ) when analysed employing an ANOVA.

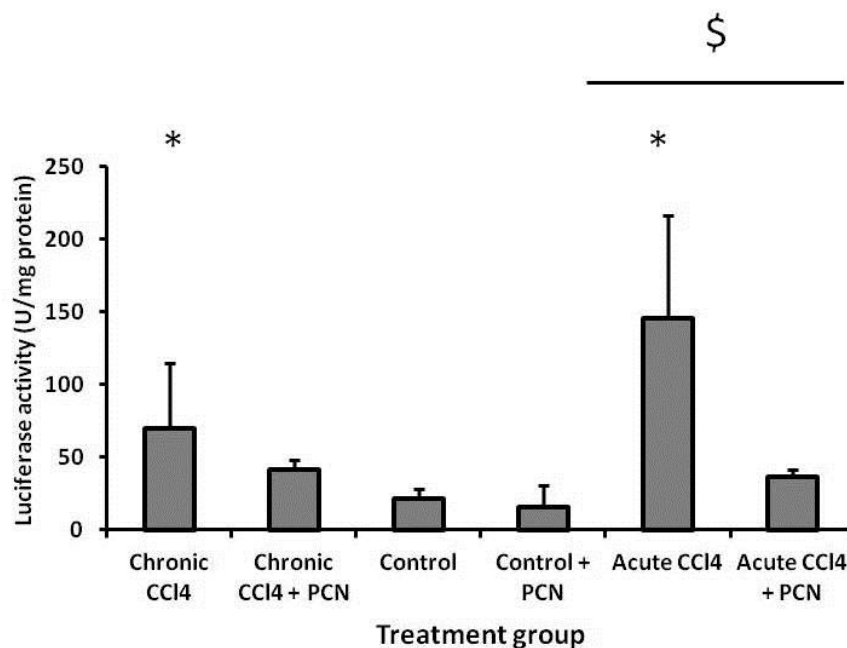


**Figure 5.10 Mean luciferase activity of liver homogenates from each treatment group.** Individual liver samples from each mouse were homogenised and mixed 1:1 with an equal volume of luciferase substrate prior to determination of luciferase activity using a bench top luminometer. The data shown is the mean and SD  $n=3$  for each treatment group, \* denotes a significant increase in luciferase activity in comparison to the controls when analysed using an ANOVA ( $p < 0.043$ ). § denotes that there was a significant difference in liver luminescence following PCN treatment, analysed using an ANOVA ( $p < 0.0068$ ).

Interestingly in this instance there was a significant reduction in the luciferase activity of the acute CCl<sub>4</sub> treatment group following PCN administration ( $p <$

0.0068, ANOVA). The findings of the liver homogenate luciferase assays are in contrast to the earlier IVIS scans and total luminescence calculations, with a statistically significant reduction in liver luminescence in the acute CCl<sub>4</sub> treatment group as opposed to the chronic CCl<sub>4</sub> treatment group as previously found.

### **5.3 PCN administration does not influence CCl<sub>4</sub> hepatotoxicity and severity of fibrosis development**

To confirm previous findings that PXR activators had no effect upon CCl<sub>4</sub> hepatotoxicity but reduced the level of hepatic fibrosis that occurred [172], a range of biochemical and IHC analyses were also performed. Firstly whole blood was collected by cardiac puncture and the serum fraction was isolated as outlined in section 2.11. The samples were analysed for both serum ALT and ALP levels and the mean and SD for each treatment group is shown in figure 5.11. The findings are consistent with previous work as there are significantly elevated ALT levels in all the CCl<sub>4</sub> treatment groups regardless of PCN dosing, when compared to the control groups that are at normal physiological levels ( $p < 0.0001$ , ANOVA). ALT is an important enzyme in amino acid synthesis expressed at high levels in hepatocytes, and is generally only found at elevated levels in the serum when centrilobular hepatocyte necrosis has been induced [2]. ALP was measured as a negative control to show serum levels are unaffected, demonstrated by the low levels of ALP in all treatment groups. Elevated ALP levels are associated with biliary/cholestatic liver injuries and are only affected by extremely severe centrilobular CCl<sub>4</sub> induced liver damage [2].

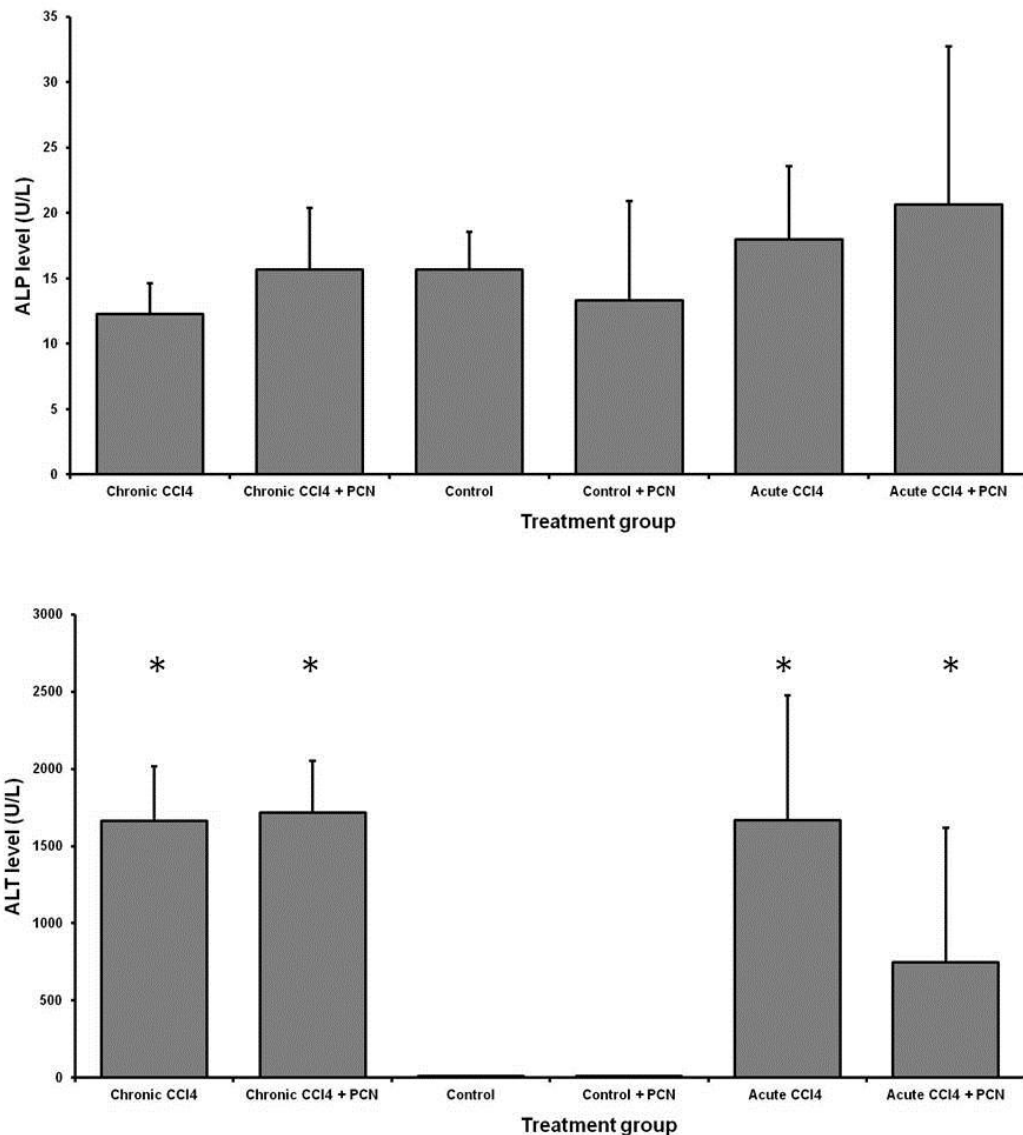


**Figure 5.11 Serum ALT and ALP concentrations.** Mice were schedule 1 killed and whole blood was removed and allowed to clot at room temperature for 1 hour. Serum was removed following centrifugation and diluted in 0.9% sodium chloride. All serum samples were analysed by Newcastle Clinical Biochemistry Department. Data are the mean and SD n=3 for each treatment group. \* denotes there was a statistically significant increase in ALT serum levels, when analysed by an ANOVA ( $p < 0.0001$ ).

IHC analysis was also performed to confirm the development of liver damage/fibrosis consistent with 4 weeks and a single dose of  $\text{CCl}_4$  administration. Figure 5.12 is a typical H&E stained section from each treatment group highlighting the  $\text{CCl}_4$  induced liver damage and that co-administration of PCN has no influence on its severity. There was an increased number of infiltrating inflammatory cells around the regions of damage (the central veins) in both

the chronic and acute CCl<sub>4</sub> treated mice; the damage was also shown by the lighter shade of pink and the loss of the clear regular repetitive/ patterned appearance of the hepatocyte nuclei as seen in the controls.

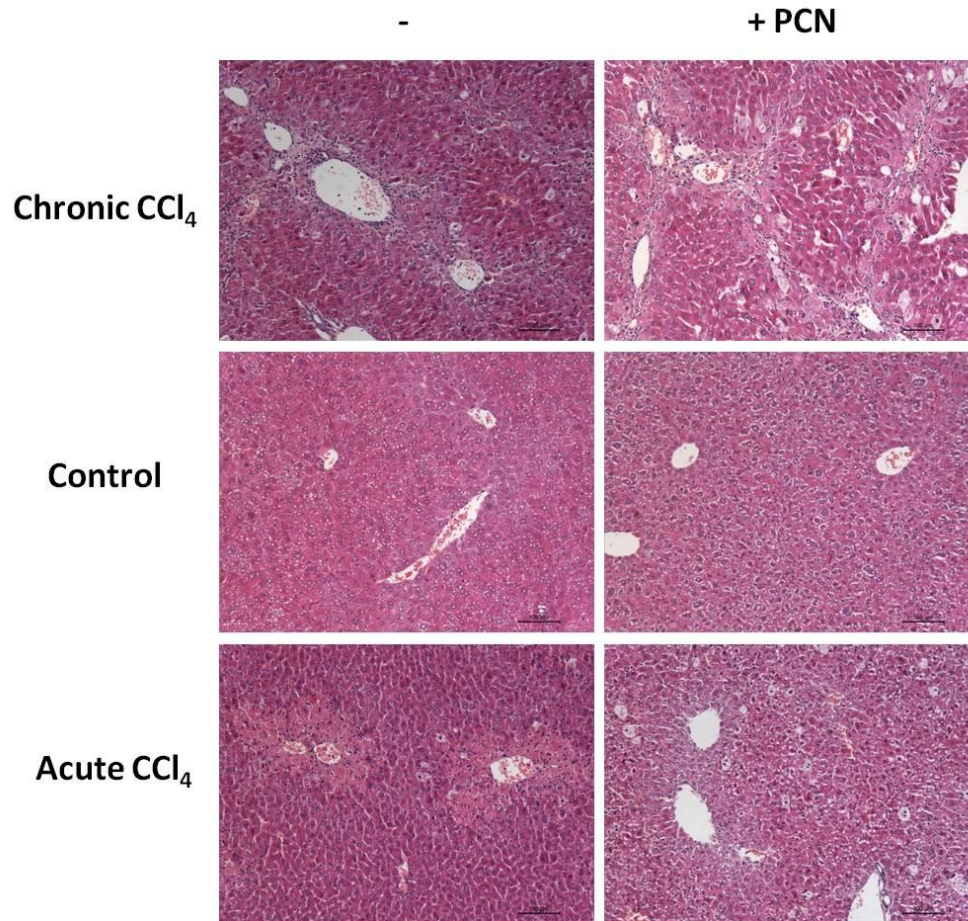


**Figure 5.12 H&E IHC analysis of all treatment groups.** Liver tissue was fixed in 10% formalin prior to paraffin embedding, 5 $\mu$ M sections were cut from each animal. Sections were dewaxed prior to haematoxylin incubation for 1 minute and extensive washing in deionised water. This was followed by a second incubation in Scott's water for thirty seconds before further washing. Sections were finally counterstained in eosin for 30 seconds before deionised water washing and dehydration and mounting. It is clear there is only liver damage in the CCl<sub>4</sub> treated livers regardless of PCN treatment and that it is located primarily in hepatocytes surrounding the central vein.

$\alpha$ SMA IHC staining was also performed as hepatic myofibroblasts are the central cell involved in liver fibrosis development, and  $\alpha$ SMA is the most prominent marker used to detect them. Figure 5.13 shows there was an increased number of  $\alpha$ SMA positive hepatic myofibroblasts in the chronic CCl<sub>4</sub> treated groups irrespective of PCN treatment. The number of  $\alpha$ SMA positive hepatic myofibroblasts was quantified and the mean cell counts and SD for each treatment group are shown in figure 5.14. There was no difference in

their number regardless of PCN treatment in all groups, however it is important to note that there are no  $\alpha$ SMA positive hepatic myofibroblasts in the control groups to be detected and there are very few if any following the single dose of  $\text{CCl}_4$  in the acute groups.

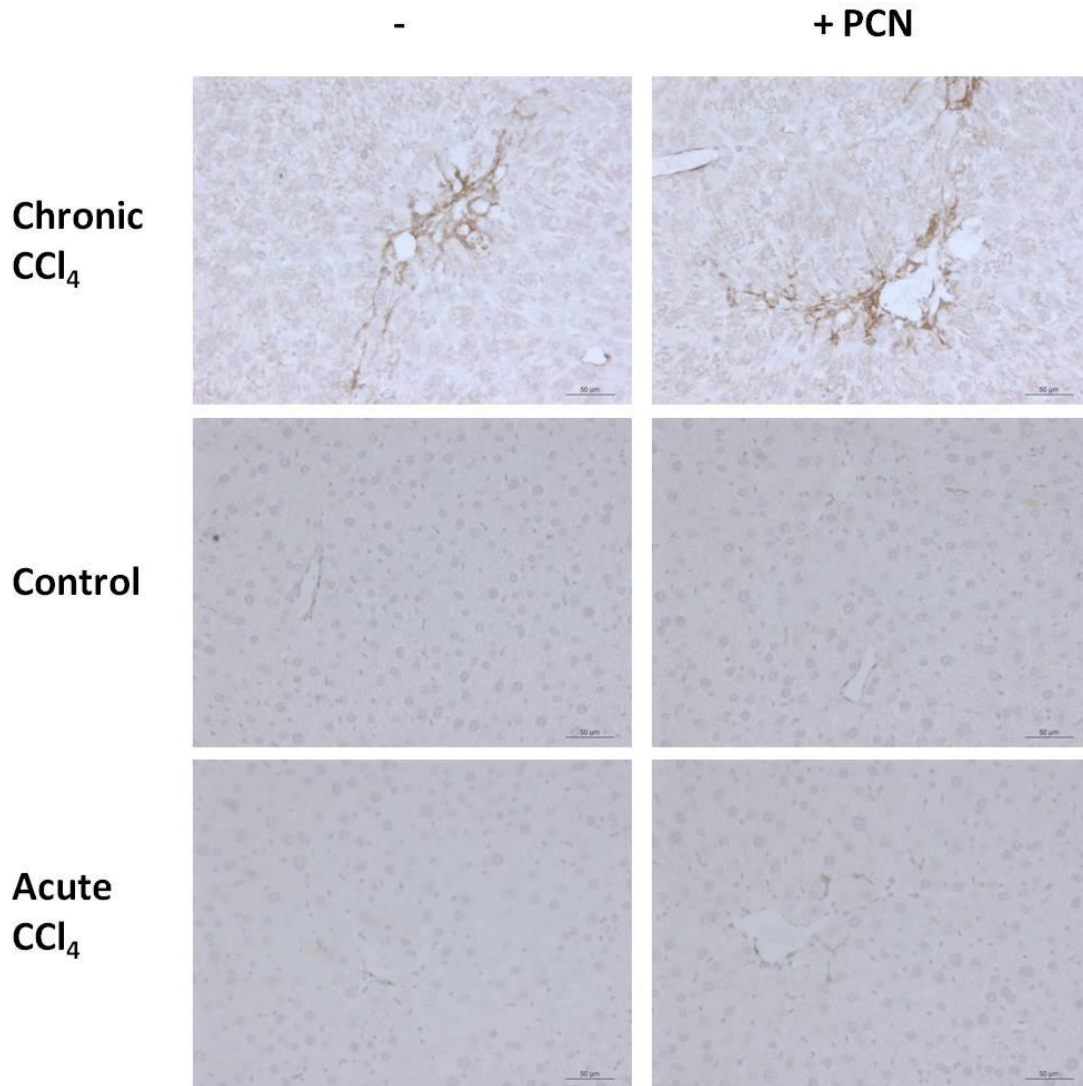


**Figure 5.13  $\alpha$ SMA IHC analysis of liver tissue from each treatment group.** Liver tissue was fixed in 10% formalin prior to paraffin embedding,  $5\mu\text{M}$  sections were cut for each animal. Sections were dewaxed prior to blocking of endogenous peroxidase activity and heat induced antigen retrieval. Followed by serum blocking and incubation for an hour at room temperature with  $\alpha$ SMA primary antibody, after PBS washing and addition of the complementary secondary antibody the level of bound antibody was detected by DAB incubation. The sections were counterstained with haematoxylin and dehydrated prior to mounting and analysis with a Leica upright microscope. (All images shown are  $\times 20$  magnification).

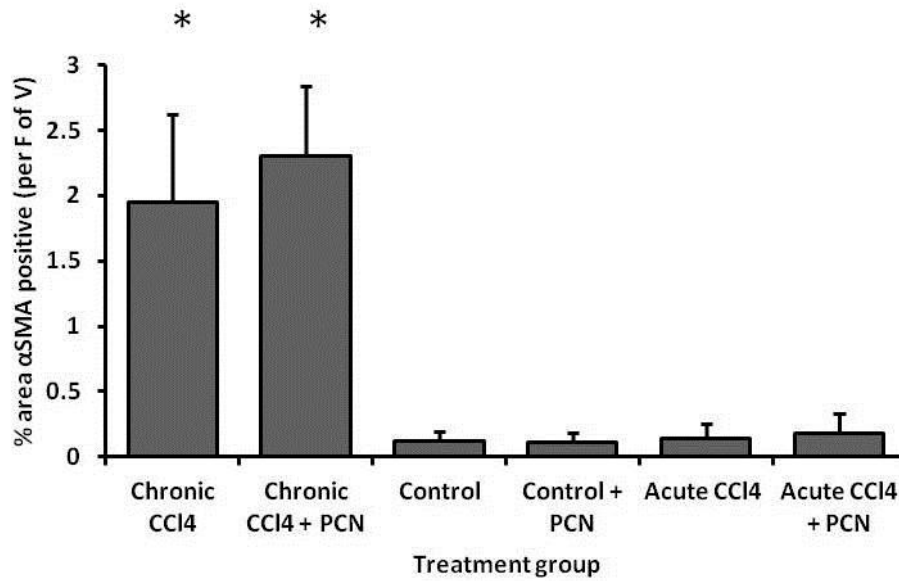


**Figure 5.14  $\alpha$ SMA IHC quantification.**  $\alpha$ SMA positive staining was quantified using Qwin software (Leica); briefly 10 random images were captured for each section and blindly quantified to determine the positive  $\alpha$ SMA stain per field of view. The data are the mean and SD n=30 percentage area of the stain for each treatment group and were tested for statistical significance using an ANOVA, \* denotes there was a statistically significant increase in  $\alpha$ SMA positive cells ( $p < 0.0001$ ).

Another prominent marker used to quantify hepatic fibrosis development is the deposition of collagens, and they can be detected by sirius red staining. Figure 5.15 is a typical image taken from each treatment group. The percentage of sirius red positive areas could also be quantified and the mean values for each treatment group are shown in figure 5.16. The values calculated reinforce the images with no discernible difference between the chronic CCl<sub>4</sub> treatment groups regardless of PCN administration. There was no obvious difference between the acute CCl<sub>4</sub> and control groups, as identical to the  $\alpha$ SMA images there was very little positive sirius red to be detected as collagen deposition and build up is a result of chronic liver damage.

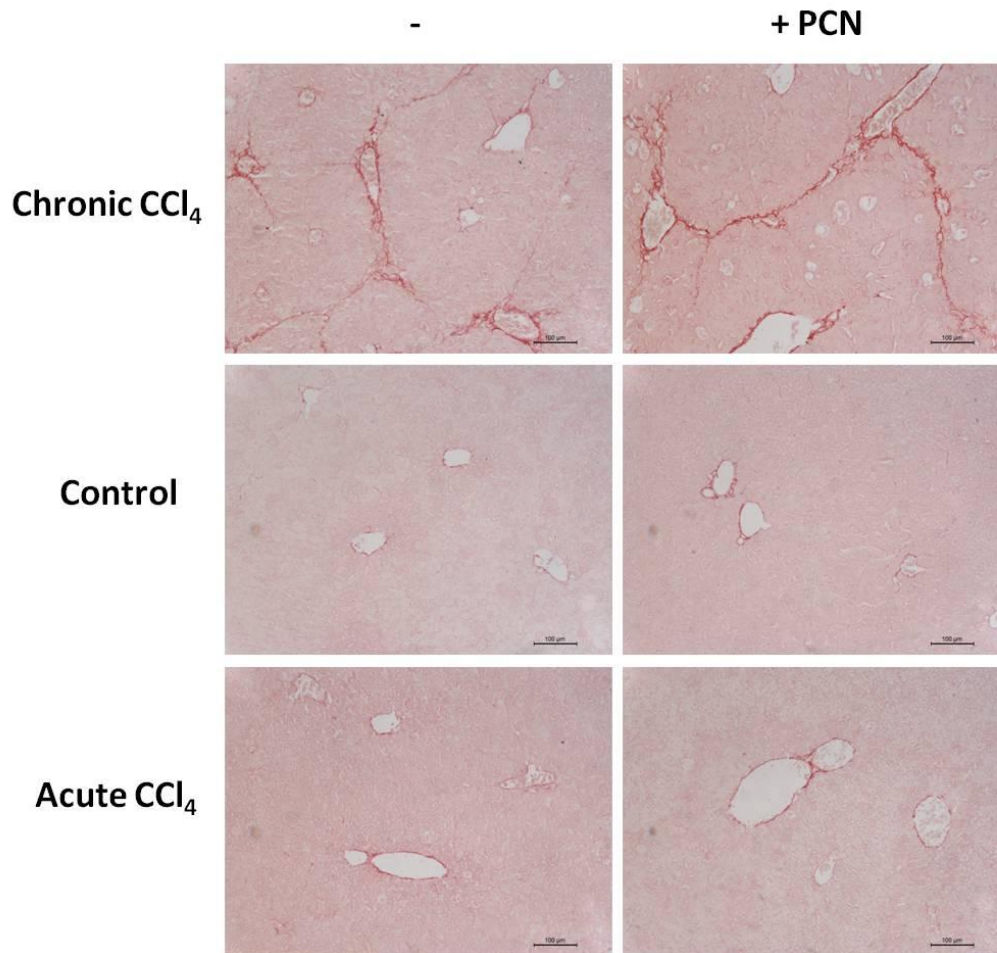


**Figure 5.15 Sirius red IHC analysis of liver tissue from each treatment group.** Liver tissue was fixed in 10% formalin prior to paraffin embedding, 5 $\mu$ M sections were cut for each animal. Sections were dewaxed prior to incubation in sirius red stain (0.036mM in saturated picric acid) for 2 hours, after 3 brief washes in acidified H<sub>2</sub>O the sections were dehydrated prior to mounting and analysis with a Leica upright microscope. (All images shown are x20 magnification).

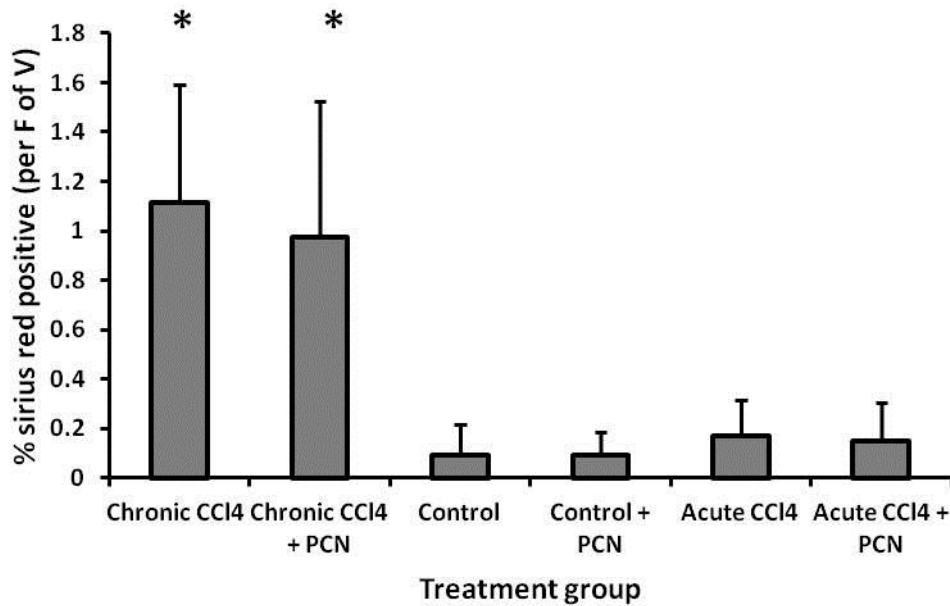


**Figure 5.16 Sirius red IHC quantification.** Sirius red positive staining was quantified using Qwin software (Leica); briefly 10 random images were captured for each section and blindly quantified to determine the positive sirius red stain per field of view. The data are the mean and SD n=30 of percentage area of the stain for each treatment group and were tested for statistical significance using an ANOVA. \* denotes there was a statistically significant increase in sirius red positive cells in comparison to the control groups ( $p < 0.0001$ ).

NIMP IHC staining was also performed to detect the presence of neutrophils in the liver tissue; neutrophils are the hallmark inflammatory cell recruited to the liver during the innate immune/ inflammatory response after liver injury [34, 228]. If PCN has had an anti-inflammatory effect this could be displayed by a reduction in the number of NIMP positive cells present in the CCl<sub>4</sub> treated livers after PCN treatment. Figure 5.17 is a typical image from each treatment group; it was clear there were an increased number of NIMP positive cells in all the CCl<sub>4</sub> treatment groups when compared to the control groups. The mean number of NIMP positive cells was quantified per field of view for each treatment group and these counts are shown in figure 5.18. There was a statistically significant increase in the number of NIMP positive cells in all CCl<sub>4</sub> treatment groups when compared to the controls ( $p < 0.0001$ , ANOVA). There was no difference in the level of NIMP positive cells in the chronic CCl<sub>4</sub> treatment group following PCN treatment, however there was a statistically significant reduction in the number of NIMP positive cells in the acute CCl<sub>4</sub> treatment group when also dosed with PCN ( $p < 0.001$ , ANOVA).

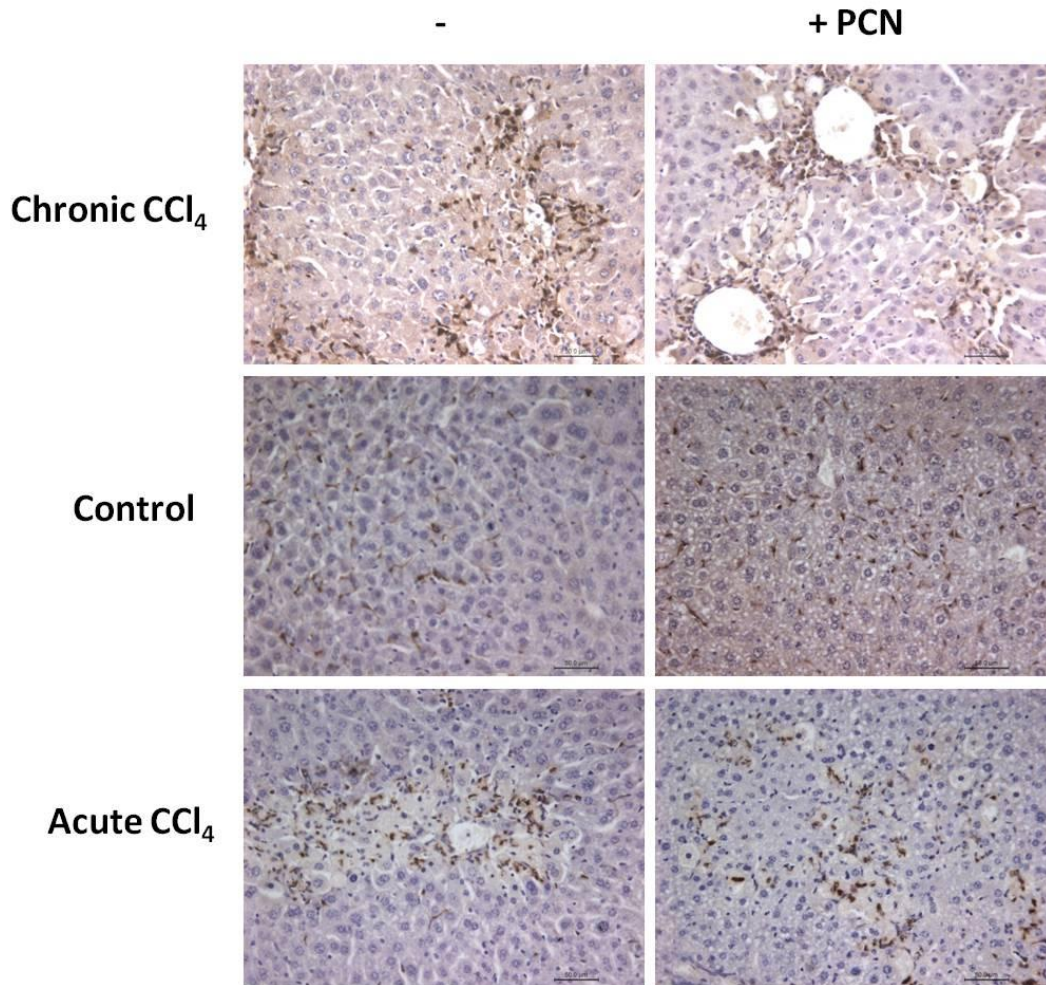


**Figure 5.17 NIMP IHC analysis of liver tissue from each treatment group.** Liver tissue was fixed in 10% formalin prior to paraffin embedding, 5 $\mu$ M sections were cut for each animal. Sections were dewaxed prior to blocking of endogenous peroxidase activity and heat induced antigen retrieval. Followed by serum blocking and incubation for an hour at room temperature with NIMP primary antibody, after PBS washing and addition of the complementary secondary antibody the level of bound antibody was detected by DAB incubation. The sections were counterstained with haematoxylin and dehydrated prior to mounting and analysis with a Leica upright microscope. (All images shown are x20 magnification). NIMP positive neutrophils were detected in all treatment groups, although at increased levels in all CCl<sub>4</sub> treatment groups.

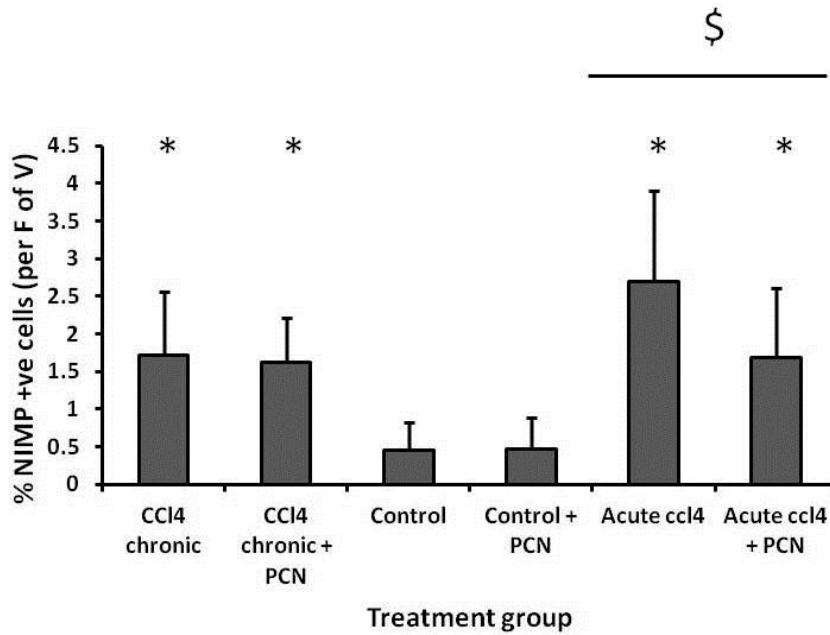


**Figure 5.18 NIMP IHC quantification.** NIMP positive staining was quantified using Qwin software (Leica); briefly 10 random images were captured for each section and blindly quantified to determine the positive NIMP stain per field of view. The data are the mean and SD n=30 of percentage area of the stain for each treatment group and were tested for statistical significance using an ANOVA, \* denotes a significant increase in NIMP positive cells when compared to the control groups ( $p < 0.0001$ ) and \$ denotes a statistically significant decrease in NIMP positive cells following PCN administration using an ANOVA ( $p < 0.001$ ).

These findings (5.18) further support the whole body *ex vivo* organ scans, and specifically the liver homogenate findings. Indicating further that PCN is anti-inflammatory and may be of use in combating liver fibrosis, shown by the statistically significant decrease in the number of NIMP positive inflammatory cells in the acute CCl<sub>4</sub> treated livers following PCN treatment ( $p < 0.001$ , ANOVA).

Finally an antibody specific to firefly-luciferase was purchased, as its detection in the liver tissue would correlate directly to the level of transgene activity (i.e. NF- $\kappa$ B activity). Following the manufacturers' guidelines the antibody was trialled at a range of dilutions (1/50 – 1/500). The images in figure 5.19A display the high level of non-specific binding encountered, and also that transgene levels are abnormally low. Tissue sections from CCl<sub>4</sub> treated mice of a separate study that did not contain the luciferase transgene were also stained (Figure 5.19B). It was clear from the high level of background signal encountered in these images that the antibody was not specific to firefly-

luciferase. A replacement antibody was obtained but the same issues were encountered, therefore the antibody was trialled in a Western blotting method to see if variations in the level of luciferase protein expressed in individual liver protein samples from each treatment group could be detected.

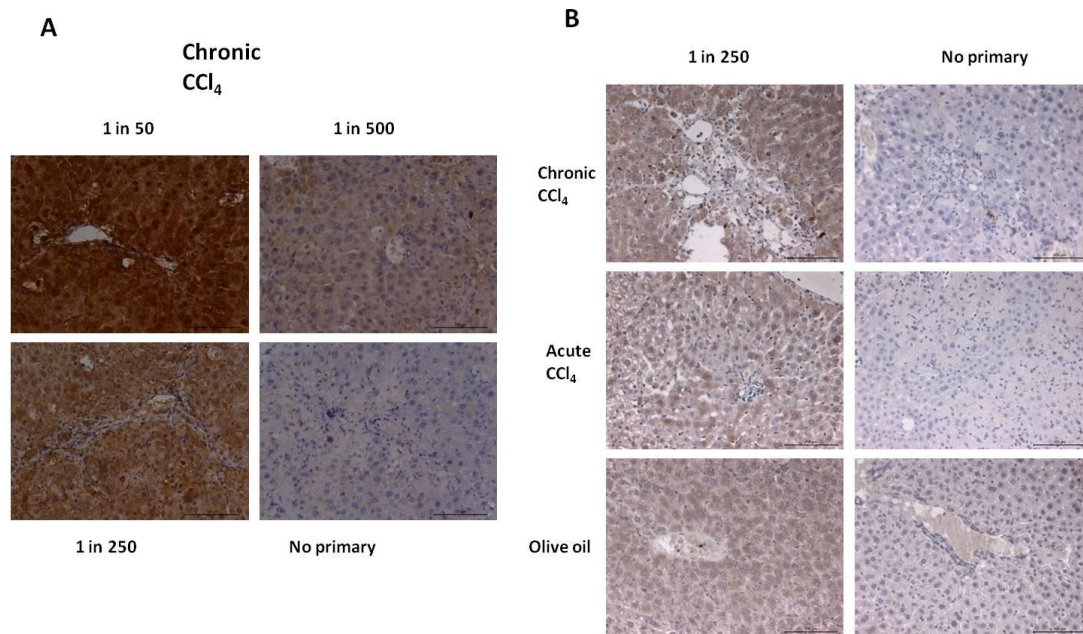


**Figure 5.19 A Optimisation of luciferase IHC analysis of liver tissue from each treatment group. B Repetition of 1/250 primary antibody dilution in non transgenic mice.** Liver tissue was fixed in 10% formalin prior to paraffin embedding, 5 $\mu$ m sections were cut for each animal. Sections were dewaxed prior to blocking of endogenous peroxidase activity and heat induced antigen retrieval. Followed by serum blocking and incubation for an hour at room temperature with luciferase primary antibody at multiple dilutions, after PBS washing and addition of the complementary secondary antibody the level of bound antibody was detected by DAB incubation. The sections were counterstained with haematoxylin and dehydrated prior to mounting and analysis with a Leica upright microscope. (All images shown are x20 magnification). It is clear that the antibody is not specific to firefly-luciferase as there are high background signals at all initial dilutions and it binds to a protein present in the non-transgenic mice as well.

Protein samples were isolated and quantified as outlined in methods 2.7, before performing the SDS-PAGE and Western blotting steps. The final developed membrane is shown in figure 5.20A; there are multiple bands in all lanes, including the negative control from wildtype mice (that do not contain the firefly-luciferase transgene). Unfortunately none of these bands were of the correct size (62 kDa as outlined in the manufacturer's guidelines). To act as a positive control Cos7 cells were transfected with the pGL3 control vector (Promega) (as this contains multiple copies of the firefly-luciferase gene). Transfection was confirmed by a luciferase assay of untransfected and pGL3

control transfected Cos7 cells (Figure 5.20B); protein was subsequently isolated from these cells as outlined in methods 2.7. A firefly-luciferase Western was performed with the Cos7 + pGL3 control protein samples included alongside the individual treatment groups (Figure 5.21). There was a weak band detected that was only present in the Cos7 + pGL3 control lane slightly smaller than the predicted product size (62 kDa) suggesting that the antibody does function and detect firefly-luciferase. There were no bands of the correct size or similar to that detected in the Cos7 + pGL3 control lane in any of the treatment group lanes; it is most likely the firefly-luciferase gene was not being expressed at a high enough level to be detected by the antibody, especially as there will be high levels of firefly-luciferase protein in the transfected Cos7 cells and yet only a weak protein band could be detected.

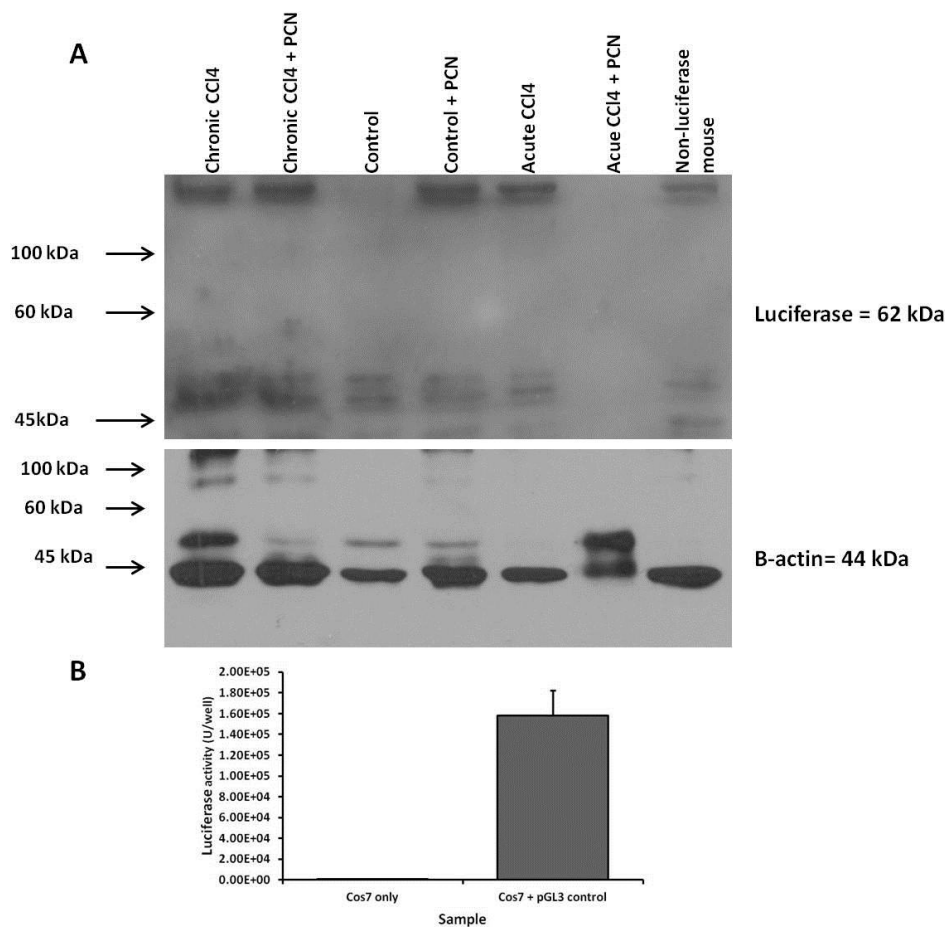


**Figure 5.20 A Firefly-luciferase western blot analysis of individual liver protein samples. B Firefly-luciferase activity of Cos7's transfected with pGL3 control plasmid.** Liver protein samples were taken diluted 1:1 with reducing loading buffer. After denaturation, 10 $\mu$ l of each sample was loaded onto a 9% acrylamide SDS-Page gel alongside and separated according to its size. Proteins were

transferred to a nitrocellulose membrane, blocked with 3% milk solution, and probed with anti firefly-luciferase antibody. Following incubation with a complimentary HRP-conjugated secondary antibody and washing, ECL reagent was added and the protein level detected by exposure to x-ray film. **B** Following transfection with pGL3 control plasmid a small aliquot of Cos7 protein was suspended in 1 x PLB, which was added to an equal volume of luciferase substrate prior to determination of luciferase activity using a bench top luminometer. The data shown is the mean and SD for 3 separate samples.

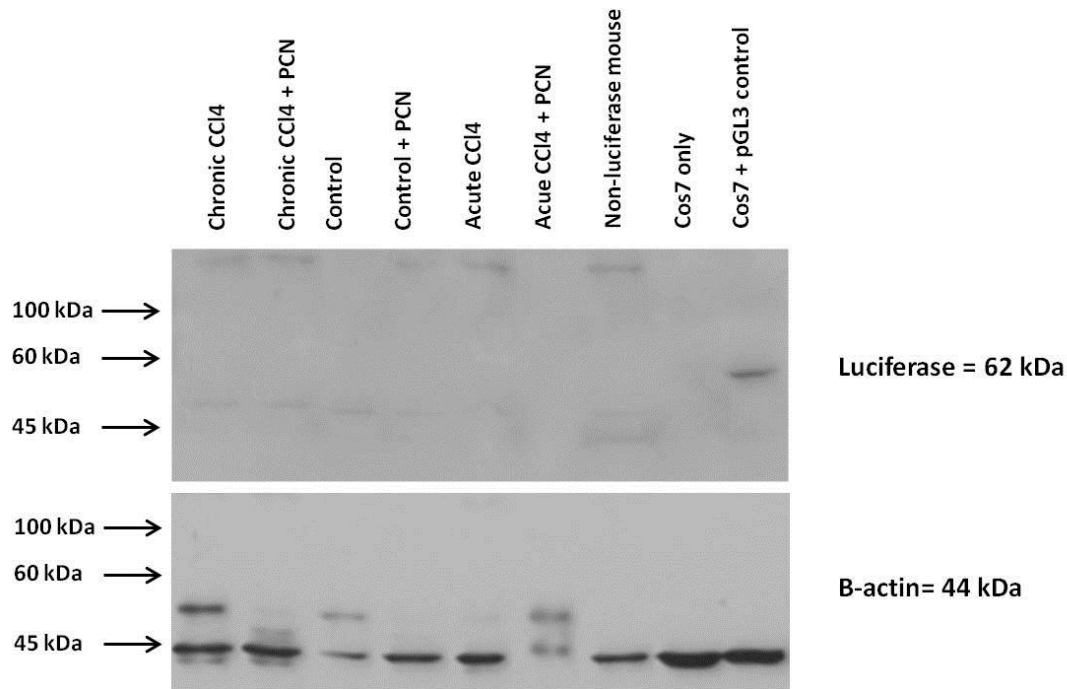


**Figure 5.21 Firefly-luciferase western blot analysis of individual liver protein samples and Cos7 + pGL3 control plasmid (positive control).** Liver protein samples were taken diluted 1:1 with reducing loading buffer. After denaturation, 10 $\mu$ l of each sample was loaded onto a 9% acrylamide SDS-Page gel alongside and separated according to its size. Proteins were transferred to a nitrocellulose membrane, blocked with 3% milk solution, and probed with anti firefly-luciferase antibody. Following incubation with a complimentary HRP-conjugated secondary antibody and washing, ECL reagent was added and the protein level detected by exposure to x-ray film.

## 5.4 Chapter discussion

The continuing escalation in the incidence of liver fibrosis and its endpoint cirrhosis [24] highlight the need for the development of novel anti-fibrotic treatment regimens. At present the only recognised treatment is transplantation but the lack of suitable donors make this a viable treatment option for only a small proportion of patients. A number of potential avenues of treatment are being investigated at present including induction of hepatic myofibroblast apoptosis and increasing MMP activity (see section 1.3 for more information). The induction of hepatic myofibroblast apoptosis is known to be mediated via the inhibition of the pro-inflammatory transcription factor NF- $\kappa$ B,

which is prominent in the maintenance of the liver fibrosis by preventing hepatic myofibroblast apoptosis [90, 91, 229].

A relatively unstudied area except for previous work within this laboratory [172-174] highlighted the anti-fibrotic benefits of PXR activators. In other diseases (most notably IBD) the anti-inflammatory effects of PXR activators have been shown to be mediated via inhibition of NF- $\kappa$ B activity [166, 170]. In this chapter we wished to ascertain whether the mode of action of PXR activators in the liver was also via NF- $\kappa$ B inhibition. To investigate this, NF- $\kappa$ B luciferase transgenic mice were administered CCl<sub>4</sub> both chronically and acutely to induce liver damage prior to administration of the rodent specific PXR activator PCN. If, as hypothesised, the mode of action was via NF- $\kappa$ B inhibition there will be a reduction in the level of luciferase transgene activity in the PCN treated mice following optical imaging when they are compared to the CCl<sub>4</sub> only treated mice.

Data presented in this chapter shows that the beneficial anti-fibrotic properties of PXR activators are mediated via NF- $\kappa$ B activity *in vivo*. Administration of PCN to both acute and chronic CCl<sub>4</sub> treated mice did not appear to reduce the level of NF- $\kappa$ B activity in the liver detected in the whole body scans performed 6 hours after PCN administration (Figure 5.3) and this was confirmed by the total luminescence values calculated (Figure 5.4B). The whole body scans and total luminescence calculations performed 24 hours after PCN administration (Figure 5.5) support the initial hypothesis, with a clear reduction in NF- $\kappa$ B activity of both the acute and chronic CCl<sub>4</sub> treatment groups following PCN treatment. This difference was statistically significant for the chronic CCl<sub>4</sub> treatment group ( $p < 0.0087$ , ANOVA), supporting our initial hypothesis that PCN is anti-inflammatory. The data from the *ex vivo* organ scans mirrored the 24 hour whole body data as there was a statistically significant reduction in the total liver luminescence in the chronic CCl<sub>4</sub> treatment group following PCN treatment (Figure 5.9B) ( $p < 0.012$ , ANOVA).

Subsequent analysis of the liver homogenates by luciferase assays to detect transgene activity and NF- $\kappa$ B induction mirrored the earlier 24 hour whole body data (Figure 5.10). However the statistically significant reduction in NF- $\kappa$ B activity as a result of PCN administration was detected in the acute CCl<sub>4</sub>

treatment group ( $p < 0.0068$ , ANOVA). It was unclear why PCN only had an effect on the acute  $\text{CCl}_4$  treated mice and not chronic  $\text{CCl}_4$  treated liver homogenates as found in the earlier scans. The only reason I can postulate was that the small animal numbers in each treatment group may have influenced the findings, especially as both the acute and chronic  $\text{CCl}_4$  mice also administered PCN luminescence levels had been reduced to a level similar to that of the control groups.

Biochemical and IHC analyses confirmed the successful induction of centrilobular liver damage, shown firstly by increased ALT serum levels in all  $\text{CCl}_4$  treatment groups (Figure 5.11B). In addition the IHC analysis performed confirmed this, displayed by the increased number of inflammatory cells present in the H&E sections of both  $\text{CCl}_4$  treatment groups (Figure 5.12). Increased  $\alpha\text{SMA}$  positive hepatic myofibroblasts (Figure 5.13) and sirius red positive collagens (Figure 5.15) were only detected in the chronic  $\text{CCl}_4$  treatment group as they are associated with chronic liver injury and a single  $\text{CCl}_4$  dose was not sufficient for either hepatic myofibroblast formation or collagen deposition.

IHC analysis of the neutrophils by NIMP staining was also performed (Figure 5.17), as neutrophil recruitment to the liver is a critical step in the initial inflammatory response following liver injury and will contribute to the perpetuation of liver injury and subsequent fibrosis development. The images (Figure 5.17) show that there was background inflammation displayed by the presence of NIMP positive neutrophils in the control groups, however there was an increased number of these cells in both the chronic and acute  $\text{CCl}_4$  treatment groups. When quantified blindly using the supplied Qwin software, there was a statistically significant decrease in the number of NIMP positive neutrophils present in the acute  $\text{CCl}_4$  treatment group following PCN treatment ( $p < 0.0001$ , ANOVA) (Figure 5.24). These data supports the earlier whole body luminescent and *ex vivo* organ scans favouring the hypothesis that PCN is anti-inflammatory and this effect is mediated via NF- $\kappa\text{B}$ .

Finally firefly-luciferase IHC was performed to try and establish in which cells the NF- $\kappa\text{B}$  transgene was activated; unfortunately the antibody was not specific to firefly-luciferase shown by the high background levels detected

following DAB incubation (Figure 5.19). Western blotting utilising the firefly-luciferase antibody on liver protein samples isolated from each individual treatment group yielded similar results (Figure 5.20A). The antibody was unable to detect firefly-luciferase in any of the protein samples, but functioning of the antibody was confirmed by repeated Western blotting including a positive control sample (Cos7 protein transfected with the pGL3 control plasmid) (Figure 5.21).

The majority of the data presented in this chapter confirms our initial belief that PXR agonists have beneficial anti-inflammatory properties mediated via NF- $\kappa$ B functioning. Although not all the findings were within the range of statistical significance, it was likely this was due to the nature of the *in vivo* study (requiring multiple injections of both CCl<sub>4</sub> and D-luciferin when imaging). Combined with the small number of animals in each treatment group any variations in dosing as a result of human error will have influenced the level of inflammation detected.

If the experiment was repeated in the future it may be beneficial to increase the dilution of CCl<sub>4</sub> in olive oil vehicle, therefore a greater volume will be injected to achieve the same dose (i.e. 120 $\mu$ l instead of 40 $\mu$ l per 20g mouse) and will minimise any potential variation in dosing. Obviously the number of mice in each treatment group could also be increased to improve the power of any findings.

As found previously PCN administration has not affected CCl<sub>4</sub> hepatotoxicity, as determined by serum ALT levels and H&E IHC analysis [172]. The beneficial anti-inflammatory properties of PCN treatment are displayed by the reduction of luciferase transgene activity in the optical images and the reduction of NIMP positive neutrophils in liver tissue detected by IHC following PCN administration.  $\alpha$ SMA and sirius red IHC indicated that PCN treatment has no beneficial anti-fibrotic properties in contrast to previous findings [172], although in this study PCN was only administered with the final dose of CCl<sub>4</sub>, whilst it was administered chronically (twice weekly) in the earlier study alongside CCl<sub>4</sub> administration. Therefore fibrosis development will have already occurred during the initial 4 weeks of CCl<sub>4</sub> treatment in this study unchecked by PXR activation. A repeat study utilising the dosing regimen of

the earlier study (twice weekly injection of PCN dissolved in the CCl<sub>4</sub>/ olive oil vehicle solution) could confirm the dual anti-fibrotic and anti-inflammatory properties of PCN following chronic liver injury.

Performing these further studies to support the initial data presented in this chapter will further advocate the potential use of PXR agonists as an anti-fibrotic treatment agent, and confirm that this response is mediated via the inhibition of NF-κB activity.

**Chapter 6.0 - Uncovering hepatic myofibroblasts inflammatory potential *in vitro* and *in vivo***

## 6.1 Introduction

As outlined in section 1.1.2, liver fibrosis development is due to a combination of the wound healing, immune and inflammatory system responses after liver insult [32, 217]. The transdifferentiation of quiescent HSCs to hepatic myofibroblasts is the crucial step in fibrosis development, as hepatic myofibroblasts are the major fibrogenic cell responsible for the increased deposition of ECM proteins (e.g. collagen type I) [230]. It is still not clear where the initiating signal for fibrosis development comes from, although it is thought to be from monocytes/ macrophages inducing inflammation and subsequent quiescent HSC activation [3]. It is well documented that there are different populations of hepatic myofibroblasts present in the liver with heterogeneous expression of various genes [36, 109, 231-233]. In this chapter we propose that a sub-set of hepatic myofibroblasts are pro-inflammatory and may themselves stimulate the activation of circulating monocytes/ macrophages responsible for the amplification of the inflammatory cycle central in liver fibrosis development (Figure 6.1).

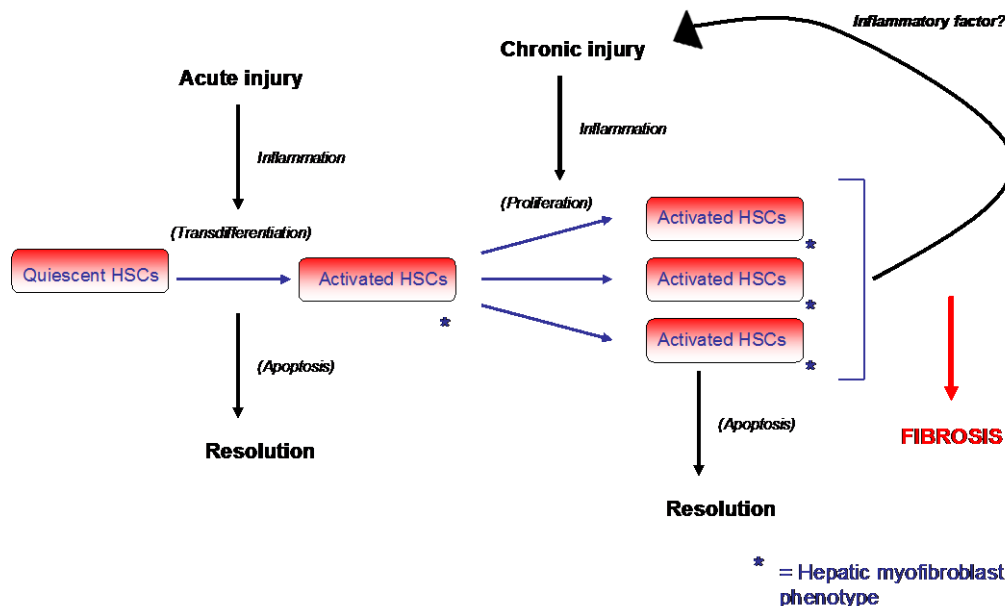


**Figure 6.1 Schematic illustration showing HSC transdifferentiation to hepatic myofibroblasts during chronic liver injury.** Outlining the potential mechanism by which hepatic myofibroblasts may activate the inflammatory cycle and maintain fibrosis perpetuation.

To investigate whether there was communication between monocytes/macrophages and hepatic myofibroblasts and specifically that hepatic myofibroblasts are pro-inflammatory a simple *in vitro* experiment was designed. Hepatic myofibroblasts were cultured with the monocytic U937-NF- $\kappa$ B cell line; U937-NF- $\kappa$ B cells contain the firefly-luciferase transgene under the control of a concatemer of NF- $\kappa$ B response elements. NF- $\kappa$ B is a major pro-inflammatory transcription factor responsible for the activation of a number of downstream inflammatory genes/ processes (e.g. IL-1, TRAF1). Following co-culture, a luciferase assay on the U937-NF- $\kappa$ B cell pellet will reveal if hepatic myofibroblasts activate NF- $\kappa$ B in U937-NF- $\kappa$ B cells. Figure 6.2 is a typical image taken on a light microscope showing the general morphology of the individual cell lines and the LX-2 and U937-NF- $\kappa$ B cells together in co-culture.

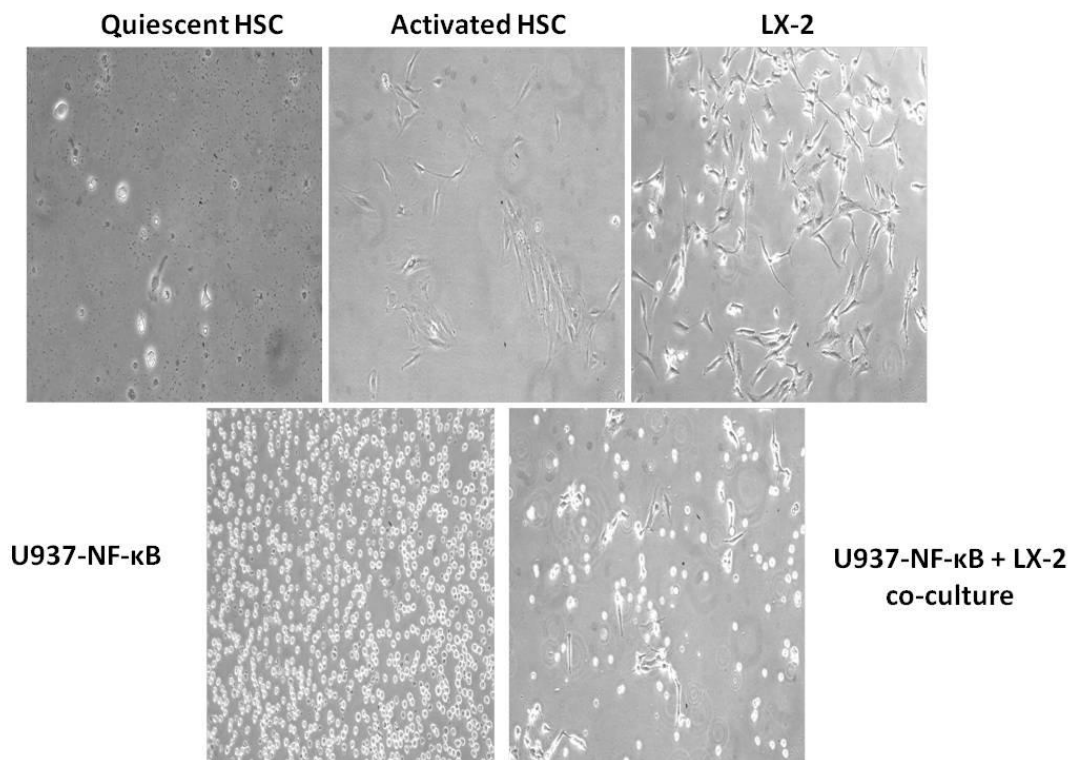


**Figure 6.2** General morphology of quiescent and activated HSCs, LX-2 and U937-NF- $\kappa$ B cell lines. Highlighting the difference between quiescent and activated HSCs (myofibroblast phenotype) and also the fact U937-NF- $\kappa$ B cells are a suspension culture and therefore the two can be cultured together.

Secondly utilising the NF- $\kappa$ B luciferase mice used earlier in chapter 5, I wish to determine the inflammatory properties of hepatic myofibroblasts *in vivo*

when they are injected directly into NF- $\kappa$ B luciferase mice. Performing luminescent scans following hepatic myofibroblast and  $\beta$ -luciferin administration it will be possible to detect the level of inflammation (NF- $\kappa$ B activity) in every cell of the body and determine if hepatic myofibroblasts are inflammatory as hypothesised. More interestingly, it will be possible to see whether this inflammation was located solely in the liver or if it affects other areas of the body as a systemic response.

## 6.2 Generation of a NF- $\kappa$ B luciferase reporter construct and stable transfection of U937 cells

The experiments reported in section 6.3 were initially performed in U937-NF- $\kappa$ B cells donated by Dr Harald Carlsen [187]. However issues were encountered when reviving the cells and selecting for successful transfectants with *Hygromycin B* treatment, as the cells would spontaneously lose all luciferase activity. The *Hygromycin B* selection marker was transfected into the U937-NF- $\kappa$ B cells in a separate vector to the NF- $\kappa$ B response element and luciferase gene (Harald Carlsen, personal communication). If this was the case the recommended *Hygromycin B* treatment may not select for cells containing the luciferase transgene (i.e. those which did not contain both vectors) leading to the loss of all luciferase activity. To avoid this issue untransfected U937s were purchased (ECACC) and the transfection procedure repeated in house with a concatemer of NF- $\kappa$ B response elements inserted into a vector that contains the firefly-luciferase gene.

Firstly the pGL4.28 vector was purchased from Promega, which encodes the firefly-luciferase reporter gene luc2CP. pGL4.28 also contains a multiple cloning region for insertion of DNA sequences (in this case 3xNF- $\kappa$ B response elements) upstream of the minimal promoter and luc2CP gene, and the vector backbone contains a mammalian selection marker for *Hygromycin B* resistance. A DNA fragment (3xNF- $\kappa$ B) was designed consisting of 3 repeats of the consensus NF- $\kappa$ B response element sequence (Figure 6.3A) and its complementary sequence. Sticky ends flanking the insert were designed specifically to restriction sites XhoI and BglII, which are also located within the

multiple cloning region of pGL4.28 at positions 34 and 47. A schematic diagram of the pGL4.28 vector is shown in figure 6.3B.

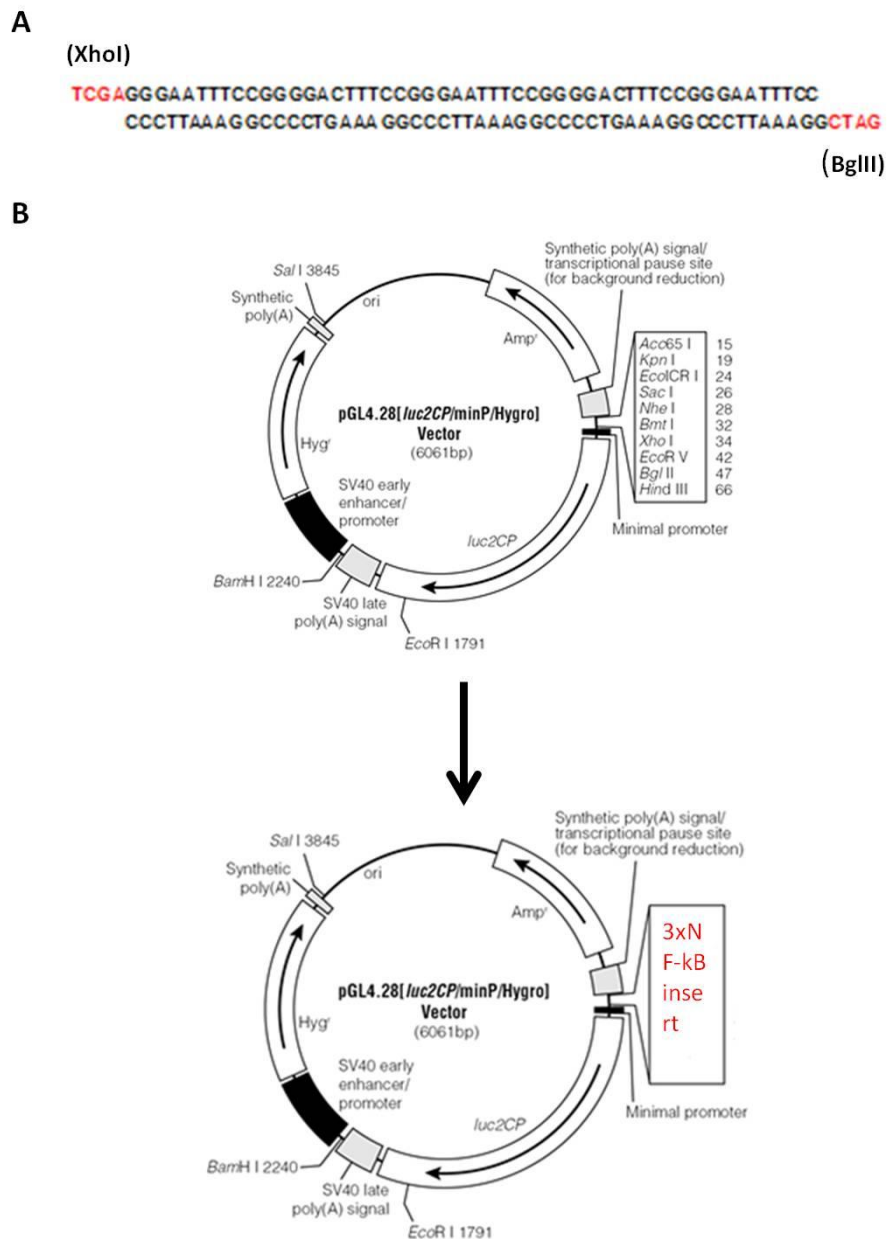


**Figure 6.3 Generation of NF-κB luciferase reporter construct.** A 3xNF-κB insert was designed containing a concatamer of 3 x NF-κB response elements flanked by XhoI and BglII restriction enzyme sites. B pGL4.28 vector outline and outline of pGL4.28 vector with insertion of the 3xNF-κB insert.

The two complementary NF-κB response element sequences were annealed together by heating at 90 °C for 5 minutes before reduction of the temperature by 1 °C every minute from 90 °C to 50 °C. The pGL4.28 vector was linearised by a double restriction digest with XhoI and BglII, the linearised vector was separated from the fragment between the two restriction sites by agarose gel

electrophoresis (Figure 6.4A) and the linearised DNA fragment was purified from the agarose gel as described in section 2.5.7.

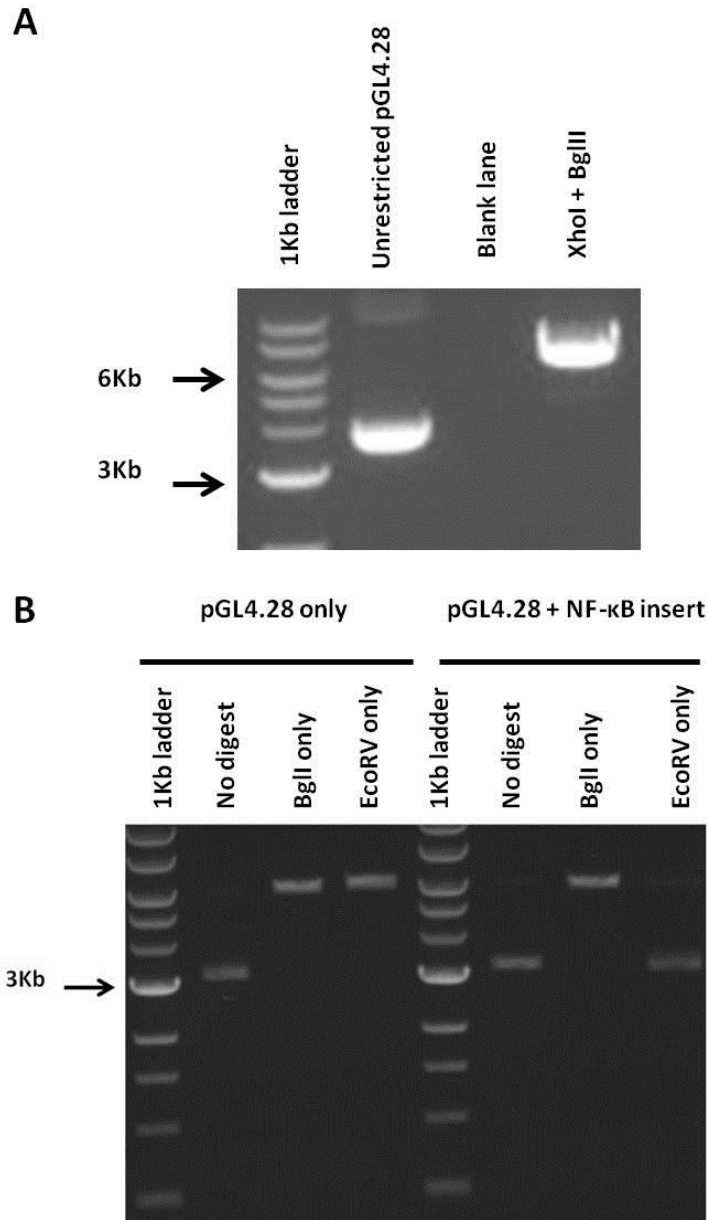


**Figure 6.4 Restriction digests to confirm insertion of the 3xNF- $\kappa$ B insert.** **A** XhoI + BglII double digest to linearise plasmid prior to ligation of 3xNF- $\kappa$ B insert into it. **B** EcoRV restriction digest to screen for correctly assembled NF- $\kappa$ B luciferase reporter construct (shown by loss of EcoRV restriction site).

The 3xNF- $\kappa$ B DNA fragment was subsequently ligated into the linearised vector as outlined in section 2.5.8. Successful ligation will result in the loss of the EcoRV restriction site in the multiple cloning region; therefore clones were screened by an EcoRV restriction digest. Figure 6.4B is an agarose gel

showing the successful ligation of the 3xNF- $\kappa$ B insert into the pGL4.28 vector; specifically it was shown by the identical migration of the pGL4.28-NF- $\kappa$ B recombinant vector when treated with EcoRV to the unrestricted pGL4.28 vector. The successful clones were subsequently sent for sequencing analysis to confirm the entire 3xNF- $\kappa$ B insert sequence had been ligated in the correct orientation (Figure 6.5).

```

nfkb      -----
miniprep  AAGGATAAGTAAGTAATATTAAGGTACGGGAGGTATTGGACAGGCCGCAATAAAATATCT
900

nfkb      -----
miniprep  TTATTTTCATTACATCTGTGTGTTGGTTTTTTGTGTGAATCGATAGTACTAACATACGCT
960

nfkb      -----
miniprep  CTCCATCAAAAACAAAACGAAACAAAACAACTAGCAAAATAGGCTGTCCCAGTGCAAGT
1020

nfkb      -----G 1
miniprep  GCAGGTGCCAGAACATTTCTCTGGCCTAACTGGCCGGTACCTGAGCTCGCTAGCCTCGAG
1080
*

nfkb      GGAATTTCCGGGGACTTTCCGGGAATTTCCGGGGACTTTCCGGGAATTTCC----- 52
miniprep  GGAATTTCCGGGGACTTTCCGGGAATTTCCGGGGACTTTCCGGGAATTTCCGATCTGGCC
1140
*****

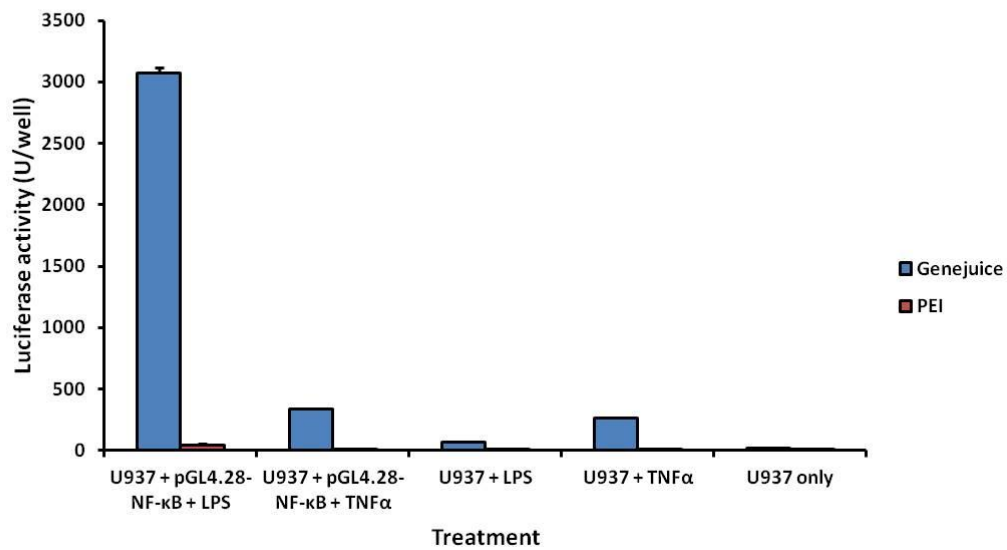
nfkb      -----
miniprep  TCGGCGCCAAGCTTAGACACTAGAGGGTATATAATGGAAGCTCGACTTCCAGCTTGGCA
1200

```

**Figure 6.5 pGL4.28-3xNF- $\kappa$ B luciferase reporter construct DNA sequencing.** Sequencing results from a single transformant miniprep highlighting the complete 3xNF- $\kappa$ B insert sequence in the correct orientation within the pGL4.28 plasmid.

Plasmid DNA was then isolated from successful clones prior to transient transfection into both Cos7 and U937 cells, which were then treated with LPS and TNF $\alpha$  to induce NF- $\kappa$ B and luciferase activity. Figure 6.6 shows that untransfected Cos7 and U937 cells expressed no luciferase activity when untreated and when treated with LPS. However both cell lines expressed a significant increase in luciferase activity after transfection with the pGL4.28 – NF- $\kappa$ B construct and treatment with LPS; indicating that the vector was functioning as intended. Stable transfection of U937s with the pGL4.28 –NF- $\kappa$ B vector was achieved by repeated treatment with the mammalian selection marker *Hygromycin B*.

A



B

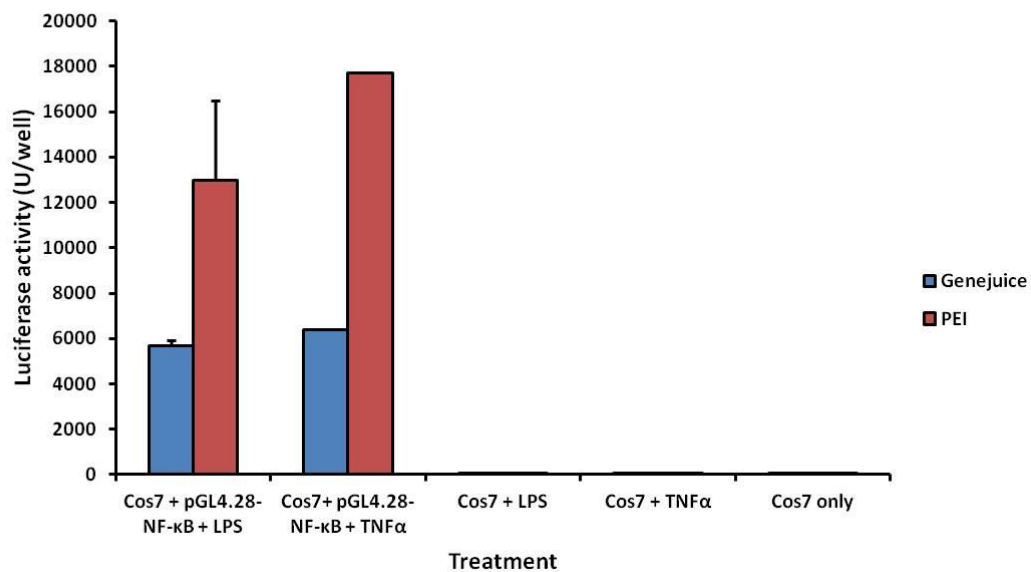


**Figure 6.6 Confirmation of NF- $\kappa$ B luciferase reporter construct functioning.** **A** U937 and **B** Cos7 were both transiently transfected (using Genejuice and PEI) with the NF- $\kappa$ B luciferase reporter construct prior to treatment with LPS and TNF $\alpha$ . There was a significant increase in luciferase activity following both LPS and TNF $\alpha$  treatment versus the untransfected control highlighting that the construct is responsive to inflammatory stimuli. Data are the mean and SD n=3.

### 6.3 LX-2 and hHSCs are pro-inflammatory when co-cultured with U937-NF- $\kappa$ B cells

Due to the lack of availability of hHSCs, the LX-2 cell line was used in their place. Initially LX-2 cells were incubated with U937-NF- $\kappa$ B cells to determine

the optimum incubation period for induction of the luciferase gene in co-culture. Figure 6.7 shows that LX-2 cells induce NF- $\kappa$ B activity in the U937-NF- $\kappa$ B cells at all time points, demonstrated by the increase in luciferase activity at all time points of LX-2/ U937-NF- $\kappa$ B cell co-culture. LPS was also added on its own as a positive control, as it has been previously shown to induce NF- $\kappa$ B and luciferase activity in U937-NF- $\kappa$ B cells [175]. From figure 6.7 it was also clear that a 6 hour incubation period yields the greatest increase in NF- $\kappa$ B activity, therefore all subsequent experiments were performed over 6 hours.

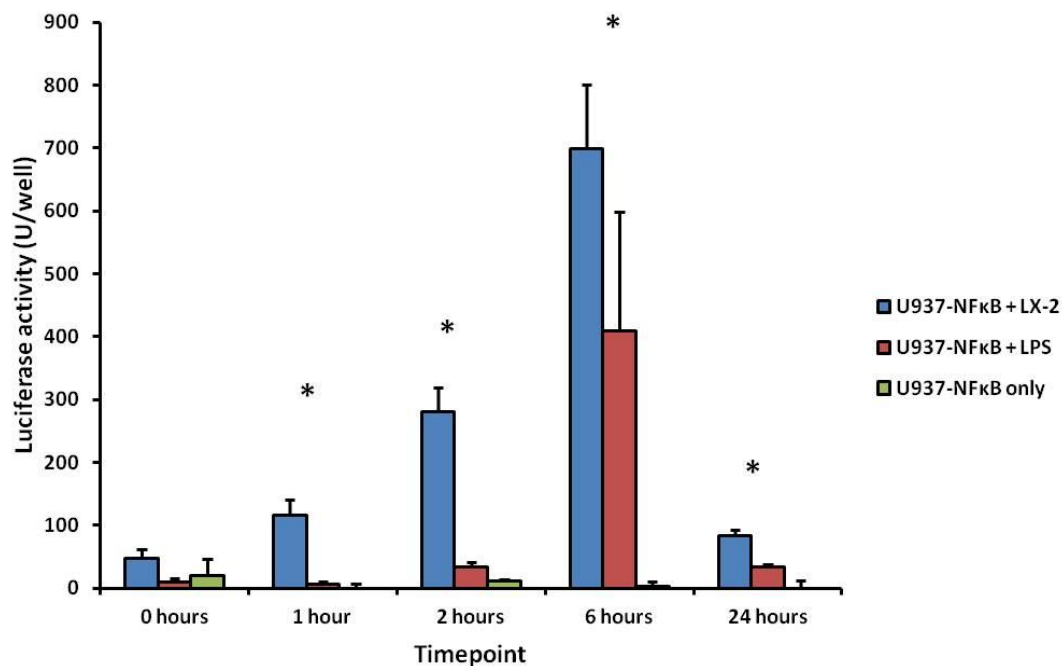


**Figure 6.7 LX-2's are pro-inflammatory and induce NF- $\kappa$ B activity in U937-NF- $\kappa$ B cells.** Co-culture of the hepatic myofibroblast LX-2 cell line with U937-NF- $\kappa$ Bs induced a significant increase in luciferase activity when compared to the U937-NF- $\kappa$ B only control at all time points. The most significant increase was seen following six hour incubation, therefore all future experiments utilised six hour incubation. (\* denotes a statistically significant increase ( $p < 0.0014$ ) in luciferase activity when compared to the U937-NF- $\kappa$ B only incubation, analysed using an ANOVA). Data are the mean and SD  $n=3$  from a single experiment, typical of three independently repeated experiments.

To confirm these initial findings U937-NF- $\kappa$ B cells were co-cultured with primary hHSCs at all stages after their initial isolation, from when they were still quiescent (48 hours after isolation), as they were transdifferentiating (8 days after isolation) and when they had fully transdifferentiated to a hepatic myofibroblast phenotype (following one passage). Figure 6.8 shows that hHSCs activate NF- $\kappa$ B in U937-NF- $\kappa$ B cells when cultured together, although

this inflammatory potential was only a trait of the activating (8 day old) HSCs, and increasing further as they develop a hepatic myofibroblast phenotype. There was no induction of NF- $\kappa$ B activity when U937-NF- $\kappa$ B cells were co-cultured with the freshly isolated quiescent hHSCs, as their primary function in the liver is the storage of retinoids [38]. These findings support our initial hypothesis that hepatic myofibroblasts are pro-inflammatory.

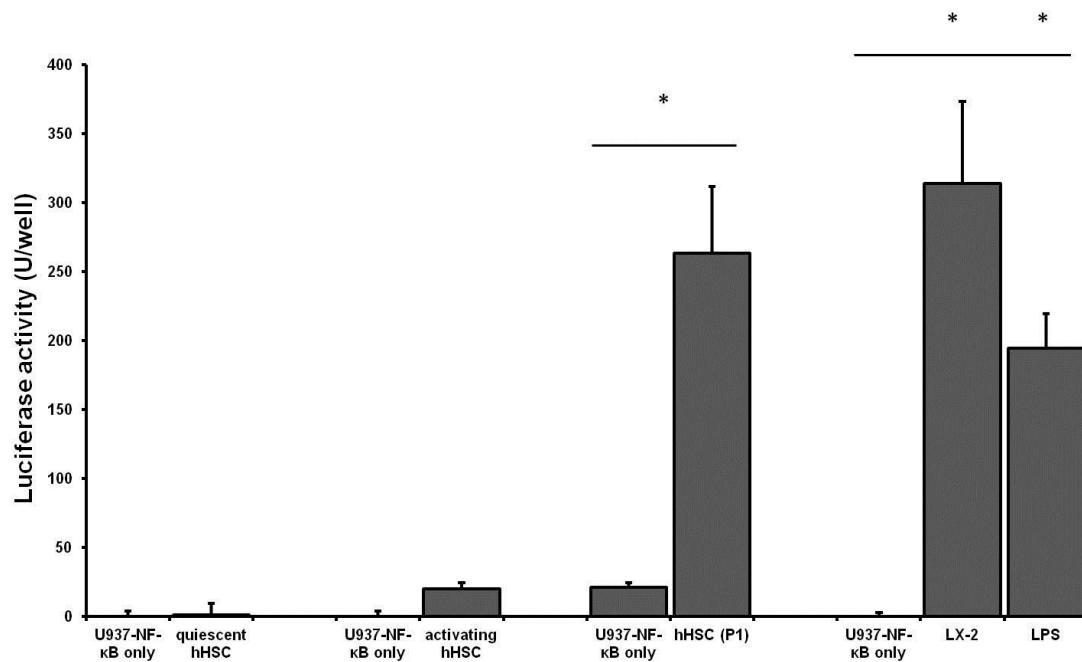


**Figure 6.8 hHSC co-culture induces NF- $\kappa$ B activity in U937-NF- $\kappa$ B cells.** HSCs were isolated and incubated with U937-NF- $\kappa$ B cells at various times after their initial isolation. A significant increase in luciferase activity was seen when the HSCs had transdifferentiated to a hepatic myofibroblast phenotype. (\* denotes a statistically significant increase ( $p < 0.0008$ ) in luciferase activity when compared to the U937-NF- $\kappa$ B only incubation, analysed using a student's t-test, unpaired). Data are the mean and SD  $n=3$  from a single experiment, typical of three independently repeated experiments.

### 6.3.1 LX-2s and hHSCs release a pro-inflammatory soluble factor

To determine whether contact between the LX-2 cells and U937-NF- $\kappa$ B cells was required for induction of NF- $\kappa$ B activity, U937-NF- $\kappa$ B cells were cultured in 48 hour LX-2 conditioned media for 6 hours as described in section 2.3.11. Figure 6.9A reveals that there was still activation of NF- $\kappa$ B in the U937-NF- $\kappa$ B cells when cultured in the LX-2 conditioned media suggesting a soluble factor

was released into the media. The level of induction by 48 hour LX-2 conditioned media was reduced when compared to the LX-2 co-culture findings, suggesting that direct contact between the cells may also play a role, in addition to the presence of the pro-inflammatory soluble factor released. Further studies demonstrated that it acts in a dose-dependent manner (Figure 6.9B); these findings were confirmed in hHSCs when identical experiments were performed (Figure 6.10).

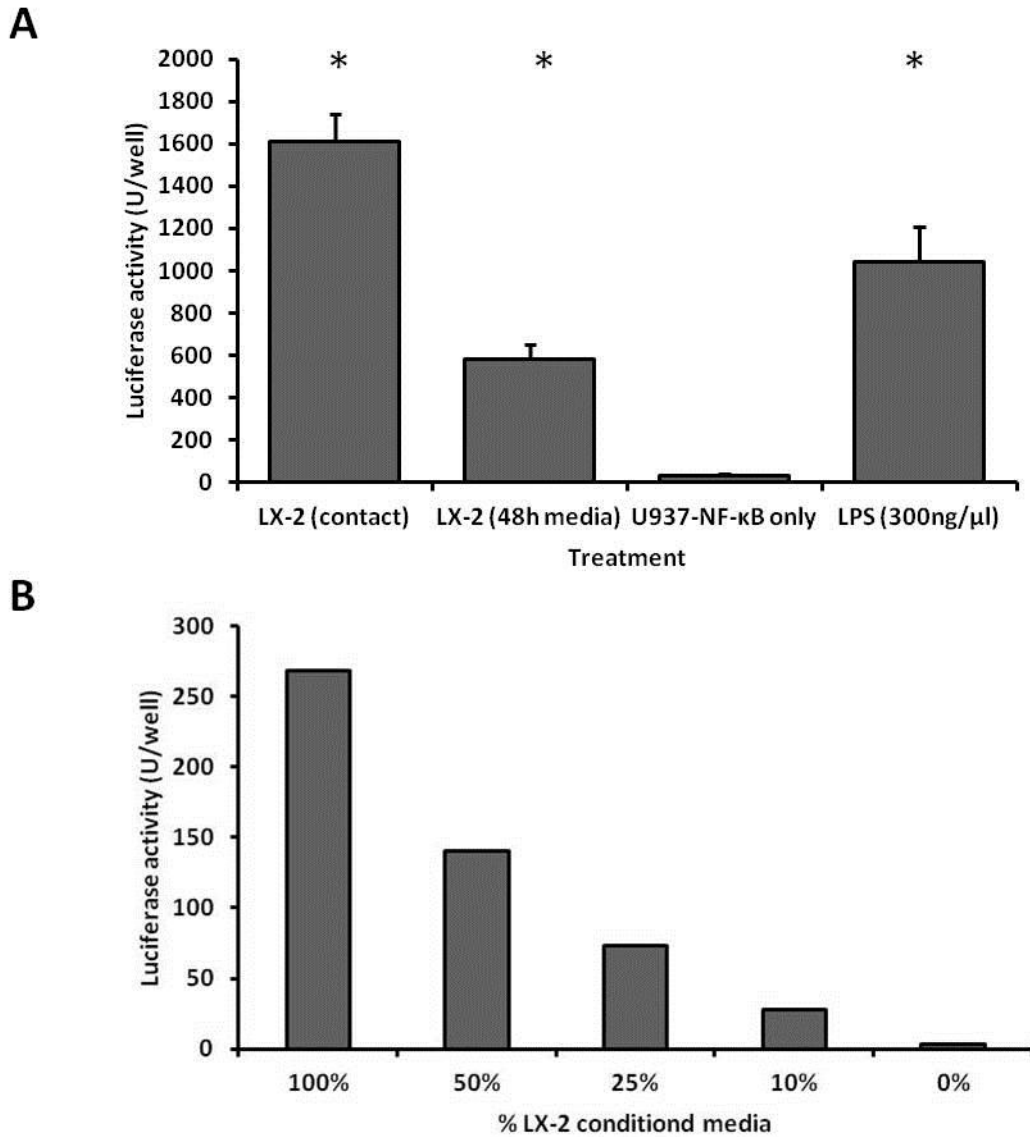


**Figure 6.9** LX-2's release a pro-inflammatory soluble factor that induces NF-κB activity in U937-NF-κB cells. **A** Culture of U937-NF-κB cells in 48 hour LX-2 conditioned media induced a statistically significant increase in NF-κB activity when compared to the U937-NF-κB only control. (\* denotes a statistically significant increase ( $p < 0.0001$ ) in luciferase activity when compared to the U937-NF-κB only incubation, analysed using an ANOVA). Data are the mean and SD  $n=3$  from a single experiment, typical of three independently repeated experiments. **B** The pro-inflammatory soluble factor was shown to act in a dose dependent manner ( $n=1$ ).

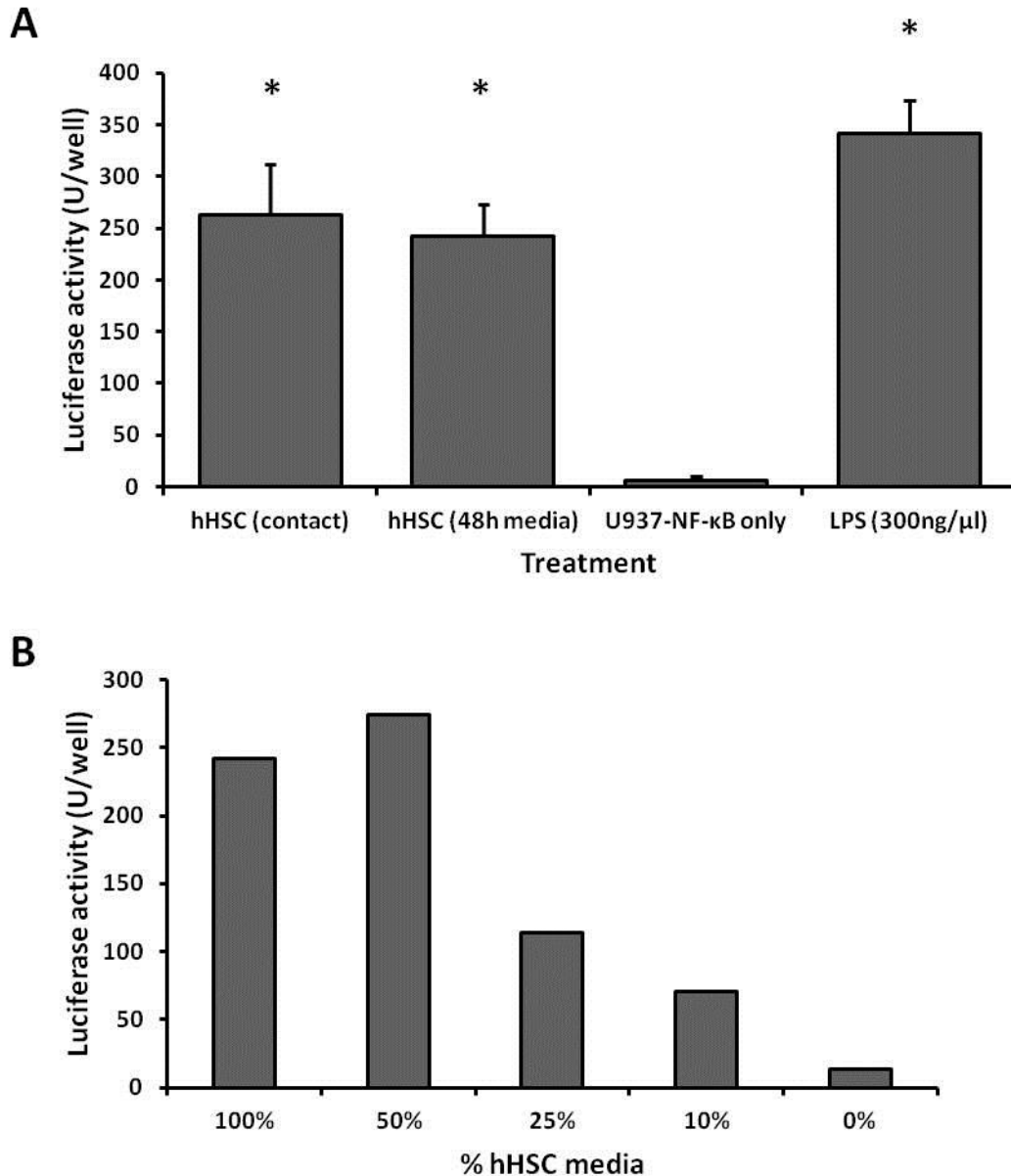


**Figure 6.10 hHSCs release a pro-inflammatory soluble factor that induces NF-κB activity in U937-NF-κB cells.** **A** Culture of U937-NF-κB cells in 48 hour hHSC conditioned media induced a statistically significant increase in NF-κB activity when compared to the U937-NF-κB only control. (\* denotes a statistically significant increase ( $p < 0.0001$ ) in luciferase activity when compared to the U937-NF-κB only incubation, analysed using an ANOVA). Data are the mean and SD  $n=3$  from a single experiment, typical of three independently repeated experiments. **B** The pro-inflammatory soluble factor was shown to act in a dose dependent manner ( $n=1$ ).

Previous unpublished work (Table 6.1) by members of this laboratory provided useful information regarding the cytokine profiles of all the major hepatic cell types. Of particular interest are the high levels of the pro-inflammatory cytokines IL-6 and IL-8 produced by hepatic myofibroblasts. Therefore U937-NF-κB cells were incubated with human recombinant IL-6

and IL-8 separately in place of LX-2 cells. IL-6 induced a statistically significant increase in luciferase activity when cultured with U937-NF- $\kappa$ B cells and IL-8 did not induce NF- $\kappa$ B activity in the U937-NF- $\kappa$ B cells as highlighted in figure 6.11. It was clear the induction of luciferase activity by IL-6 although significant was much lower when compared to LX-2 and LPS luciferase induction. IL-8 can be eliminated as the soluble factor released by LX-2 cells, but IL-6 although unlikely could be a contributing factor.

	Hepatocytes	Hepatic stellate cells	Kupffer cells	Monocytes	Macrophages
	pg.day <sup>-1</sup> . $\mu$ g cell protein <sup>-1</sup>				
<b>IL-1<math>\beta</math></b>	<b>n/d</b>	<b>n/d</b>	<b>0.09 - 0.17</b>	<b>0.00 - 3.6</b>	<b>0.00 - 0.017</b>
IL-2	n/d	n/d	n/d	n/d	n/d
IL-4	n/d	n/d	n/d	n/d	n/d
<b>IL-6</b>	<b>n/d</b>	<b>2 - 20</b> <b>increases with trans-differentiation to pro-fibrogenic phenotype</b>	<b>0 - 0.53</b>	<b>0.08 - 19.7</b>	<b>0.006 - 0.159</b>
IL-7	n/d	n/d	n/d	0 - 0.015	n/d
<b>IL-8</b>	<b>2 - 4</b>	<b>8 - 80</b> <b>decreases with trans-differentiation to pro-fibrogenic phenotype</b>	<b>1.6 - 7.2</b>	<b>4.06 - 8.76</b>	<b>5.38 - 14.5</b>
<b>IL-10</b>	n/d	n/d	n/d	<b>0.019 - 0.53</b>	<b>0.00 - 0.026</b>
IL-12	n/d	n/d	n/d	<b>0 - 0.02</b>	n/d
GM-CSF	n/d	n/d	n/d	<b>0 - 0.264</b>	<b>0.00 - 0.031</b>
<b>IFN<math>\gamma</math></b>	<b>n/d</b>	<b>n/d</b>	<b>1.3 - 1.8</b>	<b>0 - 0.062</b>	n/d
<b>TNF<math>\alpha</math></b>	n/d	n/d	n/d	<b>0.00 - 3.28</b>	<b>0.00 - 0.035</b>
<b>TNF<math>\alpha</math></b> (LPS-stimulated)	<b>n/d</b>	<b>n/d</b>	<b>0.04 - 1.06</b>	<b>4.46 - 12.3</b>	<b>0.58 - 15.7</b>

Table 6.1 – Cytokine profiles of major hepatic cell types (unpublished work by Angela Douglass).

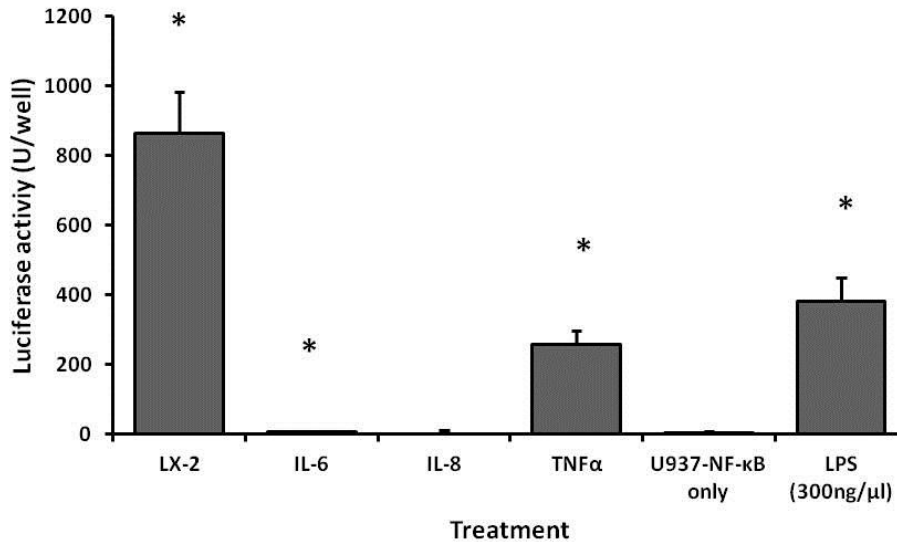


**Figure 6.11 Treatment of U937-NF-κB cells with IL-6 and IL-8 does not induce NF-κB activity in U937- NF-κBs.** Human recombinant pro-inflammatory cytokines IL-6 and IL-8 (10ng/ml) were added to U937-NF-κB cells as previous unpublished work from within this laboratory (Table 6.1) highlighted both these cytokines are found at increased levels in both hHSCs and LX-2's during fibrosis development. (\* denotes a statistically significant increase ( $p < 0.0017$ ) in luciferase activity when compared to the U937-NF-κB only incubation, analysed using a student's t-test, unpaired). Data are the mean and SD  $n=3$  from a single experiment, typical of three independently repeated experiments.

### **6.3.2 The pro-inflammatory soluble factor released by LX-2 cells is a small (<1kDa) non peptide**

To determine the identity of the pro-inflammatory soluble factor released by LX-2 cells, a range of treatments were performed to LX-2 conditioned media prior to the resuspension and culture of U937-NF-κB cells in it (see Table 2.2 for a full description of individual treatments performed).

Figure 6.12A shows firstly that the soluble factor was not affected by either heating at 90 °C or protease treatment with 10 x trypsin-EDTA, indicating that its activity is heat and trypsin resistant. Secondly removal of the endogenous steroids and other similar chemical species present in the media by charcoal/dextran stripping of the conditioned media did not alter induction of NF-κB and luciferase activity in the U937-NF-κB cells. Separation of the organic and aqueous fractions of conditioned media and the resuspension of U937-NF-κB cells in each fraction showed that the soluble factor was located in neither the aqueous or organic phase. Initially it was not possible to resuspend U937-NF-

$\kappa$ B cells in the organic phase as it resulted in their death (gauged by trypan blue viability). To counteract this, the organic phase was evaporated by heating and the residue was dissolved in RPMI-1640 media, prior to the resuspension of U937-NF- $\kappa$ B cells in this media. The lack of NF- $\kappa$ B induction from both the organic and aqueous phases when added to U937-NF- $\kappa$ B cells may suggest that there is more than one factor responsible for NF- $\kappa$ B induction and they both need to be present for significant NF- $\kappa$ B induction. Alteration of the pH for 10 minutes by the addition of hydrochloric acid and sodium hydroxide respectively to the LX-2 conditioned media prior to U937-NF- $\kappa$ B cells resuspension had no effect on the soluble factors pro-inflammatory activity.

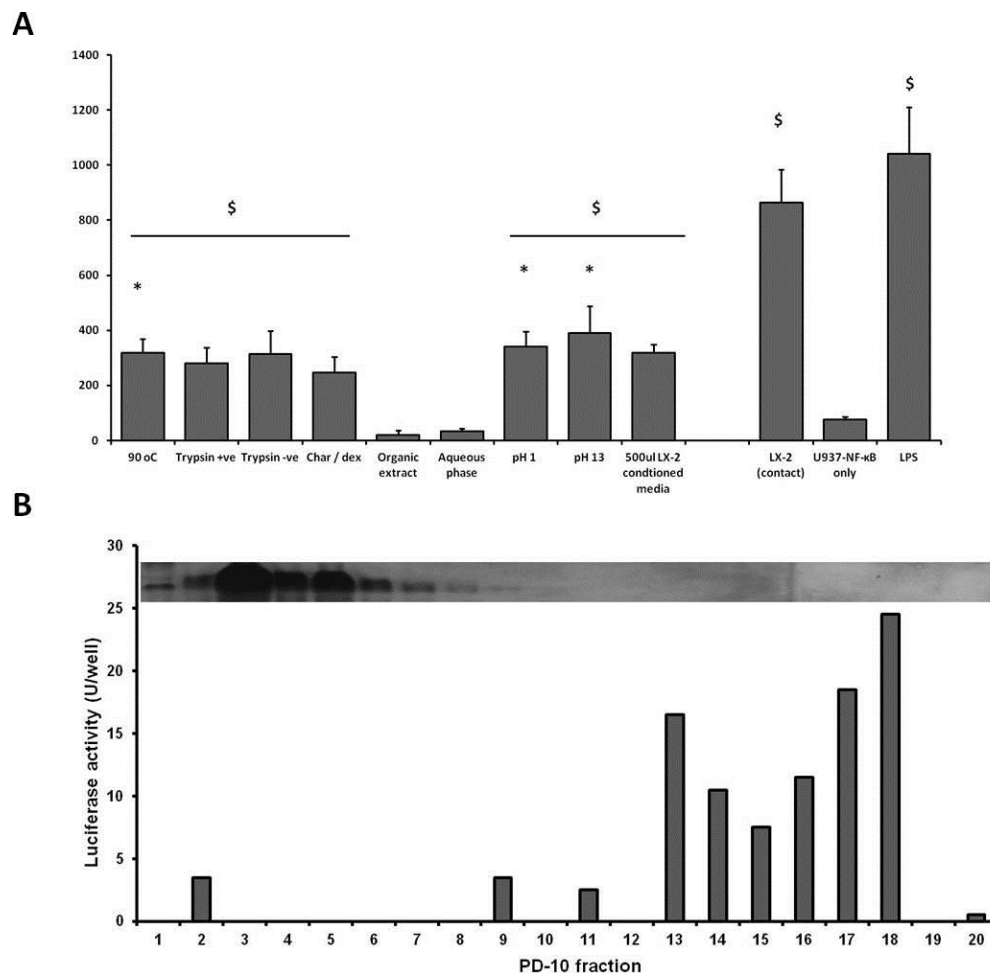


**Figure 6.12 Range of treatments to uncover more about the pro-inflammatory soluble factor. A** Variety of treatments were performed (Table 2.2) to 48 hour LX-2 conditioned media prior to its addition to U937-NF- $\kappa$ B cells. (\* denotes a statistically significant difference in luciferase activity when compared to the 500 $\mu$ l LX-2 conditioned media sample, analysed using a student's t-test,

unpaired ( $p < 0.05$ ). \$ denotes a statistically significant increase in luciferase activity when compared to the U937-NF- $\kappa$ B cells only incubation, analysed employing an ANOVA ( $p < 0.0001$ ). Data are the mean and SD  $n=3$  from a single experiment, typical of three independently repeated experiments. **B** PD-10 sepharose gel filtration revealed that the soluble factor is a small molecule as NF- $\kappa$ B activity was only induced in the later wash fractions (13 – 18).

Following the filtration of 2ml LX-2 conditioned media through a PD-10 sepharose column, a 500 $\mu$ l volume from each wash fraction was added to  $1 \times 10^5$  U937-NF- $\kappa$ B cells and incubated for 6 hours. Figure 6.12B shows both the SDS-PAGE run out of large proteins (i.e. BSA 66.5 kDa) present in each wash fraction and the luciferase activity induced by the contents of each wash. Smaller molecules are retained in the gel bed and eluted later, whilst proteins of higher MW such as BSA are eluted straight away as shown by the SDS-PAGE gel. The presence of the soluble factor was only detected in the later wash fractions (fractions 13-18) after the elution of BSA indicating that the pro-inflammatory mediator is a small molecule.

## **6.4 Screening of potential inflammatory/ fibrotic agents with U937-NF- $\kappa$ B cells**

### ***6.4.1 Treatment of U937-NF- $\kappa$ B cells with inflammatory cytokines and fibrotic compounds***

The development of liver fibrosis is a complex process with crosstalk between various signalling pathways; there are a plethora of molecules and pathways cited in the literature for being both inflammatory and fibrogenic that contribute to its development. In this section we wished to ascertain whether they may also be released by hepatic myofibroblasts and could stimulate U937-NF- $\kappa$ B cells NF- $\kappa$ B activity (see Table 2.2).

Inflammatory cytokines including IL-1 $\alpha$  and IL-1 $\beta$  were incubated in place of LX-2s with U937-NF- $\kappa$ B cells, figure 6.13A displays that neither of these cytokines induce NF- $\kappa$ B in the U937-NF- $\kappa$ B cells to the level seen when co-cultured with LX-2s. IL-1 $\alpha$  and IL-1 $\beta$  both induced a statistically significant increase in NF- $\kappa$ B but as human recombinant cytokines were added at high

physiological levels a much greater induction of luciferase activity would be expected if they were the soluble mediator released by LX-2 cells. In an attempt to ascertain whether these small increases in luciferase activity could be part of the inflammatory response seen after LX-2 co-culture U937-NF- $\kappa$ B cells were pre-treated with an IL-1 receptor antagonist (IL-1RA) for 2 hours prior to the addition of IL-1 $\alpha$  and IL-1 $\beta$  (Figure 6.13B). Unfortunately the IL-1RA did not have any effect on the level of luciferase activity induced following IL-1 $\alpha$  and IL-1 $\beta$  addition and therefore although it is unlikely, IL-1 $\alpha$  and IL-1 $\beta$  cannot be ruled out as the pro-inflammatory soluble factor released by LX-2 cells.

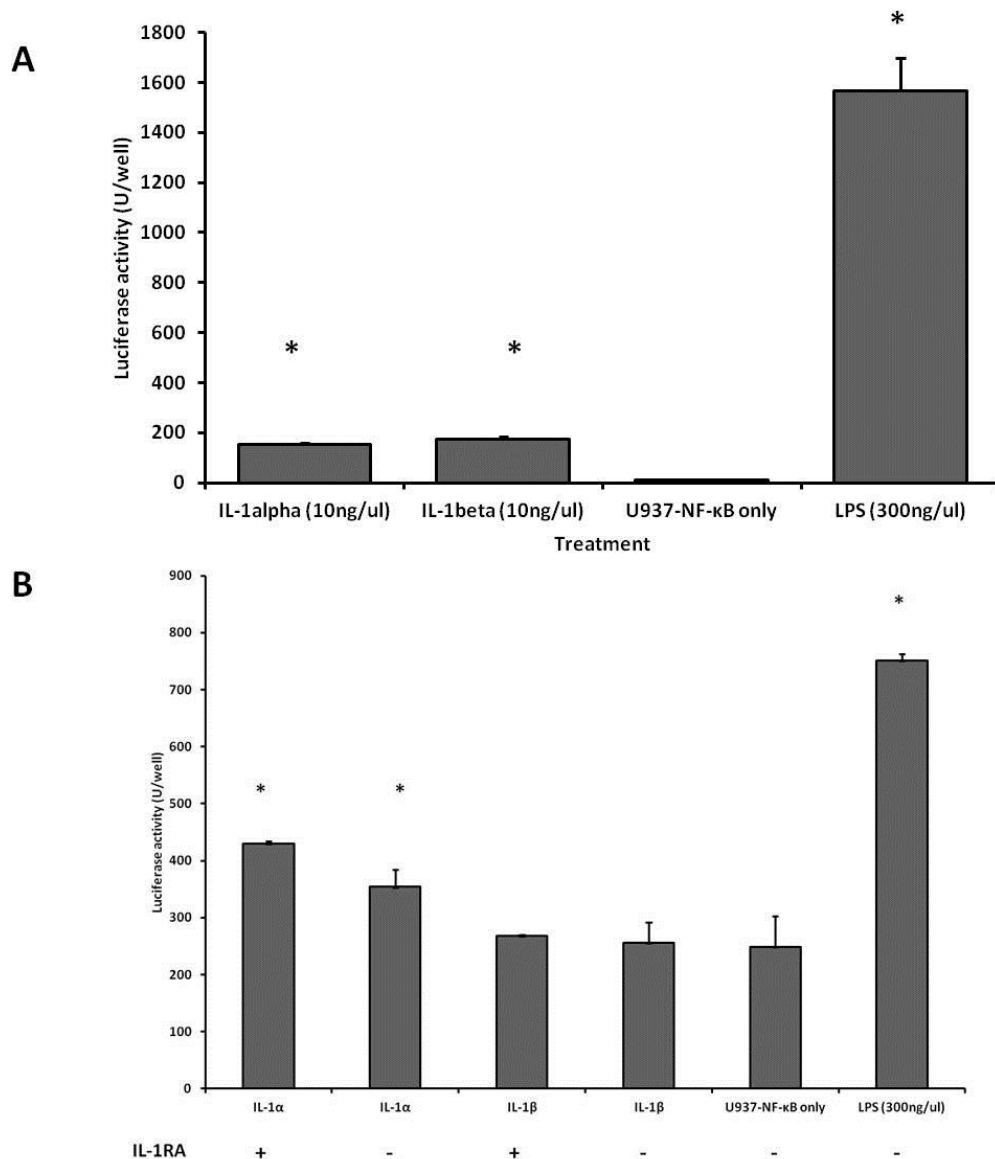


**Figure 6.13 Incubation of U937-NF- $\kappa$ B cells with the pro-inflammatory cytokines IL-1 $\alpha$  and IL-1 $\beta$ .** A Addition of human recombinant IL-1 $\alpha$  and IL-1 $\beta$  (10ng/ $\mu$ l) to U937-NF- $\kappa$ B cells resulted in a

significant increase in NF- $\kappa$ B activity compared to U937-NF- $\kappa$ B only, but this increase was much smaller than that seen with LX-2 co-culture. (\* denotes a statistically significant increase in luciferase activity when compared to the U937-NF- $\kappa$ B cells only incubation, ( $p < 0.0001$ , analysed using an ANOVA). **B** Incubation of U937-NF- $\kappa$ B cells with human recombinant IL-1 $\alpha$  and IL-1 $\beta$  was repeated following pre incubation of U937-NF- $\kappa$ B cells for 2 hours with an IL-1RA, although the IL-1RA did not appear to be functioning as it didn't influence the amount of NF- $\kappa$ B activity induced by IL-1 $\alpha$  and IL-1 $\beta$  addition. (\* denotes a statistically significant increase in luciferase activity when compared to the U937-NF- $\kappa$ B cells only incubation, ( $p < 0.014$ , analysed using a student's t-test, unpaired)). Data are the mean and SD  $n=3$  from a single experiment, typical of three independently repeated experiments.

Secondly a range of mediators that have been linked with inflammation and hepatic fibrosis development were investigated including angiotensin II [194, 234], leptin [78, 196], TIMP1 [57, 193] and serotonin [192]. Figure 6.14A demonstrates that none of these compounds induce NF- $\kappa$ B activity in the U937-NF- $\kappa$ B cells and therefore if they are released by LX-2s and HSCs are not the soluble factor that the U937-NF- $\kappa$ B cells are responding to. MCP-1 [198, 199], CXCL12 [32, 201], MIP-1 $\alpha$  [200, 235] and IP-10 [197] are cytokines known to be pro-inflammatory and important in the activation of monocytes/ macrophages and perpetuation of liver fibrosis development. Following incubation with U937-NF- $\kappa$ B cells although some of these cytokines elicited a statistically significant increase in luciferase activity (Figure 6.14B), the size of the increase was greatly reduced when compared to those elicited by LPS and LX-2 cells previously. Consequently if these cytokines are released by LX-2 cells they are unlikely to be the soluble factor, but could contribute to NF- $\kappa$ B induction later.

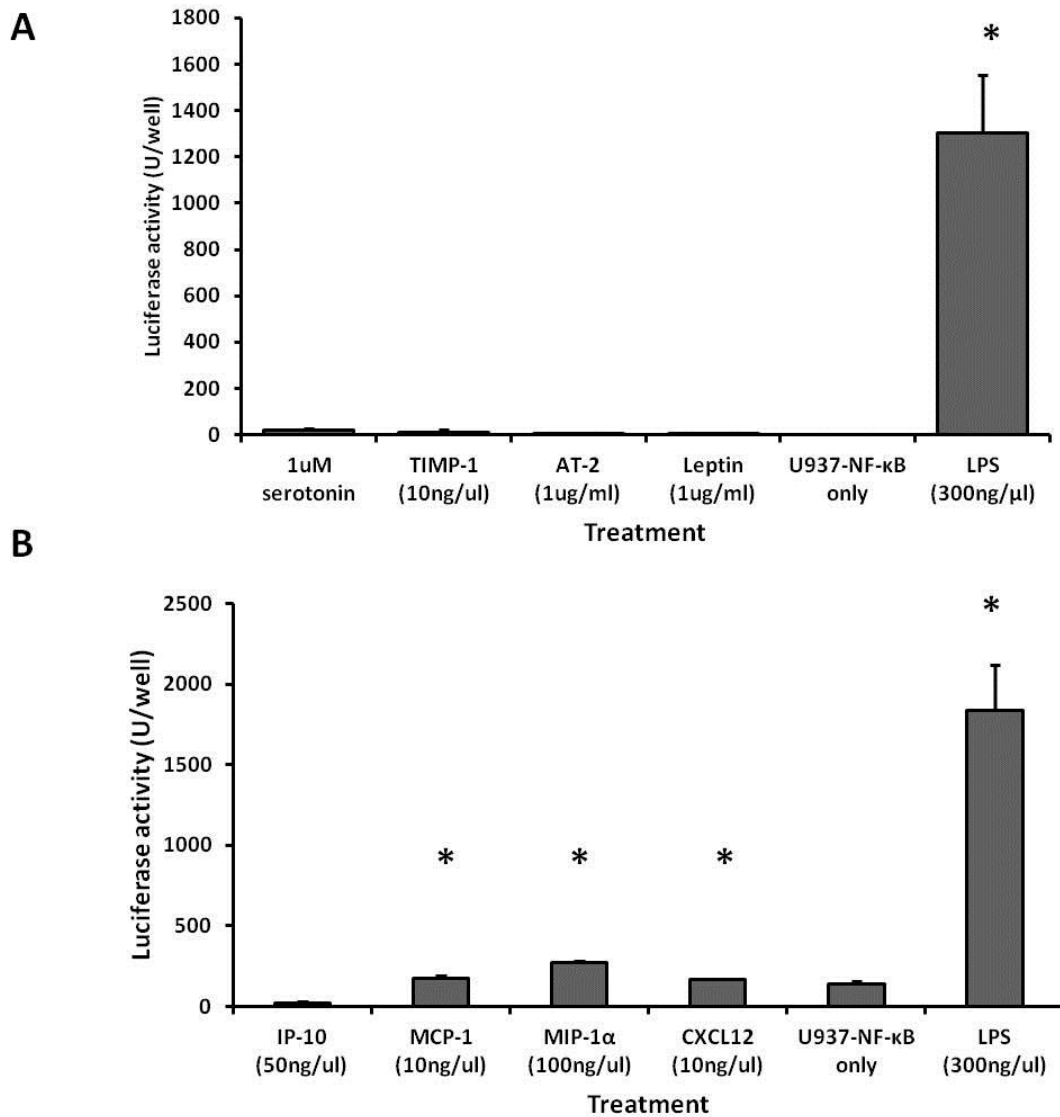


**Figure 6.14 Incubation of U937-NF-κB cells with a range of pro-fibrogenic and/ or pro-inflammatory molecules.** **A** Addition of a number of pro-fibrogenic compounds cited in the literature for their involvement in fibrosis development resulted in minimal induction of NF-κB activity. (\* denotes a statistically significant increase in luciferase activity when compared to the U937-NF-κB cells only incubation, ( $p < 0.0002$ , analysed using a student's t-test, unpaired)). **B** Addition of a number of pro-inflammatory cytokines and chemokines linked with the activation of monocytes and/ or macrophages central in fibrosis development. MCP-1, MIP-1α and CXCL12 all induce NF-κB activity in U937-NF-κB cells although not to the same level as LX-2 co-culture. (\* denotes a statistically significant increase in luciferase activity when compared to the U937-NF-κB cells only incubation, ( $p < 0.0039$ , analysed using a student's t-test, unpaired)). Data are the mean and SD  $n=3$  from a single experiment, typical of three independently repeated experiments.

#### **6.4.2 Increased production of nitric oxide (NO) and ROS does not induce NF-κB activity in U937-NF-κB cells**

Oxidative stress and the release of ROS are known to contribute to HSC activation [236, 237]; their concentration increases following hepatocyte damage further amplifying the activation of the inflammatory cycle and perpetuation of liver fibrosis development in chronic situations. To mimic the situation of high levels of ROS a variety of hydrogen peroxide ( $H_2O_2$ ) concentrations and iron sulphate ( $Fe_2SO_4$ ) were added to U937-NF- $\kappa$ B cells before determining luciferase activity; carbon monoxide (CO) was also separately bubbled through the U937-NF- $\kappa$ B cells for a short period prior to incubation and detection of luciferase activity. The role of NO was investigated firstly by the addition of sodium nitroprusside (SNP) to the culture media prior to the incubation of U937-NF- $\kappa$ B cells, SNP is broken down to release NO, which can be both cytoprotective and potentially cytotoxic to surrounding cells [238]. OxPAPC was added with and without the addition of LPS, as it is a TLR4 antagonist and therefore should inhibit LPS induction of luciferase activity in U937-NF- $\kappa$ B cells. Figure 6.15A shows that CO was the only mode of increasing ROS levels that resulted in a statistically significant increase in luciferase activity when compared to the U937-NF- $\kappa$ B cells only. Once again the level of this increase was greatly reduced when compared to the LPS and LX-2 cells NF- $\kappa$ B induction suggesting CO may have a contributory role at most to NF- $\kappa$ B induction. In addition there was no significant reduction in LPS induction of luciferase activity following OxPAPC (1 $\mu$ g/ml) treatment, suggesting that the antagonist was not functioning as advertised in this instance.

Finally the level of NO released into the culture media by LX-2 cells both separately and in co-culture with U937-NF- $\kappa$ B cells was determined by performing a Griess assay [216]. Culture media was isolated at various time points over 72 hours and the level of NO produced calculated by extrapolation against a sodium nitrite standard curve. Figure 6.15B shows that there was no significant variation in the level of NO produced over the 72 hour time course by the LX-2 cells when cultured individually or together with U937-NF- $\kappa$ B cells. Significant increases in NO concentration could only be detected when SNP was added as a positive control; these findings confirm that SNP was broken down to form NO. Taken together with the earlier results (Figure

6.15A), it confirms that the release of increased NO from LX-2 cells was not the pro-inflammatory soluble factor.

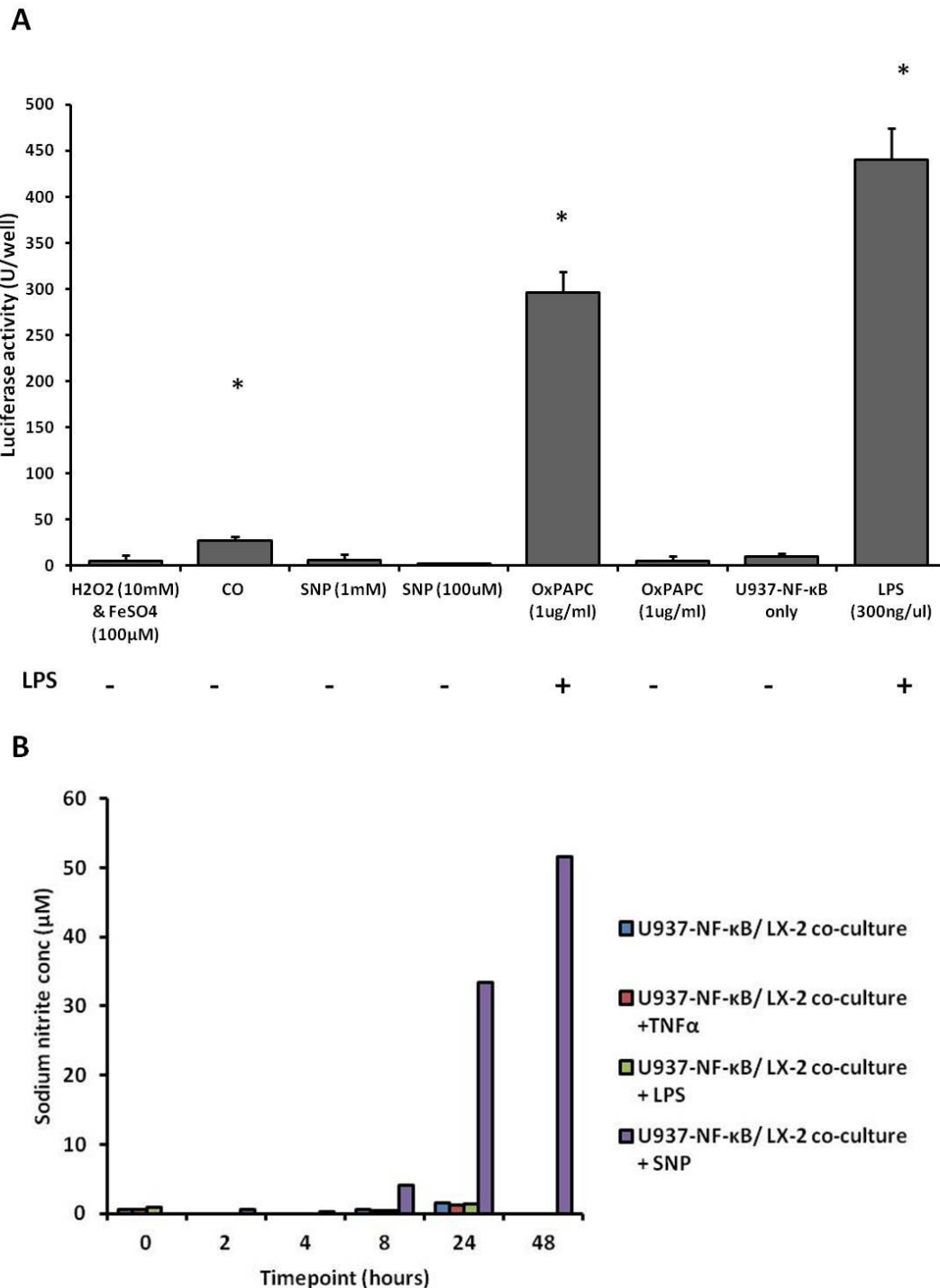


**Figure 6.15 Effect of increased ROS concentration on NF-κB activity in U937-NF-κB cells. A** Addition of H<sub>2</sub>O<sub>2</sub> and Fe<sub>2</sub>SO<sub>4</sub>, CO and SNP to increase ROS concentration in the culture media had no effect on U937-NF-κB cells NF-κB activity, the same was found with the addition of OxPAPC (TLR4 antagonist) which didn't appear to function as its addition did not abrogate LPS induction of NF-κB in U937-NF-κB cells. (\* denotes a statistically significant increase in luciferase activity when compared to the U937-NF-κB cells only incubation, (p < 0.015, analysed using a student's t-test, unpaired)). Data

are the mean and SD n=3 from a single experiment, typical of three independently repeated experiments.

**B** Gries assay was performed on LX-2's and U937-NF- $\kappa$ B cells in co-culture to determine the levels of NO released into the culture media. A significant increase in NO concentration was only detected in the positive control with SNP also added, confirming NO release from LX-2's does not responsible for NF- $\kappa$ B induction in U937-NF- $\kappa$ B cells.

## **6.5 *In vivo* studies investigating the inflammatory properties of hepatic myofibroblasts**

### **6.5.1 *NF- $\kappa$ B luciferase mice genotyping***

Firstly it was necessary to genotype the NF- $\kappa$ B luciferase mice and set up appropriate breeding cages to generate sufficient mice for subsequent experiments. DNA was isolated from the individual ear notches of each mouse (as described in section 2.6.2) and the presence of the luciferase transgene detected by PCR using primers specific to the firefly-luciferase gene (Table 2.4). Figure 6.16A is a typical electrophoresis agarose gel showing the genotype of individual mice. Figure 6.16B is the accompanying IVIS whole body scans performed on a wildtype and transgenic mouse as determined by the genotyping PCR. The IVIS images support the PCR genotyping with luciferase activity only detected in the transgenic mouse following  $\beta$ -luciferin administration.

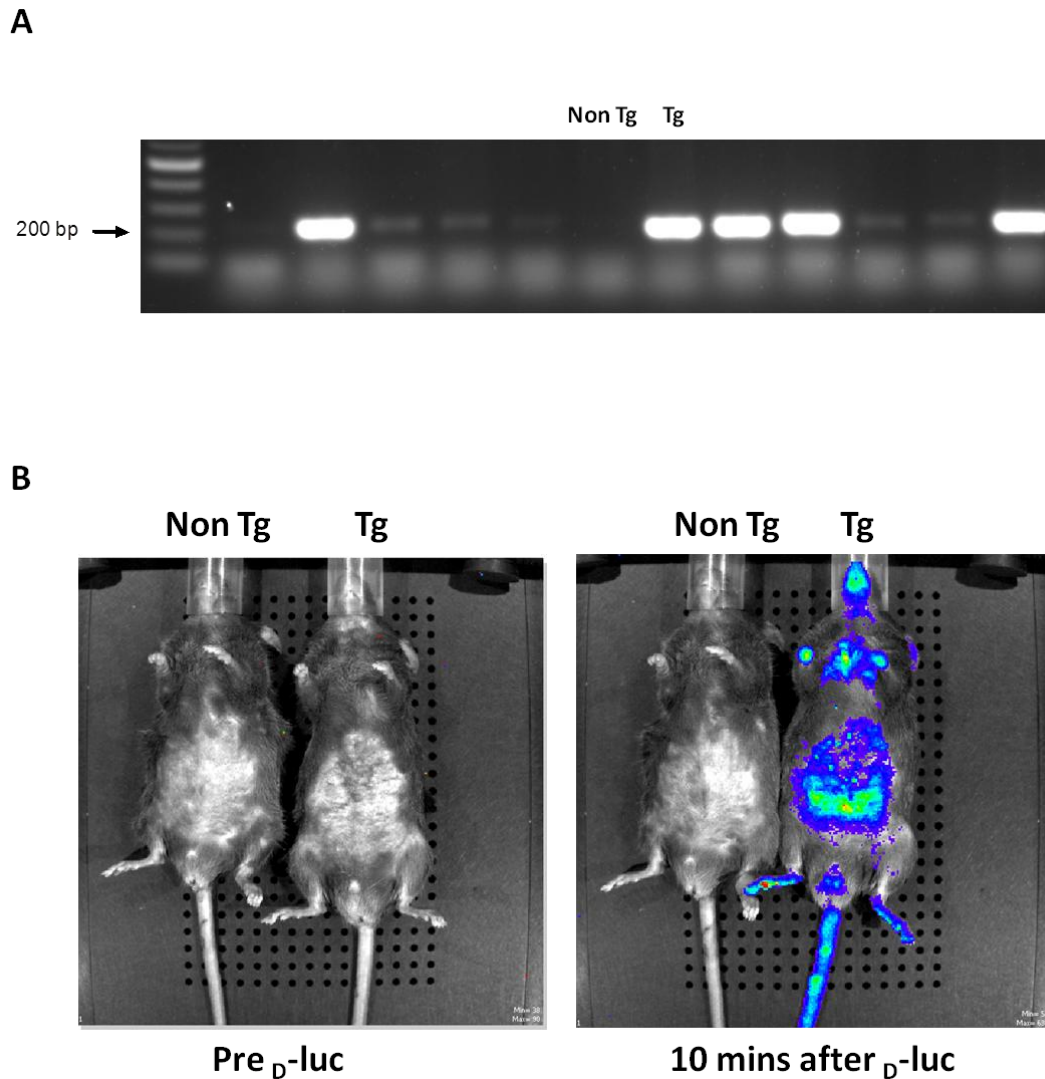


**Figure 6.16 Genotyping NF- $\kappa$ B luciferase mice.** **A** Genotyping PCR using primers specific firefly-luciferase were performed on DNA isolated from individual ear notches of each mouse, presence of the transgene was confirmed by a band at 221bp. **B** The functioning of the luciferase primers (due to the presence of weaker bands in some mice) was confirmed by the injection of 200 $\mu$ l of  $D$ -luciferin into a non-transgenic and transgenic mouse prior to IVIS imaging. A Luminescent signal was only detected in the transgenic mouse.

### **6.5.2 Pilot study of hepatic myofibroblast injection directly into NF- $\kappa$ B luciferase mice**

In the first pilot study,  $2 \times 10^5$  hepatic myofibroblasts suspended in 1 x PBS (isolated from a wildtype male NF- $\kappa$ B luciferase mouse as outlined in section 2.3.2) were injected by i.v. injection into a transgenic male NF- $\kappa$ B luciferase mouse to determine if hepatic myofibroblasts migrate specifically to the liver and induce NF- $\kappa$ B activity. Figure 6.17 are the whole body images performed

over the 72 hour time period to determine if there was an optimum time point when luciferase activity could be detected. It was apparent from these images that there was induction of NF- $\kappa$ B activity in the mouse dosed with both D-luciferin and hepatic myofibroblasts when compared to the controls and this signal originated in the upper abdominal (liver) region, suggesting that hepatic myofibroblasts are pro-inflammatory in the liver.

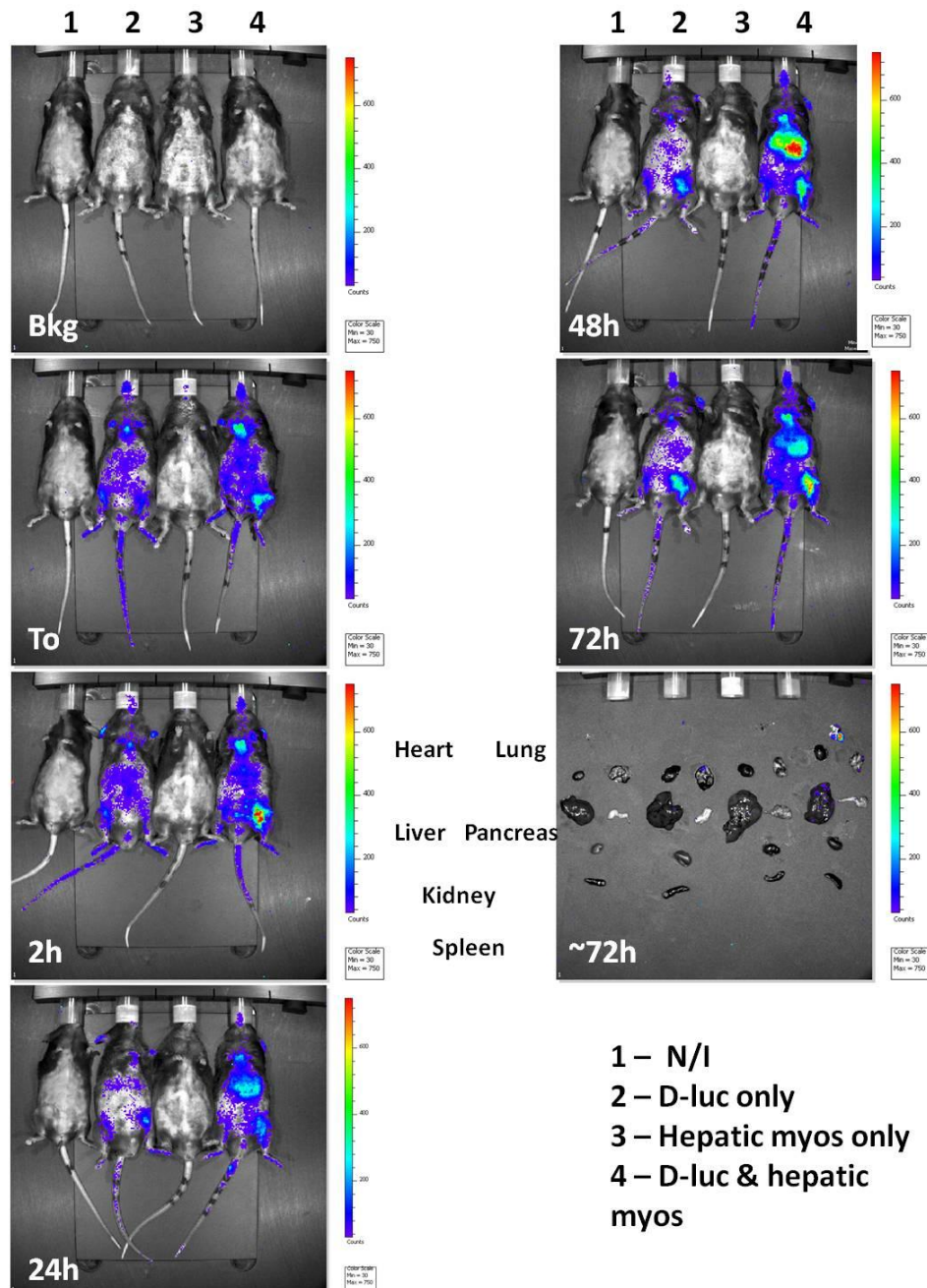


**Figure 6.17** Whole body bioluminescent scans over 72 hour time course following hepatic myofibroblast injection. Mice were anaesthetised with isoflurane and shaved ventrally prior to placing in the IVIS chamber. All scans were performed 10 minutes after i.p. injection of 200 $\mu$ l D-luciferin using a one minute exposure and bioluminescent filter setting, the images were analysed and scale bar set to

the same levels using the Image Pro Plus 4.0 software so they could be directly compared. ( Bkg – background scan prior to  $\text{D}$ -luciferin administration,  $T_0$  – Time zero immediately after  $\text{D}$ -luciferin administration, and the rest are hourly (h) time points).

ROIs available in the Image Pro-Plus 4.0 software were once again overlaid onto the images and the total luminescence for a specific region calculated; an example image and the total luminescence value for the upper abdominal (liver) region of each mouse are shown in figure 6.18. These data confirms that there was a significant increase in the upper abdominal/ liver region total luminescence of the mouse receiving both  $\text{D}$ -luciferin and hepatic myofibroblasts. Finally an *ex vivo* organ scan and ROI calculations (Figure 6.19) were performed to confirm that the luciferase signal originates in the liver. The *ex vivo* calculations confirm the signal was located in the liver with approximately a fivefold increase in liver signal detected in the mouse injected with hepatic myofibroblasts and  $\text{D}$ -luciferin, when compared to the  $\text{D}$ -luciferin only injected mouse. There was negligible luciferase activity detected in any of the other major organs of the control mice.

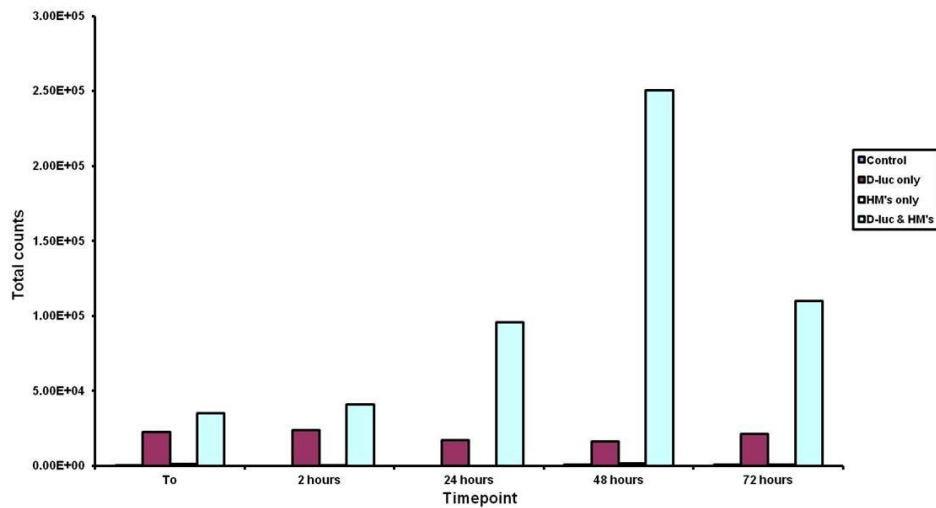
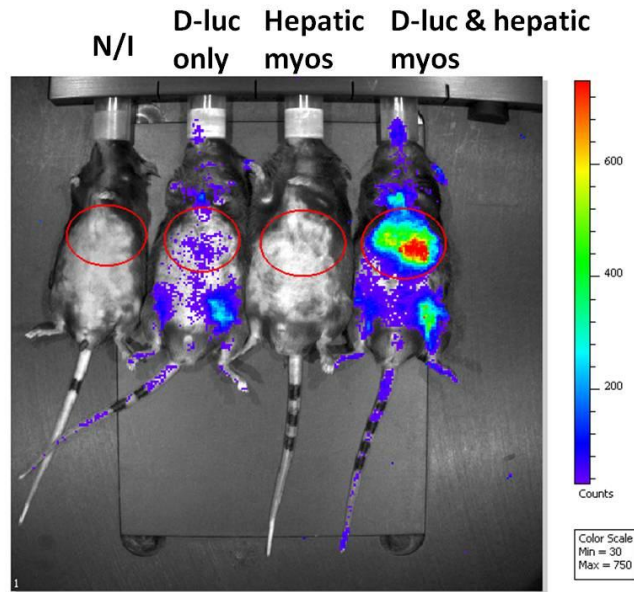


**Figure 6.18** Example whole body scan with ROIs overlaid and the calculated total luminescence values. ROIs could be overlaid onto images with the Image Pro Plus 4.0 software, allowing the calculation of total luminescence values for specific regions. The total luminescence values reveal hepatic myofibroblasts induce NF- $\kappa$ B in the upper abdominal peaking 48 hours after injection (n=1).

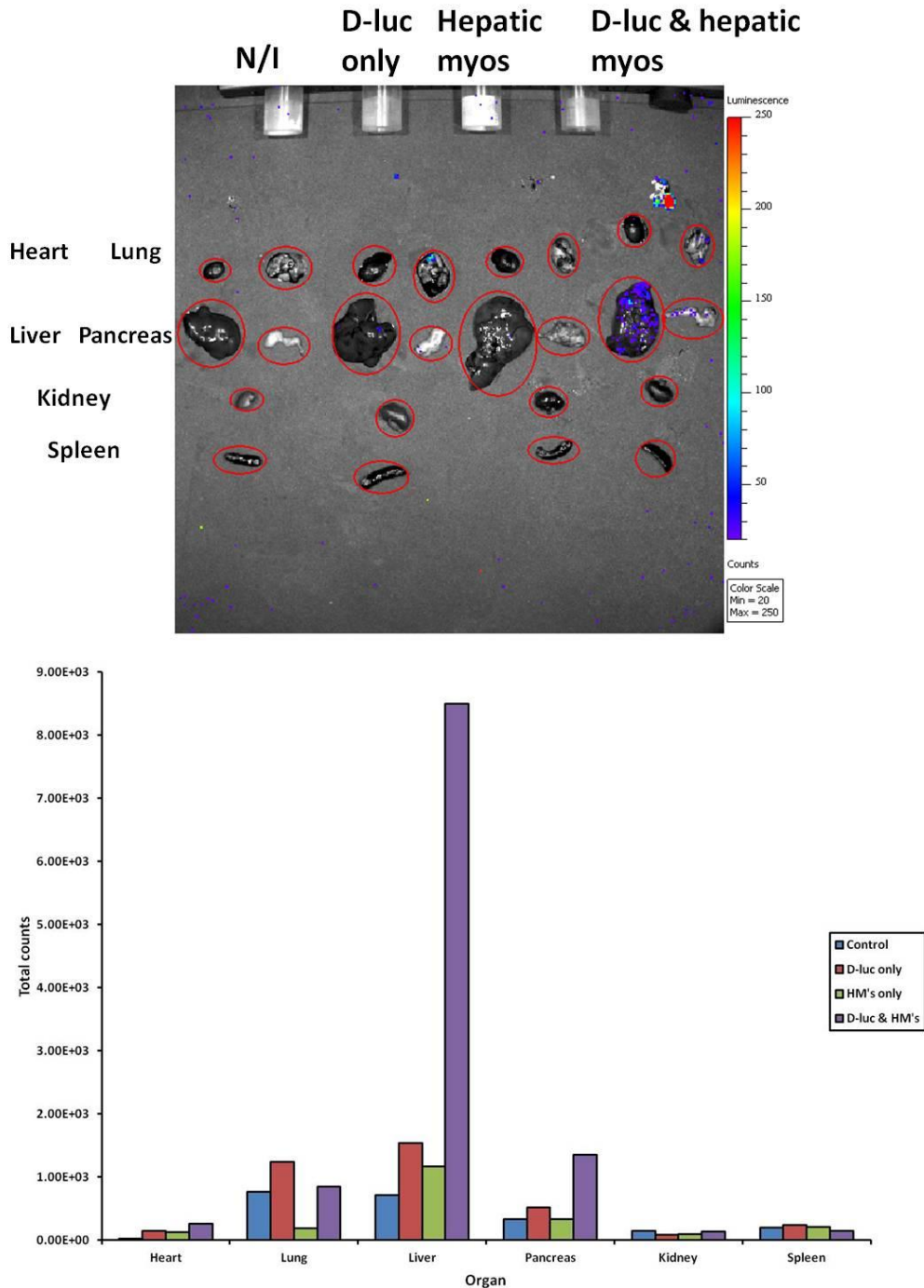


**Figure 6.19 Example *ex vivo* organ scan with ROIs overlaid and the calculated total luminescence values.** ROIs could be overlaid onto images with the Image Pro Plus 4.0 software, allowing the calculation of total luminescence values for specific excised organs. The total luminescence values reveal the induction of NF- $\kappa$ B is specifically from the liver (n=1).

These findings suggest that hepatic myofibroblasts are pro-inflammatory to the liver with a peak in NF- $\kappa$ B activity seen 48 hours after injection. The *ex vivo* organ scans (at approximately 96 hours after hepatic myofibroblast injection) confirm that the signal was from the liver as an increase in luciferase

activity was not detected in any other organs or treatments confirming the response seen was solely due to hepatic myofibroblast injection.

$\alpha$ SMA IHC analysis performed on fixed liver samples taken from each mouse indicated that there were now a small number of  $\alpha$ SMA positive cells present in the hepatic myofibroblast injected livers, which are not detected in the uninjected liver samples (Figure 6.20).

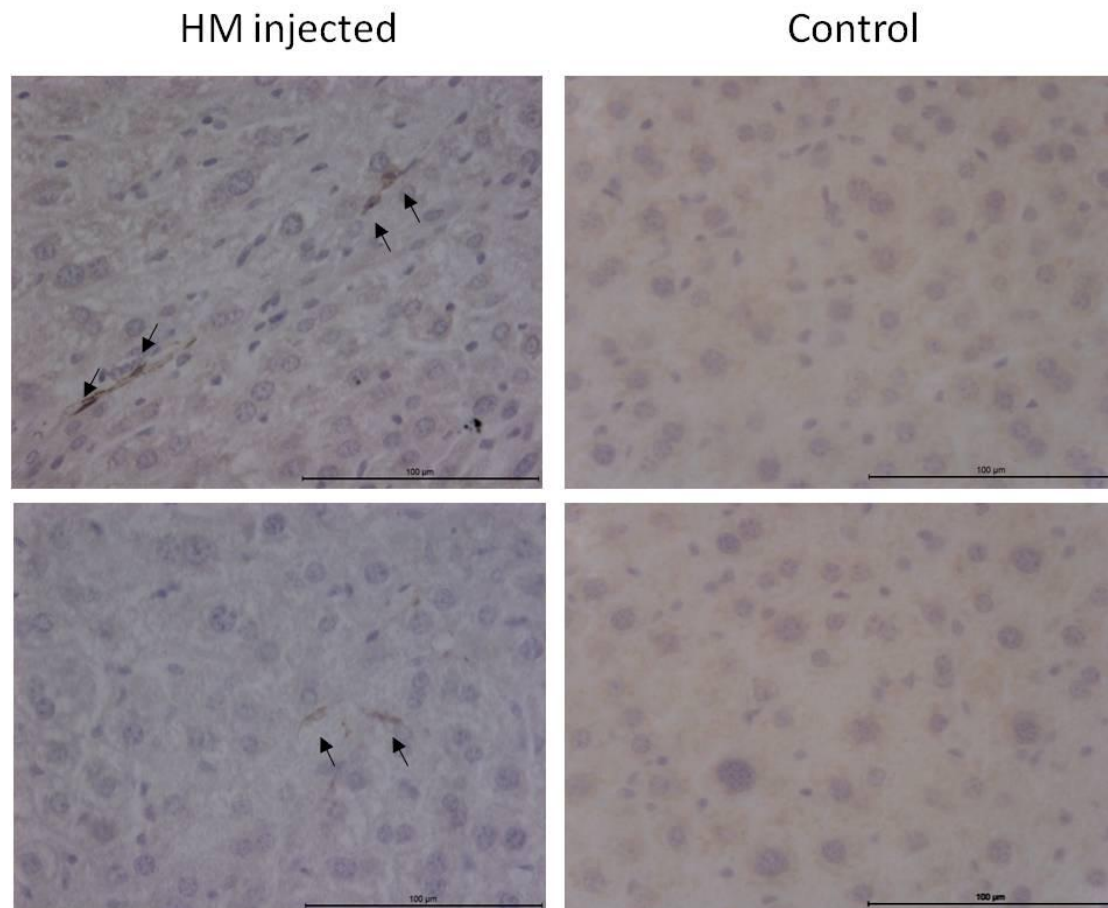


**Figure 6.20  $\alpha$ SMA IHC of liver sections from hepatic myofibroblast injected and control mice.** Liver tissue was fixed in 10% formalin prior to paraffin embedding, 5 $\mu$ M sections were cut for each animal. Sections were dewaxed prior to blocking of endogenous peroxidase activity and heat induced antigen retrieval. Followed by serum blocking and incubation for an hour at room temperature with  $\alpha$ SMA primary antibody, after PBS washing and addition of the complementary secondary antibody the level of bound antibody was detected by DAB incubation. The sections were counterstained with haematoxylin and dehydrated prior to mounting and analysis with a Leica upright microscope. (All images shown are x40 magnification).

To verify the initial pilot findings the study was repeated with an increased number of mice and also including a 'trypsin dummy' control (to confirm that when the hepatic myofibroblasts were isolated by trypsinisation and resuspension in 1 x PBS, residual trypsin-EDTA had not given NF- $\kappa$ B

induction as there will still be some present despite 1 x PBS washing).  $2 \times 10^5$  hepatic myofibroblasts or the ‘trypsin dummy’ were injected by i.v. injection and whole body images were taken over a 48 hour time period (Figure 6.21).

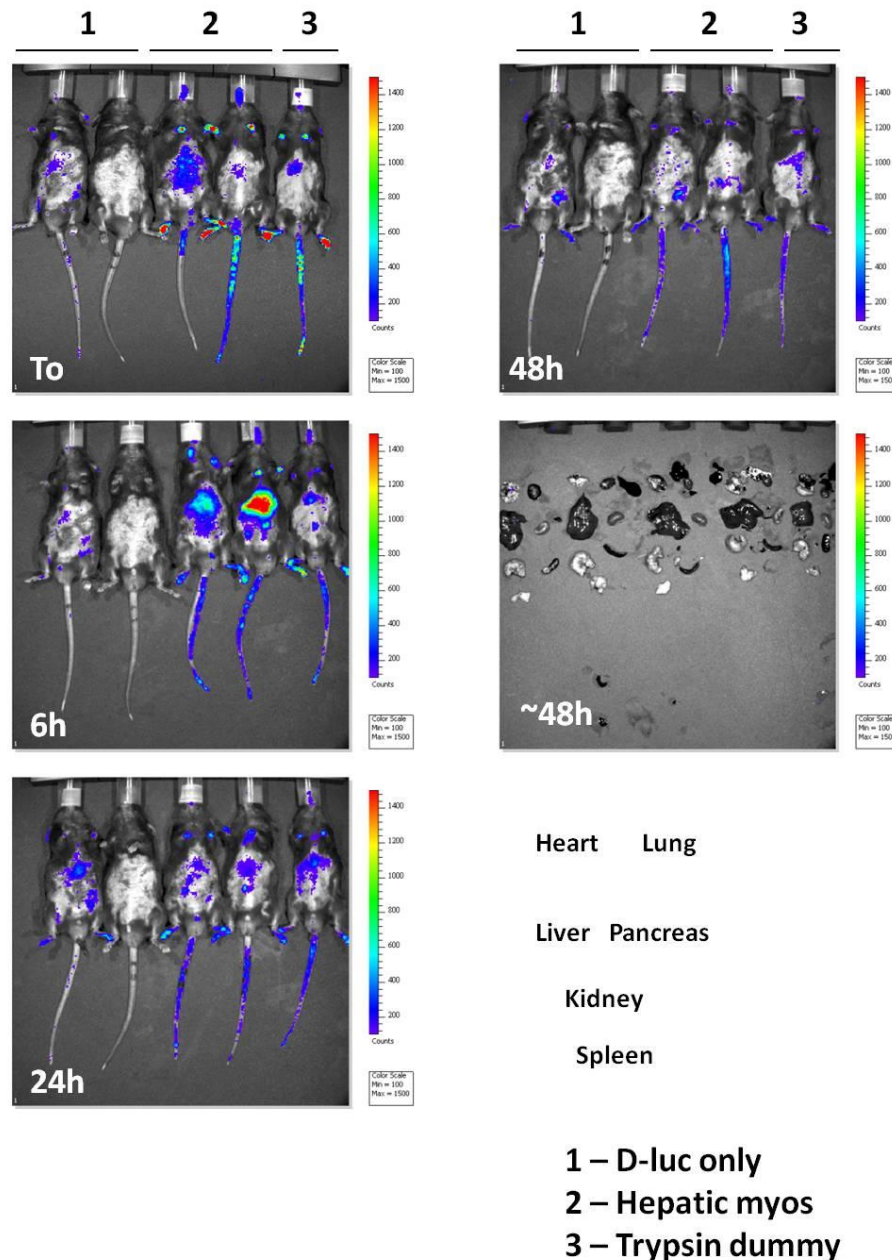


**Figure 6.21 Whole body luminescent scans over 48 hour time course following hepatic myofibroblast and ‘trypsin dummy’ injection.** Mice were anaesthetised with isoflurane and shaved ventrally prior to placing in the IVIS chamber. The scans were performed using the same settings described in figure 6.17. ( Bkg – background scan prior to  $D$ -luciferin administration,  $T_0$  – Time zero immediately after  $D$ -luciferin administration, and the rest are hourly (h) time points).

Once again a liver signal was only detected in the mice that received hepatic myofibroblasts, peaking 6 hours after hepatic myofibroblast injection; there

was no signal detected in the  $\beta$ -luciferin or the 'trypsin dummy' control mice confirming that this NF- $\kappa$ B induction was a property of the hepatic myofibroblasts. The ROI example scan and total luminescence calculation (Figure 6.22) confirm that there was no induction of NF- $\kappa$ B in the liver region of the 'trypsin dummy' or  $\beta$ -luciferin controls, whilst there was only a signal detected in the liver region at the  $T_0$  and 6 hour time points of the hepatic myofibroblast injected mice.

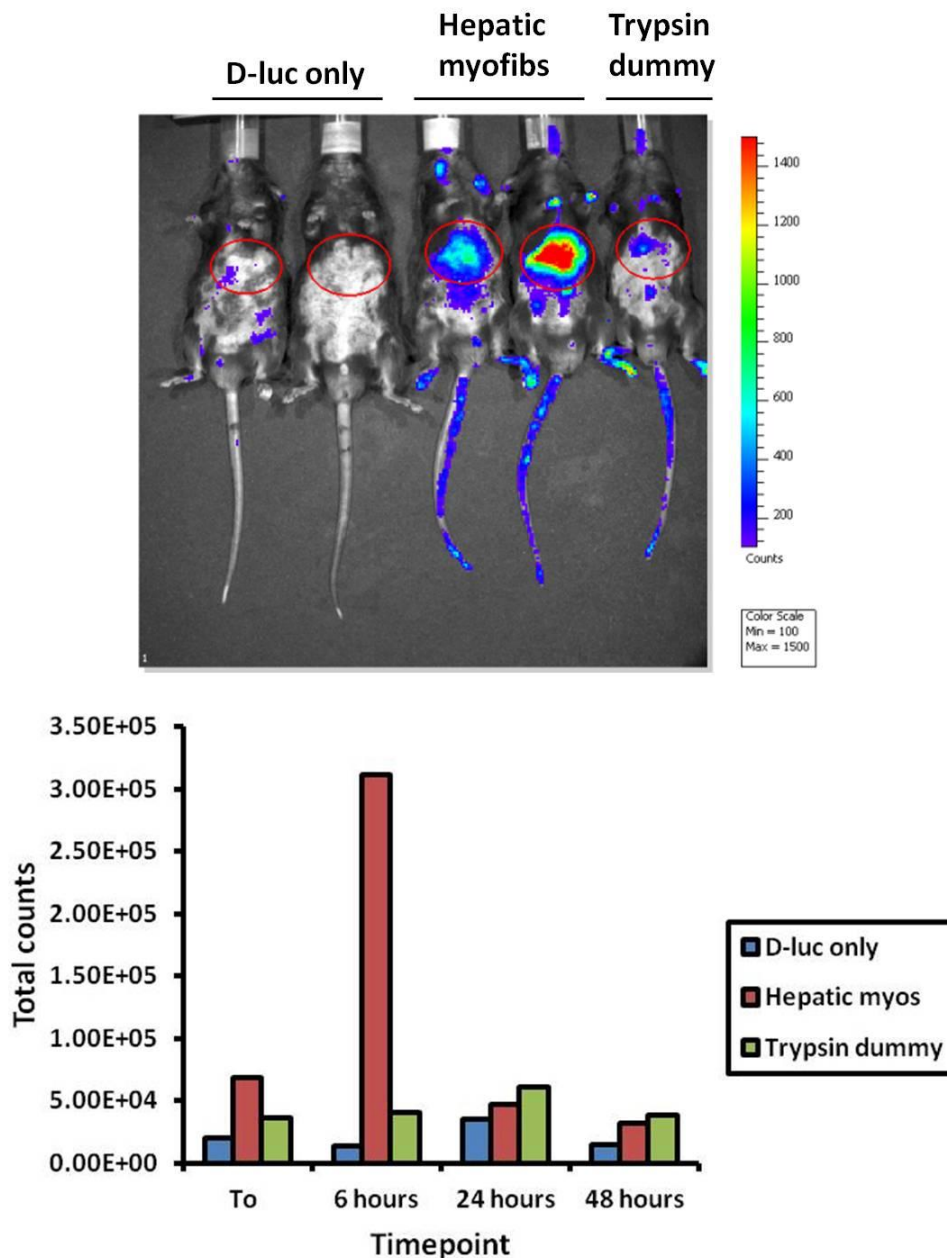


**Figure 6.22** Whole body scan with ROIs overlaid and the calculated total luminescence values. ROIs could be overlaid onto images with the Image Pro Plus 4.0 software, allowing the calculation of total luminescence values for specific regions. The total luminescence values confirm hepatic

myofibroblasts induce NF- $\kappa$ B in the upper abdominal although peaking 6 hours after injection in this study (n=2 controls and hepatic myofibroblasts injected, n=1 for trypsin dummy injected).

The *ex vivo* organ scan and ROI calculations (Figure 6.23) reveal that there was no difference in NF- $\kappa$ B activity detected between the different treatments group and that they are all at a very low level, equivalent to the  $\beta$ -D-luciferin only mice in the initial pilot study (Figure 6.18B). The *ex vivo* organ data confirms that there was a variation in the retention of the hepatic myofibroblasts within the liver during the two studies. The upper abdominal liver signal peaked at the 6 hour time point in the second study and was undetectable by the 48 hour time point. However in the initial study it peaked at approximately 48 hours, and could still be easily detected 72 hours after hepatic myofibroblast injection.

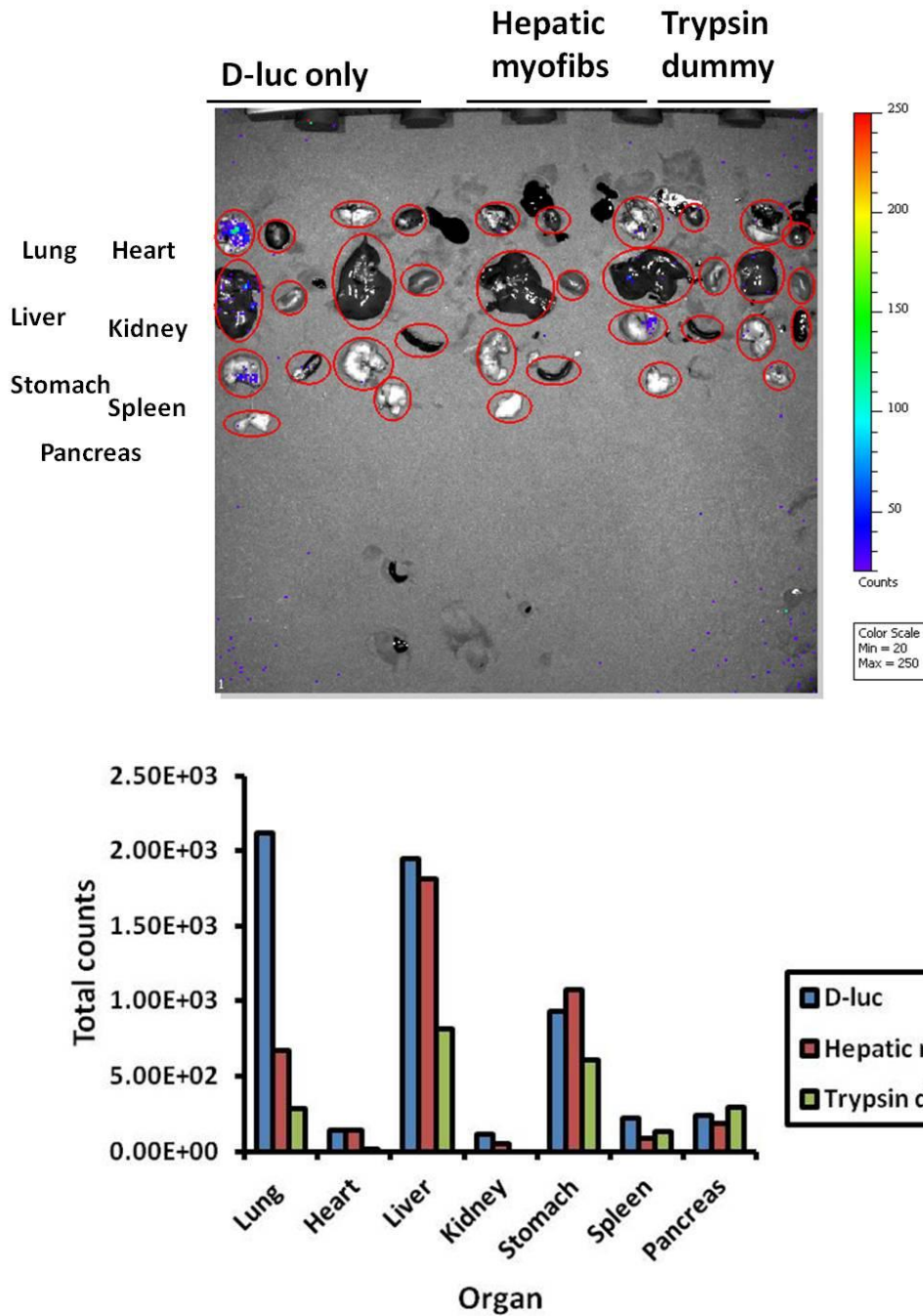


**Figure 6.23** *Ex vivo* organ scan with ROIs overlaid and the calculated total luminescence values. ROIs could be overlaid onto images with the Image Pro Plus 4.0 software, allowing the calculation of total luminescence values for specific excised organs. The total luminescence values suggest there is no variation in liver NF-κB induction in this study (n=2 controls and hepatic myofibroblasts injected, n=1 for trypsin dummy injected).

These data confirms that the induction of luciferase activity in the liver region of the hepatic myofibroblast injected mice was a result of the hepatic myofibroblasts and not an undesired result of the trypsin used in the isolation process. However in contrast to the earlier study NF-κB induction was

detected much earlier (6 hours instead of 48 hours after injection) and cannot be detected at later time points and in the final *ex vivo* organ scan.

### ***6.5.3 In vivo study to determine if hepatic myofibroblasts inflammatory traits are unique or a property of other cell types***

To determine whether these inflammatory characteristics are unique to hepatic myofibroblasts, kidney fibroblasts were isolated from a male wildtype NF- $\kappa$ B luciferase mouse, using a similar collagenase/ pronase digestion protocol as outlined in section 2.3.2.  $2 \times 10^5$  kidney fibroblasts suspended in 1 x PBS were injected via i.v. injection prior to performance of whole body scans over a 48 hour time course (Figure 6.24). The whole body images show there was a similar induction of NF- $\kappa$ B in the liver as a result of kidney fibroblast injection, although as seen before it peaks approximately 6 hours after injection and was not detected at 24 and 48 hours after injection. The total luminescence values calculated from the liver ROI confirm the observations from the whole body images; specifically that there was a significant increase in the liver ROI signal at 6 hours when compared to the D-luciferin and non inject control mice (Figure 6.25). This increase had diminished by the 24 hour time point and no difference was detectable between the different treatment groups.

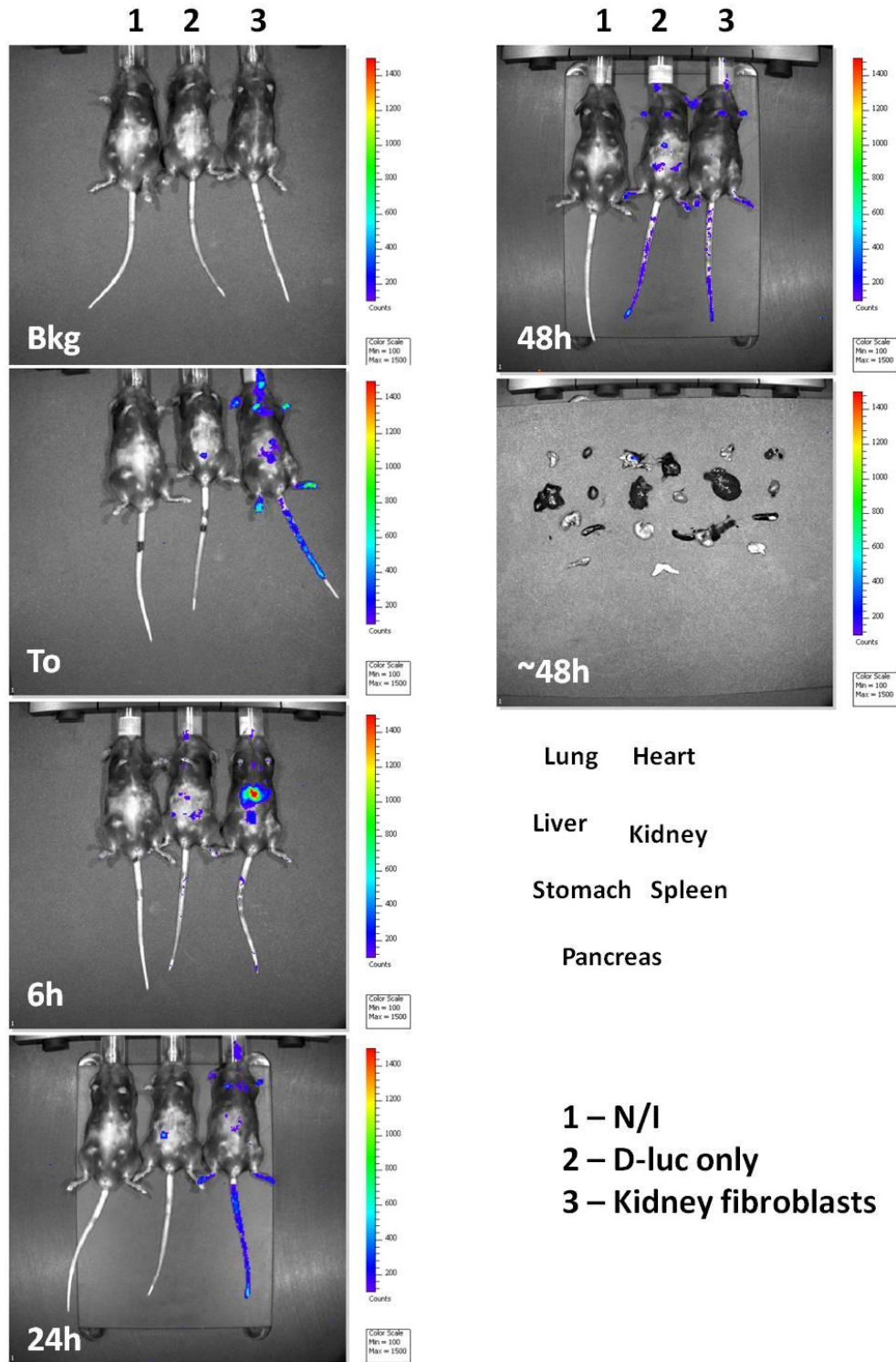


**Figure 6.24 Whole body luminescent scans over 48 hour time course following kidney fibroblast injection.** Mice were anaesthetised with isoflurane and shaved ventrally prior to placing in the IVIS chamber. The scans were performed using the same settings described in figure 6.17. (Bkg – background scan prior to  $D$ -luciferin administration,  $T_0$  – Time zero immediately after  $D$ -luciferin administration, and the rest are hourly (h) time points).

After the final 48 hour time point an *ex vivo* organ scan was performed (Figure 6.26A). The total luminescence values calculated for each individual organ show there was an increase in liver signal when injected with kidney fibroblasts in comparison to the control mice (Figure 6.26B). However the level of this increase was greatly reduced when compared to the initial hepatic myofibroblast study (Figure 6.19B), which was approximately three fold higher. Also there were similar levels of luminescence detected in the lung of the  $\beta$ -luciferin control and the stomach of both the  $\beta$ -luciferin and  $\beta$ -luciferin + kidney fibroblasts mice (Figure 6.26B). The NF- $\kappa$ B activity detected in these organs could be due to areas of localised inflammation or just abnormally high basal levels.

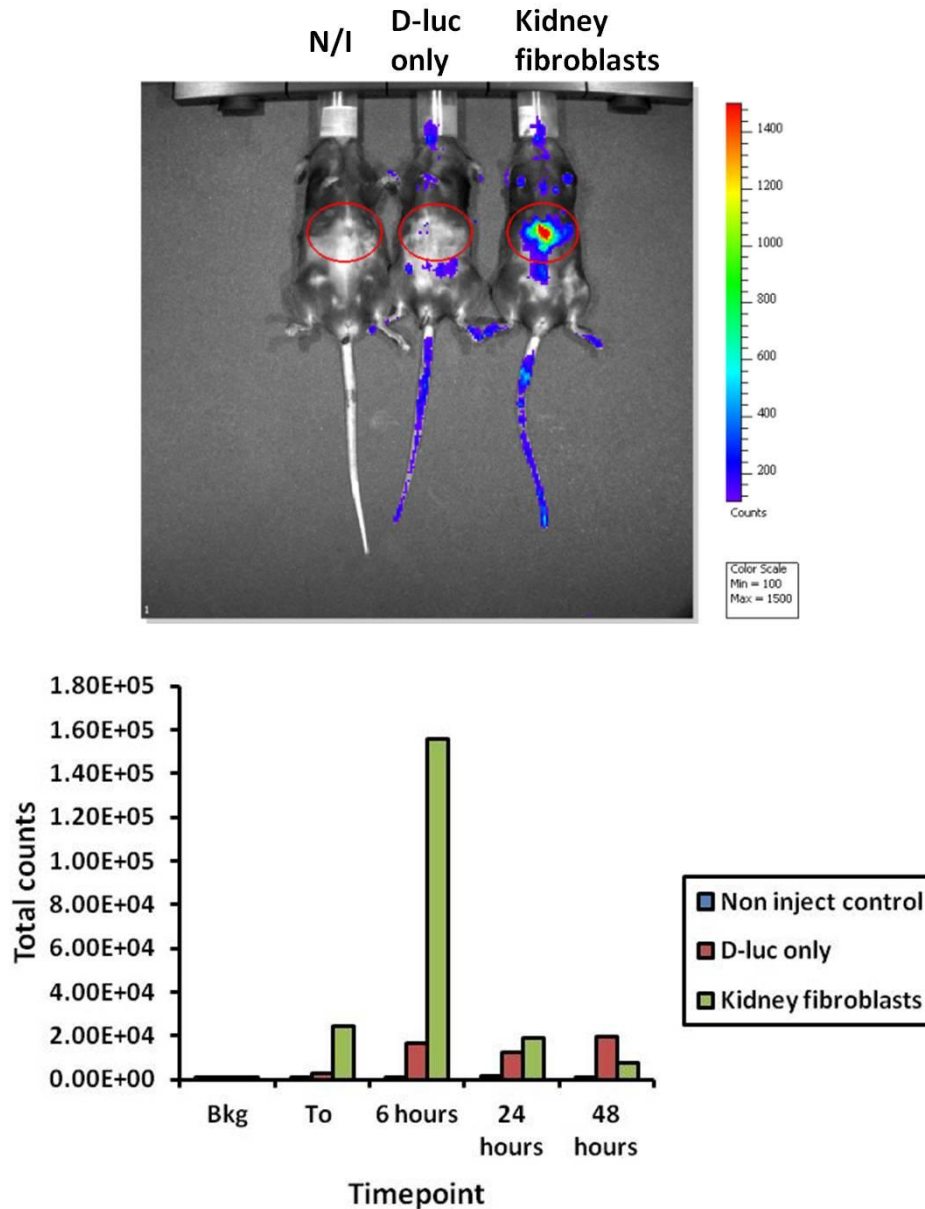


**Figure 6.25 Whole body scan with ROIs overlaid and the calculated total luminescence values.** ROIs could be overlaid onto images with the Image Pro Plus 4.0 software, allowing the calculation of total luminescence values for specific regions. The total luminescence values confirm kidney fibroblasts induce NF- $\kappa$ B in the upper abdominal peaking 6 hours after injection (n=1).

The induction of NF- $\kappa$ B in the liver region 6 hours after injection of kidney fibroblasts indicates that the inflammatory properties of hepatic myofibroblasts are not unique. As found in the previous study the inflammation peaked at approximately 6 hours and there was negligible luciferase activity detected between the treatment groups at the later time points and the *ex vivo* organ scan.

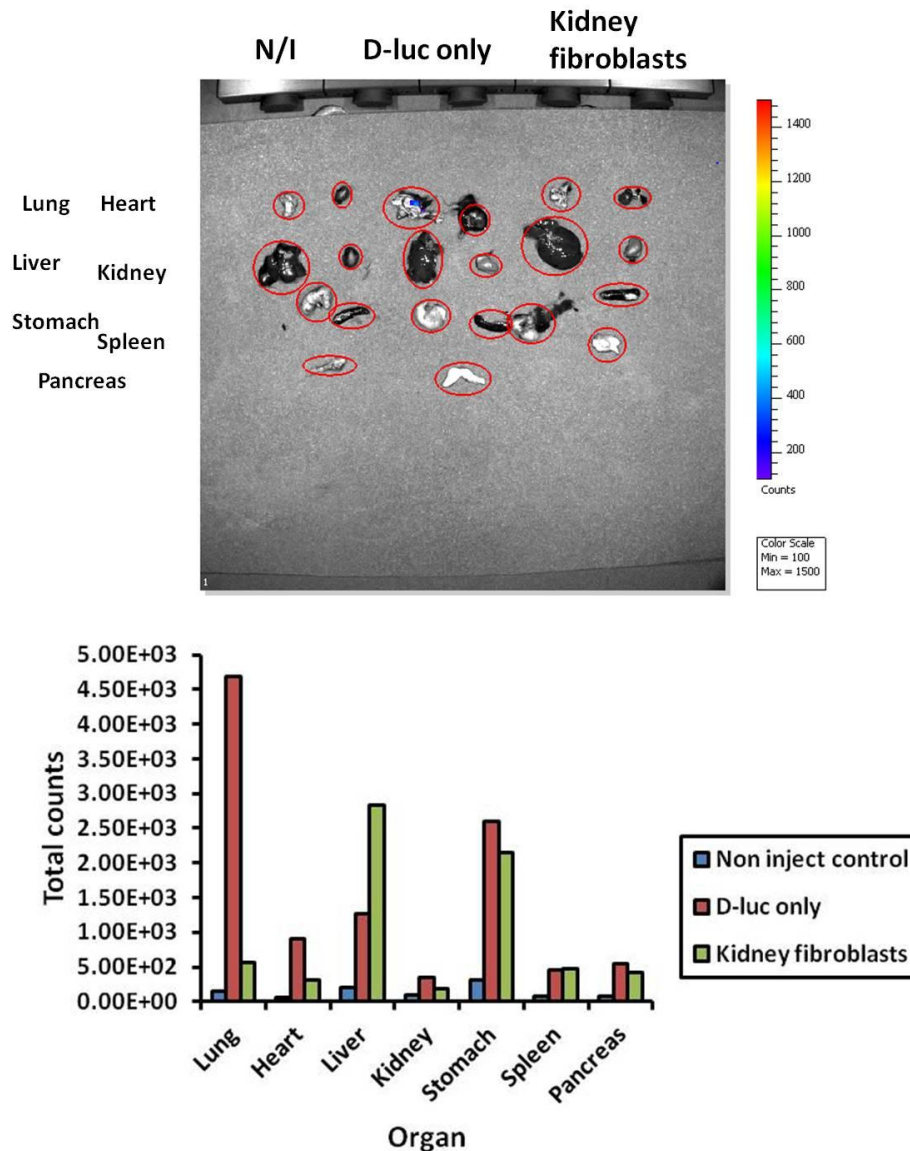
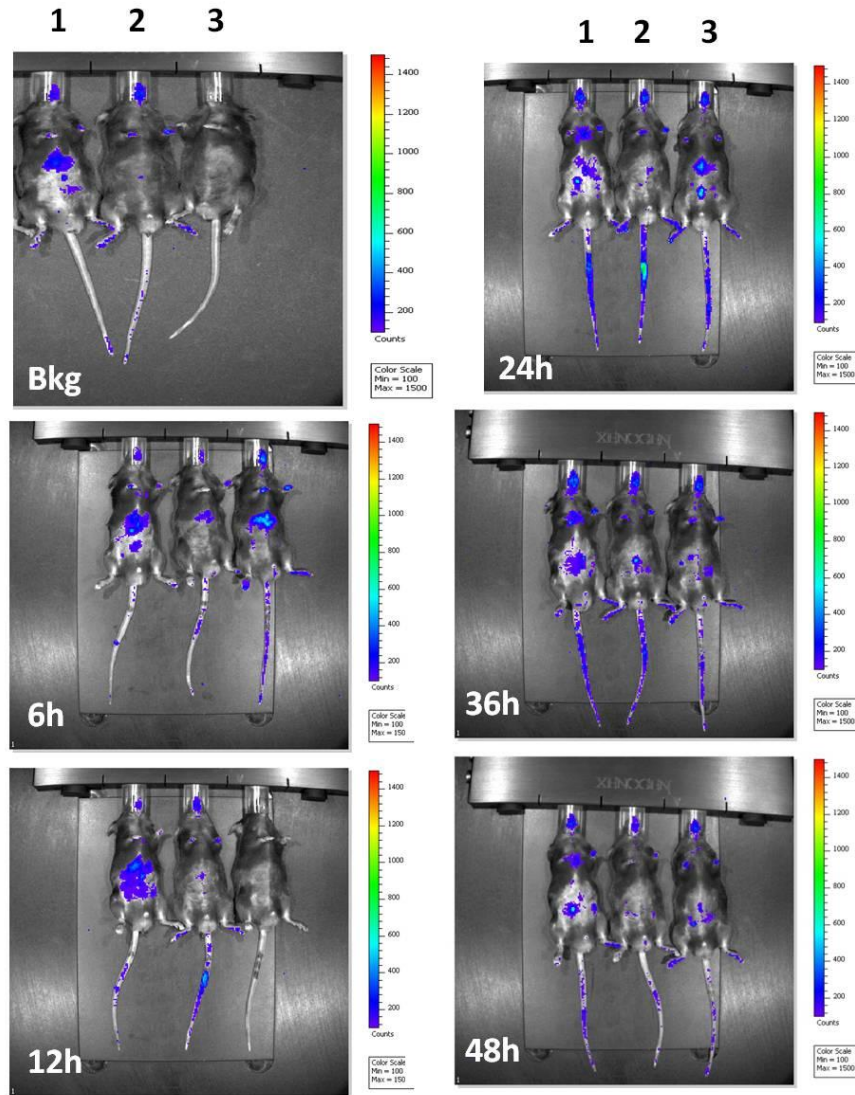


**Figure 6.26** *Ex vivo* organ scan with ROIs overlaid and the calculated total luminescence values. ROIs could be overlaid onto images with the Image Pro Plus 4.0 software, allowing the calculation of total luminescence values for specific excised organs. The total luminescence values suggest there was no variation in liver NF- $\kappa$ B induction in this study (n=1).

A follow up study was performed to confirm whether the migration of hepatic myofibroblasts to the liver and induction of NF- $\kappa$ B are specific to hepatic myofibroblasts or are common to kidney fibroblasts or particles of a similar size as well. Briefly NF- $\kappa$ B luciferase mice received  $D$ -luciferin and were imaged following i.v. injection of hepatic myofibroblasts, kidney fibroblasts or latex beads (Sigma L2778, 1 $\mu$ m average diameter). The mice were not culled so the ideal time point for detecting luciferase activity and any correlation between the different cell types could be determined.

Figure 6.27 shows the whole body luminescent images over the 48 hour timecourse following i.v. injection of hepatic myofibroblasts, kidney fibroblasts or latex beads. It was clear from these images that there was little induction in luciferase activity in the liver region of any of the treatments when compared to the previous studies.



- 1 – Hepatic myos
- 2 – Kidney fibroblasts
- 3 – Latex beads

**Figure 6.27 Whole body luminescent scans over 48 hour time course following hepatic myofibroblast, kidney fibroblast and latex bead injection.** Mice were anaesthetised with isoflurane and shaved ventrally prior to placing in the IVIS chamber. The scans were performed using the same settings described in figure 6.17. (Bkg – background scan prior to  $D$ -luciferin administration,  $T_0$  – Time zero immediately after  $D$ -luciferin administration, and the rest are hourly (h) time points).

The total luminescence values calculated from the overlaid ROI (Figure 6.28) confirm this initial observation; there was an increase in liver region total luminescence following hepatic myofibroblast injection compared to the kidney fibroblasts and latex beads mice. However this difference was minimal, especially as there was an abnormally high liver luminescence in the background scan prior to hepatic myofibroblast injection suggesting there may be some underlying inflammation present. The upper abdominal total luminescence signal of each treatment peaked 6 hours after cell injection and the hepatic myofibroblast injected mouse was higher than the other two cell types at the later time points suggesting that they may exhibit greater liver specific inflammation. Although as highlighted earlier the levels of total luminescence detected are greatly reduced when compared to the earlier studies (maximum liver region luminescence of  $6.5 \times 10^4$  compared to a maximum liver region luminescence of  $3 \times 10^5$  in the initial pilot study).

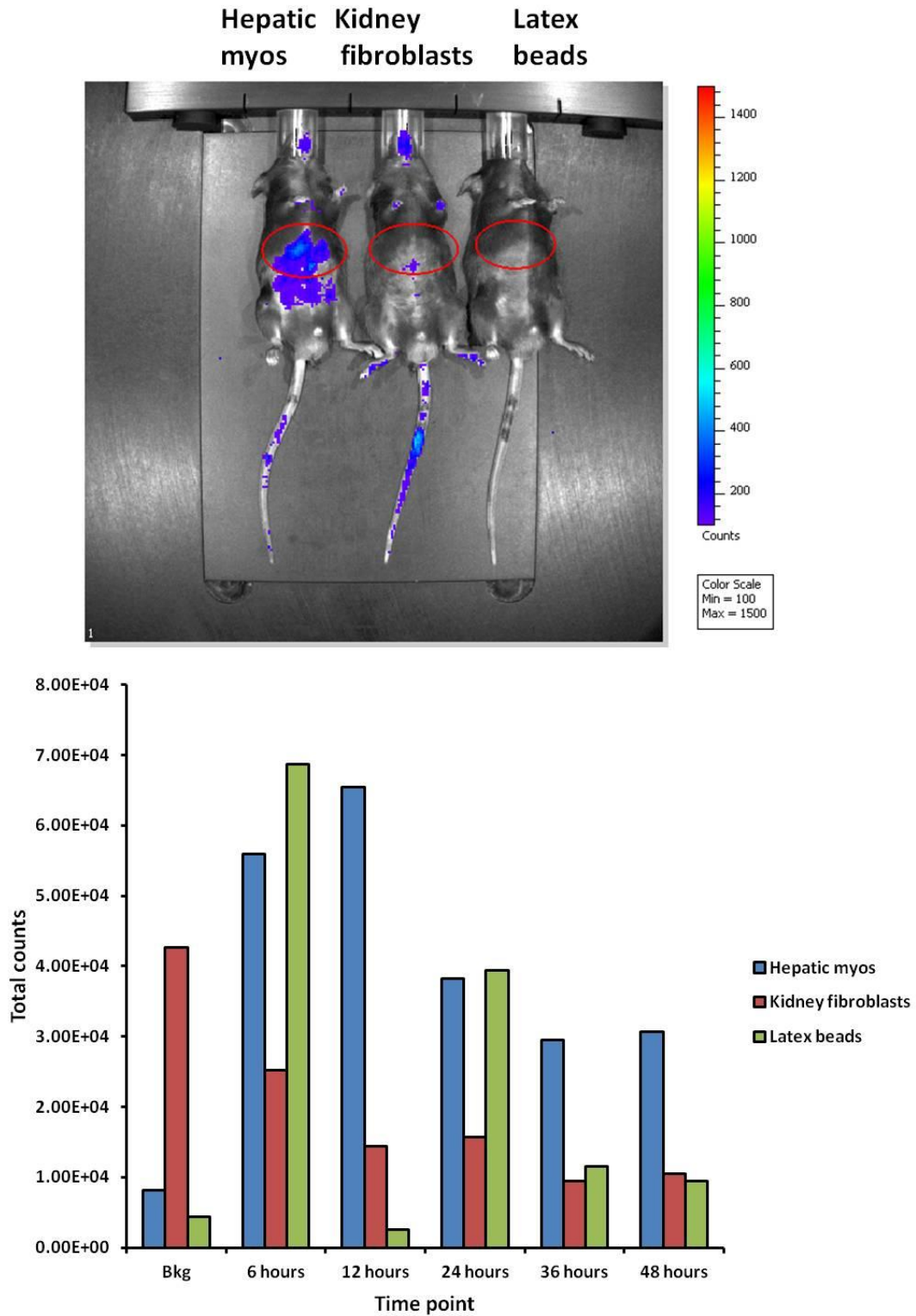


**Figure 6.28 Whole body scan with ROIs overlaid and the calculated total luminescence values.** ROIs could be overlaid onto images with the Image Pro Plus 4.0 software, allowing the calculation of total luminescence values for specific regions. The total luminescence values highlight that none of the injected cells/ particles induced a significant increase in NF-κB activity in the upper abdominal at all time points (n=1).

The reason for this loss of inflammatory activity is unknown as prior to injection the cells were prepared and quantified in an identical method to previous experiments. The only potential variation could be the passage number of the hepatic myofibroblasts and kidney fibroblasts injected, although the difference in passage number was only a single passage so it is unlikely that this will have had a significant effect on the cells' inflammatory characteristics.

#### 6.5.4 The effect of C1-3-GTX mediated hepatic myofibroblast depletion upon acute liver inflammation

A subsequent study was performed to investigate the effect of C1-3-GTX depletion of hepatic myofibroblasts upon liver inflammation in an acute CCl<sub>4</sub> model of liver injury. Figure 6.29 outlines the dosing and imaging schedule. Briefly all mice received a single dose of CCl<sub>4</sub> and immediately afterwards either C1-3 or C1-3-GTX by i.p. injection (Table 2.1).

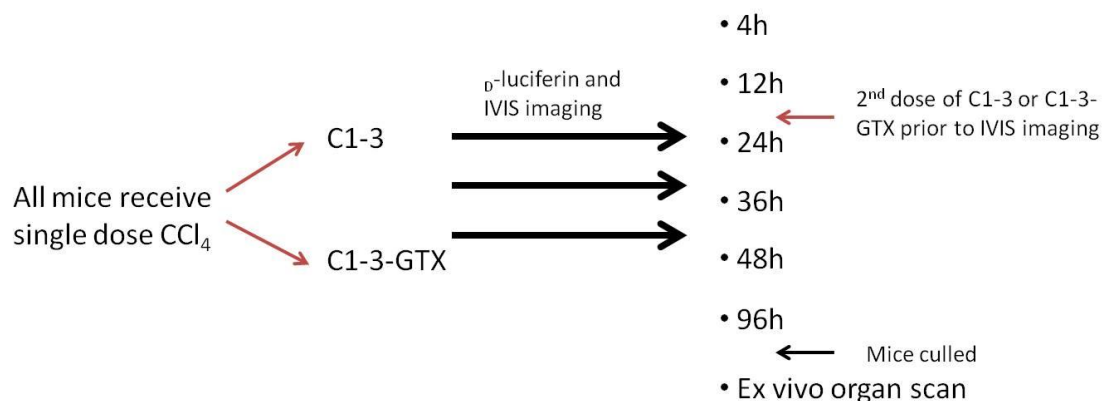


**Figure 6.29 Schematic diagram outlining the dosing and imaging regimen to determine the effect of hepatic myofibroblast depletion on NF- $\kappa$ B activity.** Each mouse received a single dose of CCl<sub>4</sub> to mimic acute liver damage; half then received 10 mg/kg C1-3 by i.p. injection whilst the second group received 10 mg/kg C1-3-GTX. The mice were then IVIS imaged at the timepoints outlined. Upon completion of the final timepoint the mice were terminated by a schedule I method. The major organs were excised and placed in the IVIS chamber and imaged using the same settings, prior to retention for subsequent IHC and biochemical analysis.

Whole body luminescent scans were then performed at regular intervals over 96 hours to determine any differences in upper abdominal (liver) NF- $\kappa$ B

activity (a 2<sup>nd</sup> dose of C1-3 or C1-3-GTX was administered 24 hours after the initial CCl<sub>4</sub> injection). The whole body scans are shown for each time point in figure 6.30. There was little that could be deciphered between the C1-3 and C1-3-GTX treatment groups by eye over the time course although there was a strong signal in one of the C1-3 treated mice at the 36 hour time point. The total luminescence values were calculated for the liver ROIs for each individual time point and are shown in figure 6.31. The level of luminescence detected was similar for both C1-3 and C1-3-GTX treatment groups at the initial time points, although from the 12 hour time point onwards there was a reduction in the level of luciferase activity detected in the C1-3-GTX treated mice. These findings support the initial hypothesis that C1-3-GTX treatment depletes the number of hepatic myofibroblasts and consequently the level of inflammation detected.

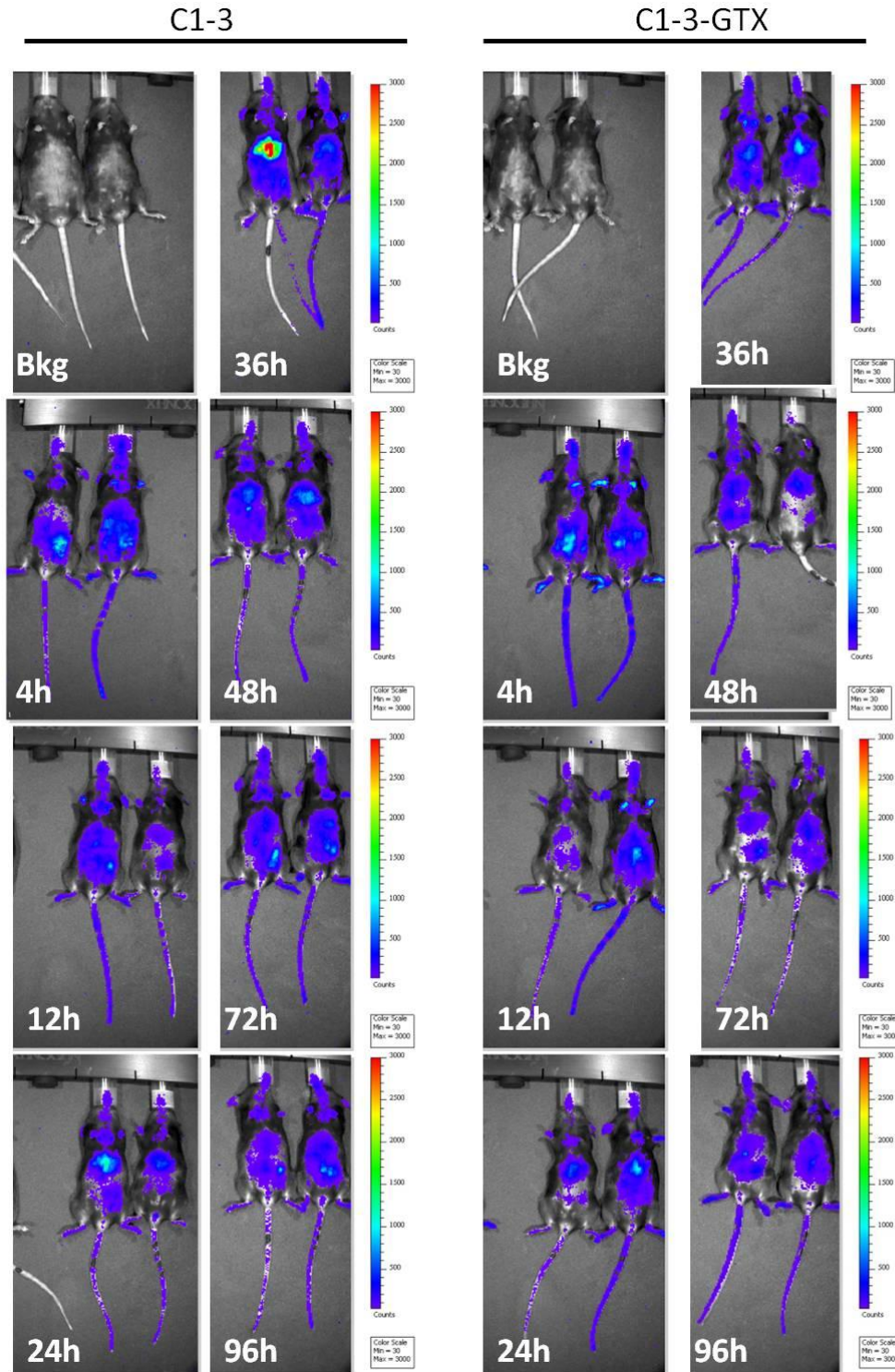


**Figure 6.30 Whole body luminescent scans over 96 hour time course following acute liver damage and C1-3 or C1-3-GTX administration.** Mice were anaesthetised with isoflurane and shaved ventrally prior to placing in the IVIS chamber. The scans were performed using the same settings described in figure 6.17. (Bkg – background scan prior to  $D$ -luciferin administration,  $T_0$  – Time zero immediately after  $D$ -luciferin administration, and the rest are hourly (h) time points).

After the final 96 hour time point an *ex vivo* scan was performed on the livers of both the C1-3 and C1-3-GTX treated mice and the mean total

luminescence calculated for each treatment group (Figure 6.32). The mean liver luminescence values support the whole body scans' data with a reduced level of luciferase activity detected in the C1-3-GTX treated mice, although the size of the difference was not as significant as seen at the earlier time points.

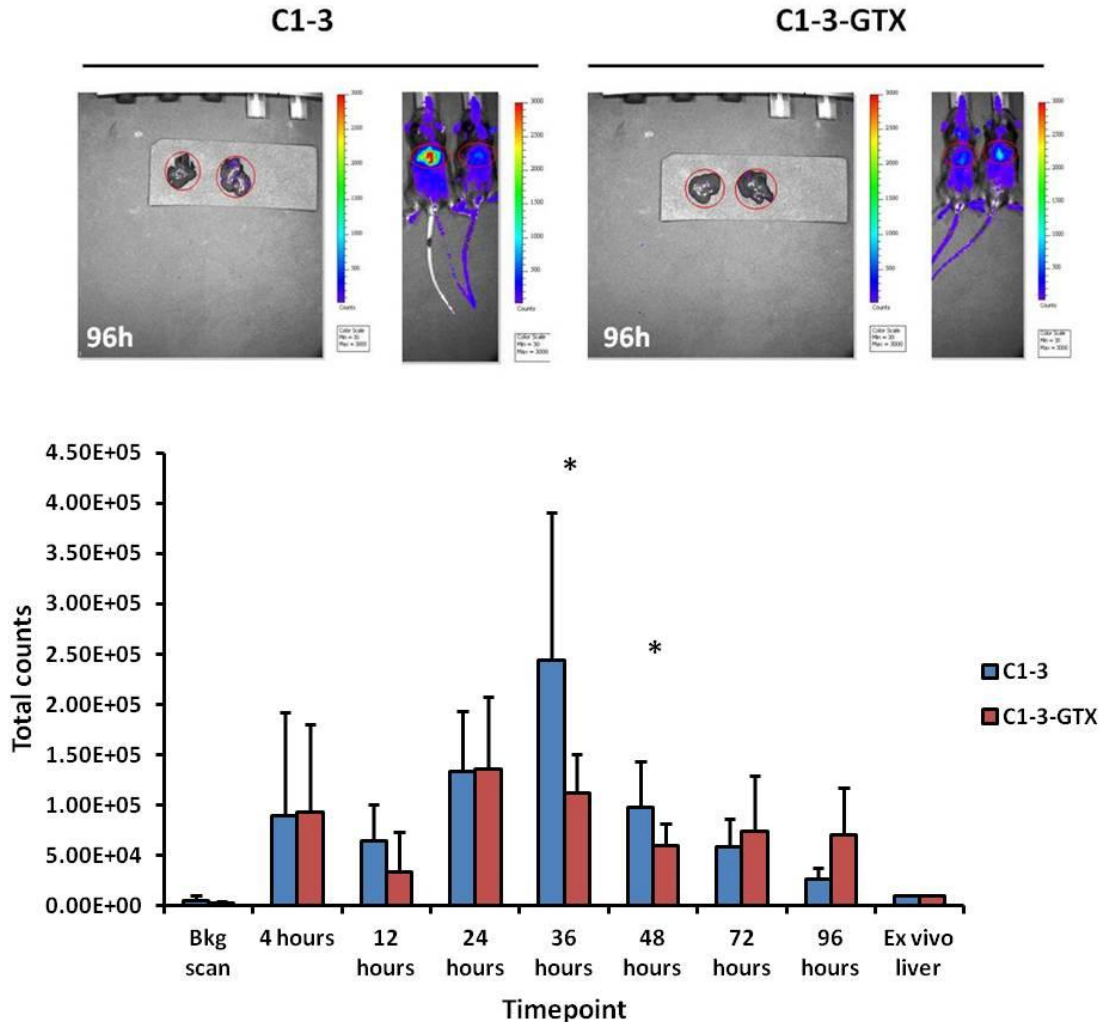


**Figure 6.31 Whole body scan with ROIs overlaid and the calculated total luminescence values.** ROIs could be overlaid onto images with the Image Pro Plus 4.0 software, allowing the calculation of total luminescence values for specific regions. The upper abdominal total luminescence values at 36 and 48 hours highlight C1-3-GTX administration has reduced the level of NF- $\kappa$ B. (\* denotes that C1-3-GTX treatment resulted in a statistically significant reduction in liver NF- $\kappa$ B levels when compared to the C1-3 only treated mice when analysed using a student's t-test, unpaired ( $p < 0.05$ ). Data are the mean and SD  $n=5$  for every timepoint except the 36 and 48 hour timepoints  $n=8$ , calculated from three independently repeated experiments.

The data from this study highlight C1-3-GTX's beneficial anti-inflammatory activity, shown by the reduction in NF- $\kappa$ B activity seen after CCl<sub>4</sub> treatment when compared to the C1-3 control mice. This reduction in luciferase activity was statistically significant at the 36 and 48 hour time points ( $p < 0.029$  and  $p$

< 0.050 respectively, student's t-test, unpaired). These findings support the earlier *in vitro* U937-NF- $\kappa$ B work and hepatic myofibroblasts *in vivo* work specifically that hepatic myofibroblasts are pro-inflammatory as their depletion with C1-3-GTX treatment reduced the level of NF- $\kappa$ B activity and liver inflammation detected. Also these data reinforces the targeted properties of the C1-3 scAb as if it wasn't specific to the hepatic myofibroblasts, there should be an overall increase in liver NF- $\kappa$ B activity as a result of hepatocyte cell death due to the elevated GTX levels. Repetition of this study with an increased number of mice will allow statistical analysis to confirm whether these preliminary findings are accurate.

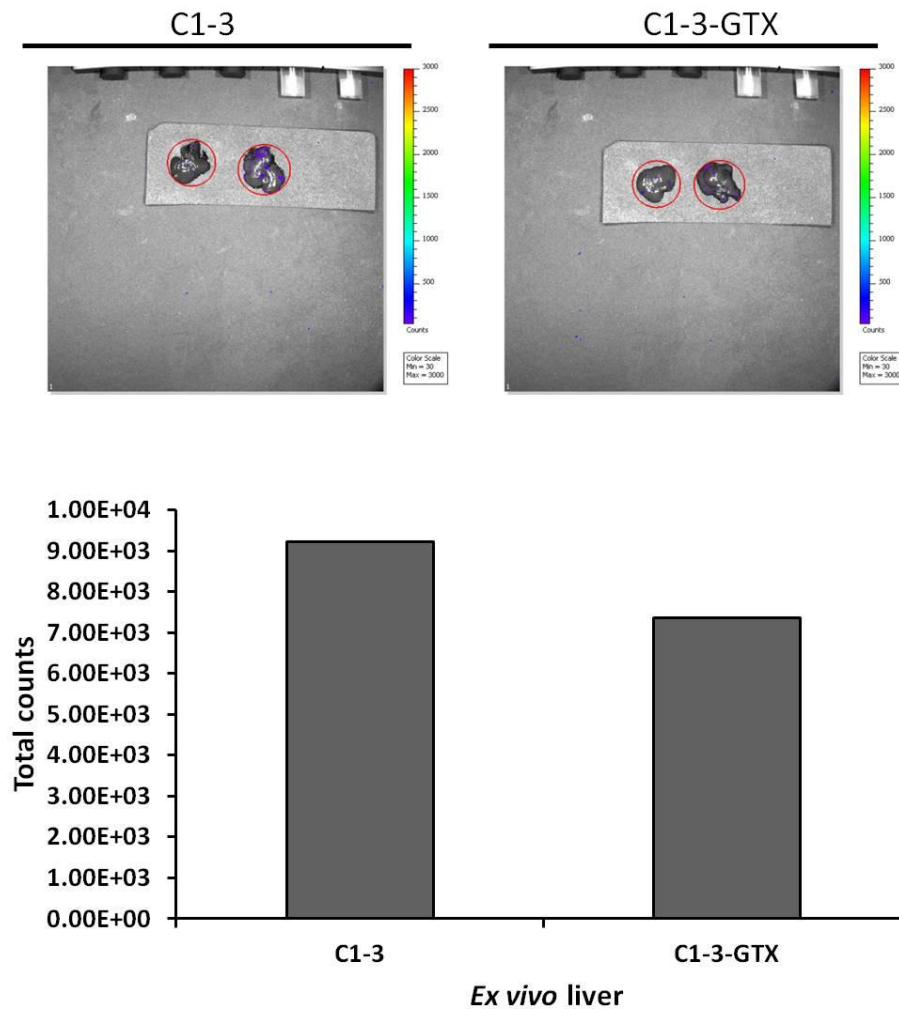


**Figure 6.32** *Ex vivo* organ scan with ROIs overlaid and the calculated total luminescence values. ROIs could be overlaid onto images with the Image Pro Plus 4.0 software, allowing the calculation of total luminescence values for the excised livers. The total luminescence values suggest C1-3-GTX administration has reduced the level of NF- $\kappa$ B activity in the liver although the reduction is much smaller than observed at the earlier time points in the whole body scans (Figure 6.30) (n=2).

## 6.6 Chapter discussion

Previous work over the past thirty years has delineated the major pathways central in the pathophysiology of liver fibrosis, predominantly the crosstalk of the inflammatory and wound healing cycles [32, 217]. When the liver is injured, hepatic myofibroblasts proliferate and function to re-model the ECM as part of a coordinated multi-cellular response that leads to the regeneration of liver tissue [32, 230]. The transdifferentiation of HSCs is a major source of hepatic myofibroblasts. However, the signal that initiates the process of transdifferentiation is not known but has been proposed to originate from monocyte and/ or macrophage-derived oxidative stress and cytokines [3]. In this chapter we investigated firstly whether the initiating signal could derive from a population of hepatic myofibroblasts themselves, through the release of a factor(s) that activate monocytes/ macrophages, which in turn release oxidizing molecules and cytokines further promoting hepatic myofibroblast transdifferentiation and liver fibrosis development.

To test this hypothesis *in vitro*, both LX-2s and primary hHSCs were cultured with the non-adherent human U937-NF- $\kappa$ B cell line (stably-transfected with a luciferase reporter gene under control of a concatamer of NF- $\kappa$ B response elements) [187]. NF- $\kappa$ B describes a series of transcription factor complexes that play a major role in the regulation of inflammatory gene expression (e.g. IL-1) [179, 239]. Secondly *in vivo* hepatic myofibroblasts were injected directly into NF- $\kappa$ B luciferase mice prior to optical imaging to ascertain whether they were pro-inflammatory by the variation in luminescence detected and also to determine if this inflammation was confined to the liver.

Following issues with revival and selection of the U937-NF- $\kappa$ B cell line supplied by Dr Carlsen, a 3xNF-KB luciferase construct was designed and transfected into U937 cells to detect NF-KB activity (Figures 6.3 – 6.6). The initial co-culture of LX-2 and hHSCs with U937-NF- $\kappa$ B cells (Figures 6.7 and 6.8) revealed that both are pro-inflammatory displayed by their statistically significant induction of luciferase activity when compared to the U937-NF- $\kappa$ B cells only. Further analysis revealed that this induction of NF- $\kappa$ B was mediated via a soluble factor released into the culture media, as addition of 48 hour LX-

2 and hHSC conditioned media also induced luciferase expression (Figures 6.9 and 6.10).

There are a multitude of inflammatory pathways/ cytokines that have been implicated in the development/ perpetuation of liver fibrosis. A range of pro-inflammatory cytokines including IL-6, IL-8, IL-1 $\alpha$  and MCP-1 (see Table 2.3 for a complete list) were incubated with U937-NF- $\kappa$ B cells in place of LX-2 cells. A number of these treatments resulted in a statistically significant increase in luciferase activity induction, as seen following LX-2 co-culture (Figures 6.11, 6.13A and 6.14). The values of these increases were significantly lower indicating that these cytokines are not the pro-inflammatory mediator released by LX-2 cells. IL-1 $\alpha$  and IL-1 $\beta$  both induced luciferase activity, so to determine if they were a contributing part of the response seen they were cultured with U937-NF- $\kappa$ B cells again in the presence of an IL-1RA. Although this IL-1RA did not have any effect (Figure 6.13B), so it is possible IL-1 $\alpha$  and IL-1 $\beta$  could be a part of the soluble factor(s) released by LX-2 cells. The inflammatory potential of ROS has previously been highlighted [236], to discount them the level of NO released by LX-2 cells released into the culture media (alone and in co-culture with U937-NF- $\kappa$ B cells) was determined by a Griess assay (Figure 6.15B). There was no significant increase in NO concentration following co-culture of LX-2 cells and U937-NF- $\kappa$ B cells over the 48 hour timecourse. Significant increases in NO concentration were only detected in the co-culture also treated with the positive control SNP. In addition the incubation of SNP and H<sub>2</sub>O<sub>2</sub> with U937-NF- $\kappa$ B cells had no impact on luciferase activity; however bubbling CO through the U937-NF- $\kappa$ B cells for ten minutes prior to incubation did result in a statistically significant increase in U937-NF- $\kappa$ B cells luciferase activity (Figure 6.15A). Once again the size of this induction was significantly lower than that induced by LX-2 co-culture with U937-NF- $\kappa$ B cells, indicating CO is unlikely to be the soluble factor released by LX-2 cells. Finally a range of treatments were performed to 48 hour LX-2 conditioned media (Table 2.3) to try and uncover the characteristics of the pro-inflammatory soluble factor. Figure 6.11 highlights that the soluble factor was unlikely to be a peptide and was a molecule of small MW (< 1kDa).

Future work will be designed to characterise the soluble factor further initially employing neutralising antibodies against target proteins, including IL-1 as previously attempted with an IL-1RA. In addition it may be beneficial to perform a dose response analysis of IL-1 $\alpha$  and IL-1 $\beta$  to determine if the concentration that was administered (10ng/ $\mu$ l) in the initial study (Figure 6.13) was within their optimal pro-inflammatory range.

In parallel further biochemical analyses will be performed to uncover the soluble factor including silver staining of the SDS-PAGE containing the later fractions eluted from the PD-10 column, which are known to contain the pro-inflammatory soluble factor. Silver staining is approximately 50 times more sensitive than standard Coomassie blue staining so any small protein bands found could be excised and sent for mass spectroscopy analysis to try and identify them.

*In vivo* injection of hepatic myofibroblasts directly into NF- $\kappa$ B luciferase mice resulted in increased luciferase transgene activity in the upper abdominal (liver) region (Figures 6.18 and 6.19) peaking 48 hours after hepatic myofibroblast injection. In a subsequent study it was confirmed the inflammation induced was due to hepatic myofibroblast injection and not the presence of residual trypsin from the isolation process (Figure 6.22). However in contrast the peak induction of NF- $\kappa$ B activity was much earlier than in the initial study (6 hours versus 48 hours after hepatic myofibroblast injection), the reason for this variation in NF- $\kappa$ B induction was unknown but could be influenced by the passage number of the cells. Alternatively the hepatic myofibroblasts viability could have varied between the two studies during the isolation and injection of hepatic myofibroblasts, although the same protocol and timeframe was used. Potentially the viability of the cells could have allowed the engraftment of the injected hepatic myofibroblasts into the liver tissue as seen at 48 hours after injection in the initial study, supported by the  $\alpha$ SMA IHC (Figure 6.20). Whilst the cells may have been less viable in the follow up studies and the inflammatory response seen at 6 hours after injection was a result of an increased number of dead cells, responsible for the increased induction NF- $\kappa$ B activity.

Repeat experiments included a range of controls such as kidney fibroblasts and latex beads to determine whether these inflammatory properties were specific to hepatic myofibroblasts or are a property of other cell types or particles of a similar size. When kidney fibroblasts were injected there was a significant increase in liver region total luminescence 6 hours after injection (Figures 6.25 and 6.26), although there was no variation in the total luminescence detected in the *ex vivo* liver scan 48 hours after injection. These results mirror the second hepatic myofibroblast study (Figures 6.22 and 6.23), suggesting that the inflammatory properties of hepatic myofibroblasts are not unique. The final study incorporated latex beads as well beside hepatic myofibroblasts and kidney fibroblasts, unfortunately in this instance none of the injected cell types resulted in a significant induction of NF- $\kappa$ B activity at any time points (Figure 6.27 and 6.28). Once again the cells were isolated and prepared identically to the previous studies; the reason for lack of NF- $\kappa$ B induction in this instance can only be postulated at (i.e. passage number and cell viability).

These preliminary findings are encouraging, suggesting hepatic myofibroblasts are also pro-inflammatory when injected *in vivo*, although further studies need to be performed to confirm the initial observations. Primarily the initial study alongside the kidney fibroblast and latex bead controls needs repeating with a minimum of three mice per treatment group as these initial experiments were performed with a single mouse in each treatment group, due to the limited number of NF- $\kappa$ B luciferase mice available. In addition all studies would be performed on the same day ensuring that there was no variation in the viability/ passage number of the cells injected. The inclusion of multiple mice in each treatment group will minimise the impact of human error (e.g.  $^{125}$ I-luciferin dosing at each time point), which could have impacted upon on the imaging outcome in the initial studies.

The pro-inflammatory trait of hepatic myofibroblasts was also confirmed following a single dose of CCl<sub>4</sub> to NF- $\kappa$ B luciferase mice and subsequent administration of either C1-3 or C1-3-GTX (Figure 6.29). Treatment with C1-3-GTX to deplete hepatic myofibroblasts resulted in a statistically significant decrease ( $p < 0.050$ , students t-test, unpaired) in liver region NF- $\kappa$ B activity 36

and 48 hours after CCl<sub>4</sub> dosing when compared to the C1-3 only treated mice (Figure 6.31), confirming that hepatic myofibroblasts are pro-inflammatory. Similarly to the earlier studies this pilot study only contained 2 mice per treatment group, therefore with increased numbers of mice and injection of a greater volume of diluted CCl<sub>4</sub> the degree of human error will be reduced and the statistical significance of any findings increased. Also repetition of the study in a chronic situation with repeated CCl<sub>4</sub> and C1-3-GTX dosing may allow greater conclusions to be drawn regarding both hepatic myofibroblasts pro-inflammatory characteristics and C1-3-GTX's dual anti-fibrotic and anti-inflammatory properties.

A future study could be performed treating fibrotic NF-κB luciferase mice with C1-3-GTX and also unconjugated GTX at various concentrations. This study could confirm the selectivity of C1-3-GTX and also reveal the effect of its targeting of quiescent HSCs and other hepatic cell types. Luminescent scans would reveal the induction of inflammation by free GTX and supporting IHC analysis would indicate the amount of damage induced by GTX and C1-3-GTX administration. The use of a GTX specific secondary antibody may also confirm that C1-3-GTX is specific to hepatic myofibroblasts and does not target Kupffer cells.

A major limitation of all the studies performed utilising the NF-κB mice is the lack of the IHC analysis of the transgene activity, therefore it may be beneficial to revisit the optimisation of the firefly-luciferase antibody trialled in chapter 5. Alternatively if a chronic study is performed involving repeated hepatic myofibroblast injection it may be possible to detect the presence of αSMA positive cells that are now present in the liver.

The data presented in this chapter demonstrates that hepatic myofibroblasts are pro-inflammatory; releasing a soluble factor *in vitro* that activates U937-NF-κB monocyte NF-κB transcriptional activity. These findings were further reinforced by the *in vivo* results, when hepatic myofibroblast injection into NF-κB luciferase mice resulted in increased liver luminescence. These data therefore suggest that myofibroblasts may regulate/ contribute to the inflammatory process and may release a soluble factor that could via the

release of pro-inflammatory molecules from monocytes/ macrophages impact on hepatic myofibroblast activity and fibrosis development.

## **Chapter 7.0 – General discussion**

## 7.1 Results summary

The incidence of liver fibrosis/ cirrhosis has been steadily increasing for the past fifty years and as a result of increased alcoholic consumption and a more sedentary life style its incidence is only expected to increase further. Liver injury in acute cases is of little consequence, due to the livers' high capacity for regeneration maintaining a constant functional capacity. However with chronic injury there is continual activation of the inflammatory and immune responses, which result in the transdifferentiation of quiescent HSCs to a pro-fibrogenic hepatic myofibroblast phenotype as part of the wound healing response in an attempt to remodel the ECM and encapsulate the injured region. Eventually the level of ECM fibrosis deposition exceeds the level at which it is also degraded, leading to increased levels of fibrous ECM. As the severity of these fibrotic bands increases there is an increased distortion of the general liver architecture and consequently a reduction in liver function.

Presently the only mode of treatment for liver fibrosis/ cirrhosis is transplantation, although this is only an option for a small minority of sufferers. Alternatively treating the underlying cause of the disease is an effective treatment, e.g. anti-viral treatment of hepatitis viral infections. Critical to development of novel anti-fibrotics is the availability of an accurate non-invasive imaging modality to diagnose and quantitate liver fibrosis at all disease stages. The current 'gold standard' liver biopsy is a highly invasive procedure and also has issues associated with sampling errors and interobserver variation in its scoring. Available non-invasive methods including serum biomarker panels and transient elastography are useful but cannot distinguish early developmental fibrosis and fatty/ fibrotic livers respectively.

The primary aims of this thesis were to try and develop a non-invasive method to diagnose and quantify hepatic fibrosis, using the hepatic myofibroblast specific properties of the scAb C1-3 when conjugated with a long wavelength fluorophore. Of equal importance despite the advances in our understanding of the pathways underpinning HSC activation the stimulus for their activation and transdifferentiation is still unknown. It has been suggested the stimulus may arise from a subset of hepatic myofibroblasts themselves, this was

investigated by co-culturing hepatic myofibroblasts with the monocytic U937-NF- $\kappa$ B luciferase cell line. NF- $\kappa$ B is a major pro-inflammatory transcription factor whose induction will result in luciferase activity when the  $\beta$ -luciferin substrate is added. Finally we wished to further elucidate the anti-fibrotic benefits of PXR activators and in particular whether their anti-inflammatory properties are mediated via NF- $\kappa$ B in an *in vivo* model of liver fibrosis.

Initially it was intended in collaboration with the chemistry department to conjugate the C1-3 scAb with a radiolabel (in this instance  $^{18}\text{F}$ -SFB) prior to injection into fibrotic and control mice. PET scans would then have been performed to determine if there was an increase in radiolabel detected in the liver region of the fibrotic mice when compared to the control mice. Unfortunately there were significant problems encountered in the setting up of the 'hot cells' in the chemistry laboratory central to the  $^{18}\text{F}$ -SFB conjugation process that are yet to be rectified. Therefore as an alternative it was elected to conjugate C1-3 with a long wavelength fluorophore (XF750) and perform identical experiments using optical imaging fluorescent scans in place of PET scans.

C1-3 was conjugated to XF750 via its primary amine and successful conjugation was confirmed by an increase in MW by both SDS-PAGE and MALDI-TOF analyses. In addition its specificity for its target antigen synaptophysin was confirmed by both a binding ELISA and BIACORE analyses. Addition of C1-3-750 to hepatic myofibroblasts *in vitro* suggested that the scAb was unable to target synaptophysin (although C1-3-FITC and C1-3-594 were both functioning), whether this was a result of XF750 presence or competitive inhibition from unlabelled C1-3 is unclear (which was detected in the MALDI-TOF analysis leftover from the conjugation reaction). The initial pilot study illustrated firstly that C1-3-750 targeted hepatic myofibroblasts *in vivo* and was potentially an indicator of fibrosis severity. Secondly both an i.v. and i.p. injection route could be employed to administer C1-3-750, although it appeared i.p. would be more suitable for non-invasive imaging of hepatic fibrosis. The final study incorporated mice with varying degrees of fibrosis severity (12, 8 and 4 week  $\text{CCl}_4$  administration) and control mice which received olive oil. Measurement of the total luminescence of the upper

abdominal liver region revealed that C1-3-750 could not be used non-invasively using an i.p. injection route. However the total liver luminescence values calculated from the *ex vivo* organ scans revealed all fibrotic mice had a statistically significant increase in liver fluorescence when compared to the controls. Subsequent  $\alpha$ SMA and sirius red IHC confirmed the increased number of hepatic myofibroblasts and collagen deposition following CCl<sub>4</sub> administration. This chapter provides proof of concept for C1-3's use as an imaging agent of hepatic fibrosis although further experiments need to be performed to optimise its use. Investigating the contribution of the pancreas signal (due to the synaptophysin positive Islet cells present) on the overall upper abdominal luminescence detected needs to be performed.

Initial IHC work by Cassiman *et al* [108] indicated that synaptophysin was expressed by both quiescent and activated HSCs. The data from the C1-3-750 imaging study supported this view, as there was an increase in total liver fluorescence of the control mice as well, suggesting that C1-3 was also binding to quiescent HSCs. Also of note was the loss of C1-3-750's functioning in a rat model of liver fibrosis, indicating that there was some variation in synaptophysin expression between mouse and rat liver. Therefore the primary aim of the second chapter was to uncover more about synaptophysin expression in whole tissue and HSCs from rat, mouse and human samples. In addition the synaptophysin expression of quiescent and activated HSCs was determined by both qRT-PCR and ICC analysis.

Firstly C1-3 binding to synaptophysin and not another target present on the surface of hepatic myofibroblasts was confirmed by fluorescent microscopy. C1-3-594 only targeted Cos7 cells transfected with either human or mouse synaptophysin and not untransfected Cos7 cells. The level of synaptophysin expression was determined by both Western blotting and by PCR utilising pre-designed primers specific to conserved regions of mouse, rat and human synaptophysin cDNA sequences. Synaptophysin was undetectable in all protein samples (both tissue samples and those isolated from HSCs) using commercially available synaptophysin antibodies. It was only detected in the neural (mouse brain) positive control sample, whilst synaptophysin could be detected in all HSC samples with each primer set although at a much lower

level than that expressed in the positive control sample. In contrast synaptophysin expression could only be detected in the mouse and rat liver tissue samples using specific primer sets, and the full transcribed synaptophysin sequence could not be detected in any organ sample. These findings coupled with ICC staining of tissue sections indicate that there was a variation in synaptophysin expression potentially as a result of a post-transcriptional modification. qRT-PCR revealed that both quiescent and activated HSCs express similar levels of synaptophysin (approximately 100 fold lower than mouse brain). ICC analysis following C1-3-594 addition to quiescent and activated HSCs demonstrated for the first time that C1-3 was able to target both cell types.

Previous work from members of this laboratory revealed the anti-fibrotic properties of PXR agonists, in this chapter we wished to ascertain whether this effect was mediated via NF- $\kappa$ B. A single dose of the PXR agonist PCN was administered to NF- $\kappa$ B-luciferase mice that had received chronic (4 weeks CCl<sub>4</sub>), acute (a single dose of CCl<sub>4</sub>) or no liver injury. Bioluminescent scans were performed in the IVIS (6 and 24 hours after PCN administration) to quantify NF- $\kappa$ B activity and inflammation levels in the liver region. *Ex vivo* organ scans were performed following the 24 hour bioluminescent scan to determine individual liver NF- $\kappa$ B levels. There was a statistically significant reduction in liver luminescence of the chronic CCl<sub>4</sub> treatment group following PCN treatment at the 24 hour scan and in the liver of the *ex vivo* organ scans. These findings indicate that PCN is anti-inflammatory as hypothesised; luciferase assays performed on homogenised liver tissue from each mouse indicated that PCN had an anti-inflammatory effect on the acute CCl<sub>4</sub> treated mice only. Subsequent IHC analysis (H&E,  $\alpha$ SMA and sirius red) demonstrated that liver damage, hepatic myofibroblast number and collagen deposition had all increased following CCl<sub>4</sub> treatment and PCN administration had no effect on CCl<sub>4</sub> hepatotoxicity. The number of neutrophils was also determined by NIMP IHC staining and there was a statistically significant reduction in their number following PCN administration in the acute CCl<sub>4</sub> treatment group reinforcing PCN's anti-inflammatory properties. Attempts were also made to try and measure the luciferase transgene directly, using a

luciferase specific primary antibody to determine if specific cells in the liver were responsible for the inflammation seen. Unfortunately these attempts were unsuccessful when using the luciferase antibody in both IHC and Western blotting techniques.

Despite major advances in our understanding of the pathogenesis of liver fibrosis, especially the central role of HSCs and their transdifferentiation to a hepatic myofibroblast phenotype the identity of the stimulus responsible for their activation is still unknown. In the final chapter I investigated whether a subset of hepatic myofibroblasts themselves are pro-inflammatory and may stimulate circulating monocytes/ macrophages resulting in the activation of the inflammatory cycle critical in fibrosis development.

To test this hypothesis the monocytic U937-NF- $\kappa$ B cell line was initially incubated with LX-2 cells (due to the limited availability of primary hHSCs) and luciferase assays were performed to determine the level of inflammation (NF- $\kappa$ B transgene activity) induced. Due to the problems encountered with revival and functioning of the U937-NF- $\kappa$ B cells supplied by Dr. Harald Carlsen it was necessary to manufacture our own U937-NF- $\kappa$ B cell line. A NF- $\kappa$ B responsive luciferase construct (pGL4.28-NF- $\kappa$ B) was generated and its functioning confirmed by transient transfection into U937 and Cos7 cells prior to LPS treatment. Stable transfection of U937-NF- $\kappa$ B cells with the construct was achieved by *Hygromycin B* selection, prior to further experimentation.

Initial co-culture of U937-NF- $\kappa$ B cells with LX-2 cells revealed that they are pro-inflammatory, and this was mediated via a soluble factor released into the media in a dose dependent manner. These findings were subsequently verified in hHSCs to confirm they weren't just a property of the LX-2 cells. Treatments performed on the LX-2 cultured media revealed that the soluble factor was a small molecule (found in the later fractions PD-10 filtration), and that it was unlikely to be a peptide (unaffected by 10 x trypsin-EDTA treatment). Incubation of a range of pro-inflammatory cytokines and fibrogenic mediators (e.g. IL-6, IL-1 $\alpha$ , IL-1 $\beta$ , MCP-1, serotonin, leptin, ROS) resulted in a statistically significant increase in luciferase activity of U937-NF- $\kappa$ B cells in some cases. However the size of these increases were much smaller than

those seen with LX-2's or LX-2 conditioned media co-culture suggesting that they are unlikely to be the soluble factor released by LX-2 cells.

An *in vivo* pilot study injecting hepatic myofibroblasts directly into NF- $\kappa$ B-luciferase mice revealed that they are pro-inflammatory *in vivo* as well and appeared to be specific to the liver (demonstrated by the increase upper abdominal liver region luminescence 48 hours after injection). Subsequent studies with controls (including latex beads and kidney myofibroblasts) were not as successful, yielding an increased liver luminescence at 6 hours after cell injection. The reason for this variation was unclear but could be due to a variation in the viability of the injected cells. A final study utilising the NF- $\kappa$ B-luciferase mice highlighted the pro-inflammatory properties of hepatic myofibroblasts as their proliferation was induced by CCl<sub>4</sub> injection prior to the administration of C1-3 or C1-3-GTX. There was a statistically significant decrease in liver region luminescence 36 and 48 hours following treatment with C1-3-GTX when compared to those treated with C1-3 only. This decrease indicates that hepatic myofibroblast depletion by C1-3-GTX treatment resulted in a reduction in liver inflammation mediated via NF- $\kappa$ B activity.

## **7.2 Project limitations and future work**

There are unavoidable limitations when utilising optical imaging techniques, primarily issues with tissue penetration and signal loss due to non specific signal absorption by body fluids. By utilising the XF750 long wavelength flurophore the level of non specific signal absorption will have been minimised as it is highest below 500nm where haemoglobin absorption is high and above 900nm where water absorption interferes with the signal detected. The poor liver region fluorescence signal detected from the i.v. injected fibrotic mouse in contrast to the high *ex vivo* liver signal of the same mouse, coupled with the high signal loss when a C1-3-750 dose was placed beneath a control liver perfectly highlight these issues of tissue penetration and signal loss associated with optical imaging. These problems are unavoidable, especially

when trying to non-invasively diagnose liver fibrosis by this method. The use of an i.p. injection route prevented non-invasive diagnosis of hepatic fibrosis due to the retention of the C1-3-750 dose in the peritoneal cavity masking any liver specific signal. In hindsight utilising an i.v. injection route with a greater number of mice to avoid repeat injections, and accepting the potential variation in dosing as a result of that injection route would have been a more appropriate way to perform the final study. Another issue was the high signal detected from the pancreas due to the presence of synaptophysin positive Islet cells. Firstly this limits the use of the antibody clinically as it is not solely specific to the liver, and utilising optical imaging it was not possible to determine and quantify the contribution of the pancreas and kidney signals to the overall liver region fluorescence detected in the whole body scans.

The majority of these issues could be rectified if as intended C1-3 was conjugated with  $^{18}\text{F}$ -SFB and PET scans were performed. Firstly PET is a much higher power technique and will improve the resolution of the signal detected. In addition it is normal practise in clinical settings to overlay PET images onto computerised tomography (CT) scans. Therefore it will be possible to identify the signal of specific organs and more accurately quantify the liver signal and fibrosis severity. Irrespective of the imaging technique used there is also the need to investigate the use of C1-3 in other causes of hepatic fibrosis, as hepatic myofibroblasts are not the only fibrogenic cell type present in the liver (e.g. portal fibroblasts which are prominent in portal fibrosis development). It would be of benefit to repeat this initial study in mice following BDL to determine the level of C1-3-750 binding and hepatic myofibroblast presence in this disease setting.

The confirmation that quiescent HSCs express similar levels of synaptophysin as 'activated' hepatic myofibroblasts indicates suggests that more caution must be used when administering C1-3 as an imaging agent. This is especially true when it is conjugated with GTX as an anti-fibrotic agent as the implications of quiescent HSC loss are unknown and need researching further. The data in chapter 4 highlighted the difficulty involved in detecting synaptophysin by both Western blotting and IHC techniques with commercially available C-terminal synaptophysin antibodies at present. This

lack of detection could be the result of a post-transcriptional modification of synaptophysin masking its detection with antibodies. Further research needs to be performed to determine if there is indeed a splice variant of synaptophysin expressed on the surface of hepatic myofibroblasts.

The major limitations of the *in vivo* study to investigate the anti-inflammatory effects of PCN in a mouse model of liver fibrosis only became apparent in hindsight. The data generated from this pilot study supported the initial hypothesis that PCN is anti-inflammatory and this was mediated via NF- $\kappa$ B displayed by the whole body and *ex vivo* liver luminescence values and NIMP IHC staining. Unfortunately it was not possible to determine luciferase transgene activity by Western blotting or IHC techniques, which would have given a greater insight into the cells responsible for NF- $\kappa$ B activity in the liver. Two different antibodies were trialled yet neither exhibited the specificity advertised for the firefly-luciferase gene. Previously PCN was shown to have anti-fibrotic properties as it significantly reduced the number of  $\alpha$ SMA positive myofibroblasts and sirius red collagen deposition. This was not found in this study although PCN was only administered acutely with the final dose of CCl<sub>4</sub>, therefore significant hepatic myofibroblast and collagen deposition would already have occurred. A future repeat study administering PCN chronically with various CCl<sub>4</sub> treatment groups (e.g. 12, 8 and 4 week administration) would allow greater conclusions to be drawn about both the anti-fibrotic and anti-inflammatory properties of PCN.

As highlighted earlier, issues were encountered when reviving and culturing the U937-NF- $\kappa$ B cells, despite *Hygromycin B* selection. In some instances the cells would spontaneously lose all luciferase activity even in response to LPS. The reason for this was unclear; potentially it was a result of the viability of the cells decreasing due to increased cell death, although this was not detected by trypan blue counting prior to experiments being performed. As the U937-NF- $\kappa$ B cells are grown as a suspension culture there was no feasible way to separate the viable and non-viable cells unlike trypsinisation for adherent cell lines. The initial co-cultures confirmed that LX-2 cells and hHSCs are pro-inflammatory and induce NF- $\kappa$ B activity, releasing a pro-inflammatory soluble factor. Despite our best efforts (protease treatment and PD-10 filtration of LX-

2 conditioned media and addition of pro-inflammatory cytokines to U937-NF- $\kappa$ B cells) the identity of the soluble factor is still unknown. The roles of potential contributing cytokines could be determined with the use of monoclonal antibodies to these targets. In addition it may be possible to perform additional biochemical/ proteomic analysis (e.g. MALDI-TOF) on later PD-10 filtered fractions of LX-2 conditioned and normal U937-NF- $\kappa$ B cells media to try and determine the soluble factor.

*In vivo* injection of hepatic myofibroblasts directly into NF- $\kappa$ B-luciferase mice resulted in induction of NF- $\kappa$ B specifically in the liver indicating they are pro-inflammatory *in vivo* as well. However there was a significant variation in response in follow up experiments when hepatic myofibroblasts, kidney fibroblasts and latex beads were injected. Whether this was due to a difference in viability of the cells was unclear, in addition these initial studies were generally only performed with a single mouse in each treatment group. Repeat studies with increased NF- $\kappa$ B-luciferase mice will minimise the effect of any human errors that will have affected the imaging outcome detected (e.g. CCl<sub>4</sub> and D-luciferin dosing). As discussed earlier in the PXR study the lack of functioning of the firefly-luciferase antibody prevents the detection of luciferase transgene activity and detection of NF- $\kappa$ B in specific hepatic cell types. Depletion of hepatic myofibroblasts by co-administration of C1-3-GTX resulted in a decrease in liver NF- $\kappa$ B activity further indicating the pro-inflammatory properties of hepatic myofibroblasts. In the future performing repeat injections of hepatic myofibroblasts may encourage greater engraftment of hepatic myofibroblasts into the liver, which may also be detectable by  $\alpha$ SMA IHC staining as well as the bioluminescent scans.

### **7.3 Conclusions**

The data presented in this thesis firstly reveals that the number of hepatic myofibroblasts can be used as an indicator of fibrosis severity, suggesting the hepatic myofibroblast specific scAb C1-3 has the potential to be utilised as a non-invasive alternative to the liver biopsy. Although further work needs to be

performed distinguishing the effect of C1-3 also targeting the pancreas and trial its conjugation to  $^{18}\text{F}$ -SFB and PET imaging, which is more clinically applicable unlike optical imaging. Further *in vitro* analysis confirmed C1-3's affinity for quiescent HSCs as well hepatic myofibroblasts and quantitative real-time PCR analysis indicated that they express identical levels of synaptophysin.

The *in vivo* imaging study further advocated the use of PXR agonists as an anti-fibrotic agent, specifically highlighting their anti-inflammatory properties. Further studies could determine whether they could be beneficial when administered alone or as part of a combined treatment regimen. Finally *in vitro* and *in vivo* studies highlighted the pro-inflammatory properties of hepatic myofibroblasts activating NF- $\kappa$ B, which could contribute to initial hepatic fibrosis development.

## **Chapter 8.0 – References**

1. PW. Tank and TR. Gest, Lippincott Williams & Wilkins Atlas of Anatomy 2009. 448.
2. MacSween R N M, et al., Pathology of the Liver. Vol. 4th edition. 2002.
3. Wallace, K., A.D. Burt, and M.C. Wright, Liver fibrosis. Biochemical Journal, 2008. **411**(1): p. 1-18.
4. Malarkey, D.E., et al., New Insights into Functional Aspects of Liver Morphology. Toxicologic Pathology, 2005. **33**(1): p. 27-34.
5. Kiernan, F., The Anatomy and Physiology of the Liver. Philosophical Transactions of the Royal Society of London, 1833. **123**(ArticleType: research-article / Full publication date: 1833 / Copyright © 1833 The Royal Society): p. 711-770.
6. Rappaport, A.M., et al., Subdivision of hexagonal liver lobules into a structural and functional unit. Role in hepatic physiology and pathology. The Anatomical Record, 1954. **119**(1): p. 11-33.
7. Oinonen, T., Lindros, Kai., Zonation of hepatic cytochrome P-450 expression and regulation. Biochem. J., 1998. **329**: p. 17-35.
8. Kuntz, E. and H.D. Kuntz, Hepatology: Principles and Practice : History, Morphology, Biochemistry, Diagnostics, Clinic, Therapy 2006: Springer.
9. Zhao, R. and S.A. Duncan, Embryonic development of the liver. Hepatology, 2005. **41**(5): p. 956-967.
10. Vrba, J., Modriansky, M., Oxidative burst of Kupffer cells: target for liver injury treatment. Biomed. Papers, 2002. **146**(2): p. 15-20.
11. Duffield, J.S., The inflammatory macrophage: a story of Jekyll and Hyde. Clin. Sci., 2003. **104**(1): p. 27-38.
12. Duffield, J.S., et al., Selective depletion of macrophages reveals distinct, opposing roles during liver injury and repair. The Journal of Clinical Investigation, 2005. **115**(1): p. 56-65.
13. Mullin EJ, Metcalfe MS., and M. GJ., Artificial liver support: Potential to retard regeneration? Archives of Surgery, 2004. **139**(6): p. 670-677.

14. Friedman, S.L., Molecular regulation of hepatic fibrosis, an integrated cellular response to tissue injury. *Journal of Biological Chemistry*, 2000. **275**(4): p. 2247-50.
15. Matsuoka, M. and H. Tsukamoto, Stimulation of hepatic lipocyte collagen production by Kupffer cell-derived transforming growth factor  $\beta$ : Implication for a pathogenetic role in alcoholic liver fibrogenesis. *Hepatology*, 1990. **11**(4): p. 599-605.
16. Henderson, N.C. and S.J. Forbes, Hepatic fibrogenesis: From within and outwith. *Toxicology*, 2008. **254**(3): p. 130-135.
17. Braet, F. and E. Wisse, Structural and functional aspects of liver sinusoidal endothelial cell fenestrae: a review. *Comparative Hepatology*, 2002. **1**(1): p. 1-17.
18. Smedsrød B, et al., Cell biology of liver endothelial and Kupffer cells. *Gut*, 1994. **35**: p. 1509-1516.
19. Lalor, P.F., et al., Recruitment of lymphocytes to the human liver. *Immunol Cell Biol*, 2002. **80**(1): p. 52-64.
20. Edwards, S., et al., Lymphocyte traffic through sinusoidal endothelial cells is regulated by hepatocytes. *Hepatology*, 2005. **41**(3): p. 451-459.
21. Fausto, N. and J.S. Campbell, The role of hepatocytes and oval cells in liver regeneration and repopulation. *Mechanisms of Development*, 2003. **120**(1): p. 117-130.
22. Wang, X., et al., The origin and liver repopulating capacity of murine oval cells. *Proceedings of the National Academy of Sciences of the United States of America*, 2003. **100**(Suppl 1): p. 11881-11888.
23. Kinnman N. and Housset C., Peribiliary myofibroblasts in biliary type liver fibrosis. *Front Biosci.*, 2002. **1**: p. 496-503.
24. Leon, D.A. and J. McCambridge, Liver cirrhosis mortality rates in Britain from 1950 to 2002: an analysis of routine data. *The Lancet*, 2006. **367**(9504): p. 52-56.

25. Tiollais, P., C. Pourcel, and A. Dejean, The hepatitis B virus. *Nature*, 1985. **317**(6037): p. 489-95.
26. Choo, Q.L., et al., Isolation of a cDNA clone derived from a blood-borne non-A, non-B viral hepatitis genome. *Science*, 1989. **244**(4902): p. 359-362.
27. Day, C.P., Natural history of NAFLD: remarkably benign in the absence of cirrhosis. *Gastroenterology*, 2005. **129**(1): p. 375-8.
28. Tilg, H. and C.P. Day, Management strategies in alcoholic liver disease. *Nat Clin Pract Gastroenterol Hepatol*, 2007. **4**(1): p. 24-34.
29. Ueno, Y., et al., Primary biliary cirrhosis: what we know and what we want to know about human PBC and spontaneous PBC mouse models. *Journal of Gastroenterology*, 2007. **42**(3): p. 189-195.
30. Feder, J.N., A novel MHC class-I-like gene is mutated in patients with hereditary haemochromatosis. *Trends in Genetics*, 1996. **12**(10): p. 398-398.
31. Ferenci, P., Wilson's Disease. *Clinical Gastroenterology and Hepatology*, 2005. **3**(8): p. 726-733.
32. Bataller, R. and D.A. Brenner, Liver fibrosis. *Journal of Clinical Investigation*, 2005. **115**(2): p. 209-18.
33. Friedman, S.L., Hepatic fibrosis -- overview. *Toxicology*, 2008. **254**(3): p. 120-9.
34. Friedman, S.L., Liver fibrosis -- from bench to bedside. *Journal of Hepatology*, 2003. **38 Suppl 1**: p. S38-53.
35. Benyon, R., Iredale, J, Is liver fibrosis reversible? *Gut*, 2000. **46**(4): p. 443-446.
36. Forbes, S.J., et al., A significant proportion of myofibroblasts are of bone marrow origin in human liver fibrosis. *Gastroenterology*, 2004. **126**(4): p. 955-963.
37. Kalluri, R. and E.G. Neilson, Epithelial-mesenchymal transition and its implications for fibrosis. *The Journal of Clinical Investigation*, 2003. **112**(12): p. 1776-1784.

38. Geerts, A., History, heterogeneity, developmental biology, and functions of quiescent hepatic stellate cells. *Seminars in Liver Disease*, 2001. **21**(3): p. 311-35.
39. Brenner, D.A., Molecular pathogenesis of liver fibrosis. *Transactions of the American Clinical & Climatological Association*, 2009. **120**: p. 361-8.
40. Casini, A., et al., Neutrophil-derived superoxide anion induces lipid peroxidation and stimulates collagen synthesis in human hepatic stellate cells: Role of nitric oxide. *Hepatology*, 1997. **25**(2): p. 361-367.
41. Canbay, A., et al., Kupffer cell engulfment of apoptotic bodies stimulates death ligand and cytokine expression. *Hepatology*, 2003. **38**(5): p. 1188-1198.
42. Jarnagin, W.R., et al., Expression of variant fibronectins in wound healing: cellular source and biological activity of the EIIIA segment in rat hepatic fibrogenesis. *The Journal of Cell Biology*, 1994. **127**(6): p. 2037-2048.
43. Pinzani, M., F. Marra, and V. Carloni, Signal transduction in hepatic stellate cells. *Liver*, 1998. **18**(1): p. 2-13.
44. Pinzani, M., PDGF and signal transduction in hepatic stellate cells. *Front Biosci.*, 2002: p. 1720-26.
45. Yoshiji, H., et al., Vascular endothelial growth factor and receptor interaction is a prerequisite for murine hepatic fibrogenesis. *Gut*, 2003. **52**(9): p. 1347-1354.
46. Marra, F., Chemokines in liver inflammation and fibrosis. *Front Biosci.*, 2002: p. 1899-914.
47. Marra, F., et al., Monocyte chemoattractant protein-1 as a chemoattractant for human hepatic stellate cells. *Hepatology*, 1999. **29**(1): p. 140-148.
48. Inagaki, Y., et al., Interferon alfa down-regulates collagen gene transcription and suppresses experimental hepatic fibrosis in mice. *Hepatology*, 2003. **38**(4): p. 890-899.

49. Li, D. and S.L. Friedman, Liver fibrogenesis and the role of hepatic stellate cells: new insights and prospects for therapy. *Journal of Gastroenterology & Hepatology*, 1999. **14**(7): p. 618-33.
50. Gressner, A.M., Cytokines and cellular crosstalk involved in the activation of fat-storing cells. *Journal of Hepatology*, 1995. **22**(2 Suppl): p. 28-36.
51. Inagaki, Y. and I. Okazaki, Emerging insights into Transforming growth factor beta Smad signal in hepatic fibrogenesis. *Gut*, 2007. **56**(2): p. 284-292.
52. Rachfal, A.W. and D.R. Brigstock, Connective tissue growth factor (CTGF/CCN2) in hepatic fibrosis. *Hepatology Research*, 2003. **26**(1): p. 1-9.
53. Friedman, S.L., et al., Isolated hepatic lipocytes and kupffer cells from normal human liver: Morphological and functional characteristics in primary culture. *Hepatology*, 1992. **15**(2): p. 234-243.
54. Rockey, D., The cellular pathogenesis of portal hypertension: Stellate cell contractility, endothelin, and nitric oxide. *Hepatology*, 1997. **25**(1): p. 2-5.
55. Arthur, M.J., et al., Secretion of 72 kDa type IV collagenase/gelatinase by cultured human lipocytes. Analysis of gene expression, protein synthesis and proteinase activity. *Biochem. J.*, 1992. **287**(3): p. 701-707.
56. Arthur, M.J.P., Fibrogenesis II. Metalloproteinases and their inhibitors in liver fibrosis. *American Journal of Physiology - Gastrointestinal and Liver Physiology*, 2000. **279**(2): p. G245-G249.
57. Murphy, F.R., et al., Inhibition of Apoptosis of Activated Hepatic Stellate Cells by Tissue Inhibitor of Metalloproteinase-1 Is Mediated via Effects on Matrix Metalloproteinase Inhibition. *Journal of Biological Chemistry*, 2002. **277**(13): p. 11069-11076.
58. Otto DA and Veech RL., Isolation of a lipocyte-rich fraction from rat liver nonparenchymal cells. *Adv Exp Med Biol.*, 1980: p. 509-517.
59. Xu, L., et al., Human hepatic stellate cell lines, LX-1 and LX-2: new tools for analysis of hepatic fibrosis. *Gut*, 2005. **54**(1): p. 142-51.

60. Wong, F.W.Y., W.Y. Chan, and S.S.T. Lee, Resistance to Carbon Tetrachloride-Induced Hepatotoxicity in Mice Which Lack CYP2E1 Expression. *Toxicology and Applied Pharmacology*, 1998. **153**(1): p. 109-118.
61. Guo, L., et al., Increased iron deposition in rat liver fibrosis induced by a high-dose injection of dimethylnitrosamine. *Experimental and Molecular Pathology*, 2006. **81**(3): p. 255-261.
62. Yoo, J.-S.H., H. Ishizaki, and C.S. Yang, Roles of cytochrome P450IIE1 in the dealkylation and denitrosation of N-nitrosodimethylamine and N-nitrosodiethylamine in rat liver microsomes. *Carcinogenesis*, 1990. **11**(12): p. 2239-2243.
63. George, J., et al., Dimethylnitrosamine-induced liver injury in rats: the early deposition of collagen. *Toxicology*, 2001. **156**(2-3): p. 129-138.
64. Pegg, A.E. and W. Perry, Alkylation of Nucleic Acids and Metabolism of Small Doses of Dimethylnitrosamine in the Rat. *Cancer Research*, 1981. **41**(8): p. 3128-3132.
65. Hirata, K., et al., Hepatic sinusoidal cell destruction in the development of intravascular coagulation in acute liver failure of rats. *The Journal of Pathology*, 1989. **158**(2): p. 157-165.
66. Böker, K., et al., Fibrosis of the liver in rats induced by bile duct ligation : Effects of inhibition of prolyl 4-hydroxylase. *Journal of Hepatology*, 1991. **13**(Supplement 3): p. S35-S40.
67. Tuchweber B, et al., Proliferation and phenotypic modulation of portal fibroblasts in the early stages of cholestatic fibrosis in the rat. *Lab Invest.* , 1996. **74**(1): p. 265-78.
68. Miyoshi, H., et al., Hepatocyte apoptosis after bile duct ligation in the mouse involves Fas. *Gastroenterology*, 1999. **117**(3): p. 669-677.
69. Davis, G.L., et al., Treatment of Chronic Hepatitis C with Recombinant Interferon Alfa. *New England Journal of Medicine*, 1989. **321**(22): p. 1501-1506.

70. Poynard, T., et al., Impact of pegylated interferon alfa-2b and ribavirin on liver fibrosis in patients with chronic hepatitis C. *Gastroenterology*, 2002. **122**(5): p. 1303-1313.
71. Moreno, M.G. and P. Muriel, Remission of liver fibrosis by interferon-alpha 2b. *Biochemical Pharmacology*, 1995. **50**(4): p. 515-520.
72. Czaja, A.J. and H.A. Carpenter, Decreased fibrosis during corticosteroid therapy of autoimmune hepatitis. *Journal of Hepatology*, 2004. **40**(4): p. 646-652.
73. Pereira, R.M., et al., Renin-angiotensin system in the pathogenesis of liver fibrosis. *World journal of gastroenterology : WJG*, 2009. **15**(21): p. 2579-2586.
74. Kim, W.-H., et al., Growth Inhibition and Apoptosis in Liver Myofibroblasts Promoted by Hepatocyte Growth Factor Leads to Resolution from Liver Cirrhosis. *The American Journal of Pathology*, 2005. **166**(4): p. 1017-1028.
75. Brown, K.E., et al., Effect of vitamin E supplementation on hepatic fibrogenesis in chronic dietary iron overload. *American Journal of Physiology - Gastrointestinal and Liver Physiology*, 1997. **272**(1): p. G116-G123.
76. Marra\*, F., et al., Ligands of Peroxisome Proliferator-Activated Receptor gamma Modulate Profibrogenic and Proinflammatory Actions in Hepatic Stellate Cells. *Gastroenterology*, 2000. **119**(2): p. 466-478.
77. Galli, A., et al., Antidiabetic thiazolidinediones inhibit collagen synthesis and hepatic stellate cell activation in vivo and in vitro. *Gastroenterology*, 2002. **122**(7): p. 1924-1940.
78. Leclercq, I.A., et al., Leptin is essential for the hepatic fibrogenic response to chronic liver injury. *Journal of Hepatology*, 2002. **37**(2): p. 206-213.
79. Kamada, Y., et al., Enhanced carbon tetrachloride-induced liver fibrosis in mice lacking adiponectin. *Gastroenterology*, 2003. **125**(6): p. 1796-1807.

80. Druker, B. and N. Lydon, Lessons learned from the development of an Abl tyrosine kinase inhibitor for chronic myelogenous leukemia. *J Clin Invest*, 2000. **105**(1): p. 3-7.
81. Joensuu, H., et al., Effect of the Tyrosine Kinase Inhibitor STI571 in a Patient with a Metastatic Gastrointestinal Stromal Tumor. *New England Journal of Medicine*, 2001. **344**(14): p. 1052-1056.
82. Yoshiji, H., et al., Imatinib mesylate (STI-571) attenuates liver fibrosis development in rats. *American Journal of Physiology - Gastrointestinal and Liver Physiology*, 2005. **288**(5): p. G907-G913.
83. George, J., et al., In vivo inhibition of rat stellate cell activation by soluble transforming growth factor  $\beta$  type II receptor: A potential new therapy for hepatic fibrosis. *Proceedings of the National Academy of Sciences*, 1999. **96**(22): p. 12719-12724.
84. Okuno, M., et al., Prevention of rat hepatic fibrosis by the protease inhibitor, camostat mesilate, via reduced generation of active TGF- $\beta$ . *Gastroenterology*, 2001. **120**(7): p. 1784-1800.
85. Zheng, S. and A. Chen, Disruption of transforming growth factor- $\beta$  signaling by curcumin induces gene expression of peroxisome proliferator-activated receptor- $\gamma$  in rat hepatic stellate cells. *American Journal of Physiology - Gastrointestinal and Liver Physiology*, 2007. **292**(1): p. G113-G123.
86. Gressner AM, et al., Roles of TGF-beta in hepatic fibrosis. *Front Biosci.*, 2002. **7**: p. 793-807.
87. Williams, E.J., et al., Relaxin inhibits effective collagen deposition by cultured hepatic stellate cells and decreases rat liver fibrosis in vivo. *Gut*, 2001. **49**(4): p. 577-583.
88. Cho, J.-J., et al., An oral endothelin-A receptor antagonist blocks collagen synthesis and deposition in advanced rat liver fibrosis. *Gastroenterology*, 2000. **118**(6): p. 1169-1178.
89. Iredale, J.P., et al., Mechanisms of spontaneous resolution of rat liver fibrosis. Hepatic stellate cell apoptosis and reduced hepatic expression of

metalloproteinase inhibitors. *The Journal of Clinical Investigation*, 1998. **102**(3): p. 538-549.

90. Wright, M.C., et al., Gliotoxin stimulates the apoptosis of human and rat hepatic stellate cells and enhances the resolution of liver fibrosis in rats. *Gastroenterology*, 2001. **121**(3): p. 685-98.

91. Oakley, F., et al., Inhibition of inhibitor of kappaB kinases stimulates hepatic stellate cell apoptosis and accelerated recovery from rat liver fibrosis. *Gastroenterology*, 2005. **128**(1): p. 108-20.

92. Oakley, F., et al., Hepatocytes Express Nerve Growth Factor during Liver Injury: Evidence for Paracrine Regulation of Hepatic Stellate Cell Apoptosis. *Am J Pathol*, 2003. **163**(5): p. 1849-1858.

93. Issa, R., et al., Mutation in collagen-1 that confers resistance to the action of collagenase results in failure of recovery from CCl4-induced liver fibrosis, persistence of activated hepatic stellate cells, and diminished hepatocyte regeneration. *The FASEB Journal*, 2003. **17**(1): p. 47-49.

94. Roderfeld, M., et al., Cytokine blockade inhibits hepatic tissue inhibitor of metalloproteinase-1 expression and up-regulates matrix metalloproteinase-9 in toxic liver injury. *Liver International*, 2006. **26**(5): p. 579-586.

95. Arendt, E., et al., Enhanced matrix degradation after withdrawal of TGF- $\beta$ 1 triggers hepatocytes from apoptosis to proliferation and regeneration. *Cell Proliferation*, 2005. **38**(5): p. 287-299.

96. Roderfeld, M., et al., Inhibition of hepatic fibrogenesis by matrix metalloproteinase-9 mutants in mice. *The FASEB Journal*, 2006. **20**(3): p. 444-454.

97. Parsons, C.J., et al., Antifibrotic effects of a tissue inhibitor of metalloproteinase-1 antibody on established liver fibrosis in rats. *Hepatology*, 2004. **40**(5): p. 1106-1115.

98. Orr, J.G., et al., Mechanism of action of the antifibrogenic compound gliotoxin in rat liver cells. *Hepatology*, 2004. **40**(1): p. 232-42.

99. Pahl, H.L., et al., The immunosuppressive fungal metabolite gliotoxin specifically inhibits transcription factor NF-kappaB. *The Journal of Experimental Medicine*, 1996. **183**(4): p. 1829-1840.
100. Beljaars, L., et al., Albumin modified with mannose 6-phosphate: A potential carrier for selective delivery of antifibrotic drugs to rat and human hepatic stellate cells. *Hepatology*, 1999. **29**(5): p. 1486-1493.
101. De Bleserc, P.J., et al., Insulinlike growth factor—ii/mannose 6-phosphate receptor is expressed on ccl4-exposed rat fat-storing cells and facilitates activation of latent transforming growth factor- $\beta$  in cocultures with sinusoidal endothelial cells. *Hepatology*, 1995. **21**(5): p. 1429-1437.
102. Gonzalo, T., et al., Short term treatment with losartan targeted to activated stellate cells reduces advanced liver fibrogenesis: a new strategy to treat liver fibrosis. *Hepatology*, 2005. **42**: p. 604A.
103. Greupink, R., et al., The Antiproliferative Drug Doxorubicin Inhibits Liver Fibrosis in Bile Duct-Ligated Rats and Can Be Selectively Delivered to Hepatic Stellate Cells in Vivo. *Journal of Pharmacology and Experimental Therapeutics*, 2006. **317**(2): p. 514-521.
104. Gonzalo, T., et al., Selective targeting of pentoxifylline to hepatic stellate cells using a novel platinum-based linker technology. *Journal of Controlled Release*, 2006. **111**(1-2): p. 193-203.
105. Hagens, W.I., et al., Cellular Targeting of the Apoptosis-Inducing Compound Gliotoxin to Fibrotic Rat Livers. *Journal of Pharmacology and Experimental Therapeutics*, 2008. **324**(3): p. 902-910.
106. Wiedenmann, B. and W.W. Franke, Identification and localization of synaptophysin, an integral membrane glycoprotein of Mr 38,000 characteristic of presynaptic vesicles. *Cell*, 1985. **41**(3): p. 1017-1028.
107. Gincel, D. and V. Shoshan-Barmatz, The Synaptic Vesicle Protein Synaptophysin: Purification and Characterization of Its Channel Activity. *Biophysical Journal*, 2002. **83**(6): p. 3223-3229.
108. Cassiman, D., et al., Hepatic stellate cell/myofibroblast subpopulations in fibrotic human and rat livers. *Journal of Hepatology*, 2002. **36**(2): p. 200-9.

109. Magness, S.T., et al., A dual reporter gene transgenic mouse demonstrates heterogeneity in hepatic fibrogenic cell populations. *Hepatology*, 2004. **40**(5): p. 1151-1159.
110. Roskams, T., et al., Neuroregulation of the neuroendocrine compartment of the liver. *The Anatomical Record Part A: Discoveries in Molecular, Cellular, and Evolutionary Biology*, 2004. **280A**(1): p. 910-923.
111. Cassiman, D., et al., Hepatic stellate cells do not derive from the neural crest. *Journal of Hepatology*, 2006. **44**(6): p. 1098-1104.
112. Baba, S., et al., Commitment of bone marrow cells to hepatic stellate cells in mouse. *Journal of Hepatology*, 2004. **40**(2): p. 255-260.
113. Kisseleva, T., et al., Bone marrow-derived fibrocytes participate in pathogenesis of liver fibrosis. *Journal of Hepatology*, 2006. **45**(3): p. 429-438.
114. Robertson, H., et al., Biliary epithelial-mesenchymal transition in posttransplantation recurrence of primary biliary cirrhosis. *Hepatology*, 2007. **45**(4): p. 977-981.
115. Elrick, L.J., et al., Generation of a monoclonal human single chain antibody fragment to hepatic stellate cells--a potential mechanism for targeting liver anti-fibrotic therapeutics. *Journal of Hepatology*, 2005. **42**(6): p. 888-96.
116. Douglass, A., et al., Antibody-targeted myofibroblast apoptosis reduces fibrosis during sustained liver injury.[Erratum appears in *J Hepatol.* 2010 May;52(5):779]. *Journal of Hepatology*, 2008. **49**(1): p. 88-98.
117. Menghini, G., One-second needle biopsy of the liver. *Gastroenterology*, 1958. **35**(2): p. 190-199.
118. Scheur, P.J., Classification of chronic viral hepatitis: a need for reassessment. *Journal of Hepatology*, 1991. **13**: p. 372-374.
119. Bedossa, P., Intraobserver and Interobserver Variations in Liver Biopsy Interpretation in Patients with Chronic Hepatitis C. *Hepatology*, 1994. **20**(1): p. 15-20.

120. Ishak, K., et al., Histological grading and staging of chronic hepatitis. *Journal of Hepatology*, 1995. **22**(6): p. 696-699.
121. Stauber, R., Lackner C., Noninvasive diagnosis of hepatic fibrosis in chronic hepatitis C. *World J Gastroenterol*, 2007. **13**: p. 4287-4284.
122. Regev, A., et al., Sampling error and intraobserver variation in liver biopsy in patients with chronic HCV infection. *American Journal of Gastroenterology*, 2002. **97**(10): p. 2614-8.
123. Collazos, J. and F. Díaz, Role of the measurement of serum procollagen type III N-terminal peptide in the evaluation of liver diseases. *Clinica Chimica Acta*, 1994. **227**(1–2): p. 37-43.
124. Guechot, J., et al., Serum hyaluronan as a marker of liver fibrosis in chronic viral hepatitis C: effect of [alpha]-interferon therapy. *Journal of Hepatology*, 1995. **22**(1): p. 22-26.
125. Lydatakis, H., et al., Non-invasive markers to predict the liver fibrosis in non-alcoholic fatty liver disease. *Liver International*, 2006. **26**(7): p. 864-871.
126. Gressner, A.-M., C.-F. Gao, and O.-A. Gressner, Non-invasive biomarkers for monitoring the fibrogenic process in liver: a short survey. *World Journal of Gastroenterology*, 2009. **15**(20): p. 2433-40.
127. Kawasaki, T., et al., Serum thrombopoietin levels in patients with chronic hepatitis and liver cirrhosis. *The American Journal of Gastroenterology*, 1999. **94**(7): p. 1918-1922.
128. Wai, C.-T., et al., A simple noninvasive index can predict both significant fibrosis and cirrhosis in patients with chronic hepatitis C. *Hepatology*, 2003. **38**(2): p. 518-526.
129. Imbert-Bismut, F., et al., Biochemical markers of liver fibrosis in patients with hepatitis C virus infection: a prospective study. *The Lancet*, 2001. **357**(9262): p. 1069-1075.
130. Afdhal, N.H. and D. Nunes, Evaluation of liver fibrosis: a concise review. *American Journal of Gastroenterology*, 2004. **99**(6): p. 1160-74.

131. Poynard, T., et al., Meta-analyses of FibroTest diagnostic value in chronic liver disease. *BMC Gastroenterology*, 2007. **7**(1): p. 40.
132. Poynard, T., et al., Overview of the diagnostic value of biochemical markers of liver fibrosis (FibroTest, HCV-Fibrosure) and necrosis (ActiTest) in patients with chronic hepatitis C. *Comp Hepatol*, 2004. **3**: p. 8.
133. Sebastiani, G., et al., Stepwise combination algorithms of non-invasive markers to diagnose significant fibrosis in chronic hepatitis C. *J Hepatol*, 2006. **44**: p. 686 - 93.
134. Rossi, E., et al., Validation of the FibroTest biochemical markers score in assessing liver fibrosis in hepatitis C patients. *Clin Chem*, 2003. **49**: p. 450 - 454.
135. Forns, X., et al., Identification of chronic hepatitis C patients without hepatic fibrosis by a simple predictive model. *Hepatology*, 2002. **36**(4): p. 986-992.
136. Adams, L.A., et al., Hepascore: An Accurate Validated Predictor of Liver Fibrosis in Chronic Hepatitis C Infection. *Clin Chem*, 2005. **51**(10): p. 1867-1873.
137. Becker, L., et al., Validation of Hepascore, Compared With Simple Indices of Fibrosis, in Patients With Chronic Hepatitis C Virus Infection in United States. *Clinical Gastroenterology and Hepatology*, 2009. **7**(6): p. 696-701.
138. Hess, C.F., et al., Diagnosis of liver cirrhosis with US: receiver-operating characteristic analysis of multidimensional caudate lobe indexes. *Radiology*, 1989. **171**(2): p. 349-351.
139. de Ledinghen, V. and J. Vergniol, Transient elastography (FibroScan). *Gastroenterologie Clinique et Biologique*, 2008. **32**(6 Suppl 1): p. 58-67.
140. Ziol, M., et al., Noninvasive assessment of liver fibrosis by measurement of stiffness in patients with chronic hepatitis C. *Hepatology*, 2005. **41**(1): p. 48-54.
141. Foucher, J., et al., Prevalence and factors associated with failure of liver stiffness measurement using FibroScan in a prospective study of 2114

- examinations. *European Journal of Gastroenterology & Hepatology*, 2006. **18**(4): p. 411-412.
142. Fraquelli, M., et al., Reproducibility of transient elastography in the evaluation of liver fibrosis in patients with chronic liver disease. *Gut*, 2007. **56**(7): p. 968-973.
143. Shaheen, A.A.M., A.F. Wan, and R.P. Myers, FibroTest and FibroScan for the prediction of hepatitis C-related fibrosis: a systematic review of diagnostic test accuracy. *American Journal of Gastroenterology*, 2007. **102**(11): p. 2589-600.
144. Aguirre, D.A., et al., Liver Fibrosis: Noninvasive Diagnosis with Double Contrast Material-enhanced MR Imaging<sup>1</sup>. *Radiology*, 2006. **239**(2): p. 425-437.
145. Castera, L., et al., Prospective comparison of transient elastography, Fibrotest, APRI, and liver biopsy for the assessment of fibrosis in chronic hepatitis C. *Gastroenterology*, 2005. **128**(2): p. 343-50.
146. Boursier, J., et al., The combination of a blood test and Fibroscan improves the non-invasive diagnosis of liver fibrosis. *Liver International*, 2009. **29**(10): p. 1507-15.
147. Mangelsdorf DJ, T.C., Beato M, Herrlich P, Schütz G, Umesono K, Blumberg B, Kastner P, Mark M, Chambon P, Evans RM., The nuclear receptor superfamily: the second decade. *Cell*, 1995. **83**: p. 835-839.
148. Kliewer, S.A., et al., An Orphan Nuclear Receptor Activated by Pregnanes Defines a Novel Steroid Signaling Pathway. *Cell*, 1998. **92**(1): p. 73-82.
149. Sandanaraj, E., et al., PXR Pharmacogenetics: Association of Haplotypes with Hepatic CYP3A4 and ABCB1 Messenger RNA Expression and Doxorubicin Clearance in Asian Breast Cancer Patients. *Clinical Cancer Research*, 2008. **14**(21): p. 7116-7126.
150. Madhu, C. and C.D. Klaassen, Protective effect of pregnenolone-16 alpha-carbonitrile on acetaminophen-induced hepatotoxicity in hamsters. *Toxicology and Applied Pharmacology*, 1991. **109**(2): p. 305-313.

151. Liu, L. and C.D. Klaassen, Regulation of hepatic sulfotransferases by steroidal chemicals in rats. *Drug Metabolism and Disposition*, 1996. **24**(8): p. 854-858.
152. Watkins, J.B. and C.D. Klaassen, Induction of UDP-glucuronosyltransferase activities in Gunn, heterozygous, and Wistar rat livers by pregnenolone-16 alpha-carbonitrile. *Drug Metabolism and Disposition*, 1982. **10**(6): p. 590-594.
153. Chen, C., J.L. Staudinger, and C.D. Klaassen, Nuclear receptor, pregnane X receptor is required for induction of UDP-Glucuronosyltransferases in mouse liver by pregnenolone-16  $\alpha$ -carbonitrile. *Drug Metabolism and Disposition*, 2003. **31**(7): p. 908-915.
154. Lehmann, J.M., et al., The human orphan nuclear receptor PXR is activated by compounds that regulate CYP3A4 gene expression and cause drug interactions. *The Journal of Clinical Investigation*, 1998. **102**(5): p. 1016-1023.
155. Kliewer, S.A., B. Goodwin, and T.M. Willson, The Nuclear Pregnane X Receptor: A Key Regulator of Xenobiotic Metabolism. *Endocrine Reviews*, 2002. **23**(5): p. 687-702.
156. Maglich, J.M., et al., Nuclear Pregnane X Receptor and Constitutive Androstane Receptor Regulate Overlapping but Distinct Sets of Genes Involved in Xenobiotic Detoxification. *Molecular Pharmacology*, 2002. **62**(3): p. 638-646.
157. Guo, G.L., et al., Induction of Rat Organic Anion Transporting Polypeptide 2 by Pregnenolone-16  $\alpha$  -carbonitrile Is via Interaction with Pregnane X Receptor. *Molecular Pharmacology*, 2002. **61**(4): p. 832-839.
158. Staudinger, J., et al., Coordinate Regulation of Xenobiotic and Bile Acid Homeostasis by Pregnane X Receptor. *Drug Metabolism and Disposition*, 2001. **29**(11): p. 1467-1472.
159. Kliewer, S.A., The Nuclear Pregnane X Receptor Regulates Xenobiotic Detoxification. *The Journal of Nutrition*, 2003. **133**(7): p. 2444S-2447S.

160. Edwards, D.P., The Role of Coactivators and Corepressors in the Biology and Mechanism of Action of Steroid Hormone Receptors. *Journal of Mammary Gland Biology and Neoplasia*, 2000. **5**(3): p. 307-324.
161. Wrighton, S.A., et al., Demonstration in multiple species of inducible hepatic cytochromes P-450 and their mRNAs related to the glucocorticoid-inducible cytochrome P-450 of the rat. *Molecular Pharmacology*, 1985. **28**(3): p. 312-321.
162. Kocarek, T.A., et al., Comparative analysis of cytochrome P4503A induction in primary cultures of rat, rabbit, and human hepatocytes. *Drug Metabolism and Disposition*, 1995. **23**(3): p. 415-421.
163. Watkins, R.E., et al., The Human Nuclear Xenobiotic Receptor PXR: Structural Determinants of Directed Promiscuity. *Science*, 2001. **292**(5525): p. 2329-2333.
164. Mathijssen, R.H.J., et al., Effects of St. John's Wort on Irinotecan Metabolism. *Journal of the National Cancer Institute*, 2002. **94**(16): p. 1247-1249.
165. Grosset, J. and S. Leventis, Adverse Effects of Rifampin. *Review of Infectious Diseases*, 1983. **5**(Supplement 3): p. S440-S446.
166. Zhou, C., et al., Mutual repression between steroid and xenobiotic receptor and NF- $\kappa$ B signaling pathways links xenobiotic metabolism and inflammation. *The Journal of Clinical Investigation*, 2006. **116**(8): p. 2280-2289.
167. Morgan, E., Regulation of cytochromes P450 during inflammation and infection. *Drug Metab Rev.*, 1997. **29**: p. 1129-1188.
168. Auphan, N., et al., Immunosuppression by Glucocorticoids: Inhibition of NF- $\kappa$ B Activity Through Induction of I $\kappa$ B Synthesis. *Science*, 1995. **270**(5234): p. 286-290.
169. Yamamoto, Y. and R.B. Gaynor, Therapeutic potential of inhibition of the NF- $\kappa$ B pathway in the treatment of inflammation and cancer. *The Journal of Clinical Investigation*, 2001. **107**(2): p. 135-142.

170. Shah, Y.M., et al., Pregnane X receptor activation ameliorates DSS-induced inflammatory bowel disease via inhibition of NF- $\kappa$ B target gene expression. *American Journal of Physiology - Gastrointestinal and Liver Physiology*, 2007. **292**(4): p. G1114-G1122.
171. Hogaboam CM, S.K., Chensue SW, Steinhauser ML, Lukacs NW, Gauldie J, Strieter RM, Kunkel SL., Macrophage inflammatory protein-2 gene therapy attenuates adenovirus- and acetaminophen-mediated hepatic injury. *Gene Ther.*, 1999. **6**: p. 573-84.
172. Marek, C.J., et al., Pregnenolone-16 $\alpha$ -carbonitrile inhibits rodent liver fibrogenesis via PXR (pregnane X receptor)-dependent and PXR-independent mechanisms. *Biochemical Journal*, 2005. **387**(Pt 3): p. 601-8.
173. Haughton, E.L., et al., Pregnane X receptor activators inhibit human hepatic stellate cell transdifferentiation in vitro. *Gastroenterology*, 2006. **131**(1): p. 194-209.
174. Wright, M.C., The impact of pregnane X receptor activation on liver fibrosis. *Biochemical Society Transactions*, 2006. **34**(Pt 6): p. 1119-23.
175. Axon, A., et al., A mechanism for the anti-fibrogenic effects of the pregnane X receptor (PXR) in the liver: inhibition of NF- $\kappa$ B? *Toxicology*, 2008. **246**(1): p. 40-4.
176. Kweon, Y.-O., et al., Gliotoxin-mediated apoptosis of activated human hepatic stellate cells. *Journal of Hepatology*, 2003. **39**(1): p. 38-46.
177. Wallace, K., et al., The PXR is a drug target for chronic inflammatory liver disease. *Journal of Steroid Biochemistry & Molecular Biology*, 2010. **120**(2-3): p. 137-48.
178. Elsharkawy, A.M. and D.A. Mann, Nuclear factor- $\kappa$ B and the hepatic inflammation-fibrosis-cancer axis. *Hepatology*, 2007. **46**(2): p. 590-597.
179. Gilmore, T.D., Introduction to NF- $\kappa$ B: players, pathways, perspectives. *Oncogene*, 2006. **25**(51): p. 6680-6684.
180. Ribeiro PS, C.-P.H., Solá S, Castro RE, Ramalho RM, Baptista A, Moura MC, Camilo ME, Rodrigues CM., Hepatocyte apoptosis, expression of

death receptors, and activation of NF-kappaB in the liver of nonalcoholic and alcoholic steatohepatitis patients. *Am J Gast*, 2004. **99**(9): p. 1708-17.

181. Oakley, F., et al., Nuclear Factor-κB1 (p50) Limits the Inflammatory and Fibrogenic Responses to Chronic Injury. *The American Journal of Pathology*, 2005. **166**(3): p. 695-708.

182. Racanelli, V. and B. Rehermann, The liver as an immunological organ. *Hepatology*, 2006. **43**(S1): p. S54-S62.

183. Elsharkawy, A.M., et al., Persistent activation of nuclear factor-kappaB in cultured rat hepatic stellate cells involves the induction of potentially novel Rel-like factors and prolonged changes in the expression of IkappaB family proteins. *Hepatology*, 1999. **30**(3): p. 761-9.

184. Lv P, L.H., Zhou XP, Xiao YJ, Paul SC, Si XM, Zhou YH., Reversal effect of thalidomide on established hepatic cirrhosis in rats via inhibition of nuclear factor-kappaB/inhibitor of nuclear factor-kappaB pathway. *Archives of Medical Research*, 2007. **38**(1): p. 15-27.

185. Friedman, S.L., et al., Hepatic lipocytes: the principal collagen-producing cells of normal rat liver. *Proceedings of the National Academy of Sciences*, 1985. **82**(24): p. 8681-8685.

186. Friedman, S.L., *The Cellular Basis of Hepatic Fibrosis -- Mechanisms and Treatment Strategies*. *New England Journal of Medicine*, 1993. **328**(25): p. 1828-1835.

187. Carlsen, H., et al., In Vivo Imaging of NF-κB Activity. *The Journal of Immunology*, 2002. **168**(3): p. 1441-1446.

188. Trim, J.E., et al., Upstream Tissue Inhibitor of Metalloproteinases-1 (TIMP-1) Element-1, a Novel and Essential Regulatory DNA Motif in the Human TIMP-1 Gene Promoter, Directly Interacts with a 30-kDa Nuclear Protein. *Journal of Biological Chemistry*, 2000. **275**(9): p. 6657-6663.

189. Choi, I., et al., IL-6 induces hepatic inflammation and collagen synthesis in vivo. *Clinical & Experimental Immunology*, 1994. **95**(3): p. 530-535.

190. Mancini, R., A. Benedetti, and A.M. Jezequel, An interleukin-1 receptor antagonist decreases fibrosis induced by dimethylnitrosamine in rat liver. *Virchows Archiv*, 1994. **424**(1): p. 25-31.
191. Gieling, R.G., K. Wallace, and Y.-P. Han, Interleukin-1 participates in the progression from liver injury to fibrosis. *American Journal of Physiology - Gastrointestinal and Liver Physiology*, 2009. **296**(6): p. G1324-G1331.
192. Ruddell, R.G., et al., A role for serotonin (5-HT) in hepatic stellate cell function and liver fibrosis. *American Journal of Pathology*, 2006. **169**(3): p. 861-76.
193. Hemmann, S., et al., Expression of MMPs and TIMPs in liver fibrosis – a systematic review with special emphasis on anti-fibrotic strategies. *Journal of Hepatology*, 2007. **46**(5): p. 955-975.
194. Oakley, F., et al., Angiotensin II activates I kappaB kinase phosphorylation of RelA at Ser 536 to promote myofibroblast survival and liver fibrosis. *Gastroenterology*, 2009. **136**(7): p. 2334-2344.e1.
195. Potter, J.J., et al., Transdifferentiation of Rat Hepatic Stellate Cells Results in Leptin Expression. *Biochemical and Biophysical Research Communications*, 1998. **244**(1): p. 178-182.
196. F. Marra, S. Aleefi, C. Bertolani, I. Petrai, F. Vizzutti., Adipokines and liver fibrosis. *European Review for Medical and Pharmacological Sciences*, 2005. **9**: p. 279-284.
197. Zeremski, M., et al., Intrahepatic levels of CXCR3-associated chemokines correlate with liver inflammation and fibrosis in chronic hepatitis C. *Hepatology*, 2008. **48**(5): p. 1440-1450.
198. Marra, F., et al., Cultured human liver fat-storing cells produce monocyte chemoattractant protein-1. Regulation by proinflammatory cytokines. *The Journal of Clinical Investigation*, 1993. **92**(4): p. 1674-1680.
199. Sprenger, H., et al., Induction of neutrophil-attracting chemokines in transforming rat hepatic stellate cells. *Gastroenterology*, 1997. **113**(1): p. 277-285.

200. Ajuebor, M.N., et al., CCL3/MIP-1 $\alpha$  is pro-inflammatory in murine T cell-mediated hepatitis by recruiting CCR1-expressing CD4<sup>+</sup> T cells to the liver. *European Journal of Immunology*, 2004. **34**(10): p. 2907-2918.
201. Wald, O., et al., Involvement of the CXCL12/CXCR4 pathway in the advanced liver disease that is associated with hepatitis C virus or hepatitis B virus. *European Journal of Immunology*, 2004. **34**(4): p. 1164-1174.
202. Hensley, K., et al., Dietary choline restriction causes complex I dysfunction and increased H<sub>2</sub>O<sub>2</sub> generation in liver mitochondria. *Carcinogenesis*, 2000. **21**(5): p. 983-989.
203. Browning, J.D. and J.D. Horton, Molecular mediators of hepatic steatosis and liver injury. *The Journal of Clinical Investigation*, 2004. **114**(2): p. 147-152.
204. Billiar, T.R., et al., Modulation of nitrogen oxide synthesis in vivo: NG-monomethyl-L-arginine inhibits endotoxin-induced nitrate/nitrite biosynthesis while promoting hepatic damage. *Journal of Leukocyte Biology*, 1990. **48**(6): p. 565-9.
205. Geller M.D, D.A., et al., Nitric Oxide Synthase Expression Is Induced in Hepatocytes in Vivo during Hepatic Inflammation. *Journal of Surgical Research*, 1993. **55**(4): p. 427-432.
206. Bochkov, V.N., et al., Protective role of phospholipid oxidation products in endotoxin-induced tissue damage. *Nature*, 2002. **419**(6902): p. 77-81.
207. Vogelstein, B. and D. Gillespie, Preparative and analytical purification of DNA from agarose. *Proceedings of the National Academy of Sciences*, 1979. **76**(2): p. 615-619.
208. Chomczynski, P. and N. Sacchi, Single-step method of RNA isolation by acid guanidinium thiocyanate-phenol-chloroform extraction. *Analytical Biochemistry*, 1987. **162**(1): p. 156-159.
209. Manchester, K., Value of A<sub>260</sub>/A<sub>280</sub> ratios for measurement of purity of nucleic acids. *Biotechniques*, 1995. **19**(2): p. 208-210.

210. Wilfinger, W.W., K. Mackey, and P. Chomczynski, Effect of pH and ionic strength on the spectrophotometric assessment of nucleic acid purity. *Biotechniques*, 1997. **22**(3).
211. Yuan, J., et al., Statistical analysis of real-time PCR data. *BMC Bioinformatics*, 2006. **7**(1): p. 85.
212. Lowry, O.H., et al., Protein measurement with the folin phenol reagent. *Journal of Biological Chemistry*, 1951. **193**(1): p. 265-275.
213. Laemmli, U.K., Cleavage of Structural Proteins during the Assembly of the Head of Bacteriophage T4. *Nature*, 1970. **227**(5259): p. 680-685.
214. Junqueira, L., G. Bignolas, and R. Brentani, Picrosirius staining plus polarization microscopy, a specific method for collagen detection in tissue sections. *The Histochemical Journal*, 1979. **11**(4): p. 447-455.
215. Fox, M., et al., Detection of *Aspergillus fumigatus* mycotoxins: immunogen synthesis and immunoassay development. *Journal of Microbiological Methods*, 2004. **56**(2): p. 221-230.
216. Winter, H., et al., Therapeutic T cells induce tumor-directed chemotaxis of innate immune cells through tumor-specific secretion of chemokines and stimulation of B16BL6 melanoma to secrete chemokines. *Journal of Translational Medicine*, 2007. **5**(1): p. 56.
217. Reeves, H.L. and S.L. Friedman, Activation of hepatic stellate cells--a key issue in liver fibrosis. *Frontiers in Bioscience*, 2002. **7**: p. d808-26.
218. Kovar, J.L., et al., A systematic approach to the development of fluorescent contrast agents for optical imaging of mouse cancer models. *Analytical Biochemistry*, 2007. **367**(1): p. 1-12.
219. Wiedenmann, B., et al., Synaptophysin: a marker protein for neuroendocrine cells and neoplasms. *Proceedings of the National Academy of Sciences*, 1986. **83**(10): p. 3500-3504.
220. Carpino, G., et al., Alpha-SMA expression in hepatic stellate cells and quantitative analysis of hepatic fibrosis in cirrhosis and in recurrent chronic hepatitis after liver transplantation. *Digestive and Liver Disease*, 2005. **37**(5): p. 349-356.

221. Gibson AP, H.J., Arridge SR., Recent advances in diffuse optical imaging. *Phys Med Biol.*, 2005. **21**(50): p. 1-43.
222. Frangioni, J.V., In vivo near-infrared fluorescence imaging. *Current Opinion in Chemical Biology*, 2003. **7**(5): p. 626-634.
223. Parungo, C.P., et al., Intraoperative identification of esophageal sentinel lymph nodes with near-infrared fluorescence imaging. *The Journal of Thoracic and Cardiovascular Surgery*, 2005. **129**(4): p. 844-850.
224. Poynard, T., et al., Natural history of HCV infection. *Best Practice & Research Clinical Gastroenterology*, 2000. **14**(2): p. 211-228.
225. Barrett, T., et al., In vivo Diagnosis of Epidermal Growth Factor Receptor Expression using Molecular Imaging with a Cocktail of Optically Labeled Monoclonal Antibodies. *Clinical Cancer Research*, 2007. **13**(22): p. 6639-6648.
226. Donath, M. and P. Halban, Decreased beta-cell mass in diabetes: significance, mechanisms and therapeutic implications. *Diabetologia*, 2004. **47**(3): p. 581-589.
227. Gambhir, S.S., Molecular imaging of cancer with positron emission tomography. *Nat Rev Cancer*, 2002. **2**(9): p. 683-693.
228. Kershenovich DS and A. Weissbrod, Liver fibrosis and inflammation. A review. *Annals of Hepatology*, 2003. **2**(4): p. 159-63.
229. Elsharkawy, A.M., F. Oakley, and D.A. Mann, The role and regulation of hepatic stellate cell apoptosis in reversal of liver fibrosis. *Apoptosis*, 2005. **10**(5): p. 927-39.
230. Iredale, J.P., Models of liver fibrosis: exploring the dynamic nature of inflammation and repair in a solid organ. *The Journal of Clinical Investigation*, 2007. **117**(3): p. 539-548.
231. Friedman, S.L., Hepatic stellate cells: protean, multifunctional, and enigmatic cells of the liver. *Physiological Reviews*, 2008. **88**(1): p. 125-72.

232. Parola, M., F. Marra, and M. Pinzani, Myofibroblast like cells and liver fibrogenesis: Emerging concepts in a rapidly moving scenario. *Molecular Aspects of Medicine*, 2008. **29**(1): p. 58-66.
233. Russo, F.P., et al., The Bone Marrow Functionally Contributes to Liver Fibrosis. *Gastroenterology*, 2006. **130**(6): p. 1807-1821.
234. Friedman, S.L., The answer: angiotensin II. The question: what do inflammation, oxidant stress and fibrogenesis have in common? *Journal of Hepatology*, 2004. **40**(6): p. 1050-2.
235. Ramadori, G., et al., Physiology and pathophysiology of liver inflammation, damage and repair. *Journal of physiology and pharmacology : an official journal of the Polish Physiological Society*, 2008. **59 Suppl 1**: p. 107-17.
236. Svegliati Baroni, G., et al., Fibrogenic effect of oxidative stress on rat hepatic stellate cells. *Hepatology*, 1998. **27**(3): p. 720-726.
237. Wheeler, M.D., et al., The role of kupffer cell oxidant production in early ethanol-induced liver disease. *Free Radical Biology and Medicine*, 2001. **31**(12): p. 1544-1549.
238. Wink, D.A. and J.B. Mitchell, Chemical biology of nitric oxide: insights into regulatory, cytotoxic, and cytoprotective mechanisms of nitric oxide. *Free Radical Biology and Medicine*, 1998. **25**(4): p. 434-456.
239. Cogswell, J.P., et al., NF-kappa B regulates IL-1 beta transcription through a consensus NF- kappa B binding site and a nonconsensus CRE-like site. *The Journal of Immunology*, 1994. **153**(2): p. 712-723.

**Chapter 9.0 - Published abstracts and manuscripts**

## 9.1 Abstracts

### 9.1.1 British Toxicology Society (BTS) Annual Conference 2009

#### Hepatic myofibroblasts are pro-inflammatory and activate NF- $\kappa$ B in monocytes via a soluble factor.

Stephen Hill<sup>1</sup>, Matthew C Wright<sup>1</sup>

<sup>1</sup>Institute Cellular Medicine, Newcastle University, UK. [Stephen.Hill1@ncl.ac.uk](mailto:Stephen.Hill1@ncl.ac.uk)

When the liver is injured, hepatic myofibroblasts proliferate and function to re-model the extracellular matrix as part of a coordinated multi-cellular response that leads to a regeneration of liver tissue (Wallace *et al*, 2008). The trans-differentiation of hepatic stellate cells is a major source of hepatic myofibroblasts. However, the signal that initiates the process of trans-differentiation is not known but has been proposed to originate from monocyte and/or macrophage-derived oxidative stress and cytokines (Wallace *et al*, 2008). We hypothesize that the initiating signal could derive from a population of myofibroblasts themselves, through release of a factor(s) that activate monocytes /macrophages, which then release oxidizing molecules and cytokines to further promote trans-differentiation. To test this hypothesis, a human liver myofibroblast (LX-2) cell line was cultured with a non-adherent human U-937 monocyte cell line stably-transfected with a luciferase reporter gene under control of a concatamer of NF- $\kappa$ B response elements (Axon *et al*, 2008).

LX-2 (adherent) and U-937 (non-adherent) cells were routinely cultured in Dulbecco's modified eagle media (DMEM) and RPMI-1640 media respectively, both supplemented with 10% foetal calf serum (FCS) and antibiotics. For experiments, LX-2 cells in 6 well plates were cultured to 50% confluence, washed 3 times with phosphate buffered saline and cultured with  $1 \times 10^5$  U-937 cells in RPMI-1640 media and where indicated bacterial lipopolysaccharide (LPS). U-937 cells were incubated for 6 hours at 37°C, pelleted by centrifugation and re-suspended in a fixed volume of lysis buffer prior to determination of luciferase activity using a Dual-glo kit (Promega).

Table 1 shows that un-stimulated U-937 cells expressed low levels of luciferase activity. LPS – an established activator of NF- $\kappa$ B – significantly induced luciferase activity in U-937 cells as expected (Axon *et al*, 2008). Table 1 also shows that co-culturing U-937 cells with LX-2 cells significantly induced luciferase expression. Addition of LX-2-conditioned media also induced luciferase expression.

**Table 1.** Activation of NF- $\kappa$ B/induction of luciferase expression in U-937 cells.

Cultured cells		LPS (300ng/ml)	Luciferase activity (u/well)
LX-2 (myofibroblast)	U-937-NF- $\kappa$ B-luc (monocyte)		
-	-	-	226 $\pm$ 6.8
+	-	-	227 $\pm$ 5.6
-	+	-	234 $\pm$ 6.5
+	+	-	1420 $\pm$ 235.6*
+ <sup>\$</sup>	+	-	804 $\pm$ 69.2*
-	+	+	607 $\pm$ 67.9*

<sup>\$</sup>U-937 cells were treated with LX-2-condition medium (cells not in co-culture).

\*Significantly different from untreated U-937 cells using Student's T-test (two tailed), P > 95%. LPS, bacterial lipopolysaccharide.

NF- $\kappa$ B describes a series of transcription factor complexes that play a major role in the regulation of inflammatory gene expression. These data demonstrate that human liver myofibroblasts release a soluble factor that activates monocyte NF- $\kappa$ B transcriptional activity. These data therefore suggest that myofibroblasts regulate the inflammatory process and may release a soluble factor that could – *via* the release of pro-inflammatory molecules from monocytes and macrophages - impact on myofibroblast activity.

### References

Wallace K *et al.*, Liver fibrosis. *Biochem. J.* 2008; 41:1-18.

Axon A, *et al.* A mechanism for the anti-fibrogenic effects of the pregnane X receptor (PXR) in the liver: inhibition of NF-kappaB? *Toxicology.* 2008; 246:40-4.

Acknowledgements – Funded by the ESPRC.

### **9.1.2 International Society for Hepatic Sinusoidal Research (ISHSR) symposium 2010**

#### **Hepatic myofibroblasts are pro-inflammatory and activate NF- $\kappa$ B in monocytes *via* a soluble factor.**

Stephen Hill<sup>1</sup>, Matthew C Wright<sup>1</sup>

<sup>1</sup>Institute Cellular Medicine, Newcastle University, UK. [Stephen.Hill1@ncl.ac.uk](mailto:Stephen.Hill1@ncl.ac.uk)

After liver injury hepatic myofibroblasts proliferate re-modelling the extracellular matrix as part of a multi-cellular response leading to regeneration of liver tissue (Wallace *et al.*, 2008). The trans-differentiation of hepatic stellate cells is a major source of hepatic myofibroblasts. However, the signal initiating this trans-differentiation is unknown but proposed to originate from monocyte/macrophage-derived oxidative stress (Wallace *et al.*, 2008). We hypothesize that the signal could derive from a population of myofibroblasts themselves releasing a factor(s) that activates monocytes/macrophages, which then release oxidizing molecules and cytokines further promoting trans-differentiation. To test this hypothesis, LX-2 (human liver myofibroblast) cell line was cultured with human U-937 monocyte cell line stably-transfected with a luciferase reporter gene controlled by NF- $\kappa$ B response elements.

LX-2 cells were cultured in 6 well plates to 50% confluence, washed with 1xPBS before co-culture with  $1 \times 10^5$  U-937 cells, incubated for 6 hours at 37°C. U-937 cells were pelleted by centrifugation and re-suspended in passive lysis buffer prior to determination of luciferase activity.

Un-stimulated U-937 cells expressed low levels of luciferase activity, bacterial lipopolysaccharide – an established activator of NF- $\kappa$ B – significantly induced luciferase activity as expected (Axon *et al.*, 2008). Co-culture of U-937 cells with LX-2 cells significantly induced luciferase expression, as did the addition of LX-2-conditioned media.

These data demonstrate that hepatic myofibroblasts release a factor that activates monocyte NF- $\kappa$ B transcriptional activity, therefore suggesting that myofibroblasts regulate the inflammatory process and may release a soluble factor that could – *via* the release of pro-inflammatory molecules from monocytes/macrophages - impact on myofibroblast activity.

## References

Wallace K *et al.*, Liver fibrosis. *Biochem. J.* 2008; 41:1-18.

Axon A, *et al.* A mechanism for the anti-fibrogenic effects of the pregnane X receptor (PXR) in the liver: inhibition of NF-kappaB? *Toxicology.* 2008; 246:40-4.

**Acknowledgements** Funded by the ESPRC.

### 9.1.3 North East Postgraduate Conference (NEPG) 2011

#### Using the fluorescently labelled scAb C1-3 as a potential imaging agent of hepatic myofibroblasts and fibrosis

Stephen J. Hill, Anne Lakey and Matthew C. Wright.

Liver Research Group, Newcastle University, UK. [Stephen.hill1@ncl.ac.uk](mailto:Stephen.hill1@ncl.ac.uk)

A major obstacle limiting the discovery of novel anti-fibrotics is the lack of an effective way to rapidly quantify hepatic fibrosis, both in experimental and clinical studies. The aim of this investigation was to examine the potential of the hepatic myofibroblast-specific C1-3 scAb conjugated to a fluorescent dye as an imaging agent for hepatic fibrosis.

The C1-3 scAb was expressed in *e-coli*, purified and fluorescently labelled with CF750 (a fluorophore that emits light at a max 777nm) to generate the conjugate C1-3-<sup>CF750</sup>. C1-3-<sup>CF750</sup> was injected into both fibrotic (CCl<sub>4</sub> induced) and control mice. Upon completion of the CCl<sub>4</sub> treatment regimen, both whole body and ex vivo organs fluorescent scans were performed using IVIS optical imaging equipment.

Successful conjugation of C1-3 and CF750 was confirmed by SDS-PAGE and MALDI-TOF. C1-3-<sup>CF750</sup> retained its affinity and specificity for its target antigen (synaptophysin) as determined by both a synaptophysin specific ELISA. The *ex vivo* organ scans of the fibrotic mice (at all time points) exhibit significantly higher fluorescence than both the C1-3-<sup>CF750</sup> control and non-inject control mice. Sirius red and  $\alpha$ SMA immunohistochemical analysis confirmed the varying degrees of liver fibrosis induced between the different CCl<sub>4</sub> groups.

Fluorescently labelled C1-3 provides an effective way to determine liver fibrosis severity, in this instance the scAb cannot be used non-invasively, as only the *ex vivo* organ scans exhibit a significant difference between the control and fibrotic animals. However, a radioligand (e.g. <sup>18</sup>F-SFB) conjugated to the scAb, utilising the high sensitivity of positron emission topography would maximise the potential of C1-3 as a targeted imaging agent for liver fibrosis.

Funded by the EPSRC.

## 9.2 Published manuscripts

**The PXR is a drug target for chronic inflammatory liver disease.**

Wallace K, Cowie DE, Konstantinou DK, Hill SJ, Tjelle TE, Axon A, Koruth M, White SA, Carlsen H, Mann DA, Wright MC.